

2009 SUMMER RESEARCH PROGRAM FOR HIGH SCHOOL JUNIORS

AT THE

UNIVERSITY OF ROCHESTER'S

LABORATORY FOR LASER ENERGETICS

STUDENT RESEARCH REPORTS

PROGRAM COORDINATOR

Dr. R. Stephen Craxton

April 2010

Laboratory Report 360

2009 SUMMER RESEARCH PROGRAM FOR HIGH SCHOOL JUNIORS

AT THE

UNIVERSITY OF ROCHESTER'S

LABORATORY FOR LASER ENERGETICS

STUDENT RESEARCH REPORTS

PROGRAM COORDINATOR

Dr. R. Stephen Craxton

LABORATORY FOR LASER ENERGETICS

University of Rochester

250 East River Road

Rochester, NY 14623-1299

During the summer of 2009, 16 students from Rochester-area high schools participated in the Laboratory for Laser Energetics' Summer High School Research Program. The goal of this program is to excite a group of high school students about careers in the areas of science and technology by exposing them to research in a state-of-the-art environment. Too often, students are exposed to "research" only through classroom laboratories, which have prescribed procedures and predictable results. In LLE's summer program, the students experience many of the trials, tribulations, and

rewards of scientific research. By participating in research in a real environment, the students often become more excited about careers in science and technology. In addition, LLE gains from the contributions of the many highly talented students who are attracted to the program.

The students spent most of their time working on their individual research projects with members of LLE's scientific staff. The projects were related to current research activities at LLE and covered a broad range of areas of interest including experimental diagnostic development, computational modeling of implosion physics, laser physics, experimental and theoretical chemistry, materials science, cryogenic target characterization, target vibration analysis, and computer control systems. The students, their high schools, their LLE supervisors, and their project titles are listed in the table. Their written reports are collected in this volume.

The students attended weekly seminars on technical topics associated with LLE's research. Topics this year included laser physics, fusion, holography, glass fracture, nonlinear optics, electrostatics, and electronic paper. The students also received safety training, learned how to give scientific presentations, and were introduced to LLE's resources, especially the computational facilities.

The program culminated on 26 August with the "High School Student Summer Research Symposium," at which the students presented the results of their research to an audience including parents, teachers, and LLE staff. Each student spoke for approximately ten minutes and answered questions. At the symposium the 13th annual William D. Ryan Inspirational Teacher Award was presented to Mr. Jeffrey Klus, a mathematics teacher at Fairport High School. This award honors a teacher, nominated by

alumni of the LLE program, who has inspired outstanding students in the areas of science, mathematics, and technology. Mr. Klus was nominated by Nicholas Hensel and Angela Ryck, participants in the 2008 Summer Program.

A total of 249 high school students have participated in the program since it began in 1989. The students this year were selected from a record 80 applicants. Each applicant submitted an essay describing their interests in science and technology, a copy of their transcript, and a letter of recommendation from a science or math teacher.

In the past, several participants of this program have gone on to become semifinalists and finalists in the prestigious, nationwide Intel Science Talent Search. This tradition of success continued this year with the selection of Harvest Zhang as one of the 300 semifinalists nationwide in this competition.

LLE plans to continue this program in future years. The program is strictly for students from Rochester-area high schools who have just completed their junior year. Application information is mailed to schools and placed on the LLE website in early February with an application deadline near the end of March. For more information about the program, please contact Dr. R. Stephen Craxton at LLE.

This program was supported by the U.S. Department of Energy Office of Inertial Confinement Fusion under Cooperative Agreement No. DE-FC52-08NA28302.

High School Students and Projects (Summer 2009)			
Name	High School	Supervisor	Project Title
Dustin Axman	Irondequoit	R. Rombaut, R. Russo	A Graphical User Interface to Oscilloscopes
Leela Chocklingham	Brighton	K. L. Marshall	Abrasion-Resistant Anti-Reflective Sol-Gel Coatings
Ted Conley	McQuaid	J. Bromage	Automated Injection for High-Power Fiber Amplifiers
Cheryl Liu	Pittsford Sutherland	J. P. Knauer	Neutron Detection with High Bandwidth and High Dynamic Range
Trevor Lu	Webster Thomas	D. H. Edgell	X-Ray Phase-Contrast Characterization of Cryogenic Targets
Evan Miller	Pittsford Mendon	J. A. Delettrez	Electron Reflection in Monte Carlo Simulations with the Code GEANT
Lindsay Mitchel	Spencerport	R. S. Craxton	Exploration of the Feasibility of Polar Drive on the LMJ
Justin Owen	Irondequoit	R. W. Kidder, C. Kingsley, M. Spilatro	Using Networked Data Services for System Analysis and Monitoring
Ben Petroski	Livonia	W. T. Shmayda	Water Desorption from Metallic Surfaces at Room Temperature
Aaron Van Dyne	Brighton	J. A. Marozas	Parameter Optimization of 1-D Multi-FM SSD on the NIF
Marisa Vargas	Webster Thomas	C. Dorrer, K. L. Marshall	Laser Beam Shaping with Optically Patterned Liquid Crystals
Kate Walden	Wayne	T. C. Sangster, M. Burke	Bulk Etch Rate Properties of NaOH/Ethanol as a CR-39 Nuclear Track Detector Etchant
Victor Wang	Webster Thomas	K. L. Marshall	Computational Modeling of Optically Switchable Azobenzenes
Paul Watrobski	Penfield	W. Theobald	UV Probe Beam for Plasma Characterization and Channeling Experiments
Mia Young	Penfield	R. Epstein	Including Emissivity in the Analysis of Implosion Radiographs
Harvest Zhang	Brighton	L. D. Lund	Resonance and Damping Characteristics of Cryogenic Fusion Targets

A Graphical User Interface to Oscilloscopes

Dustin Axman

A Graphical User Interface to Oscilloscopes

D. Axman

West Irondequoit High School

Advised by Ralph Russo and Robert Rombaut

Laboratory for Laser Energetics
University of Rochester
250 East River Road
Rochester, NY 14623

Abstract

A graphical user interface (GUI) was created that allows a user to control and display data from an oscilloscope by communicating across a network. The GUI provides a convenient way to observe diagnostic signals throughout the OMEGA laser system. The GUI displays a graph of the data received from each channel of the oscilloscope, showing the signal's shape as well as other attributes. The user is able to continuously update the display with the most recent data or, at any time, acquire a single trace. The user is also able to arm the oscilloscope or force its trigger. The GUI communicates with the server program using ICE (Internet Communication Engine), a software package used for network communications. This program will allow scientists to analyze the shape of the laser pulse before and after it goes through the amplification process.

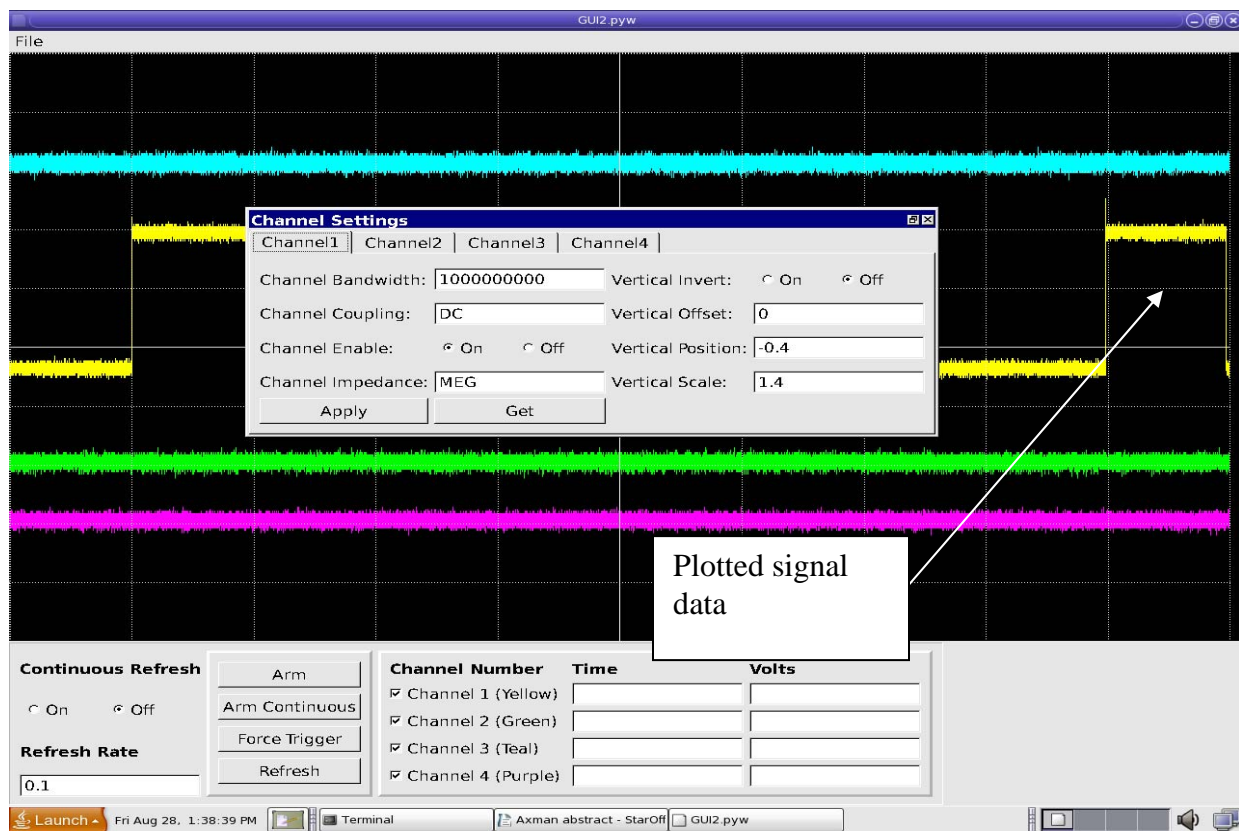


Figure 1. Graphical user interface display, showing the Channel Settings dialog box.

Introduction

The motivation for this project was that viewing data from the OMEGA laser was not yet as streamlined as it could be. This project entailed the creation of a GUI to enhance the user's ability to view and understand the data by gathering and arranging it in the most aesthetic and understandable way possible. The main component of the GUI is the graphical display of the signal data. This data is sent to the client program (a program whose main function is the receiving of data over a network) from the server (a program whose main function is distributing data over a network) as a list of bytes, a list that is twice the size of the actual number of samples. This series of bytes is then converted into floating point numbers, which represent the data collected from the oscilloscope.

Graphical User Interface

An example of the display generated by the GUI is shown in Figure 1. The colored curves represent the signals (voltage vs. time) of channels 1 to 4. One of the primary problems encountered during the creation of this graphical display of the signal data was the fact that there are more samples and therefore more corresponding times on the horizontal axis for each of these samples than there are horizontal pixels on the screen, with approximately one thousand samples per horizontal pixel. This problem causes information to be lost due to the inability to display the difference in times of each sample's acquisition. The way that this problem was solved was that the information was first stored so that it could be easily referenced with precision and specificity in terms of time. Then, when the information was graphed, instead of simply graphing each sample by plotting it on the pixel that graphically represents the sample's time of occurrence in relation to the total time of the pulse, it was determined that the best way to save display time and memory usage was, in each group of

samples per horizontal pixel, to find the largest voltage and the smallest voltage, translate them into a relative pixel coordinate and draw a vertical line between them, essentially creating a “best fit line” for the graphed points. This was done because when all one thousand points are plotted in the horizontal space of one pixel they appear as a simple line to the user regardless. Incorporated into this graphical display is a function for more specific observation of point values. This function makes it such that the user is able to drag his or her mouse on the graph and the time and voltage at that point will be displayed at the bottom of the screen for each channel that is enabled (see Figure 1).

On the bottom bar a key for the channels is displayed with a check box next to each channel. Un-checking this check box will cause the channel to be hidden on the graph and rechecking it will cause it to be shown. If the channel is disabled then the box is automatically made blank. There is also an option for enabling a continuous refresh of the graph and box in which the refresh rate can be specified in Hertz. There are also a number of functions that can be performed such as doing a manual refresh on the graph, forcing the trigger, arming single shot, and arming continuously. Any time the scope is armed it will acquire data on the next trigger. Continuous arm causes the scope to acquire data at a fixed periodic rate while a single shot arm only acquires once. By forcing the trigger the user can force the scope to capture the pulse before the conditions are met for automatic triggering.

At the top left corner of the screen is the file menu, which displays several commands: Scope Settings, Channel Settings, and Exit. Exit will close out the window cleanly and end all data acquisition from the server. Scope Settings will open up a dialog box (see Figure 2) with all of the channel independent settings for the oscilloscope. Channel Settings will open a dialog box (see Figure 1) with all of the channel specific settings for the oscilloscope. These settings will be displayed under several tabs, one for each channel, so that it is easy to change settings

for individual channels. Many of these settings are self-explanatory; however, some such as the horizontal scale, the trigger level, position, and slope require explanation. The horizontal scale is the scale in seconds, or the number of seconds per interval. The trigger level is the minimum level of trigger signal required to trigger the scope. The trigger position is a position in time defined somewhere on either side of the trigger signal. The slope is a check on whether the slope of the pulse should be rising or falling to set off the trigger. When the fields for the settings are altered by the user the text turns blue so that the user knows what was changed. When the user hits the “Apply” button it sends the changes to the server program and the server sets the scope with the new attributes. The client then retrieves the attributes back from the scope and displays it in the fields as black text. The reason for this is so that if an invalid value (a value that cannot be computed such as a word where a numerical value is required or a number that is not supported by the program) is entered into a field and then set, the field will not display an incorrect value. For example, if an extremely small number were entered for the horizontal scale, the scope would only set the horizontal scale to the lowest possible value; this value would then be displayed as the actual value and not the unobtainable one the user entered. The “Get” button causes the settings to be changed to those on the scope and the text in all fields to return to the color black.

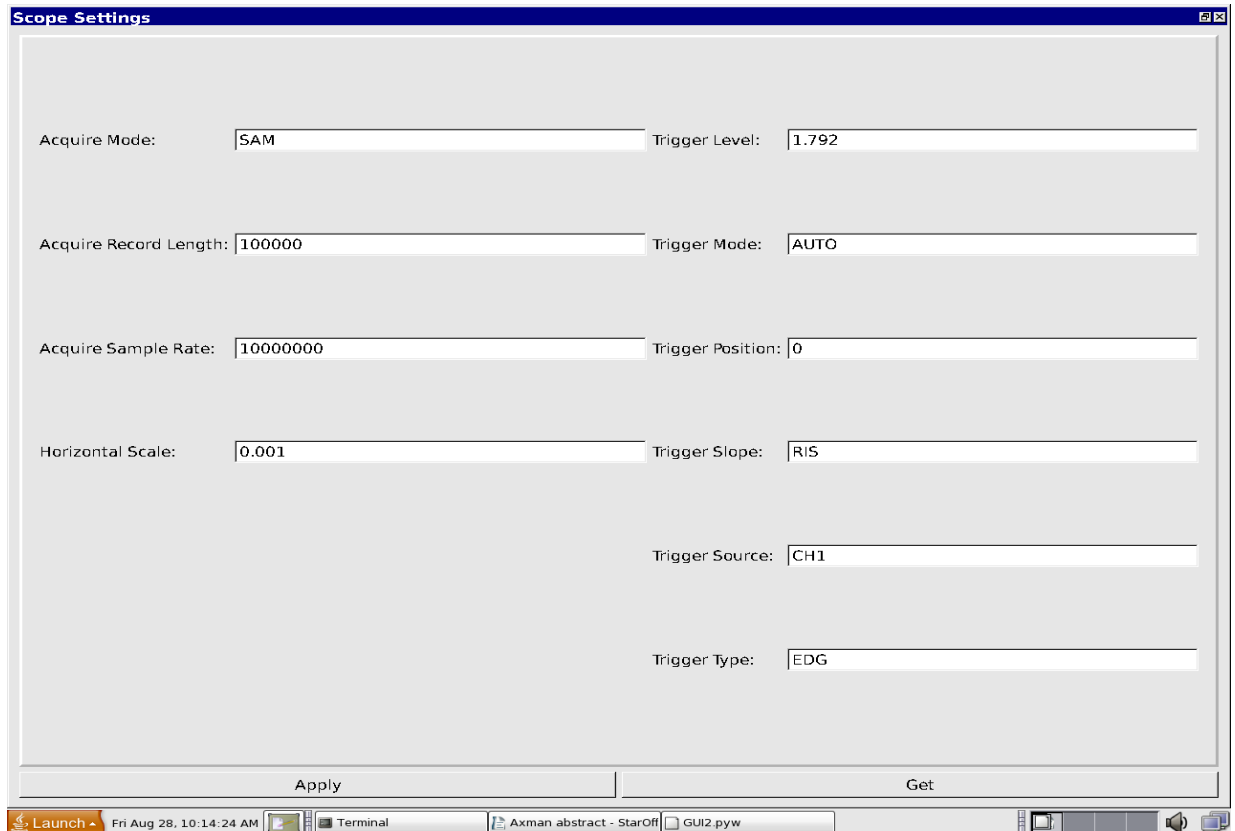


Figure 2. Scope Settings dialog box, used for channel-independent scope settings

As shown in Figure 1 the channel dependent settings are set up in roughly the same format as the channel independent settings with the obvious difference being that the channel settings have tabs for the settings of specific channels. This dialog box contains settings for changing quantities such as the vertical offset, vertical position, and vertical scale. This dialog box also allows the user to enable or disable certain channels. When a channel is disabled it will no longer be read by the oscilloscope, or displayed on the GUI. The same features incorporated in the scope settings dialog are also present in the channel settings dialog.

This program uses Internet Communications Engine (ICE) (see [1]) to communicate across the network with the server. ICE is a language-independent software package which means that it can be used to communicate between two programs that are written in completely different languages. ICE works by establishing a proxy and sending interpreted commands

across this proxy to be reinterpreted on the other end. Since the client was created in Python (see [2,3]) and the server was created in C++, a language independent software package was essential. One limitation of the current program is that it takes up to 3.2 seconds to acquire the data from the server for all four channels and another 2 seconds to format it. Although much has been done to streamline the program as much as possible these times are still relatively long. A possible improvement to make the client more responsive would be to enable threading, which would allow for parallel execution of some functions. The client program has had every possible adjustment made so as to maximize its speed and efficiency.

Conclusion

A graphical user interface has been successfully created and will hopefully be implemented on the OMEGA laser system in the near future. This program will allow scientists to observe diagnostic signals throughout the Omega laser facility. Having a convenient program to view data from multiple oscilloscopes is a useful tool for scientists to visualize and analyze diagnostic data. The results of this effort can be extended to enable remote viewing and control of virtually any oscilloscope in the laser system.

References

1. "Manual for Ice." *Welcome to ZeroC, the Home of Ice*. July 2009. Web. 28 Aug. 2009. <<http://www.zeroc.com/>>.
2. Lutz, Mark, and David Ascher. *Learning Python, Second Edition*. North Mankato: O'Reilly Media, Inc., 2003. Print.
3. Summerfield, Mark. *Rapid GUI Programming with Python and Qt*. Prentice Hall, 2007. Print.

Abrasion-Resistant Anti-Reflective Sol-Gel Coatings

Leela Chockalingham

Abrasion Resistant Anti-Reflective Sol-Gel Coatings

Leela Chockalingam
Brighton High School

Advisor: Kenneth L. Marshall

University of Rochester
Laboratory for Laser Energetics
Summer High School Research Program 2009

1. Abstract

Many optics in both the OMEGA and OMEGA EP lasers are coated with anti-reflective (AR) silane sol-gel to maximize their transmittance. Although these coatings are highly resistant to both airborne contaminants and laser damage, they are susceptible to mechanical damage by abrasion, and thus require extra care during the handling, installation and alignment of sol-gel optics. Previous “hardened” sol-gel AR formulations achieved physical robustness through exposure to ammonia, but were highly susceptible to degradation by atmospheric contaminants. In this work, alternate cross-linking agents for improving both mechanical robustness and contamination resistance were studied. The effectiveness of acryloyl chloride and glyoxal as “hardening” agents was evaluated through both solution and vapor-phase exposure. A drag-wipe testing protocol was developed for these chemically modified sol-gel AR coatings to determine their abrasion resistance as a function of hardening agent and exposure time. Results showed that glyoxal modification of AR coatings is effective in improving abrasion resistance, while contamination resistance and laser damage resistance need to be explored further.

2. Introduction

Silane modified sol-gel coatings are deposited on many optics in the OMEGA laser. The surface of every optic has a potential loss in transmission due to the difference between its refractive index and that of air (Fresnel loss). Sol-gel coatings function as an anti-reflective (AR) layer by minimizing this difference in refractive index. The sol-gel is synthesized from tetraethylorthosilicate (TEOS), an alkoxy silane compound, by a base-catalyzed condensation reaction.¹ In this process TEOS reacts with ethanol in the presence of ammonia. The alkoxy groups (OR) on the TEOS are replaced with hydroxyl groups, with an alcohol as a byproduct (OHR). The hydroxyl groups bond together to form silicon-oxygen bonds through a condensation reaction. Over time these siloxane chains condense in three dimensions to form colloidal particles. After the sol-gel colloidal suspension is deposited onto the surface of an optic, the loss of solvent increases the rate of condensation and the particle network tightens, forming a “xerogel”.^{2,3} Figure 1 shows this reaction schematically.

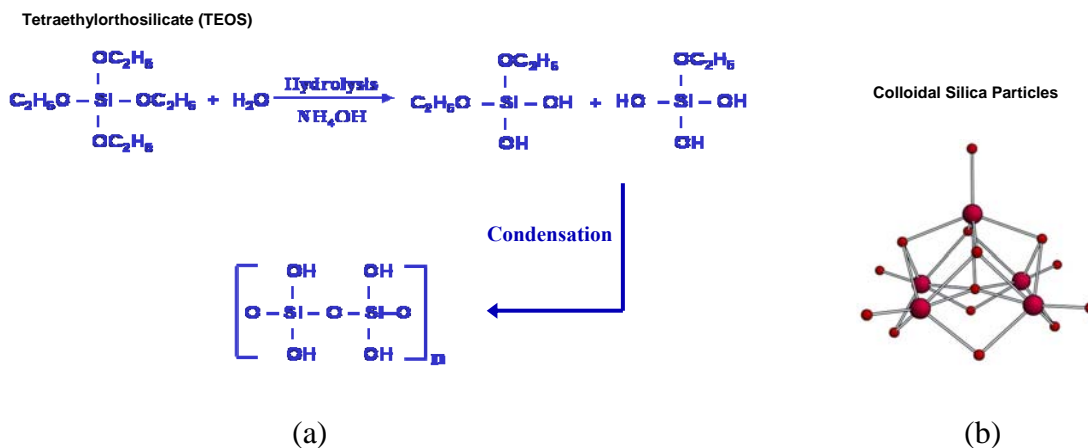


Fig.1: Formation of sol-gel particles. (a) Base-catalyzed condensation of TEOS with ethanol forms siloxane chains; (b) with time, the chains extend in three dimensions to form a network of colloidal silica particles. Further treatment of the colloidal silica particles with a reactive silane increases their contamination resistance.

Because of the presence of volatile and semi-volatile contaminants (organic compounds, water) in the laser-bay air, standard TEOS based sol-gel AR coatings lose their transmission efficiency over periods of several months.⁴ The current silane modified TEOS based sol-gels used in OMEGA have extended working lifetimes due to their excellent contamination and laser damage resistance,⁴ but are very sensitive to abrasion. Previously, sol-gel AR coatings were treated through cross-linking of hydroxyl groups with ammonia vapor for 24 hours to increase their physical robustness. Although this method is very effective in improving abrasion resistance without decreasing transmission significantly, the contamination resistance of these "ammonia-hardened" sol-gels is not significantly better than standard TEOS sol-gel AR coatings.

In this study TEOS based sol-gel solutions were modified using a series of organic cross-linking agents, including glyoxal, acryloyl chloride and triethoxyvinylsilane with ethylene glycol dimethacrylate.⁵ Figures 2-4 show how these materials react with the OH groups on the surface of the sol-gel coating to improve its abrasion resistance.

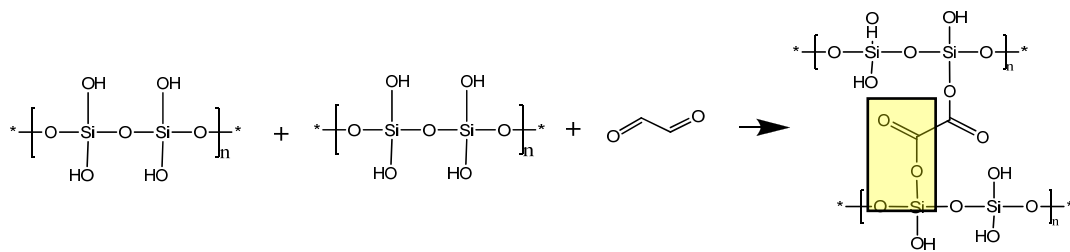


Fig.2: Cross-linking reaction of glyoxal with the siloxane surface of the sol-gel particle. The yellow box shows the cross-link point between siloxane chains.

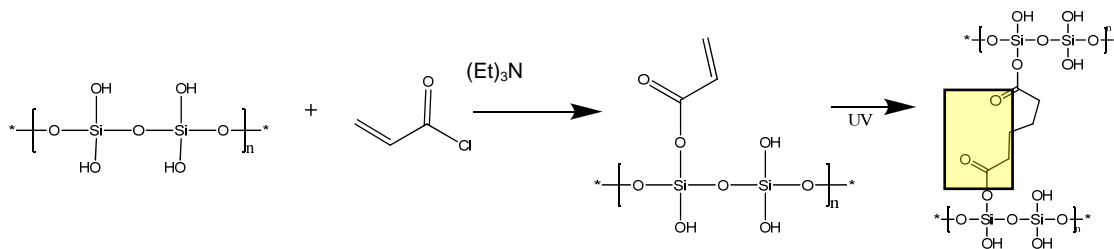


Fig. 3: Cross-linking reaction of acryloyl chloride with the siloxane surface of the sol-gel particle. The yellow box shows the cross-link point between the siloxane chains.

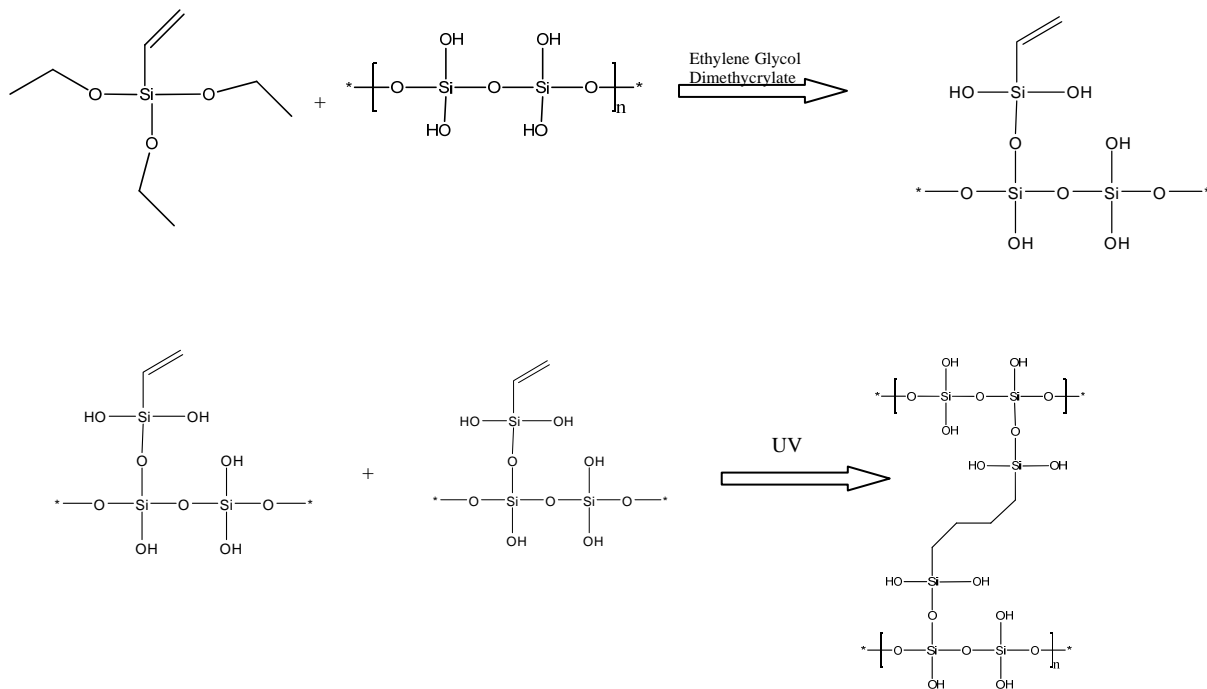


Fig. 4: Cross-linking reaction of triethoxyvinylsilane with the siloxane surface of the sol-gel particle. This reaction differs from those shown in Figs 2 and 3 in that it utilizes a free-radical mechanism initiated by UV light.

For both the acryloyl chloride and glyoxal cross-linking agents, studies of cross-linking efficiency and abrasion resistance were conducted by exposure of the sol-gel-coated substrate to a saturated vapor-phase environment of the cross-linking agent as well

as cross-linking directly in the coating solution. Experiments with triethoxyvinyl silane were conducted only in the solution phase.

The effectiveness of these cross-linking agents in terms of improving abrasion resistance was measured using a drag-wiping protocol. Preliminary testing of contamination resistance was also conducted. The goal of this project was to find a cross linking agent that would achieve both abrasion resistance and contamination resistance without affecting the transmission of the AR coating.

3. Experimental Data

The un-modified TEOS based AR coating was prepared using 22.0425 L of ethanol, 2.320 L of TEOS, and 717.5 ml of ammonium hydroxide (NH₄OH). For glyoxal and acryloyl chloride vapor saturation trials, a previously prepared TEOS based sol-gel “stock” solution was spin-coated onto substrates in a Class 100 laminar flow hood housed in a Class 10,000 clean room. The substrate surface was first completely flooded with sol-gel solution with the spin-coater at rest. The substrate was then spun at 2000 RPM for 40 sec, which removed excess coating material and distributed the remaining solution evenly over the substrate surface. Both the spin time and speed affect the thickness of the AR coating, which in turn affects the transmission efficiency of the coating as a function of wavelength. After spin coating the substrates were allowed to dry for 24 hours.

The optical transmission of the substrates both before and after sol gel AR coating was tested using a Perkin Elmer Lambda 900 UV-VIS-NIR spectrophotometer over a wavelength range of 300 nm to 1500 nm. Over the area where the coating acted as an AR

layer (500 nm to 800 nm) the transmittance of the substrate after coating was increased by an average of 5.5% .

Vapor-phase crosslinking experiments were conducted by exposing the substrates to a vapor-saturated environment of the cross-linking agent in a sealed container for 24 hours. The optical transmission of the exposed coatings was then measured again to determine any changes in transmission caused by the cross-linking reaction.

For solution-phase cross-linking experiments, solutions of acryloyl chloride (5% and 10% wt/wt) and glyoxal (2%, 4%, 6%, 8% and 10% wt/wt) in the stock TEOS sol-gel solutions were prepared. Triethylamine was added to the acryloyl chloride solutions as a catalyst. The glyoxal and acryloyl chloride modified sol-gel solutions were spin coated and dried for 24 hours in a Class 100 laminar flow hood housed in a Class 10,000 clean room. Subsequently, the acryloyl chloride substrates were irradiated under a UV lamp for 90 minutes, to promote cross-linking. Then the coatings' abrasion resistance and optical clarity were tested.

Abrasion resistance was tested qualitatively by means of a drag-wiping protocol developed specifically for this measurement. Figure 5 illustrates the testing process. The sol-gel AR coated substrate was placed on a clean dry surface and a clean room wipe was placed on the AR coated surface. Additional substrates (each with a mass of 7.4 grams) were placed on top of the wipe and the wipe was dragged across the surface of the sol-gel coated substrate. The substrate was then examined by optical microscopy in reflection to assess the amount of coating abrasion. The process was repeated with an increasing mass load (more substrates) until significant coating damage was observed.

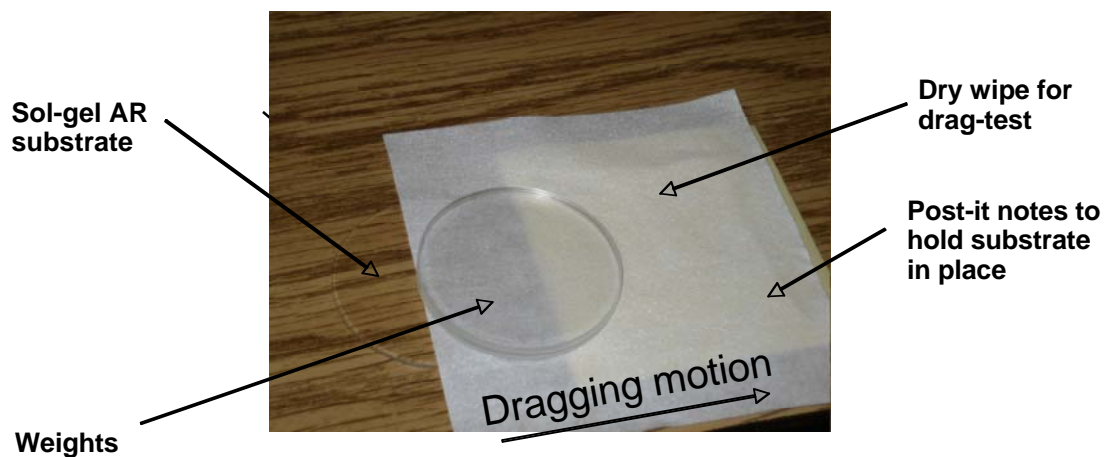


Fig. 5: Abrasion resistance drag-wipe testing process for modified sol-gel coatings. Additional mass in the form of substrates is added to the wipe until significant sol-gel coating damage is observed.

After the initial testing of transmission and abrasion resistance, the modified sol-gel coatings were left to age for four weeks. The abrasion resistance of the glyoxal-modified coatings substantially increased after this aging period, in some cases by a factor of 6. Figure 6 presents the abrasion resistance values for these four-week aged coating samples. All cross-linking agents demonstrated an increase in abrasion resistance over the standard TEOS based sol-gel. The glyoxal-modified AR coatings prepared by solution deposition demonstrated the highest abrasion resistance, with the 8% glyoxal modified coating showing no damage under the highest mass loads tested. The photomicrographs in Fig. 6 compare the abrasive damage sustained by a standard TEOS sol-gel coating and a glyoxal-modified coating after drag-wiping with the maximum sustainable load for each coating. The TEOS coating shows severe abrasion with only 7.4 g load, whereas the glyoxal-modified coating is able to withstand a 21x greater drag-wipe load while showing only minimal damage.

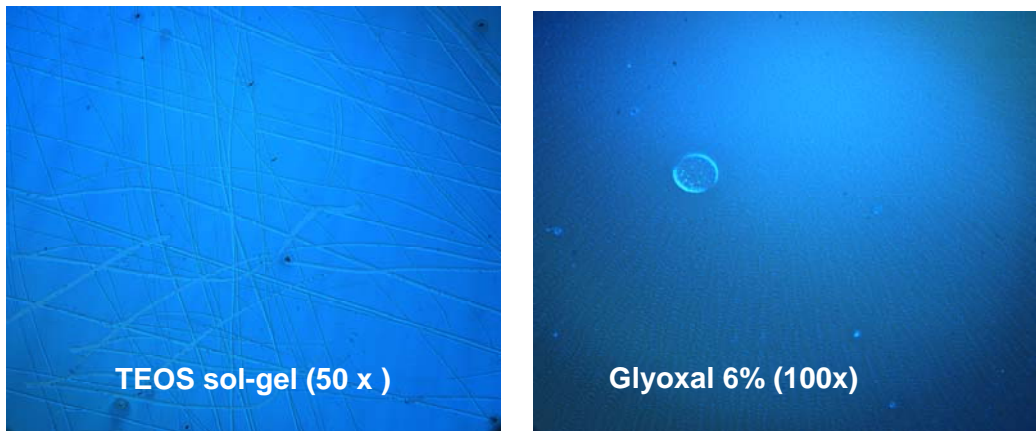
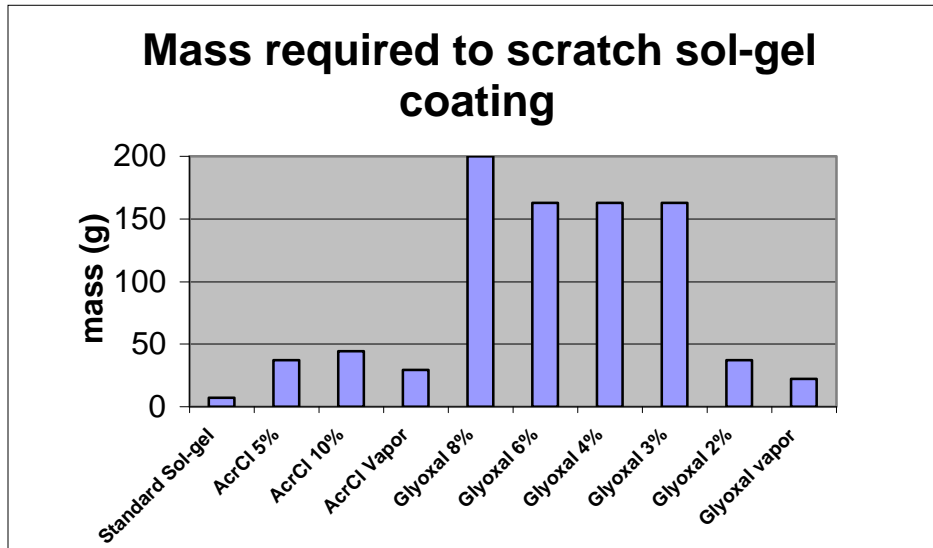
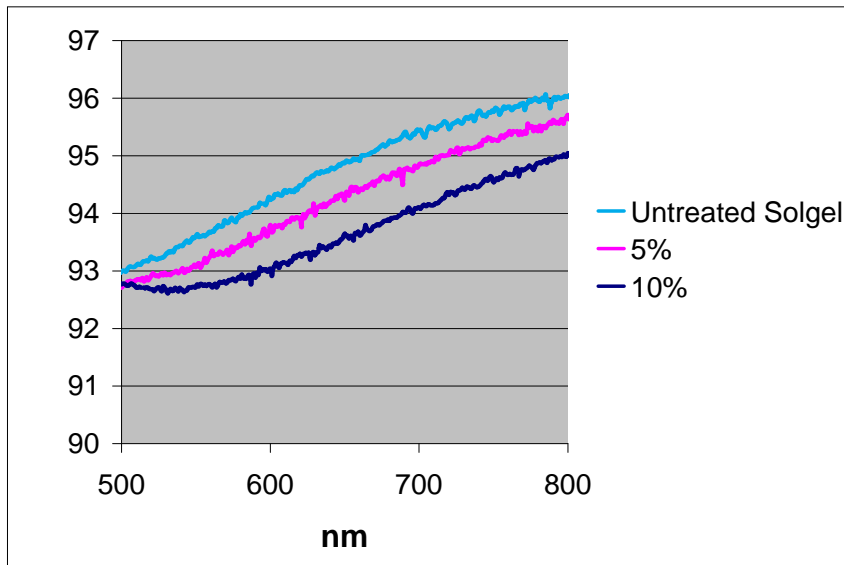


Fig. 6: *Top*: Abrasion resistance data for modified sol-gel coatings aged for 4 weeks. *Bottom*: Photomicrographs of standard TEOS sol-gel AR and 6% glyoxal-modified sol-gel AR after drag-wiping with 7.4 g and 160 g mass loads, respectively.

Figure 7 shows optical transmission data for both acryloyl chloride-modified and glyoxal- modified sol-gel AR coatings as a function of cross-linking agent concentration. Overall, the glyoxal modified coatings showed higher abrasion resistance than the acryloyl chloride modified coatings.

Acryloyl chloride-modified sol-gel coatings Transmission spectra



Glyoxal-modified sol-gel coatings Transmission spectra

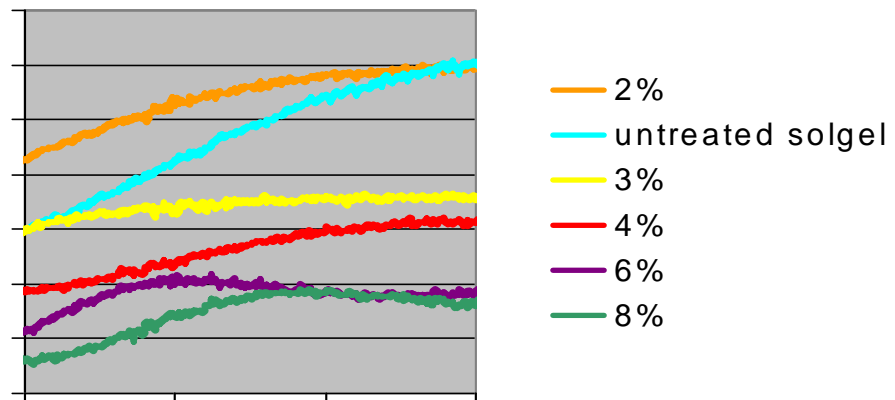


Fig. 7: Transmission spectra of modified sol-gel coatings as a function of cross-linking agent concentration. *Top*: Transmission spectra for acryloyl chloride-modified sol-gel coatings. *Bottom*: Transmission spectra for glyoxal-modified sol-gel coatings. Included with both sets of transmission spectra are a transmission profile for a standard (non-modified) sol-gel coating as a reference.

A change in transmission of the cross-linked sol-gel AR coatings was observed as a function of time after preparation. Figure 8 shows this change in optical transmission for two representative glyoxal-modified coatings at two different cross-linker concentrations. The 4.4% glyoxal-modified coating demonstrated an increase in optical transmission, while the 8% glyoxal-modified coating demonstrated a decrease in transmission. This change in transmission may be due to either loss of volatiles (solvent) or a very slow change in coating morphology due to extended cross-linking occurring at a very slow rate. Loss of solvent could produce either an increase or decrease in transmission, depending on whether the refractive index of the coating is increased or decreased by the solvent loss. Extended slow cross-linking may be causing an increase in sol-gel particle size (a change in surface morphology), with a concurrent increase in forward (or backward) scattering- either of which would result in transmission loss. Further work needs to be done to understand the full nature of this time-based change in optical and mechanical properties.

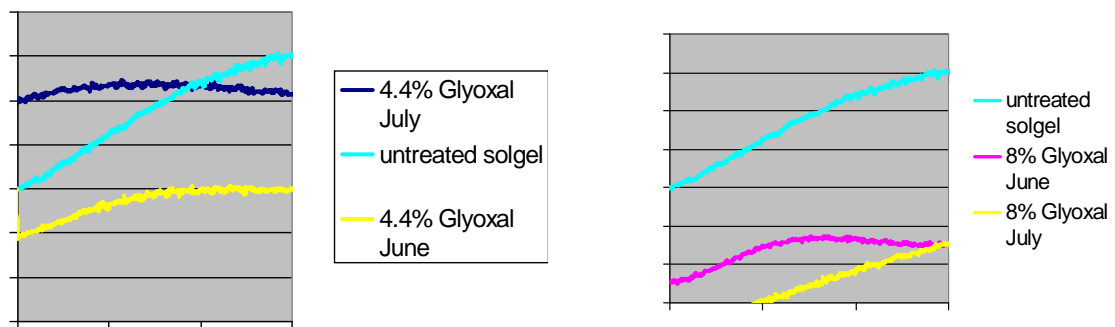


Fig. 8: Optical transmission of glyoxal-modified coatings as a function of aging time. *Left:* Coating modified with 4.4% wt glyoxal. *Right:* Coating modified with 8 wt% glyoxal. Transmission curves for a standard (non-crosslinked) sol-gel coating are included for reference.

Preliminary testing was done with triethoxyvinylsilane (TEVS) combined with ethylene glycol dimethacrylate. The procedure was adapted from that used to prepare the silane-modified sol-gels currently in use in OMEGA. The standard TEOS-based sol-gel stock solution was added to a light-proof flask and stirred for 3 hours. Ammonium hydroxide was added and the mixture was stirred for another two hours. The solution was sealed and left to sit for three days. The solution was then refluxed to evaporate off excess ammonia. The TEVS was then added at 10%, 20%, and 30% wt/wt to three 25 ml portions of the sol-gel solution. A few drops of ethylene glycol dimethacrylate were also added to each portion as a free radical catalyst. Sixty ppm of hydroquinone was added to prevent the TEVS from undergoing intra-molecular cross-linking. These solutions were sealed in light-proof containers and left to react for 3 days. The modified sol-gel solution was then filtered to remove the hydroquinone prior to spin-coating. After spin-deposition, the coating was irradiated while still wet to prevent the evaporation of ethylene glycol dimethacrylate. The TEVS-modified coating at a cross-linking concentration of 30% shows improved transmission as compared to a standard sol-gel coating (Fig 9). In terms of abrasion resistance, the 30% TEVS coating scored a “6” on the abrasion index test, which corresponds to a drag load of 44.4 grams- roughly equivalent to the abrasion resistance shown by the 2% glyoxal modified coating or any of the acryloyl chloride-modified coatings.

Preliminary experiments were conducted on both glyoxal-modified and TEVS-modified sol-gel AR coatings using iso-octane to test the effectiveness of these coatings to contamination by an organic vapor. Figure 10 shows that the transmission for a

glyoxal- modified coating after exposure to iso-octane vapor is comparable to that of an unmodified TEOS based sol-gel, while the TEVS-modified coating had excellent contamination resistance. This enhanced contamination resistance is believed to be due to the same mechanism responsible for producing the high contamination resistance in earlier silane-modified sol-gel coatings- the presence of bulky, hydrophobic silane functional groups on the sol-gel particle.

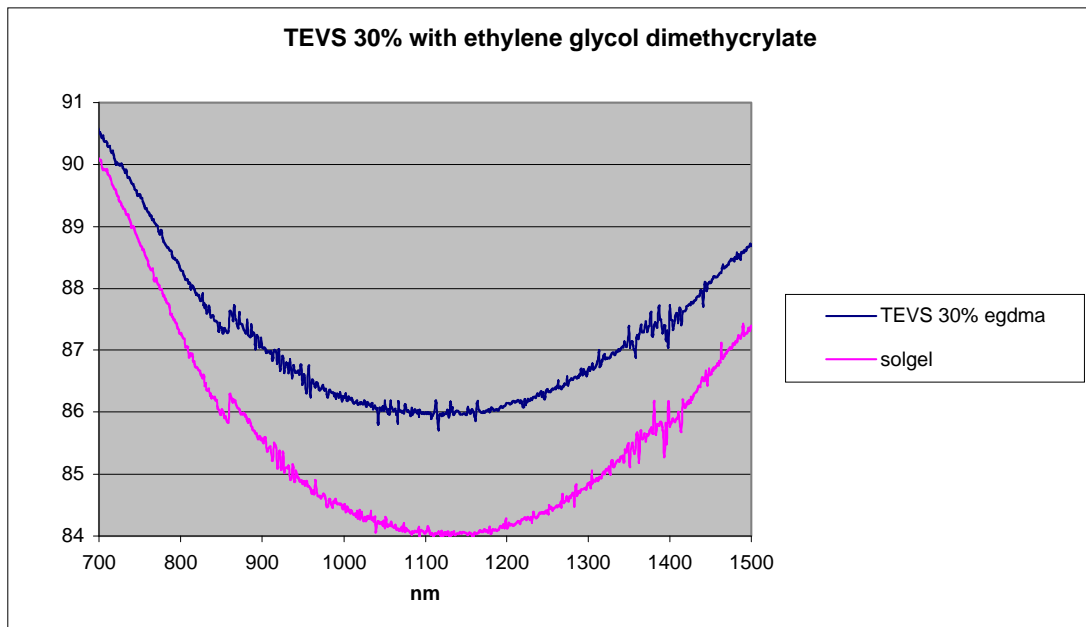


Fig. 9: Optical transmission of a TEVS –modified sol-gel AR sample. Data on a standard sol-gel AR is included for reference.

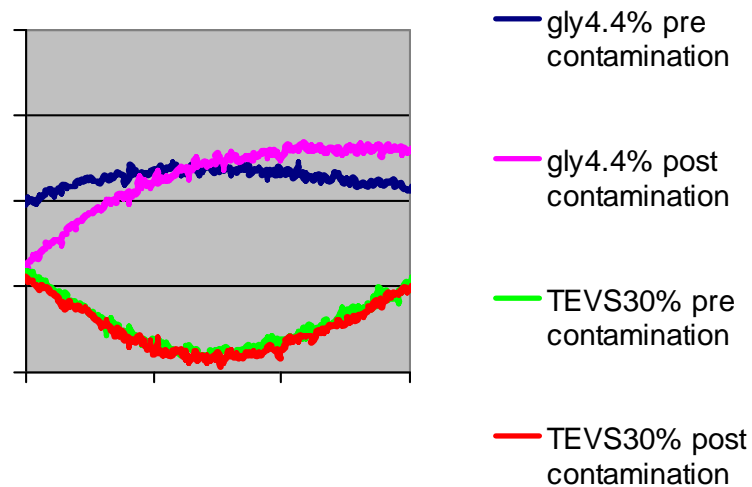


Fig. 10: Change in transmission of glyoxal and TEVS-modified sol-gel coatings after a 24 hr exposure to an environment saturated with iso-octane vapor.

4. Conclusion

Sol-gel AR coatings were modified by both vapor-phase and solution phase treatment with several organic cross-linking agents to improve their abrasion resistance. A drag-wipe protocol was developed to evaluate the abrasion resistance of these modified coatings. Glyoxal-treated sol-gels demonstrated a 6x – 20x improvement in abrasion resistance (depending on cross-linker concentration) that increased over time as the coating aged. Changes in the transmission of the coatings with time were also observed. Further research into the aging process, and how that affects the optical transmission of glyoxal-modified coatings may show how the transmission may be improved. Also, the surface morphology of the glyoxal-modified coatings and its effect on optical transmission is an area that will require further research. Triethoxyvinylsilane modified ARs showed very promising preliminary results, but need to be further tested.

For these new coatings to be viable for use in OMEGA and OMEGA EP, their laser resistance and contamination resistance needs to be further tested. If future work in this area continues to yield promising results, the mechanical durability and contamination resistance of these coatings will greatly extend their useful life in high peak power laser systems.

5. Acknowledgements:

I would like to thank the Laboratory for Laser Energetics and the program supervisor Dr. Stephen Craxton for giving me the opportunity to participate in the high school summer internship program. I would also like to thank my advisor, Mr. Kenneth Marshall for helping me complete my project, as well as University of Rochester students Chris Sileo and Eric Glowacki.

6. References:

- (1) Comparative study on hydrophobic anti-reflective films from three kinds of methyl-modified silica sols. Y.Xu, D.Wu, Y.Sun *et.al.* ***Journal of Non-Crystalline Solids.*** 351(2005): 258-266
- (2) Antireflective silica with thin films with super water repellence via a sol-gel process. Y. Xu, W. Hao, Z. Li *et.al.* ***Applied Optics,*** 42(2003) n1: 108-112
- (3) Durable sol-gel antireflective films with high laser-induced damage thresholds for inertial confinement fusion. Y.Xu, L.Zhang, D.Wu. *et.al.* *Optical Society of America.* 22(2004): 905-912
- (4) K. L. Marshall, V. Rapson, Y. Zhang, G. Mitchell, and A. L. Rigatti, "Contamination Resistant Sol-Gel Coatings for High Peak Power Laser Applications," published in the Proceedings of the OSA Topical Meeting on Optical Interference Coatings, Tucson, AZ, 3-8 June 2007.
- (5) K. L. Marshall, E. Glowacki, C. Sileo, L. Chockalingam, J. Lee, V. Guiliano, and A. Rigatti, "Improving the Abrasion Resistance of Organosilane-Modified Sol-Gel Coatings for High-Peak-Power Laser Applications", presented at the OSA Topical Meeting on Optical Interference Coatings, Tucson, AZ, 6-11 June 2010

Automated Injection for High-Power Fiber Amplifiers

Ted Conley

Automated injection for High-Power Fiber Amplifiers

Ted Conley
McQuaid Jesuit High School
LLE Advisor: Dr. Jake Bromage
Summer 2009

Abstract

New ytterbium-doped fiber amplifiers are enabling femtosecond systems to produce gigawatt peak powers [1]. A critical development is the fiber itself. New photonic crystal fibers (PCF) have large single-mode effective areas ($<2300 \mu\text{m}^2$) and high pump absorptions (30 dB/m), raising the power at which nonlinear pulse distortion occurs. The nature of the design, however, has some limitations. Single-mode operation is only possible if the fiber is kept straight. Therefore, instead of the typical 0.25-mm diameter fibers that can be coiled and fusion spliced, the large-mode-area PCF fibers are 1.6-mm diameter rods. One consequence is that the pump and signal beams must be injected into the fiber using free-space optics. The output beam quality of the amplifier degrades with significant misalignment at injection [2]. For this project, control software was written to (a) observe the amount of misalignment at the signal injection, (b) calculate the required correction, and (c) move the signal beam by issuing commands to a motorized mirror. Closed-loop control was demonstrated with correction times of roughly 10 seconds, and corrected for deviations as large as the fiber core diameter.

1. Introduction

1.1 Photonic-crystal fiber amplifiers

Fiber amplifiers have unique thermal advantages over solid-state amplifiers due to their geometry. Their large aspect ratio (long length to small diameter) provides a large surface area to active volume ratio, which improves heat dissipation. The geometry also provides efficient amplification due to the long path lengths available for absorbing the pump light. However, the aspect ratio is less advantageous at higher peak powers. When high energy pulses propagate down the fiber, the intensity of the light can become much larger than in other solid-state amplifiers because of the small area of the fiber mode. At sufficiently high intensities, nonlinear distortion of the pulse occurs in the fiber [3]. For short-pulse amplifiers, the dominant nonlinearity is due to instantaneous modification of the refractive index of the glass by the time-varying intensity of the pulse. This in turn modifies the phase of the pulse. Hence, this effect is called 'self-phase modulation' (SPM).

One way to compare the threshold for SPM between different fiber amplifiers is by their nonlinearity coefficient, γ [3]

$$\gamma = \frac{n_2 \omega_0}{c A_{\text{eff}}} \quad (1)$$

where n_2 is the nonlinear index of the glass ($2.4 \times 10^{-16} \text{ W/cm}^2$), ω_0 is the optical frequency, and c is the speed of light. A_{eff} is the critical parameter that fiber designers can use to improve the power-handling capabilities of the fiber. Doubling A_{eff} approximately doubles the length over which a pulse can propagate for the same amount of nonlinear distortion. Alternatively, twice the power can be propagated over the same length of fiber.

New fiber designs such as the photonic crystal fiber (PCF) have been introduced to increase A_{eff} . PCFs have a double-cladding structure created by the presence of two arrays of air holes that run

the length of the fiber. The presence of air within the fiber lowers the average refractive index of the regions containing the arrays, permitting confinement of light by total internal reflection. The structure of the fiber used for this project is displayed in Fig. 1 and was studied in detail by Schmidt *et al.* [4].

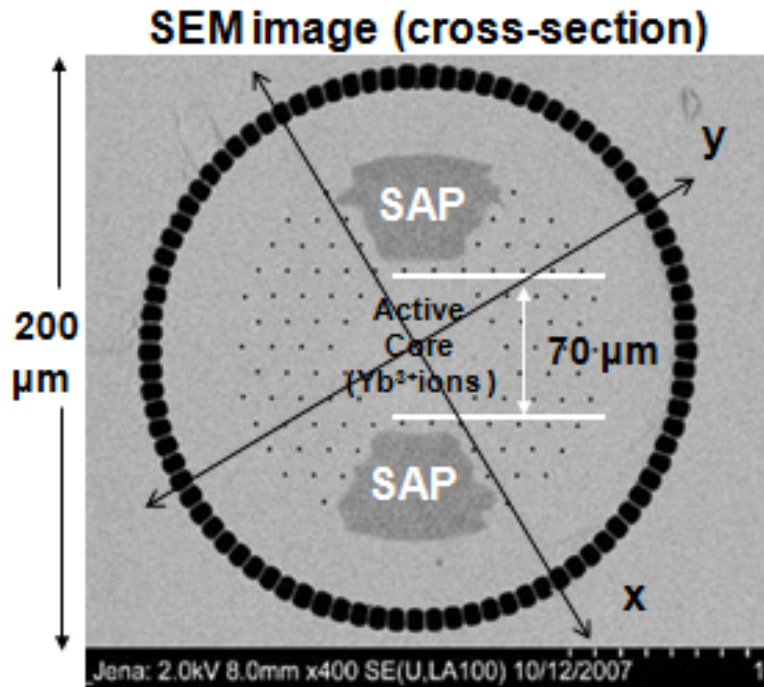


Fig. 1: Scanning electron microscope image of a cross section of the photonic crystal fiber amplifier displaying the multiple arrays of air holes used for radiation confinement. Labels indicate differing regions of the fiber and their dimensions. The actual orientation of the fiber is indicated as well; the x axis denotes the horizontal orientation and the y axis the vertical.

Three types of structures are used here. The first is an circular ring of air holes. This creates a large refractive index difference that can confine light even when it propagates at large angles down the fiber (i.e., with high numerical aperture, NA). This light is guided by this ring up to a half-angle of 37° , which corresponds to a numerical aperture of 0.6. The ring is used to confine the amplifier pump, 976-nm light from multimode-fiber pigtailed diodes, to a 200- μm diameter region down the fiber. Tight confinement of the pump light ensures efficient pumping of the ytterbium ions that dope the 70- μm -diameter region in the core of the fiber. The pump absorption of 30 dB/m is approximately 6 times

higher than found in standard single-mode fiber amplifiers, and allows the fiber length to be reduced to less than a meter.

The second structure consists of a hexagonal matrix of smaller air holes. Their size is $1.1 \mu\text{m}$ and they are spaced $11 \mu\text{m}$ apart. Their role is to lower the average index of the region surrounding the core of the fiber, to guide the signal light at 1030 to 1050 nm. In contrast to the strong guiding of the pump light, the guiding of the signal light is extremely weak ($\text{NA} \approx 0.02$, or a maximum half-angle of 1.1°). This is done to ensure that only the lowest-order mode, the fundamental mode, can successfully propagate down the fiber. Higher-order modes, which would severely degrade the beam profile of the amplified signal, leak out of the fiber structure, and therefore are reduced at the output of the fiber amplifier. The advantage of this design is that A_{eff} for the signal is $2300 \mu\text{m}^2$, 100 times larger than the effective area of standard singlemode amplifiers, and corresponds to a mode-field diameter of $55 \mu\text{m}$. The disadvantage of this weak-guiding approach is that the fiber cannot be bent or the fundamental mode will also leak out of the fiber. Therefore, the fiber is rigidly encased in a 1.6-mm diameter glass rod.

The third type of structure is the two boron-doped stress-applying parts (SAP) that are used to create stress birefringence within the fiber. This is a standard technique for changing the polarization properties of the fiber [4]. The SAPs modify the refractive index seen by the signal. If the signal is polarized vertically (along a line connecting the SAPs), the mode is confined. If, however, the orthogonal polarization is launched, the mode is not confined and the light leaks out of the fiber. In this way, the polarization of the input signal is preserved at the output.

1.2 Application: Ultra-broadband Front-End Project

A new project is underway at the Laboratory for Laser Energetics (LLE) to create an ultra-broadband front end (UFE) for upgrading OMEGA EP to produce extremely short pulses (approximately 30 fs) with high energies (>500 J). High-power PCF amplifiers are being used in the prototype front end

to produce the seed pulses required for the upgrade, which must have approximately 200 nm of bandwidth, centered at 910 nm. The PCF amplifier is part of a fiber chirped-pulse amplifier system that creates 10- μ J pulses at a 1-MHz repetition rate. These pulses are used to (a) generate white-light continuum using a sapphire plate, and (b) amplify the continuum in a noncollinear optical parametric amplifier. (For more details, see [5]). Key requirements of the PCF amplifier are good beam quality and long term stability. This project addressed both of these requirements by actively correcting the signal beam injection at the input to the amplifier.

1.3 Experimental set-up

Figure 2 shows the experimental system. In the UFE prototype, the fiber rests on a metal v-shaped mount that is mounted on the optical table at two points.

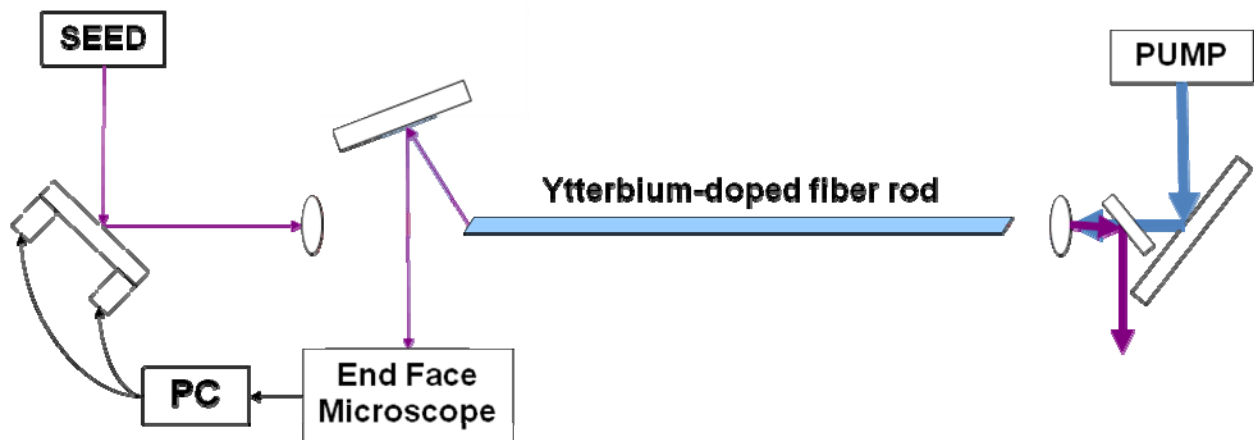


Fig. 2: Diagram of the experimental set-up. The box labeled SEED represents previous optical elements that create the seed pulse. Ovals represent lenses, and plain white rectangles represent mirrors. The blue parallelogram represents the fiber itself.

The blue arrows represent the path taken by the pump light into the fiber, while the purple arrows denote the seed and eventually the output laser beam. The relative powers are indicated by the thickness of the arrows. The signal power is 0.45 W at input and increases to 16 W at output. The pump light input power is 60 W. The seed beam is reflected off the mirror on the left, to which actuators are attached to provide control. The beam then passes through a lens which focuses the light to a point for

injection. Some of the signal light is reflected into the end face microscope (EFM) objective along with much of the excess pump light. The signal gains energy along the length of the fiber, exits, disperses, and is refocused by a second lens. Figure 3 displays an overhead photograph of the actual optical array.

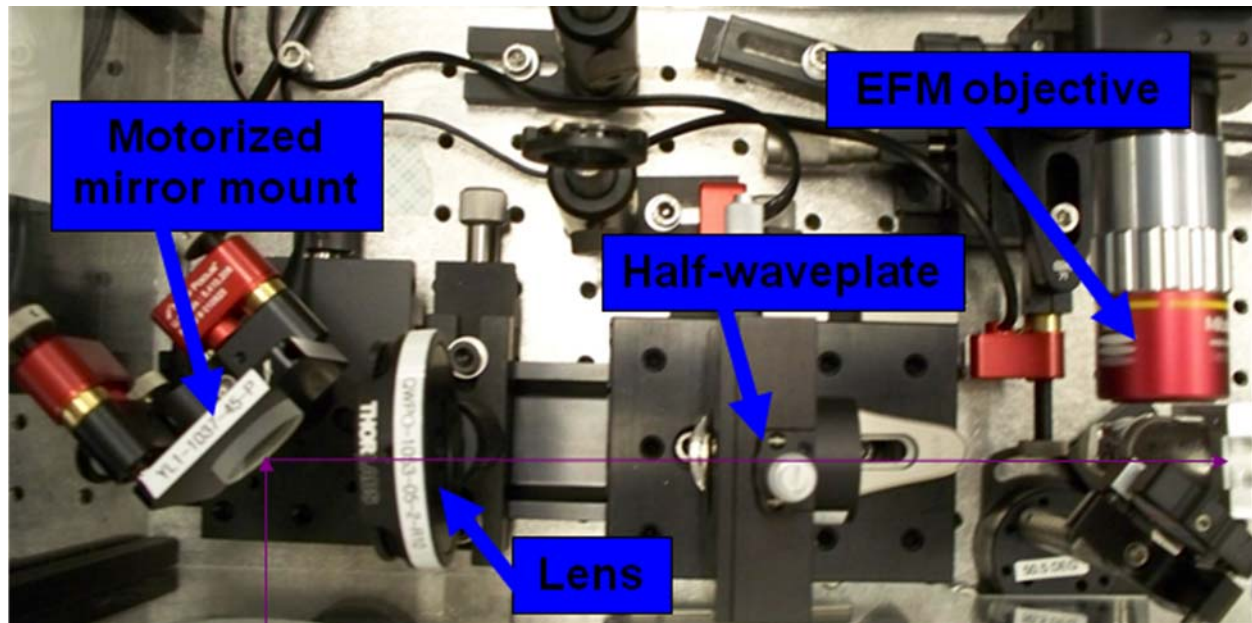


Fig. 3 A top view of the optical components leading up to the fiber including the motorized mirror mount, lens, and half-waveplate which locks the signal polarization for injection.

1.4 Statement of the problem

The properties of the PCF, while advantageous for short-pulse amplification, raise issues that are not typical for fiber amplifiers.. The rigid rod design means that traditional fusion splicing techniques cannot be used to integrate the PCF into a system. Instead the pump and signal light must be launched into the fiber through free-space injection. The performance of the amplifier is sensitive to error in the injection alignment. If the misalignment is of the order of the mode-field diameter ($55\ \mu\text{m}$), coupling into the fundamental mode of the fiber is severely reduced and, therefore, the output of the amplifier is lower by more than an order of magnitude. Less severe misalignment also causes problems. Higher-order modes (HOM's) that have different mode profiles and propagation velocities can also be launched if the injection is offset from center. Although the PCF is designed not to propagate such modes, the fiber length is short enough (0.8 m) that some fraction of the HOM can still be present at the output of

the amplifier. Interference between the fundamental mode (LP_{01}) and the HOM's distorts the beam profile. The distortion can be significant even when the relative powers differ more than an order of magnitude because it is an interference effect [6]. Injection offsets of 30% of the mode-field diameter ($15\ \mu\text{m}$) can increase the amount of the LP_{11} HOM from -18 dB to -13 dB [2].

These issues would be less detrimental if the fiber input was held in a fixed position to within a few microns. Heating by the pump, however, causes a number of competing effects that change the position of the center of the active core due to thermal expansion. These effects were reduced by adding a chilled-water cooling system in the fiber mount. Nonetheless, since the fiber rests in a v-shaped mount, as the diameter of the fiber expands, the target injection site changes position. The displacement observed is not in one dimension directly upwards, as viewed in a traditional x-y plane through the fiber face, but generally has an x component as well. Figure 4 shows the displacement in both the x and y dimensions over more than one hour.

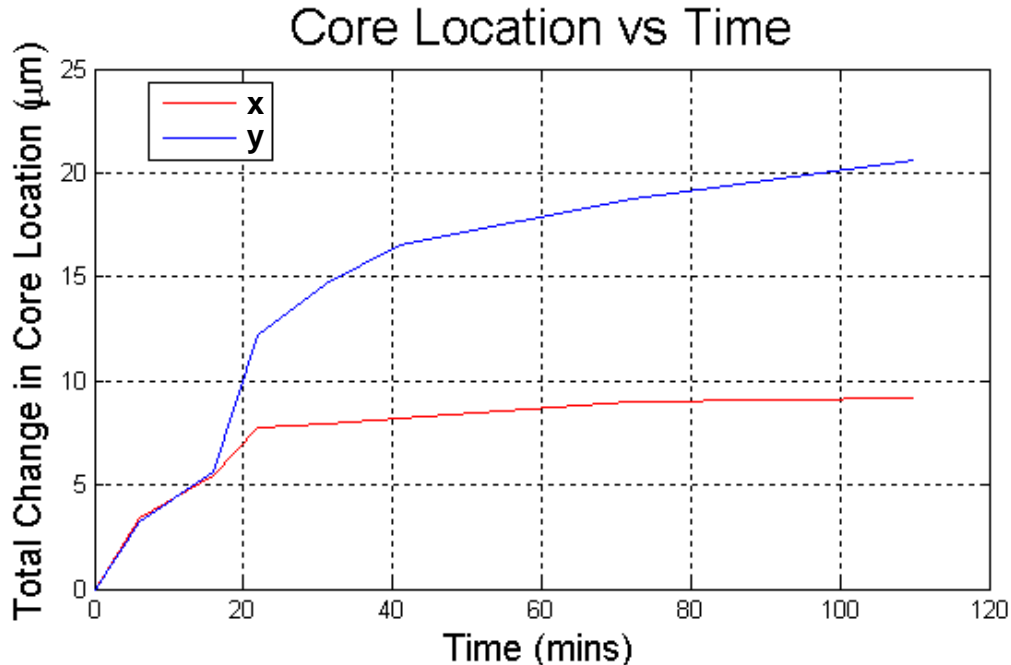


Fig. 4: Graph of the cumulative change in core position over time as the system heats up. Red and blue lines graph total displacement in the X and Y dimensions respectively, both in the positive direction on a traditional co-ordinate plane.

This unidirectional movement may be due to the orientation of the active core within the fiber and the position of the fiber in relation to the fiber mount. The doped core is not in the exact center of this specific fiber and the stress applying parts (SAP) are actually askew in this fiber. An alternative hypothesis is that the diameter of the fiber itself expands, and due to the v-shaped mount the active core rises as operation progresses (see Fig. 5).

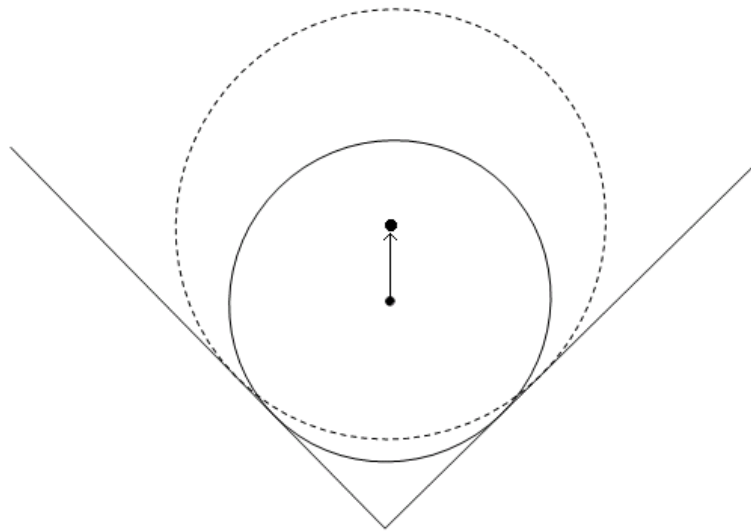


Fig. 5: Diagram of one hypothesis for how thermal expansion of the fiber creates one vector component of misalignment. (Scales are exaggerated for clarity).

Another theory is that the mount itself absorbs much of the heat dissipated from the fiber. Since the mount is fixed to an optical table at two points, the thermal expansion of the mount causes it to bow upwards at the center. The fiber is not entirely rigid and conforms to the new shape of the fiber mount causing the end face of the fiber to change position and orientation, thus additionally dislocating the target injection site.

The maximum rate of change of the position of the target injection site can be estimated from Fig. 4. When the system is first turned on the rate of change is the highest at approximately

0.5 $\mu\text{m}/\text{min}$. This continuous change in the active core location required constant manual adjustments of the signal injection. To simplify operation, it was decided that the adjustment process should be automated.

2. Methods

2.1 Automated Alignment Approach

The approach to developing a system that would automatically align the beam with the target injection site required three main tasks:

1. The system must be able to acquire some sort of readable data about the relative positions of the ideal signal injection site and the signal location. The data needs to be readily available, required by the desired real time function of the system, and easily processed.
2. The system must be able to evaluate the acquired data and calculate the injection error between signal location and ideal signal location.
3. The system must then be able to transfer this error value into commands sent to some external control system that will mechanically correct the injected signal beam.

2.2 Implementation

The data is acquired in the form of an image created by the combination of pump and signal light captured by an end-face microscope (EFM) (see Fig. 2). The end face of the fiber that the signal is injected into is polished to an angle of about 4° , reflecting approximately 4% of the signal light to the EFM. (The 4° angle is required so that the amplifier does not lase from reflections between its end faces). A substantial amount of excess pump light is also captured by the EFM pickoff, providing a background by illuminating the pump core with the exception of the SAP's. The superimposition of these two light sources creates a distinct image such as that shown in Fig. 6(a); the circular signal region has the highest intensity, followed by the pump core without the SAP's at a significantly lower intensity, and finally the SAPs and the region surrounding the core are dark. The image is recorded by a CCD camera as a 640×480 matrix of intensity values and later evaluated for the locations of the signal and

target core. This entire process is handled using LabVIEW, a program that uses a graphical user interface (GUI) that represents data flow as a circuit to create virtual instruments (VIs) for data acquisition and instrument control. LabVIEW's IMAQ functions allowed simple communication with the EFM's CCD for frequent image snapping and continuous evaluation.

MATLAB, a high-level matrix manipulation software package, was used to evaluate the EFM image. MATLAB also supports LabVIEW integration, so once created, the MATLAB algorithm could be easily used as a function within the overall VI. The image is processed in two discrete segments, one to locate the signal within the image and another more complex process to locate the target injection site. Fundamental to both processes is the calculation of the centroid of the intensity distribution. Similar to calculating the center of mass of an object, the centroid calculation factors in intensity and distance from an axis to calculate the centroid coordinate for one dimension. When applied to both axes, this calculation yields a point denoting the "center of intensity" of a matrix of intensity values. The centroid calculation was applied to a number of sub-images, obtained by manipulations of the original intensity array to separate certain components.

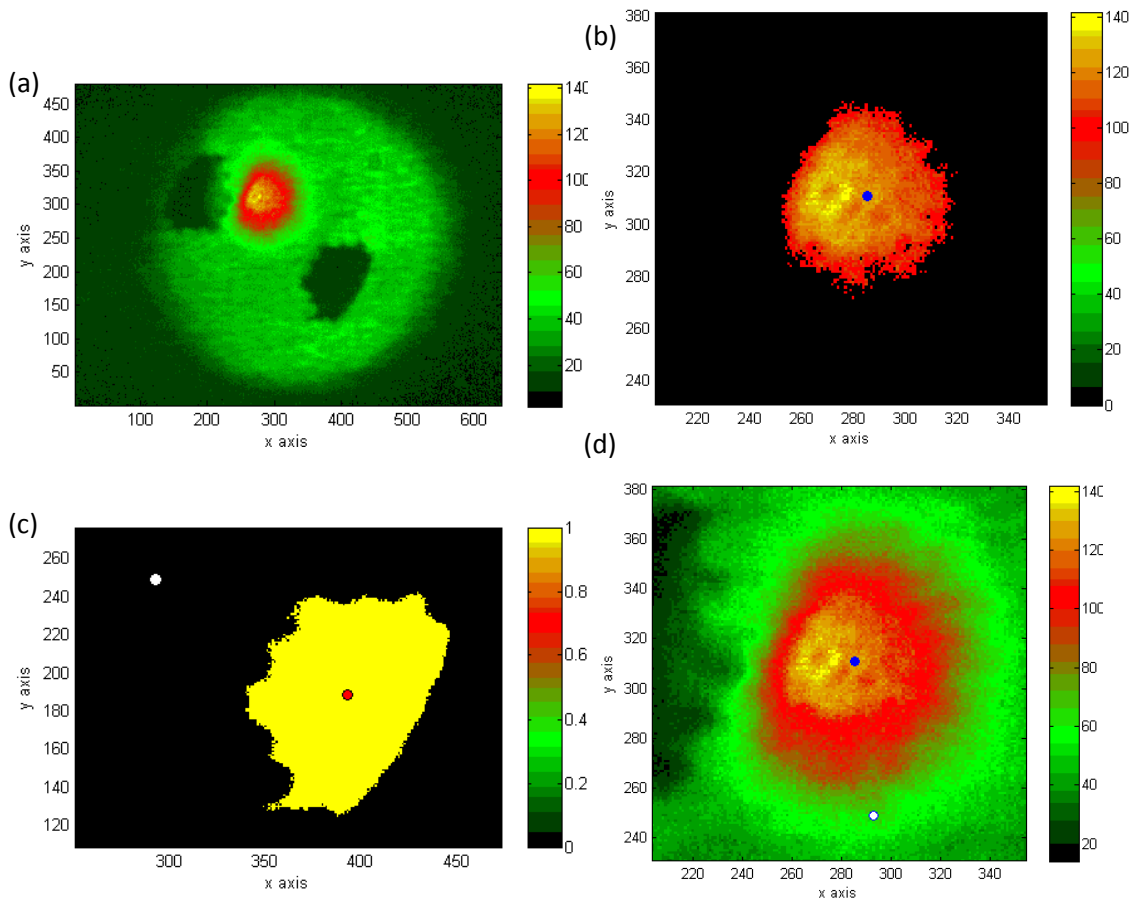


Fig. 6: Series of images representing the process used to calculate the misalignment at injection. Sub-image (a) displays the original image derived from the unaltered matrix of intensity values obtained from the CCD. Sub-image (b) shows the product of the signal locations process, a smaller region including only the signal with the centroid indicated with a blue marker. Sub-image (c) shows the product of the target location process, a smaller region with the centroids of the SAP and ideal injection site indicated. Sub-image (d) shows the combination of the calculated actual and ideal injection locations.

A number of the sub-images used in calculations are displayed in Fig. 6. The sub-image used to find the location of the signal beam is calculated by simply applying a strict threshold to the original image, [see Fig. 6 (a)]. “Thresholding” an image entails setting all values below a certain level, a threshold value, to zero, creating a separate image consisting of only the pixels of highest intensity. When a threshold is applied to the original image, the resulting matrix includes only the signal pulse and occasionally a hot pixel separate from that beam. Since the centroid calculation is fairly sensitive to pixels a large distance from the main distribution, it is performed a number of times, each time narrowing down the region of

interest (ROI). The program calculates a centroid, uses that point as a reference to establish a smaller ROI, which contains only the signal with no extra space for extraneous pixels, to yield the image labeled shown in Fig. 6 (b). The algorithm then calculates the centroid of this smaller image only. This allows the program to avoid the influence of extreme value pixels when calculating the true center of the signal beam.

The process used to calculate the injection target uses the SAP's. These reference point are more difficult to locate. The original image is binarized; that is, any value above a certain arbitrary level is set to a value of one, and every value below that level is set to zero. This creates an image depicting only the outline of the fiber, with the SAPs as blank spots within that outline. This image is used to find an extremely rough value for the center of the fiber. Each row or column is summed, and since every pixel now has the same value the row with the highest sum is taken to be a diameter of the circle, or very close, and used as the y-value for the center of the circle. The same is done for the columns to obtain the x coordinate. This point is not reliable enough to use for the target of injection but it is stable enough for the program to use it as a reference point and generally locate an SAP based on relative positions. An ROI is established based on the rough center to zoom in on the SAP and the sub-image is re-inverted to give the region defining the SAP the positive values. The centroid of this region is calculated, and that point is used to establish a more accurate ROI. The centroid of the second ROI containing the SAP, which creates the image labeled Fig. 6 (c), is taken to be the center of the SAP. The position of the ideal injection site relative to the SAP location is known, so the location of the injection site is obtained from the stable SAP center location. Once the signal and target locations are known the error is calculated by subtracting the coordinates of the target from the coordinates of the signal, yielding the change necessary to align the two, as shown in Fig. 6 (d).

Once the program obtains these error values it must convert them into commands usable by the motors that adjust the path of the signal beam. The mount for the final mirror contains two picomotor

actuators (New Focus, model 8807) that change the pointing of the signal with an angular resolution of $0.7 \mu\text{rad}$ in both directions. After the mirror, the signal beam passes through the focusing lens, and the angular shifts are changed to lateral translations at the input face of the PCF. The error values, measured in pixels, are converted to motor commands, measured in steps, using ratios obtained from a calibration process executed at the initiation of the VI in which the program moves the motors various numbers of steps and records the change in signal location based on those movements. The changes and motor counts are plotted and the slope of the resulting least-squares fit is used for the ratio. This procedure is used for each direction in each dimension and also records ratios for the change in signal location in one dimension created by a motor movement in the other dimension, yielding eight total ratios for conversion. The VI then uses the built-in linear algebra functions in LabVIEW to convert the error values to the necessary motor counts. In order to avoid counterproductive movement the VI runs a number of Boolean checks and prevents the calculation of any motor commands that would move the signal further from the target. A possible solution to positive x error could include more positive x direction movement, and then the negative correction, so the VI tests error values and prevents such corrections. The obtained motor counts are then inserted into prefabricated commands prepared to be compatible with the driver used to communicate with the actuators and sent. The motors adjust the mirror, correcting the error, and the process repeats.

3. Discussion

3.1 Performance

The system's utility is defined by two characteristics, speed of tracking and the maintenance of accuracy over time. The developed VI exceeds requirements for both criteria. The fiber drift is slow at approximately $0.5 \mu\text{m}/\text{min}$, as shown in Fig. 4. The maximum frequency of adjustment (approximately once per second) by the VI is more than enough to keep the signal within an acceptable error range; the operational speed was artificially slowed by the inclusion of a delay so that the actuators were not

adjusting too frequently. The system also maintains error values well within the empirically determined error range of $\pm 5 \mu\text{m}$. Figure 7 shows a graph displaying a typical trial of the performance of the system in regards to speed and accuracy. The system reacts very quickly and maintains error values for both x and y within the accepted range, denoted by bold black lines.

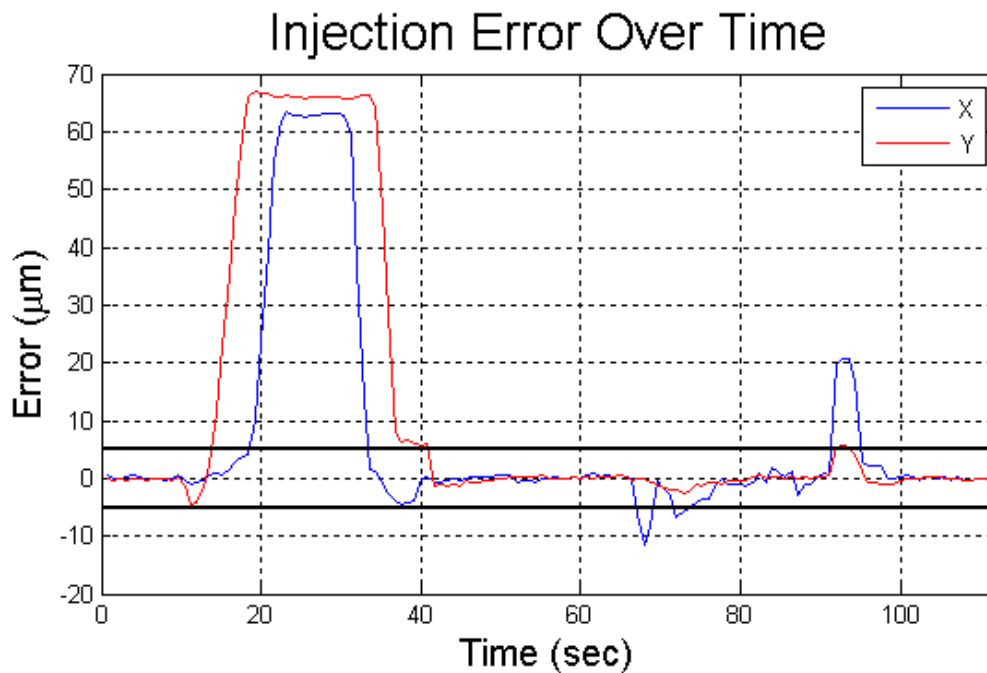


Fig. 7: Graph of injection error versus time for a test run of the software's tracking capabilities. The significant displacement spikes around 20, 70, and 90 seconds are the result of manually induced misalignment to test the program's tracking capability.

3.2 Precautions

One concern with automated alignment is always the risks associated with system failure. In this application, the risks are significant. If the signal is not injected into the fiber core, the available gain of the amplifier is not saturated, increasing the possibility that it will lase, producing a short, intense pulse through self pulsation [7,8]. These pulses can be intense enough that they can irreversibly damage the PCF and the optical components that come before and after it. If the program were to incorrectly analyze an image of the fiber end and divert the signal beam away from the fiber face entirely while the pump was operating at full power the optical system could be damaged. The VI

contains a number of precautions to guard against this. The system runs Boolean checks on all outgoing motor commands, disallowing any action that attempts to move the motors more than a previously set distance limit. If the program attempts such a dangerous command all autonomous tracking is halted, the user is notified, and manual control is restored.

4. Conclusion

The rigid structure of PCFs that provides their nonlinearity and thermal advantages also prevents the use of traditional splicing techniques, necessitating the use of free-space injection. The high-power operation of the PCF results in the dissipation of high amounts of excess heat, causing the location of the optimal injection site to shift during operation. A software program was designed to analyze images taken from an end face microscope to monitor and correct free-space injection. After performance tests, the system was found to exceed requirements for speed and accuracy.

5. Acknowledgements

Many thanks to my supervisor Dr. Jake Bromage for all of his guidance over the course of the program, and to Dr. Craxton for selecting me for the program in the first place.

6. References

- [1] J. Limpert, *et al.*, 'High Repetition Rate Gigawatt Peak Power Fiber Laser Systems: Challenges, Design, and Experiment,' *IEEE Journal of Selected Topics in Quantum Electronics*, **15**, 159 (2009)
- [2] J. Bromage, *et al.* 'Optimizing injection into large-mode-area photonic crystal fiber amplifiers by spatially resolved spectral interferometry', presented at the *Conference for Lasers and Electro-Optics*, paper CWD3, Baltimore, MD (2009)
- [3] G. Agrawal, *Nonlinear Fiber Optics*, 2nd ed. (Academic, San Diego, 1995)
- [4] O. Schmidt, *et al.* 'Single-polarization ultra-large-mode-area Yb-doped photonic crystal fiber,' *Opt. Express* **16**, 3918 (2008)

- [5] J. Bromage, *et al.* 'High-Resolution Spatio-Spectral Characterization of Noncollinear Optical Parametric Amplifiers," presented at *Advanced Solid-State Photonics*, paper AME5, San Diego, CA (2010)
- [6] S. Wielandy, 'Implications of higher-order mode content in large mode area fibers with good beam quality,' *Opt. Express* **15**, 15402 (2007).
- [7] P. Le Boudec, *et al.*, 'Self-pulsing in Er³⁺-doped fiber laser', *Opt. Quantum Electron.*, **25**, 359, (1993).
- [8] F. Brunet, *et al.* 'A Simple Model Describing Both Self-Mode Locking and Sustained Self-Pulsing in Ytterbium-Doped Ring Fiber Lasers,' *J. Lightwave Technol.* **23**, 2131 (2005)

Neutron Detection with High Bandwidth and High Dynamic Range

Cheryl Liu

Neutron Detection with High Bandwidth and High Dynamic Range

Jiaping Cheryl Liu

Pittsford Sutherland High School
Pittsford, NY

Advisor: Dr. James P. Knauer

Laboratory for Laser Energetics
University of Rochester
Rochester, NY

November 2009

Abstract

A neutron diagnostic for inertial confinement fusion (ICF) experiments was designed and fabricated that is suitable for both the OMEGA and National Ignition Facility (NIF) laser systems. The diagnostic measures the spectrum of fusion neutrons that are generated at peak compression. The neutrons are downshifted, or lose energy, as they escape depending on the areal density (ρr) of the imploded target. A greater number of downshifted neutrons indicates a greater ρr , a measure of the success of an ICF implosion. The neutrons are detected by transferring energy to charged particles. The neutron detector uses a foil of polyethylene as a source of protons with which neutrons can exchange energy by elastic collisions. The detector also utilizes tungsten as a shield for x-ray radiation emitted from the target. The neutron detector exhibits high bandwidth and an exceptional dynamic range of 10^{10} which is ideal for measuring neutron spectra from implosion and ignition experiments. The detector will be tested with protons from the Multi-Terawatt laser, tested with neutrons from OMEGA, and ultimately used to diagnose NIF implosion and ignition experiments.

1. Introduction

Inertial confinement fusion (ICF) is a process where nuclear fusion reactions are initiated by rapidly heating and compressing a target, typically in the form of a pellet that consists of a thin plastic external layer and an internal mixture of the hydrogen isotopes deuterium and tritium. ICF implosions create the possibility of cleaner, limitless, and more cost effective energy. For fusion power to be considered practical, a state of ignition must be achieved. Ignition refers to the point at which the energy given off in the fusion reactions is high enough to cause fusion reactions in the surrounding fuel. This causes a chain reaction that allows the

majority of the fuel to undergo a nuclear “burn” and produces more output energy than the energy consumed by the laser. Currently, lasers consume more energy than they produce during implosions and thus for an implosion to be considered successful the energy produced must be much higher than the laser energy. The OMEGA laser at the University of Rochester has 60 laser beams that focus up to 30 kJ of energy onto targets. Although very powerful, it cannot obtain ignition. The Lawrence Livermore National Laboratory’s National Ignition Facility (NIF) is a new 1.8 MJ, 192-laser-beam system designed to achieve nuclear fusion ignition completed in 2009.¹ The NIF replaced the OMEGA laser facility as the most powerful laser system in the world.

In ICF experiments, primary energetic neutrons are produced by two reactions:



Neutrons generated from deuterium-deuterium reactions have energies of 2.45 MeV while neutrons generated from deuterium-tritium reactions have higher energies of 14.1 MeV.

The fusion neutrons travel through the relatively “cold” fuel shell of the target and some are scattered. The neutrons are down-scattered or downshifted, meaning that they lose energy as they escape. Some neutrons will scatter more than others, creating a spectrum of the downshifted neutrons. The downscattered neutrons are generated when the areal density (ρr), the density ρ of the cold fuel shell times its thickness r , is high. A high areal density is important for the success of an implosion because the chain reaction of ignition requires compression of a sufficient thickness of fuel (ρr). Typically, DT fuel is used as the inner fuel of the target. Sufficient ρr is necessary for chain reactions to occur because alpha particles traveling through the compressed fuel deposit their energy only when the ρr is high enough. Neutron diagnostics

that measure the neutron spectra therefore enable the ρr to be measured, providing valuable information on the success of implosion and ignition experiments.

This work exhibits the design and fabrication of a new neutron “diode” which will be able to measure full neutron spectra with a much higher bandwidth and dynamic range than existing detectors. Figure I gives a schematic of the design concept of the neutron diode and the correspondence of the neutron spectrum to the recorded signal of the detector.

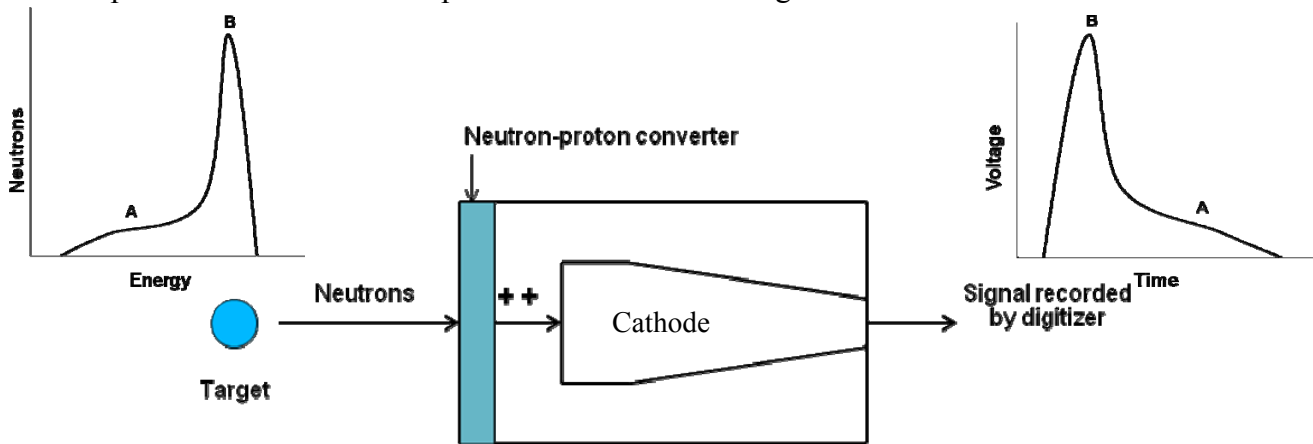


FIG. I. Design concept for neutron diode in target chamber

Incoming neutrons encounter a plastic converter foil where they transfer energy to protons. Energy transfers within the diode from neutrons to charged particles are crucial for detecting neutrons because neutrons are electrically neutral particles and thus do not respond to electric fields. The neutrons can transfer almost all of their kinetic energies to protons during direct, elastic collisions because of the similarity in their masses. A proton flux exits the plastic neutron-proton converter and attracts towards the negatively charged cathode. Secondary electrons are emitted from proton bombardment upon the cathode. Together the electrons and protons produce an electrical current and a signal voltage across a 50 Ω impedance that is recorded by a digitizer. Figure I shows the concept that neutrons of higher energy arrive at the diode first and thus the signals from higher energy neutrons are recorded first.

Prior to this work, the concept of this diode has not been used in neutron detectors because of the low neutron-proton cross section. However, this detector is feasible because of the large neutron yield expected from the National Ignition Facility. In this work, a neutron detector was designed and fabricated. The detector exhibits higher bandwidth and higher dynamic range than existing neutron detectors. Simulations of expected signals have been made for the Multi-Terawatt (MTW), OMEGA, and NIF laser systems. The neutron diode will first be tested with protons from the MTW laser, a high intensity laser at the Laboratory for Laser Energetics. The diode will then be used to diagnose implosions on the OMEGA system. Ultimately, it will be used to diagnose ignition experiments on the NIF.

2. Design of the detector

2.1 Design concept

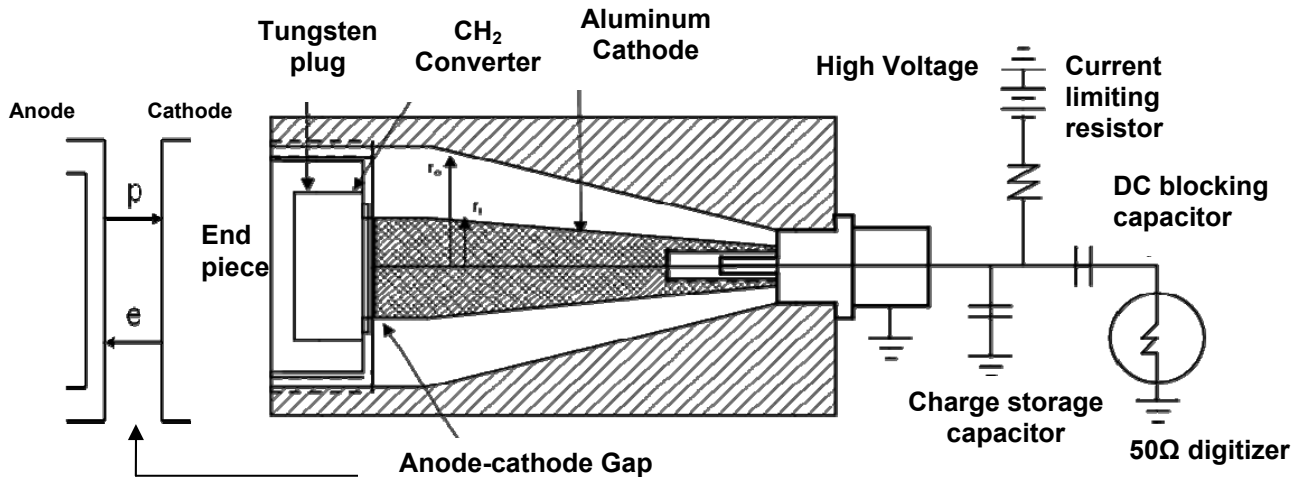


FIG. II. Detailed drawing of neutron diode and anode-cathode gap

Figure II shows a detailed drawing of the neutron diode and with a zoom on the anode-cathode gap. The main parts include a cathode, a washer which serves as the anode, an end piece holding a tungsten plug to close the detector and block unwanted radiation, a plastic (CH_2) neutron-proton converter, a set screw to attach the connector, and a main housing compartment

to lodge and protect all the above parts. The gap between the anode and the cathode creates an electric field with protons flowing towards the cathode and electrons toward the anode, or the washer. The current limiting resistor prevents the current from reaching the high voltage. High voltage is applied through a commercially available² bias tee. The DC blocking capacitor ensures that the high voltage does not go across the 50 Ω digitizer. The charge storage capacitor helps maintain the voltage across the cathode-anode gap between the CH₂ foil and cathode. The signal is recorded by the 50 Ω digitizer.

The neutron-proton scattering cross section is crucial for calculating the number of protons expected to reach the cathode. Table I shows a comparison of calculated and experimental values for the neutron-proton cross section for 14 MeV neutrons.

TABLE I. Summary of calculated and experimental n-p cross sections

Type of data	Energy (MeV)	Cross Section (barns)	Reference
Calculated	14	0.694 ± .019	Agno ³
Calculated	14	0.69	Sleator ⁴
Calculated	14	0.6929	Bame, Haddad, Perry ⁵
Calculated	14	0.70 ± 0.06	Salant and Ramsey ⁶
Calculated	14.10	0.689 ± 0.005	Poss, Salant, and Yuan ⁷
Experimental	14.10	0.688	Poss, Salant, and Yuan ⁷
Experimental	14.12	0.687	Coon, Graves, and Barschall ⁸
Calculated	14.20	0.675 ± 0.02	Meyer and Nyer ⁹

From these data, the average neutron-proton cross section is 0.69 barns or $6.9 \times 10^{-25} \text{ cm}^2$ for 14.1 MeV neutrons. The neutron-proton section is $2 \times 10^{-24} \text{ cm}^2$ for 2.523 MeV neutrons.¹⁰

The quantum efficiency of protons to electrons is also required. Figure III shows the yields of secondary electrons per primary proton for aluminum.

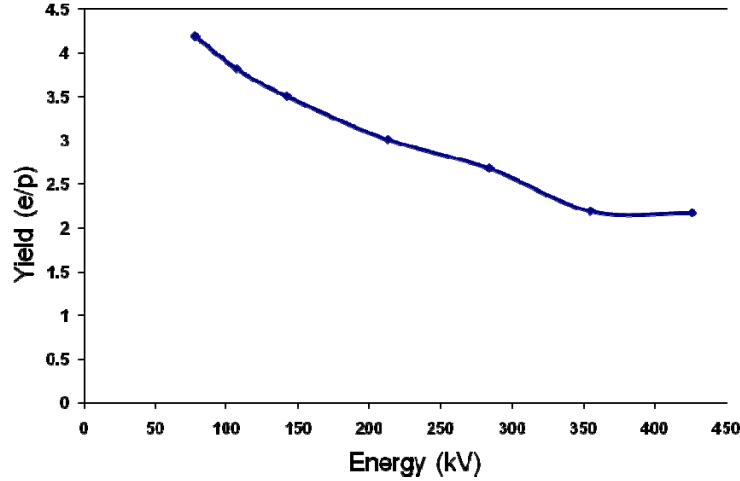


FIG. III. Yield of secondary electrons per primary proton on an aluminum target. Experimental yield obtained by Hill et al.¹¹

Based on Figure III, the quantum efficiency can be assumed to be two electrons per proton for protons with energies above 400 kV.^{11,12}

The expected signal can be calculated through a series of steps. The number of neutrons (N_n) reaching the converter is given by:

$$N_n = Y \cdot (A_d / 4\pi d^2) \quad (3)$$

where Y is the neutron yield, d is the distance from the target and A_d is the area of the cathode of the detector.

The number of protons (N_p) produced in the converter can be calculated by:

$$N_p = N_n \cdot \tau \cdot \sigma \cdot r \quad (4)$$

where τ is the proton-neutron cross section, σ is the number of protons per cm^3 in the converter and r is the depth of the converter. Low density polyethylene (LDPE), the converter used for the neutron diode, has a density of 0.92 g/cm^3 , a molecular weight of approximately 14 g/mol and two protons per molecule, giving $\sigma = 8 \times 10^{22} \text{ protons/cm}^3$. Low density polyethylene was chosen because of its large proton density as shown in Table II and because it is more readily available than high density polyethylene (HDPE).

TABLE II. Comparison of proton densities of different materials

Material	Density of Material (g/cm ³)	Proton density (protons/cm ³)
CH	1.02	4.72 x 10 ²²
CH ₂ (LDPE)	0.92	7.92 x 10 ²²
CH ₂ (HDPE)	0.95	8.17 x 10 ²²
H ₂ O	1.00	6.69 x 10 ²²

The neutron diode is designed to measure the neutron spectrum from 9 to 15 MeV with 5% accuracy. To achieve this, the neutron detector requires a high enough dynamic range. The dynamic range of the neutron detector is defined as

$$DR_{\max} = V_{\max} / V_{\min} \tag{5}$$

where V_{\max} is the maximum detectable voltage and V_{\min} is the minimum detectable voltage. If the maximum and minimum signal voltages are S_{\max} and S_{\min} , respectively, and are to be measured with a precision ϵ , it is required that

$$DR_{\max} = S_{\max} / S_{\min} \cdot (1 / \epsilon)^2 \tag{6}$$

Using $\epsilon = 0.05$, this will require a detector with a dynamic range of at least 4.0×10^6 if the signal ratio S_{\max} / S_{\min} is 10^4 .

Scintillators and chemical vapor deposition (CVD) diamond detectors typically have a dynamic range of 4×10^4 to 4×10^6 . These detectors are useful for measuring the neutron spectrum for implosion experiments with lower neutron yields and detecting single neutrons; however they cannot fully measure neutron spectra for implosion experiments of higher peak yields, such as ignition reactions. Because the neutron diode has a minimum output voltage of 0.1 μ V and a maximum output voltage of 1.2 kV, the diode has an estimated dynamic range

(DR_{\max}) of 10^{10} and thus is able to measure the full neutron spectrum for the higher peak yields of break-even and ignition campaign experiments.

2.2. Detailed design

The neutron diode was designed using Ashlar Vellum’s *Graphite*¹³ computer aided design program. Figure IV shows the key parts of the fabricated diode. The design process and individual pieces of the neutron diode are detailed in this section.

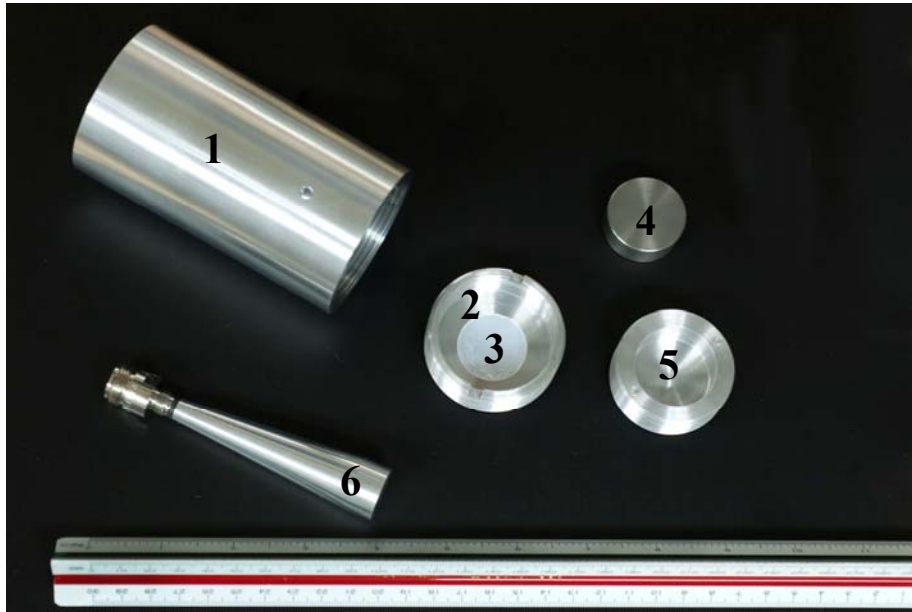


FIG. IV. Parts of the detector unassembled. Labeled are the key parts of the detector. (1) Housing (2) Threaded washer (3) Polyethylene converter (4) Tungsten plug (5) End piece (6) Cathode

For the detector to avoid unwanted reflected signals while measuring the signal, maintaining uniform impedance is crucial. A large surface area of the cathode is desired so that a higher number of protons will hit it and produce a larger signal. Thus, the cathode is tapered so the frontal surface has a large surface area and the rear is fitted to the smaller connector.

However, because the cathode is tapered the inside of the housing is also tapered to maintain uniform impedance (Z) throughout the detector. Equation (7)¹⁴ is used:

$$Z = 60 \ln (r_o/r_i) \Omega \quad (7)$$

where r_o is the outer radius and r_i is the inner radius which are labeled on Figure II. An impedance of 50Ω was chosen to match the recorder input impedance. Choosing 10 mm for r_i or the inner radius of the housing compartment at the converter end of the detector, 23 mm is obtained for the outer radius, r_o . By choosing a r_i of 4 mm at the connector end of the cathode, a r_o of 9.2 mm must be used.

To accommodate the electrical connection to the detector, a type N connector was chosen because of the need to bias the cathode with a high voltage. To fit this connector, a tapped 8.4 mm space was set in the back of the detector. In order to easily attach the cathode and the connector to the main housing, the cathode was drilled and tapped for a $\frac{1}{4}$ ”-28 thread so that a set screw can be screwed into the cathode.

The aluminum threaded washer serves to hold both the neutron-proton converter and end piece in place. It is tapped for a 2”-12 thread and a $1 \frac{3}{4}$ ” -12 thread so that the end piece can be screwed onto it and to allow for adjustments within the housing. The washer leaves a 1 mm space in the front for the 1 mm polyethylene converter to fit into.

In order to create an electric field between the washer (anode) and the cathode, a small gap large enough for a proton to travel in 100 picoseconds was included. This gap was calculated to be 0.6 mm, but for the purposes of the detector it was rounded to 0.5 mm.

The aluminum housing features a tapered shape and two threaded openings: one in the front for the end piece and one in the rear of the detector for the connector. Because various gases may enter the detector in the target chamber, two cinched plugs are placed on opposite sides of the main housing. These allow gases such as air to escape the detector.

The end piece serves a dual function: it closes and protects the detector but more importantly it serves to shield the detector from gamma and x-rays emitted from the target during

implosions. The measure of the effectiveness of the material as a gamma shield is called the “half value thickness,” that is, the thickness of a material that will reduce the gamma ray exposure by 50 percent. To maximize the absorption of gamma and x-ray radiation from the imploded target, a substance with a very low half thickness is desired. Tungsten has one of the lowest half value thicknesses of 0.04 cm, and unlike other substances with very low half value thicknesses such as uranium, it does not emit excess radiation through decay and thus does not create excessive, unwanted background signal. Also, while tungsten absorbs x-ray radiation, it will not absorb or shield any neutrons. Because of tungsten’s low half value thickness, a 13 mm tungsten plug is employed as part of the end piece.

Aluminum was chosen as the material for a majority of the parts, because aluminum, unlike other metals such as stainless steel, does not react or become activated during implosion experiments and thus does not create unwanted background signals.

3. Comparison with other neutron detectors

There are several types of detectors that are currently used for neutron detection. The most popular and effective are scintillators and chemical vapor deposition (CVD) fabricated diamond detectors.

Table III gives a comparison of several existing neutron diagnostics with the new neutron diode. All data for the neutron diode are calculated values while values for other types are experimental or commercially available.^{15,16} It is evident that the new neutron diode displays much higher bandwidth (shorter rise and decay times) than both scintillator and CVD diamond detectors as well as an exceptionally large dynamic range in comparison to existing neutron

diagnostics. In addition to high dynamic range and bandwidth, the neutron diode is shielded for x-ray radiation and it is less sensitive to gamma radiation because of the tungsten shielding.

TABLE III. Comparison of the bandwidth and dynamic range of the new neutron diode with other types of detectors

Type of detector	Rise time	Decay time	Dynamic Range
Nonplastic Scintillator ¹⁵	250 ns	Up to 2 ms	10 ⁴
Plastic Scintillator ¹⁵	<1 ns	2-3 ns	10 ⁵
Liquid Scintillator ¹⁵	<1 ns	<1 ns	10 ⁴
CVD diamond detector ¹⁶	200 ps	5 ns	10 ⁴
Neutron diode	46 ps	275 ps	10 ¹⁰

4. Results

Calculations of expected signals have been developed for the Multi-Terawatt (MTW) laser system, the OMEGA laser system, and the new National Ignition Facility (NIF) .

4.1 Predicted signals for the Multi-Terawatt laser

The Multi-Terawatt laser system emits protons and gamma rays in laser-solid interactions when targets are irradiated with short pulse lasers. Protons originate from layers of contamination on the target surfaces. MTW is suitable for testing the new neutron diode because of its proton emission. The CH₂ converter will be unnecessary for these tests and will be taken out from the washer because the diode will directly detect protons.

Calculations have been made to ensure that the protons emitted will be able to override the gamma radiation that is also emitted based on previous target shots. To further attenuate the background photon signal, a 0.01 cm aluminum transmission filter will be placed in the space in

the washer in place of the CH₂ converter. The filter will attenuate photons with energies less than 7000 eV.

To estimate the signal from protons, the expected proton spectrum on MTW is necessary. This has not been previously measured. However, Kaluza et al.¹⁷ present a proton spectrum from a laser system similar to MTW for targets of different thickness aluminum foils (see Fig. V). Figure V gives $dN_p/(dE \cdot d\Omega)$, the number of protons in energy interval dE and solid angle $d\Omega$ as a function of proton energy E .

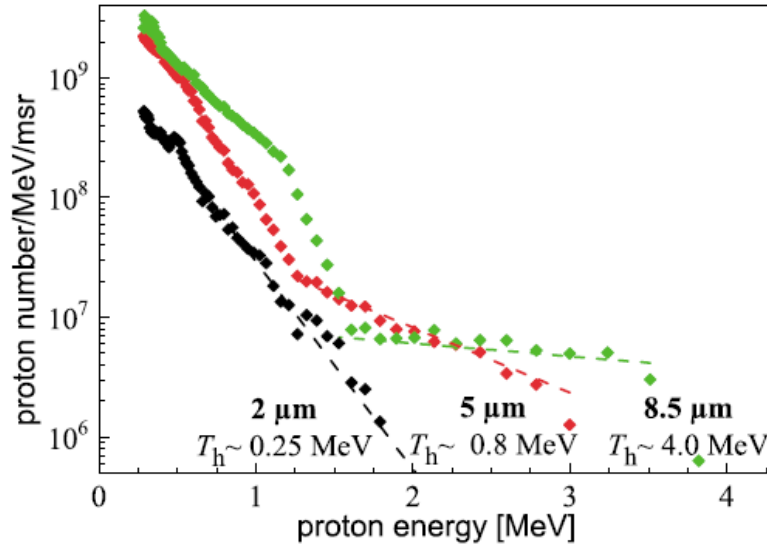


FIG. V. Proton spectra from aluminum foils of varying thickness

The signal received by the detector depends on the rate of arrival of protons at the detector dN_p/dt and is calculated as follows:

$$dN_p/dt = dN_p/dE \cdot dE/dt \quad (8)$$

$$dN_p/dE = dN_p/(dE \cdot d\Omega) \cdot \Delta\Omega \quad (9)$$

$$\Delta\Omega = A_d/d^2 \quad (10)$$

where dN_p/dE is the number of protons as a function of proton energy, dE/dt is the proton energy as a function of time, $\Delta\Omega$ is the solid angle of the detector, A_d is the area of the frontal

surface of the cathode and d is the distance from the target chamber center that the detector will be placed. Since $E = \frac{1}{2} m (d/t)^2$, dE/dt is given by

$$dE/dt = (1/d\sqrt{m}) \cdot 2E^{3/2} \quad (11)$$

The number of electrons as a function of time is given by

$$dN_e/dt = dN_p/dt \cdot QE \quad (12)$$

where QE is the quantum efficiency. The current can then be calculated:

$$I = (dN_e/dt + dN_p/dt) \cdot q_e \quad (13)$$

where q_e is the charge of an electron. Using Ohm’s law with a 50Ω resistance will yield the voltage signal. Figure VI shows the expected signals from the protons from aluminum targets when the detector is placed 90 cm away from the target chamber center. Higher voltages are expected at later times because more protons of lower energies arrive at later times. This is different from the case of fusion neutrons where a small number of neutrons come at later times, but applying the neutron diode in MTW serves to test the diode.

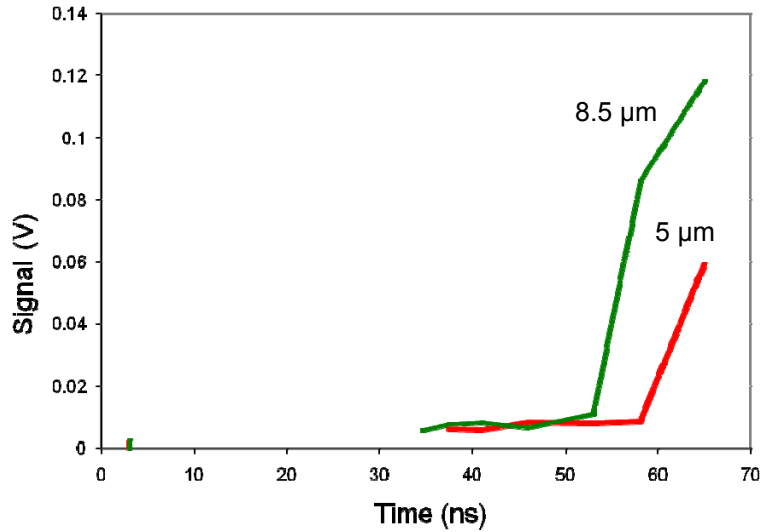


FIG. VI. Calculated signals from protons on the MTW laser as a function of time, based on the spectra of FIG. V for 8.5 and 5 μm aluminum targets.

4.2 Predicted signals for OMEGA

OMEGA implosions typically have neutron yields (Y) in the range of 10^9 to 10^{14} . Figure VII shows the predicted neutron spectra from two typical OMEGA implosion experiments¹⁸ with areal densities (ρr) of 100 and 200 mg/cm^2 . The two ρr curves show that an increased ρr corresponds to more downscattered neutrons. Thus ratios of the number of downscattered neutrons can determine the ρr , a measure of the success of the implosion. These calculations show that as the ρr doubles, the number of neutrons/MeV doubles. The graph is shown in terms of the number of neutrons/total DT neutron yield/MeV.

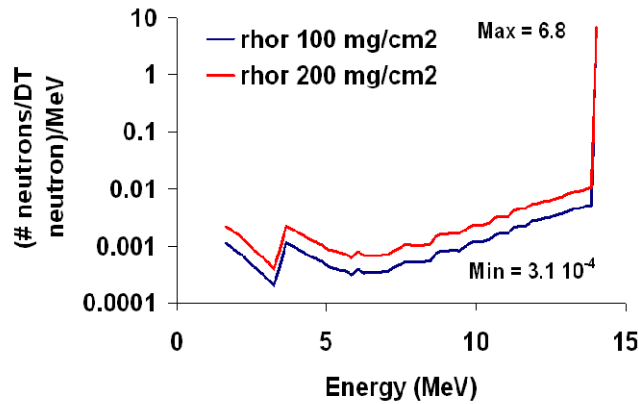


FIG. VII. DT Neutron spectrum from an OMEGA implosion experiment

Using Equations (8) through (13) with N_p replaced by N_n and the neutron-proton cross sections, the expected signals have been calculated and are shown in Figure VIII with an estimated total neutron yield of 10^{10} . Placing the detector a distance of 40 cm away from the target chamber center on OMEGA, a reasonable maximum signal of 0.19 volts with a ρr of 200 mg/cm^2 is obtained which is well in within the detectable signal range. The signal peaks at 7.69 ns as a result of the 14.1 MeV DT neutrons. The diode will be able to detect neutrons for implosions yielding up to 10^{13} at a distance of 40 cm away from the target chamber center because of the large dynamic range.

The minimum signal ($4 \mu\text{V}$) is above the minimum output voltage ($0.1 \mu\text{V}$), and so the neutron diode should be easily capable of measuring the neutron spectra for future implosion experiments on OMEGA.

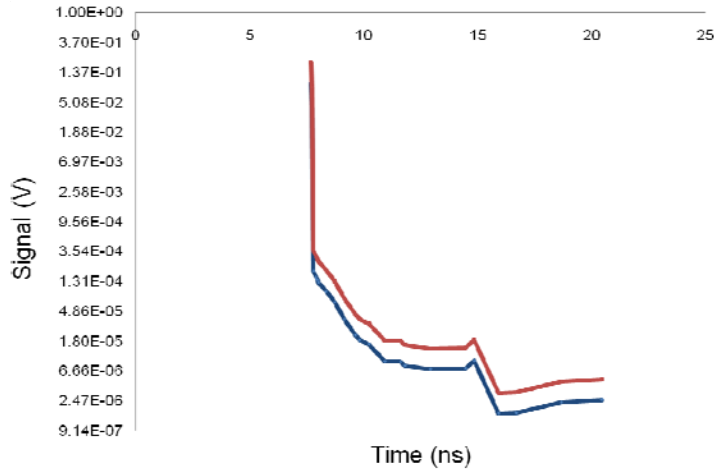


Fig VIII. Expected signal from OMEGA with a neutron yield of 10^{10} , showing the downscattered neutrons for two values of areal density, ρr . The blue curve corresponds to a ρr of 100 mg/cm^2 while the curve in red corresponds to a ρr of 200 mg/cm^2 .

4.3 Predicted signals for the National Ignition Facility

Figure IX shows simulated neutron spectra for the tritium hydrogen deuterium (THD) campaign on the NIF laser system.¹⁸ The THD campaign uses targets filled with mostly tritium to produce implosions that are hydrodynamically equivalent but produce a reduced number of neutrons. Thus the campaign is a plan for testing and perfecting the target fuel content and target chamber conditions to be done on the NIF to ensure all conditions are ideal before attempting real ignition experiments. In colors are spectra from targets with 0.5% D_2 fuel that are not meant to ignite and serve as tests for the NIF. In black is a spectrum with 50% D_2 fuel that was calculated without alpha particle deposition to serve as model for a non-igniting target. The ρr is determined by the region of 9 MeV to 15 MeV neutrons.

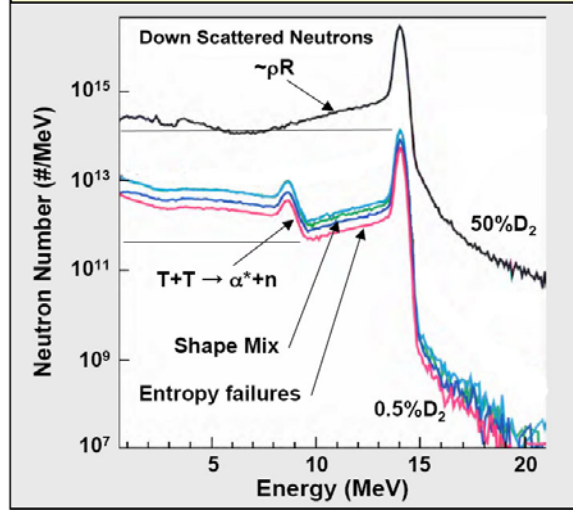


FIG. IX. Simulated neutron spectra for NIF for 50:50 DT (black curve) and for THD targets containing 0.5% D₂ (colors)

The typical neutron yield on the NIF ranges from 10^{13} to 10^{18} . For initial experiments with lower neutron yields, the detector can be placed 40 cm away from the target chamber center like the experiments using OMEGA. For 50% D₂ experiments with higher neutron yields, it will be necessary to move the detector farther away to 400 cm from the target chamber center so the signal is within the dynamic range of the detector.

Figure X(a) shows the expected signal on the NIF when the neutron diode is placed 400 cm from the target chamber center (TCC) for ignition campaign experiments using targets of 50% D₂ fuel while Figure X(b) shows that of targets using 0.5% D₂ fuel placed 40 cm away from the target chamber center. Figure X(a) peaks at 77.2 ns with a voltage of 233.3 V and Figure X(b) peaks at 7.72 ns with a voltage of 6.67 V. The discrepancy between the times is due to the different distances between the diode and the center of the target chamber. Both signals are within the detectable range of the neutron diode and thus the diode can be used effectively on the National Ignition Facility.

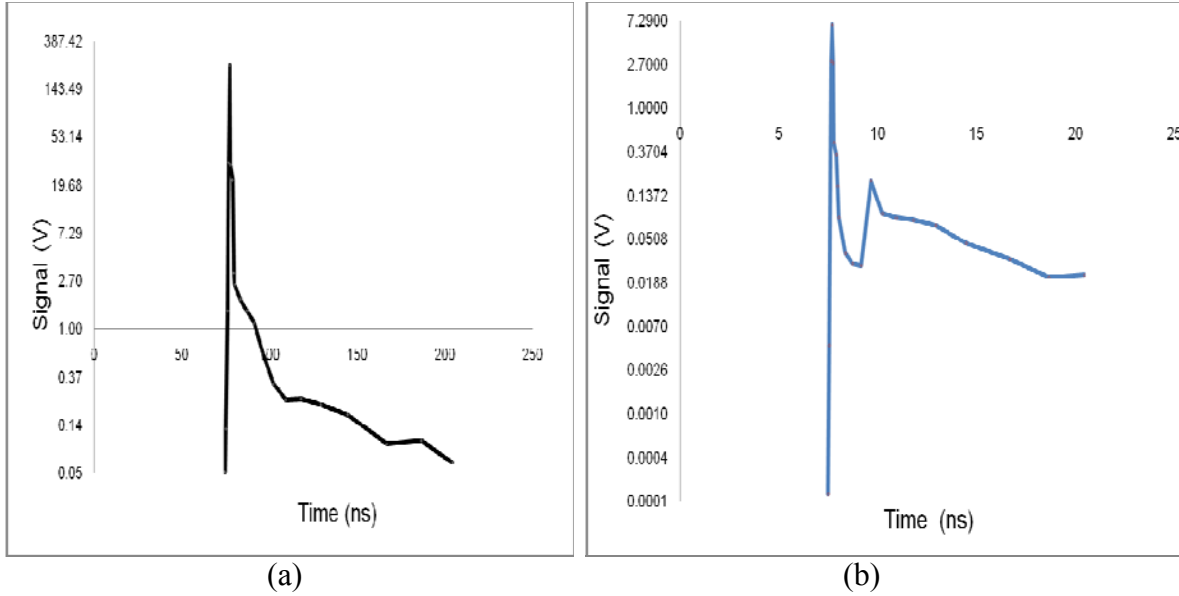


FIG. X. Expected signals on the NIF corresponding to
 (a) 50% D_2 curve with detector placed 400 cm from TCC (black)
 (b) 0.5% D_2 curve with detector placed 40 cm from TCC (blue)

Conclusion:

A neutron detector with high bandwidth and dynamic range was designed and fabricated. Expected signals were calculated for the MTW, OMEGA, and NIF laser systems. These signals are all within the dynamic range of the detector with the detector placed 90 cm away from the target chamber center for MTW, 40 cm away for OMEGA and 400 cm during THD ignition campaign experiments of the NIF.

It has been demonstrated from the predicted signals that the detector is useful not only for the MTW and OMEGA laser facilities but also for the new laser facility at the NIF. The next step is to test the neutron diode on MTW, using protons to simulate results on OMEGA and the NIF. From there, the diode can be further used to diagnose OMEGA experiments and eventually ICF ignition campaign experiments on the NIF.

The diode presented in this work is significant because it has an exceptional dynamic range that will enable it to measure the full neutron spectra of implosion and ignition campaign

experiments. On the National Ignition Facility, the detector will be used to measure the success of THD ignition campaign experiments, helping to bring fusion experiments closer to providing a source of clean, limitless energy.

Acknowledgements:

I would like to thank my advisor, Dr. James P. Knauer for his immense support, advice, and patience. I would also like to thank Dr. R. S. Craxton, the University of Rochester’s Laboratory for Laser Energetics and the United States Department of Energy for providing me the opportunity to participate in this inspiring program.

References:

1. E. I. Moses, *Fusion Sci Technol.* **44**, 11 (2003).
2. Picosecond Pulse Labs, Inc. (http://www.picosecond.com/product/product.asp?prod_id=90)
3. Ageno *et al.*, *Phys. Rev.* **71**, 20 (1947).
4. W. Sleator, *Phys. Rev.* **72**, 207 (1947).
5. S. J. Bame, *et al.*, *Rev. Sci. Instrum.* **28**, 12 (1957).
6. E. O. Salant and N. F. Ramsey, *Phys. Rev.* **57**, 1075 (1940).
7. H. Poss, *et al.*, *Phys. Rev.* **87**, 11 (1952).
8. Coon *et al.*, *Phys. Rev.* **88**, 562 (1952).
9. D. I. Meyer and W. Nyer, Los Alamos Report No. 1279 (1951).
10. Fields, *et al.*, *Phys. Rev.* **94**, 389 (1954).
11. A. G. Hill, *et al.*, *Phys. Rev.* **55**, 463 (1939).
12. S. Bartholome, *et al.*, *Nucl. Instrum. And Meth. In Phys. Res. B* **125**, 13 (1997).

13. *Graphite*, Ashlar-Vellum, Inc., 9600 Great Hills Trail, Suite 150W-1625, Austin, TX 78759, 2001.
14. D. Gray, *American Institute of Physics Handbook*, 3rd ed. (McGraw-Hill, New York, 1972), p. 5-57.
15. Amcrys-H, Inc., 60 Lenin Ave, Kharkov 310001, Ukraine, 1998.
16. G. J. Schmid, *et al.*, *Rev. Sci. Instrum.* **74**, 1828 (2003).
17. M. Kaluza, *et al.*, *Phys. Rev. Lett.* **94**, 045003 (2004).
18. J. P. Knauer, private communication (2009).

X-Ray Phase-Contrast Characterization of Cryogenic Targets

Trevor Lu

X-Ray Phase-Contrast Characterization of Cryogenic Targets

Trevor Lu

Webster Thomas High School,
Webster, NY

Advisor: Dana Edgell

Laboratory for Laser Energetics
University of Rochester,
Rochester, NY

Abstract

In order to obtain ignition and high gain in an implosion, a cryogenic target's ice layer must be almost perfectly spherically symmetric. The Cryogenic Fill-Tube-Target Test Facility (CFTF) can be used to create and characterize cryogenic target ice layers. X-ray phase contrast imaging on the CFTF uses a small-spot-size x-ray source to irradiate the target with x-rays that are recorded by an x-ray camera on the opposite side of the target. X-rays that pass through the ice layer at nearly tangential angles undergo strong refraction, resulting in light and dark rings in the camera image. Asymmetries and imperfections in the ice surface are characterized by analyzing these rings. To better understand the behavior of these rings, the ray-tracing code Icarus was used to simulate the rings. In particular, the effects of a finite spot size and the energy distribution of the x-ray source were studied and compared with experimental measurements of the rings.

Introduction

The OMEGA-60 laser¹ in the Laboratory for Laser Energetics is primarily used to

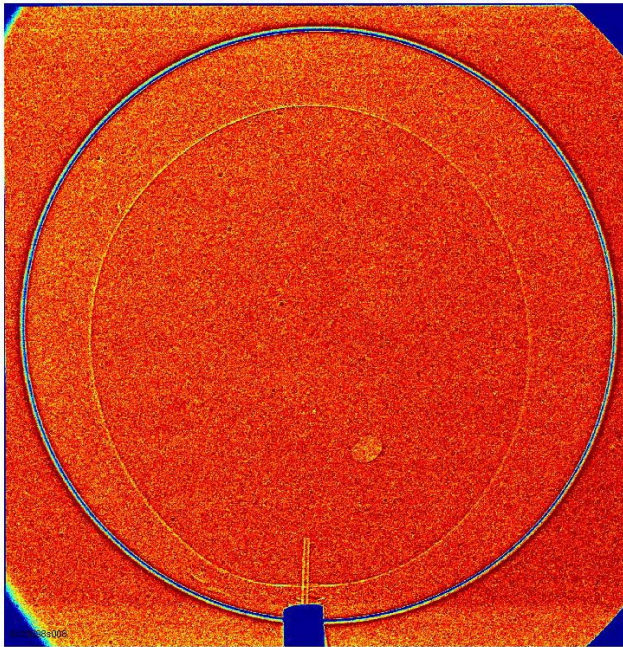


Figure 1: X-ray phase contrast image of a cryogenic target. The blue circle in the image is the outer edge of the target. The very asymmetric inner yellow "ring" is indicative of the shape of the inner ice layer. This image is of a very poor quality ice layer and is shown here to emphasize the usefulness of these images in diagnosing layer quality. Typical ice layers produced at LLE are much more symmetric.

conduct fusion reactions. To do this, it launches 60 laser beams at a suspended cryogenic target with enough concentrated heat to trigger an implosion. These cryogenic targets are made up of a very thin plastic shell surrounding a thin layer of DT ice. The central region contains some residual DT gas. The difficulty is that the slightest imperfections on the ice surfaces of these targets will cause a section to implode faster or slower than the rest of the layer, resulting in a failed implosion.

In order to characterize the imperfections of the ice layer, a cryogenic target is observed through x-ray phase-contrast imaging² (Figure 1). Refraction of x-rays that strike the edge of the ice causes bright rings to appear in the image. It is the replication and study of these rings that is the focus of this project.

X-Ray Phase-Contrast Imaging

The new Cryogenic Fill-Tube-Target Test Facility (CFTF) shown in Figure 2 is specifically designed to test cryogenic targets for imperfections through backlit optical shadowgraphy and x-ray phase-contrast propagation imaging. A tungsten anode launches x-rays at a target suspended in a target chamber which are then received by a 1340 x 1300, 16 bit x-ray camera. The target can be rotated inside the chamber so that images can be recorded for many views and a 3D reconstruction of the target can be produced.

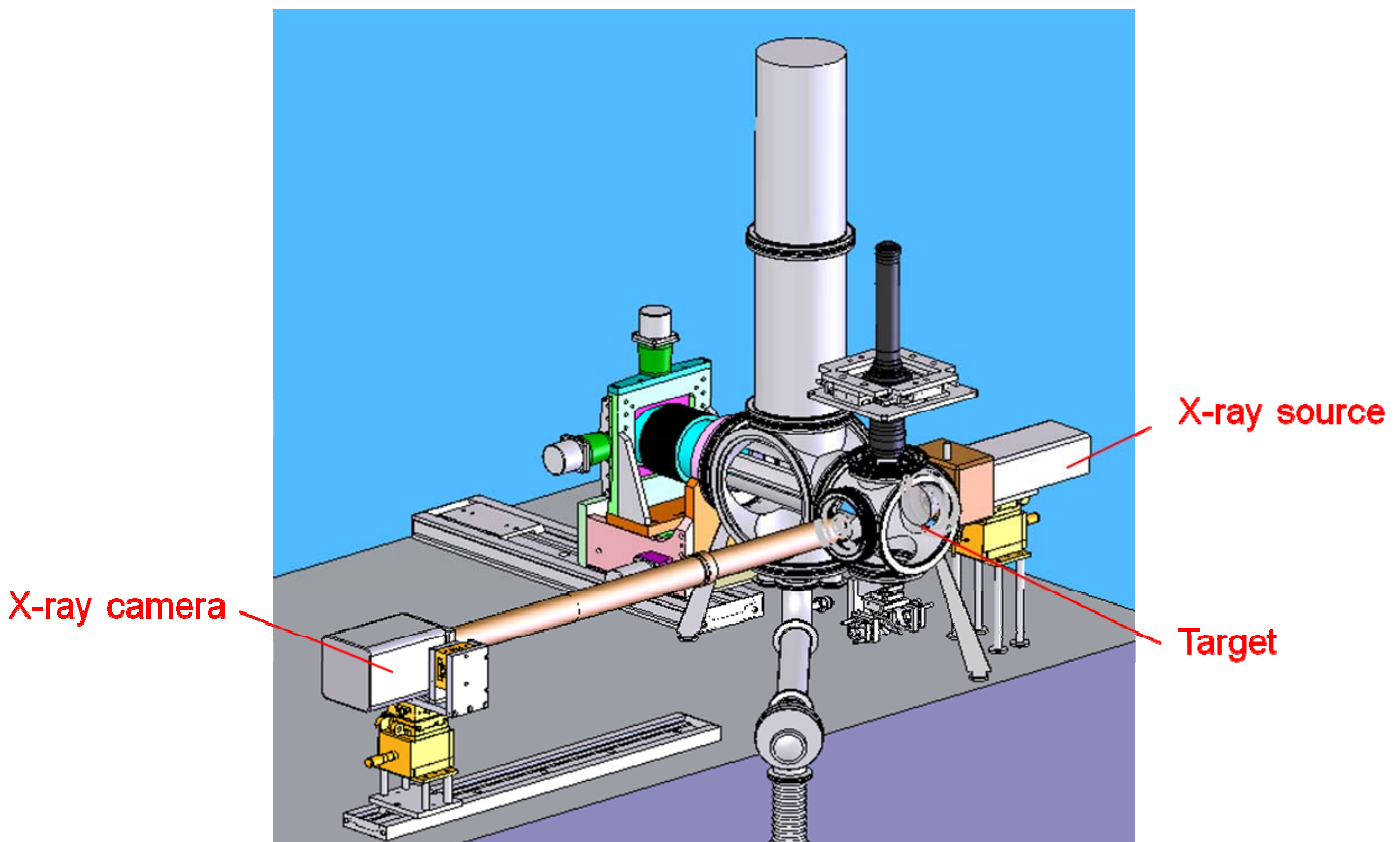


Figure 2: The Cryogenic Fill-Tube-Target Test Facility

The x-rays pass through the target with almost no deflection from a straight line as shown in Figure 3.

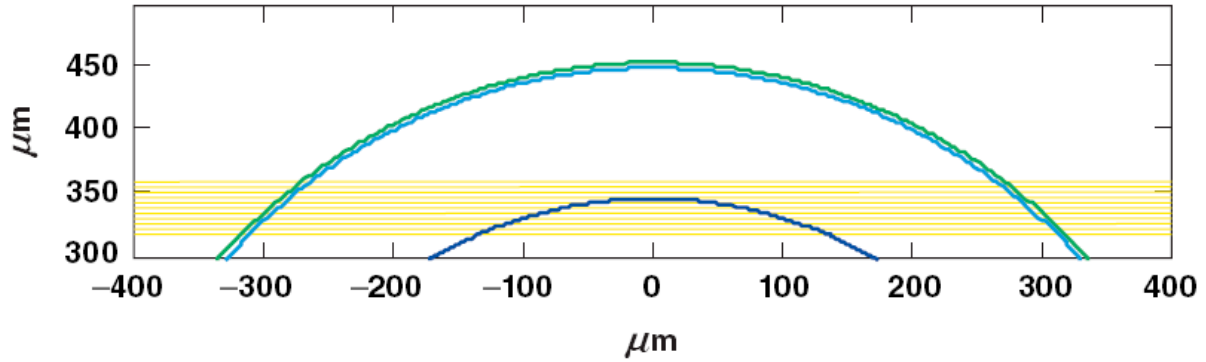


Figure 3: Ray trace of x-ray paths through a cryogenic target. The dark blue circle is the inside surface of the ice layer.

However, when the rays are allowed to travel the distance to the camera (about 1m) a deflection due to refraction becomes noticeable for those rays that are nearly tangential to the inner ice surface as shown in Figure 4.

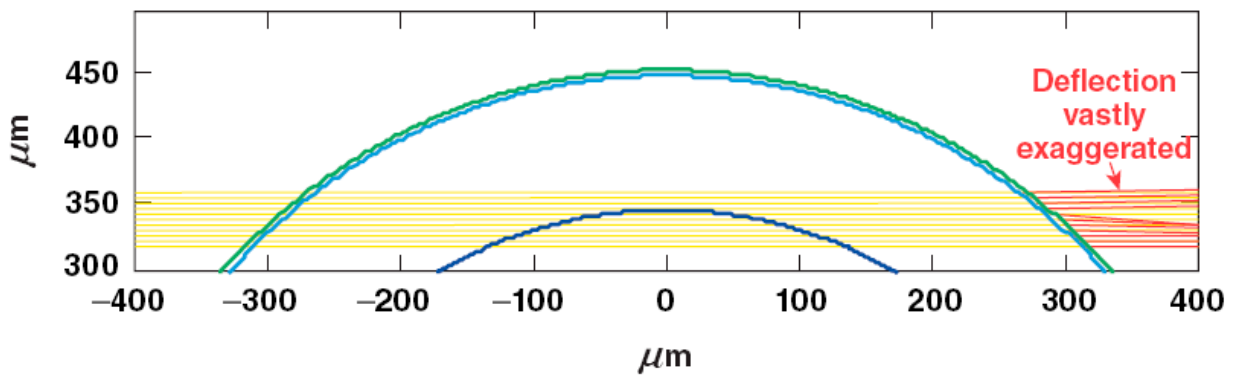
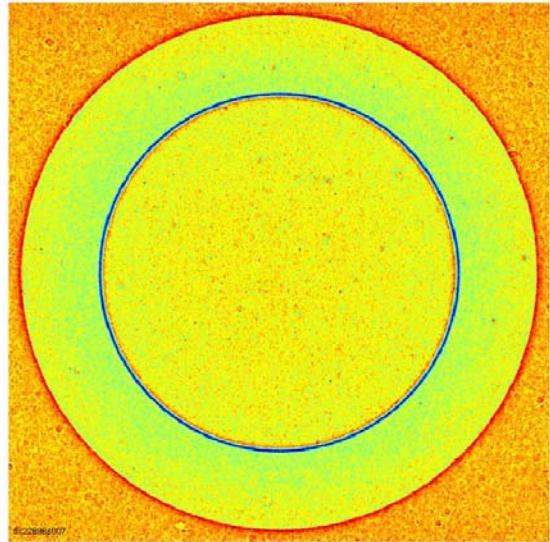


Figure 4: Same as Figure 3 except that the emerging ray deflections have been greatly exaggerated. The small deflection due to refraction of those rays that are nearly tangential to the inner ice surface becomes apparent when the camera is placed a meter away from the target.

The variation in x-ray intensity due to the deflection of the x-rays results in a ring appearing in the phase-contrast image (the blue/orange ring in Figure 5).

To determine where the actual ice layer is, the position of the ring relative to the ice surface must be calculated.

Figure 5: Experimental x-ray phase contrast image of a thick walled plastic shell used for calibration purposes. The deflection of the x-rays creates a ring in the image. The dark blue ring (low intensity) indicates where the rays have been deflected from. The fainter orange ring (higher intensity) inside the blue ring is where the rays have been deflected to.



The Icarus Program

Developed to model actual x-ray paths, Icarus is a comprehensive program that simulates the CFTF. It launches rays according to the x-ray's source position and energy, follows these ray paths using Snell's law, and then calculates final ray positions at the x-ray camera. Great care was taken to make sure the model geometry is an accurate representation of the CFTF. By varying the parameters of both the x-rays and the target, we can determine the exact location of the ice layer. The bright ring created by refraction in the simulation is compared to the actual bright ring location in the x-ray image and the ray-trace model target parameters are adjusted until the simulations match the recorded image. By applying the model to real experimental runs, in this way, the ice thicknesses of real cryogenic targets can be determined. As such, much time was taken to fine tune this program to produce results as similar to actual experimental data as possible.

The first main task was creating a finite source spot. At first the program used a single point source for the x-rays. In this construction, every ray originates from a single, microscopic point as shown in Figure 6. Obviously, this is not a realistic technique as

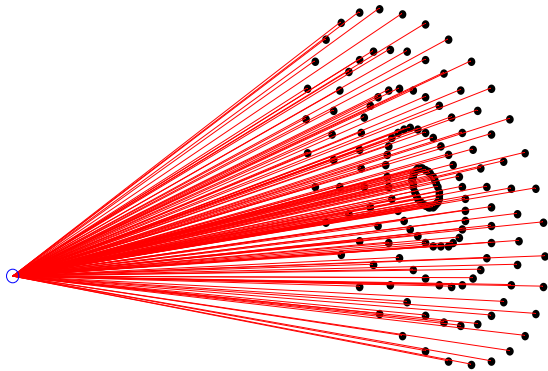


Figure 6: In the ray trace point source all rays in the model are launched in a cone from a single point. Only a limited number of rays are shown in this image for clarity. In an actual ray trace run, many more rays would be used

the CFTF x-ray source has a finite spot size.

As such, the program was modified to reflect this by using an entire conglomeration of these point sources in a pattern similar to that shown in Figure 7. This single point turned into many

rings of multiple points, launching an array of x-rays.

To produce quicker runs, a limited number of points

in each ring were used (about 8). Nevertheless, this

final finite spot used in Icarus resulted in a much more precise simulation of the CFTF.

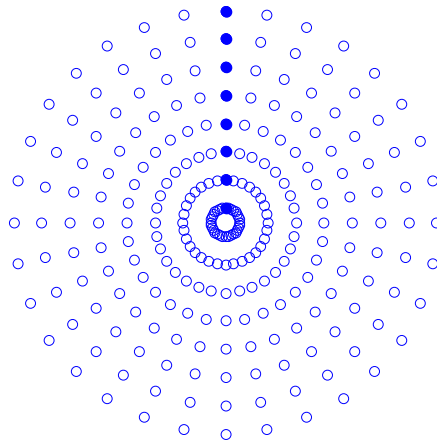


Figure 7: In the ray trace finite spot size model, many separate point sources are spread over the appropriate spot area to simulate the finite source size. Each circle in this figure represents a separate point source.

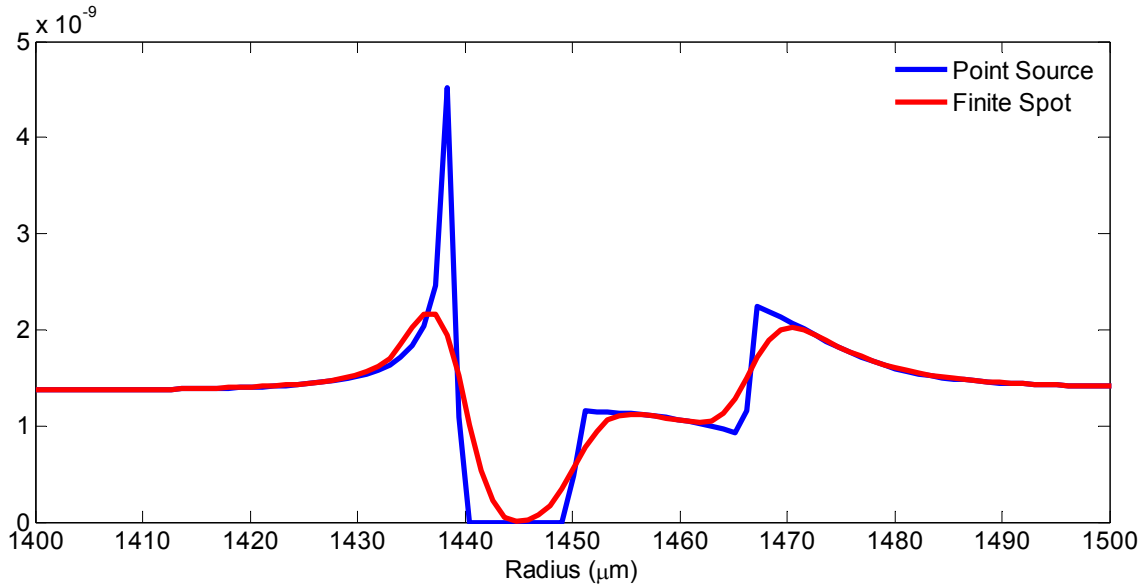


Figure 8: A comparison of the ray-trace predictions of the outer region of a cryogenic target for the point source (blue) and the finite spot size source (red). The target comprised a DT layer inside a plastic shell of inner and outer radii 1447 and 1467 μm .

Simulations were performed for a target with an ice layer of inner radius 1151 μm on the inside of a plastic shell of outer radius 1467 μm and thickness 20 μm . Results are shown in Figure 8 for both a point source and a finite source. It can be seen that the spot produced much smoother results than the jagged, abrupt variations of the point source. The intensity of 0 from about 1440 μm to 1450 μm corresponds to the discontinuity in emerging ray directions seen in Figure 4. Then from about 1450 μm to 1465 μm the x-rays appear to be passing through the inside of the plastic layer. The x-rays have a higher intensity level from 1465 μm on, passing through the outside of the plastic layer. One of the major points of this work is to determine from the lineout where the actual interface is located. Producing results that more accurately match experimental data will facilitate this process.

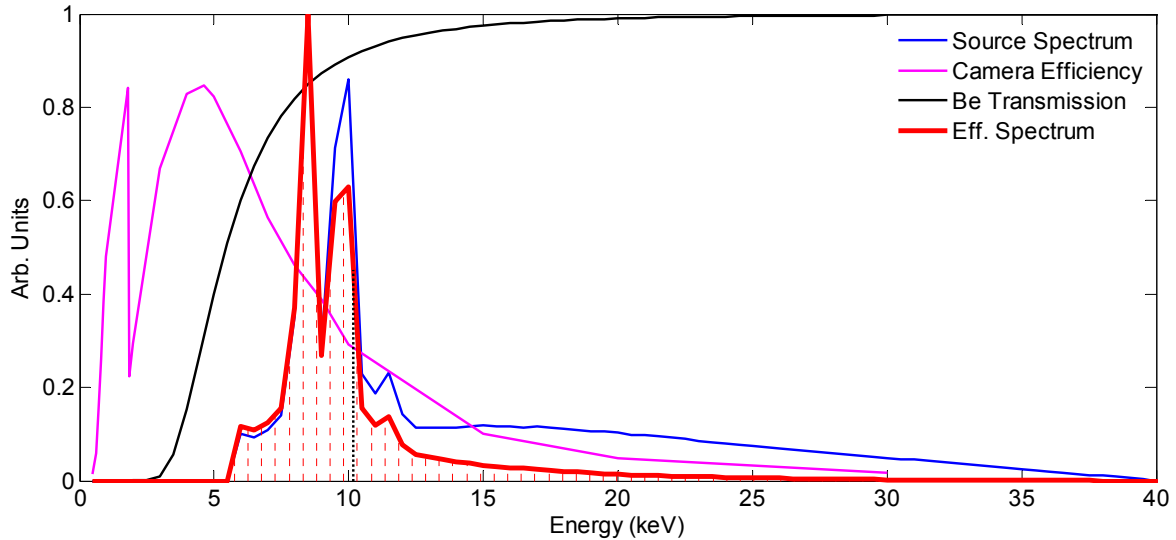


Figure 9: An effective x-ray energy spectrum (red) was produced by multiplying the actual source spectrum (blue) with the camera efficiency (pink) and the beryllium window transmission (black). The effective spectrum was normalized to have a maximum of 1.0.

An equally important task was incorporating a realistic x-ray energy spectrum for the CFTF system into the Icarus program rather than assuming that all the x-rays had the same energy as originally done in Icarus. The first factor to be accounted for was the spectrum of x-rays produced by the source (see the blue curve of Figure 9). These x-rays are mostly around 8 or 9 keV but many x-rays have higher energies. Since these high energy x-rays refract less and blur the image, it is vital that their effect is minimized. Next, the camera's variation in efficiency based on the x-rays' energies was accounted for (see the thin pink curve of Figure 9). The camera was extremely efficient at detecting the lower energy x-rays, but it had difficulty recording the more energetic x-rays. At 10 keV the camera was operating at less than 50% efficiency. The last factor that had to be taken into account was the several beryllium windows within the CFTF (see the black curve of Figure 9). In order to pass through these barriers, the rays needed to have a minimum amount of energy. Those at lower energy levels were

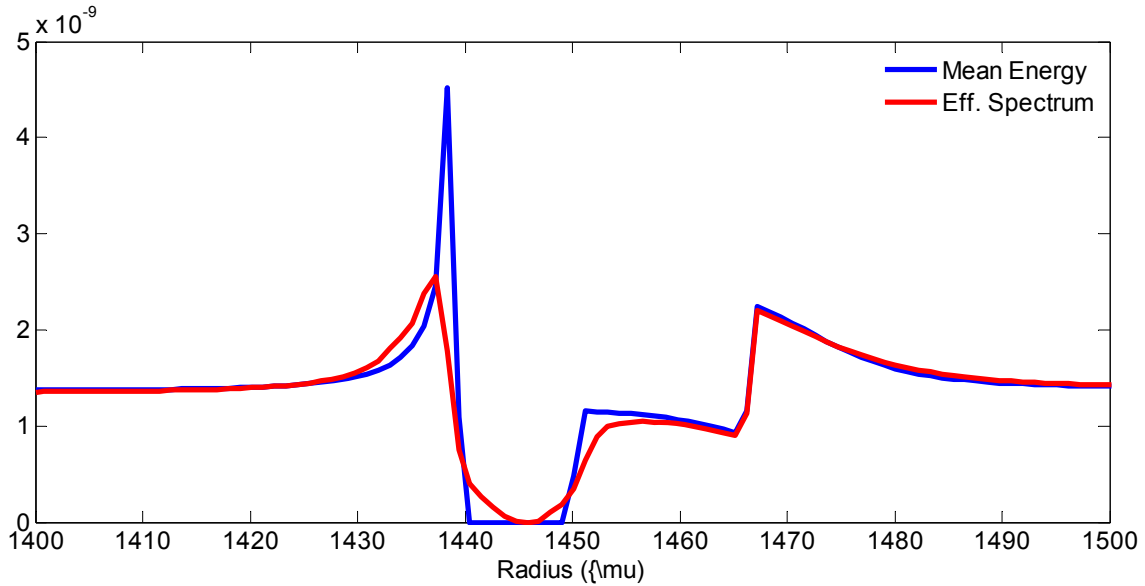


Figure 10: A comparison of the ray-trace predictions for the target of Figure 8 for the single x-ray energy case (blue) and the effective energy spectrum case (red). In both cases a point source is used.

completely blocked. Multiplying these three factors together, an effective energy spectrum was produced, as shown in Figure 9 (the thick red curve).

When this effective energy spectrum was incorporated into Icarus, the new results also became much smoother, more accurately reflecting the CFTF (Figure 10).

To compare with experiment, predictions were made that included both the finite spot size and integration over the energy spectrum. The results are shown in Figure 11, where the red curves indicate the predictions and the blue dots the experimental measurements. For both the inner and outer surfaces the agreement is very close. These results provide confidence that the interface locations can be accurately identified.

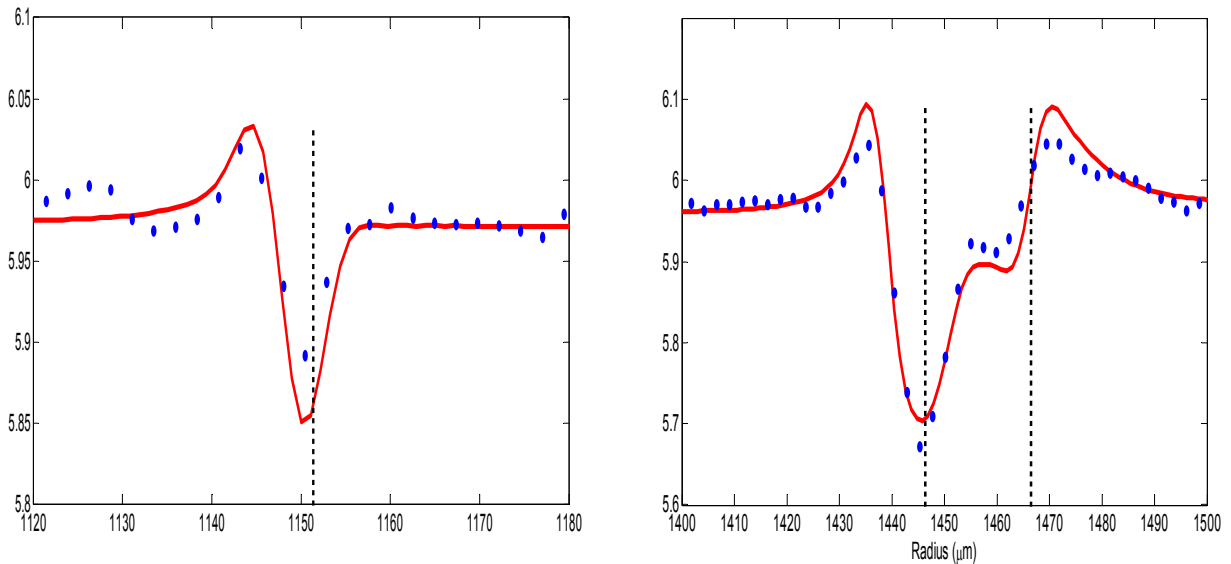


Figure 11: A comparison of experimentally measured x-ray intensities (dots) with the Icarus ray trace predictions when both the finite spot size and effective energy spectrum are accounted for. a) The rings produced by the inner ice surface ; b) the rings produced at the shell surfaces. The actual surface locations are indicated by the vertical dotted lines.

Conclusion

The Icarus program was greatly refined in order to produce a more accurate representation of experimental runs. It was found that a finite spot size and energy spectrum incorporating the source energies, camera sensitivity, and beryllium window produced an excellent match to runs conducted by the CFTF. These results can hopefully be used to more accurately characterize the thickness of ice layers and to pinpoint deviations from uniformity on cryogenic target ice layers.

Acknowledgements

I would like to thank Dr. Dana Edgell for his tremendous support and for taking his time to guide me on this project. It is truly generous of him to volunteer his own personal time to mentor a high school student. From him I have learned much about high-level programming and the field of science itself. Adding to that, I would also like to thank Dr. Stephen Craxton for putting in all the hours to run the High School Summer Research Program. I have personally seen him working into the long hours of night. His hard work and dedication does not go unnoticed. Furthermore, I would like to thank Ben Smith for helping me learn MatLab and my fellow interns for their companionship and support.

References

¹ T. R. Boehly, et al., "Initial Performance Results of the OMEGA Laser System," Opt. Commun. 133, 495 (1997).

² B.J. Koziowski, et al., "Quantitative characterization of inertial confinement fusion capsules using phase contrast enhanced x-ray imaging", J. Appl. Phys., 99, 063103 (2005).

Electron Reflection in Monte Carlo Simulations with the Code GEANT

Evan Miller

Electron Reflection in Monte Carlo Simulations with the code GEANT

Evan Miller

Pittsford Mendon High School
Pittsford, NY

Advisor: Dr. Jacques Delettrez

Laboratory for Laser Energetics
University of Rochester
Rochester, NY

August 2009

Abstract

Target preheat is a significant concern in inertial confinement fusion experiments because, when the temperature of the target becomes too large, the areal density (density times radius) required for ignition cannot be attained. The majority of preheat comes from fast electrons produced when the laser interacts with the target. When these energetic electrons are slowed by collisions, they release high-energy x rays. The energy profile of these x rays is thus a very useful diagnostic of the preheat problem. This energy profile has been obtained from Monte Carlo simulations using the code GEANT. The GEANT code simulates electron transport in the target ending either with the electron's loss of all kinetic energy through collisions or with its escape. In reality, only a negligible number of electrons escape before the target becomes charged enough to reflect the remaining electrons back into the target. A FORTRAN program was written to model the specular reflection of these electrons back into the target. The results of this program are then used as input for another GEANT run with the reflected electrons. This allows for more accurate simulation of electron transport and of the profile of the x rays generated. Nevertheless, it has been found that electron reflection is not a major factor in CH coated Cu spheres.

Introduction

Target preheat is one of the major obstacles to achieving ignition in ICF experiments. Because the fast electrons produced by the laser-target interaction heat the DT fuel in the target before it has been compressed, they prevent the compression of the target to the requisite areal density. The areal density of the fuel has to be large enough for the energy in the alpha particles (helium ions) produced by the initial fusion reactions to be re-deposited in the DT core. The laser pulse itself can only provide the energy for fusion reactions in the central hot core; the main fusion reactions will result from the

heating by the kinetic energy of the alpha particles produced by the initial reactions. While some of the helium nuclei will escape, when that proportion is reduced by increasing the areal density, more energy will be re-deposited in the core, and more fusion reactions will occur.

One cause of target preheat is from fast electrons (> 20 keV) produced in the corona by the two-plasmon decay instability, which results from the interaction of the high intensity laser beam with the expanding plasma. The main diagnostic used to measure the fast electrons is the hard x-rays (HXR) produced as the electrons are slowed down in the target. Experiments were carried out by Yaakobi¹ to measure both the preheat level and the HXR emission from a copper sphere coated with a plastic layer. The analysis was carried out with Monte Carlo simulation of electron transport, which produced a HXR emission that could be compared with that obtained in experimental results. These Monte Carlo simulations did not include the reflection of the electrons at the target outer surface due to the electric field created by a small number of escaping electrons. This paper explores the effects of electron reflection in the Monte Carlo simulation of HXR emission by the fast electrons.

Shortcomings of Previous Monte Carlo Simulations

In his investigation of the relation between preheat and HXR emission, Yaakobi used Monte Carlo simulations to compare to the HXR spectrum generated experimentally.¹ These simulations were run with the code GEANT,² a Monte Carlo code designed to model the transport of particles through matter. A large number of electrons are run through the code as a set of discrete random paths set with a certain collision probability between the electrons and background material, resulting in the electrons slowing down and scattering. The model is time independent. When Yaakobi did his analysis with GEANT, he did not take into account the fact that most of the electrons scattered in the outward direction are reflected at the outer edge of the target by a “sheath.” After the first electrons created

escape the target, an electrostatic sheath is established at the target outer edge as the target becomes positively charged. The electrostatic field forces most of the electrons subsequently arriving at the sheath back into the target. It is possible that these electrons could create significant amounts of HXR's, which would change the results of the simulations.

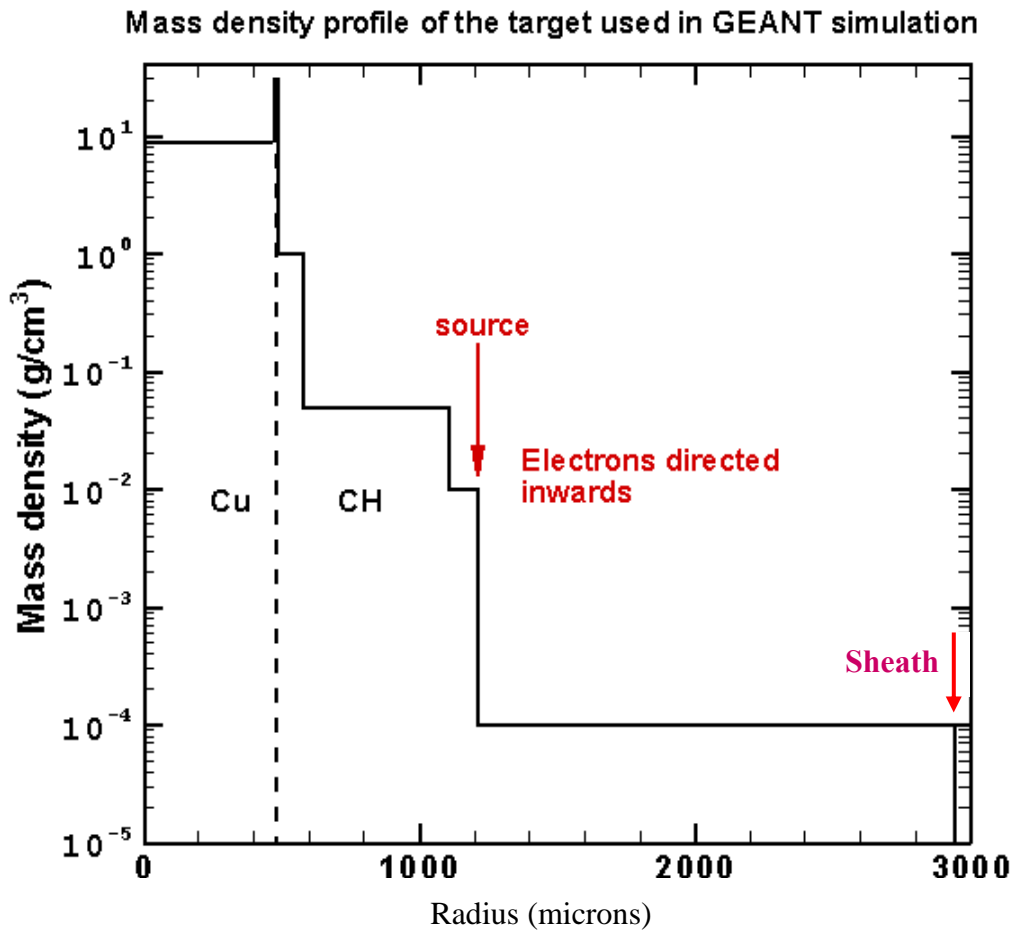


Figure 1: Density profile from the hydrodynamic simulation used in the GEANT simulation.

The target used in our simulations was a solid 600- μm -radius Cu sphere coated with 10 μm of CH. Unlike in the Yaakobi simulation, which was carried out with the solid target, a representation of the actual density profile from the hydrodynamic simulations was used, as shown in Fig. 1. A step

profile was constructed to model the continuous density profile because of the discrete nature of the GEANT material input. The electron source was a beam of energy 100 keV created at the position in the corona where the laser beam interacts with the expanding plasma.

Electron Reflection Model

Since GEANT does not include reflection of the electrons at the outer boundary, the simulations are carried out in at least two steps. In the first step, the electrons are transported from a given source, and the position, angle and energy, of electrons reaching a boundary are recorded in a file. In the next step, the reflected electrons are used as a source for further transport; another step can be taken if necessary. In the model the electrons are specularly reflected at the outer boundary of the target. Neglecting the energy loss to the outward motion of the sheath upon reflection, the kinetic energy of the reflected electron will be the same as that of the incident electron. This allows us to set the kinetic energy of the reflected electrons, for the second GEANT run, equal to the kinetic energy output by the initial GEANT run.

The direction to be used as a source in the second GEANT run is computed from the outgoing angle formed with the radius vector at the point on the sphere of exit and the exit velocity, as shown in Figure 2. In reality, electrons exit the target, are turned around by the field in the vacuum and reenter the target at a different position, as seen in Figure 2(a). Since the re-entry angle is the same as the exit angle, the reflection can be modeled with a specular reflection at the target outer boundary, as shown in Figure 2(b).

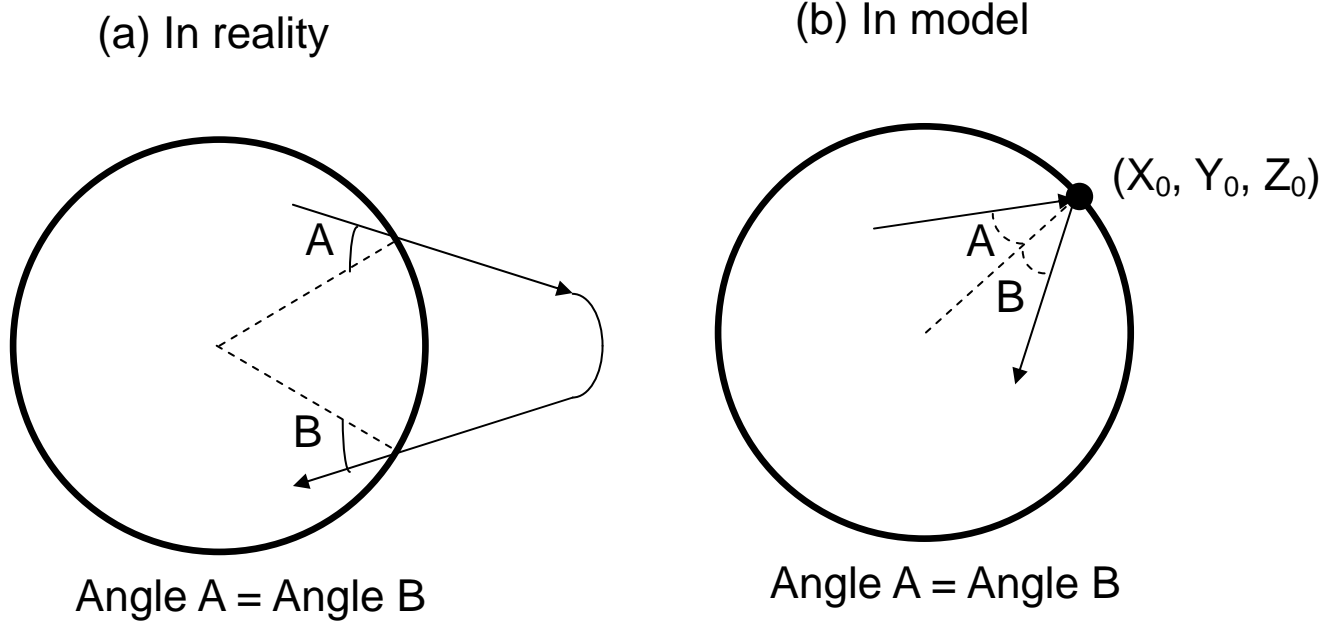


Figure 2: The path of electrons in the code and in reality

The angle between the incoming velocity and the radius is set equal to the angle between the outgoing velocity and radius. The angle between two lines is equal to the difference of the arctangents of their slopes: $\arctan(V_x/V_y) - \arctan(X_0/Y_0) = \arctan(X_0/Y_0) - \arctan(V_{x0}/V_{y0})$, where X_0, Y_0 , and Z_0 are the coordinates of the position at the target surface (outer edge of the corona) where the electron is reflected, V_{x0}, V_{y0} , and V_{z0} are the directional cosines of the incident trajectory, and V_x, V_y , and V_z are the reflected directional cosines. This is done twice in two planes to account for all three dimensions. As a result, we can calculate the ratios of the directional cosines (V_x, V_y , and V_z) of the reflected direction:

$$A = V_x/V_y = \tan(2.0 * \arctan(X_0/Y_0) - \arctan(V_{x0}/V_{y0})) \quad (1)$$

$$B = V_x/V_z = \tan(2.0 * \arctan(X_0/Z_0) - \arctan(V_{x0}/V_{z0})). \quad (2)$$

Since V_{x0} and V_{y0} are directional cosines, $V_x^2 + V_y^2 + V_z^2 = 1$. Because the method outlined above calculates a line for the reflected velocity, the direction, into or out of the sphere, is indeterminate. In order to calculate this direction and to guarantee that the electrons are reflected back into the target, the

dot product of the reflected velocity with the target normal ($X_0V_x+Y_0V_y+Z_0V_z$) is set less than zero.

Using Eqns. (1) and (2) for V_y and V_z , we require that $V_x(X_0+Y_0/A+Z_0/B)<0$. If $(X_0+Y_0/A+Z_0/B)<0$, then $V_x>0$. If $(X_0+Y_0/A+Z_0/B)>0$, then $V_x<0$. The sign of V_x is thus

$-\text{Abs}(X_0+Y_0/A+Z_0/B)/(X_0+Y_0/A+Z_0/B)$. Therefore:

$$V_x = - (\text{Abs}(X_0+Y_0/A+Z_0/B)/(X_0+Y_0/A+Z_0/B)) / \text{SQRT}(1+(A^{**2.0})+(B^{**2.0})). \quad (3)$$

Using this value we can also calculate V_y and V_z . This equation loses accuracy as V_{x0} approaches zero, so all the velocities are calculated from the largest incoming velocity. For example, if V_{y0} is the

largest of the incoming velocities, V_y is calculated first, then V_x and V_z are calculated in terms of V_y .

These values are then used as inputs for a second GEANT run for the reflected electrons, the results of

which would show the effects, or lack thereof, of electron reflection. In retrospect, much of this process

was unnecessary as $V_x=-V_{x0}$, $V_y=-V_{y0}$, $V_z=-V_{z0}$, sending the electrons along the same path that they

came, would have yielded the same results due to spherical symmetry.

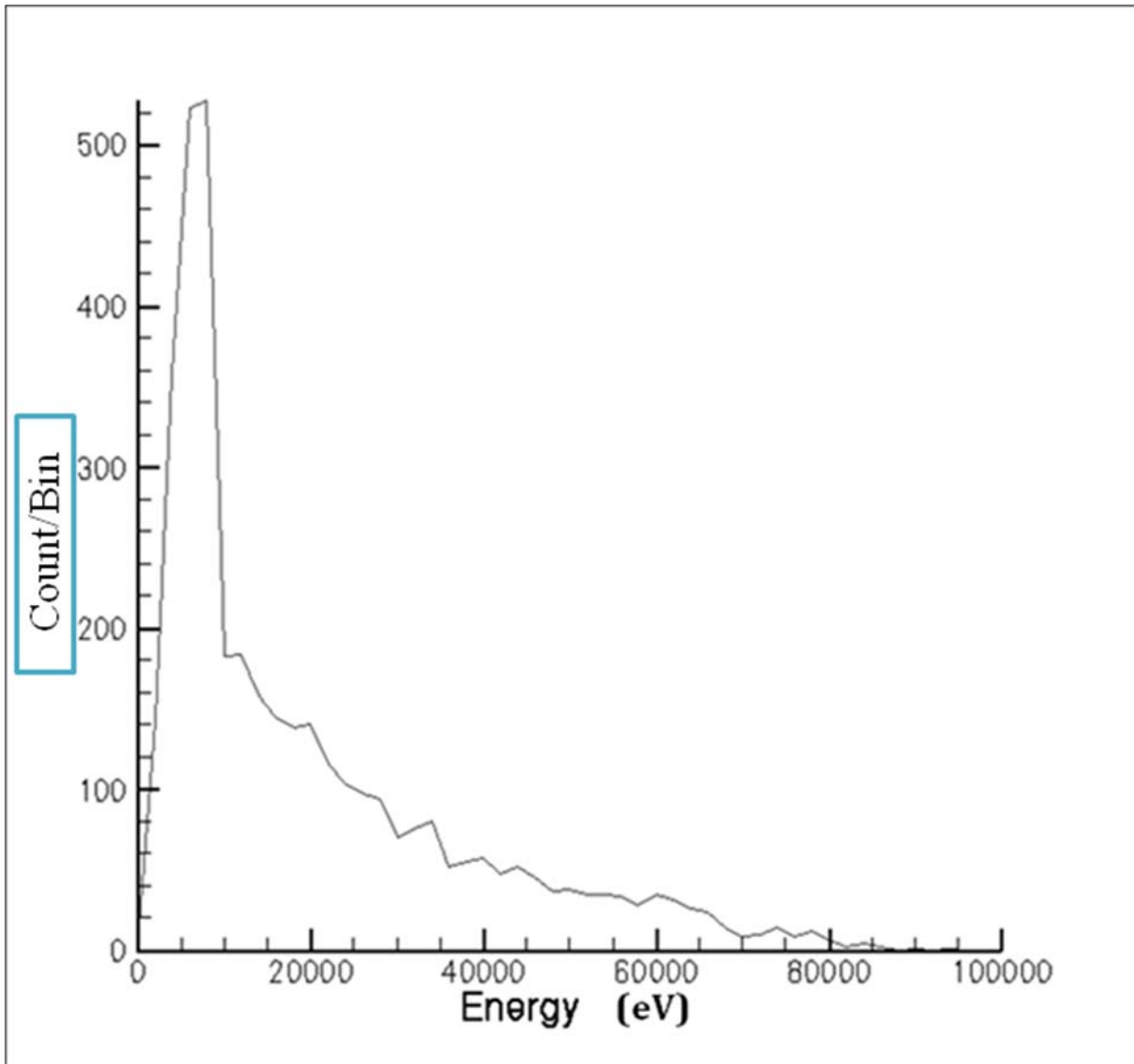


Figure 3: The Energy Profile of x rays produced in the first run

Results of simulations

The results of the second GEANT run with the reflected electrons did not produce a single new HXR as compared to the number produced in the first run as seen in the number of HXR “particles” shown in Figure 3. The reflected electrons were just not numerous or energetic enough to create a single x-ray event. It is possible that using a larger number of electrons in the first run would have

resulted in a larger number of reflected electrons and, hence, in the emission of a small number of HXR's, much fewer than were produced in the first run. The result of this analysis confirms the accuracy of the previous analysis done by Yaakobi by showing that electron reflection is not a factor in Monte Carlo analysis of preheat.

Conclusion

A methodology was developed to determine whether reflecting the escaped electrons in simulations with the Monte Carlo code GEANT modified the results of previous analysis of the HXR emission from fast electrons in a plastic-coated copper ball. The escaping electrons were collected and used as a source for a second GEANT run. The lack of HXR emission from the second GEANT run confirms the estimation by Yaakobi that electron reflection is not a major factor in his Monte Carlo simulation of fast electron transport.

Acknowledgements

Thanks to my advisor, Dr. Delettrez, for all the help he has given me along the way, to the program director, Dr. Craxton, to Po-Yu Chang for the work he did changing the code GEANT, and to the other interns for a great summer.

References

1. B. Yaakobi, O. V. Gotchev, R. Betti, and C. Stoeckl, *Fast-Electron Transport in Spherical Laser Targets*, Phys. Plasmas **12**, 062703 (2005)
2. S. Agostinelli et al., Nucl. Instrum. Methods Phys. Res. A 506, 250 (2003).

Exploration of the Feasibility of Polar Drive on the LMJ

Lindsay Mitchel

Exploration of the Feasibility of Polar Drive on the LMJ

Lindsay M. Mitchel

Spencerport High School

Spencerport, New York

Advisor: Dr. R. S. Craxton

Laboratory for Laser Energetics

University of Rochester

Rochester, NY

March 2010

Abstract

The Laser MegaJoule (LMJ), a laser system being constructed in France, is very similar to the U.S. National Ignition Facility (NIF) and is also designed to operate using an indirect drive configuration. However, it is desirable that the LMJ, like the NIF, have the capability to operate using direct drive, despite its less favorable geometry. Currently two types of direct drive experiments are planned for the NIF: initial implosions of hydrogen-filled glass targets with low energy (≤ 1.0 MJ) to produce neutrons to test diagnostics, and later implosions of cryogenic targets with higher energy (1.5 MJ) to obtain breakeven. These experiments employ a method known as polar drive in which beams are repointed toward the equator. The possibility of doing these experiments on the LMJ has been explored using the two-dimensional simulation code *SAGE*. Optimum designs for both experiments were created by adjusting parameters including the beam defocus distance and the beam pointings, and by using a new asymmetric beam shape. The levels of uniformity obtained are comparable to those expected for the NIF, proving that polar drive is feasible on the LMJ.

1. Introduction

Fusion is a nuclear reaction in which light nuclei of hydrogen combine, resulting in a heavier nucleus and a large release of energy. The light nuclei are isotopes of hydrogen and are called deuterium (D) and tritium (T). The deuterium nucleus has one proton and one neutron, and the tritium nucleus has one proton and two neutrons. Fusion of light nuclei can occur when lasers are shot at a capsule. Typically, the capsule is a spherical shell with a diameter of about 1 mm, is filled with hydrogen gas, and can be made from a variety of materials including plastic and glass. The laser bombardment causes the shell of the capsule to ablate outward. As a result, an equal and opposite force is applied to the inside of the capsule which implodes or compresses the

hydrogen to high temperatures, pressures, and densities. These conditions enable the hydrogen nuclei to overcome electrostatic forces (repellent forces between the positively charged nuclei) and fuse into a helium nucleus. This nucleus is responsible for 20% of the fusion energy. This energy can be deposited into the compressed hydrogen, initiating further fusion reactions in a self-sustaining chain reaction, a process called ignition. Ignition is obtained when there is a sufficient thickness of compressed hydrogen, which requires a laser with sufficient energy. A consequence of ignition is break-even. Break-even is when the energy output is equivalent to the energy input. The energy released from the fusion reactions could potentially satisfy the world's energy needs indefinitely. In order to reach these goals a capsule must be imploded uniformly.

Two methods are being explored to obtain the uniform implosion of a capsule. The first is direct drive,¹ in which the laser beams are pointed uniformly from all directions toward the center of the capsule, as illustrated in Figure 1a. The second method is indirect drive,² illustrated in Figure 1b. The indirect drive target is made of a hohlraum and a spherical capsule. The hohlraum is a cylinder (usually gold in material) and is similar in shape to a soda can with holes at both ends. The laser beams enter the holes and are absorbed by the walls of the hohlraum. The hohlraum walls release x rays, which bombard and uniformly implode the capsule located in the center of the hohlraum.

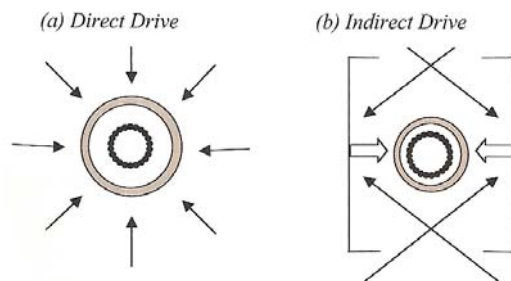


Figure 1. (a) In direct drive beams are uniformly pointed at the center of the capsule from all directions. (b) In indirect drive the beams enter the holes of the hohlraum and are absorbed by its walls. The walls release x rays which bombard and implode the capsule.

The U.S. National Ignition Facility (NIF) is a 192-beam laser fusion facility, designed with sufficient energy to achieve ignition and a consequent energy output 10 times greater than

the energy input. The NIF is designed for indirect drive using a hohlraum with a vertically oriented axis. The beams of the NIF are arranged into four rings in each of the upper and lower hemispheres, with angles θ of 23° to 50° from the axis, in order to enter the hohlraum holes. It is desirable that the NIF have the capability to operate using direct drive. Direct drive is a convenient way of producing neutrons necessary to test diagnostics. Also, direct drive presents a possible alternative method of achieving ignition and breakeven. However, due to the NIF beam configuration, if the beams are pointed at the center of the capsule there will be a lack of absorbed laser energy near the equator of the capsule, leading to a subsequent lack of drive or implosion in this area and an imploding shell that is elliptical rather than spherical (see Figure 2a). To compensate for this problem the laser beams can be repointed away from the center of the capsule, toward the equator, in a method known as polar drive³ (see Figure 2b). Designs exist which prove that polar drive is a feasible method for uniform target implosion on the NIF³⁻⁷.

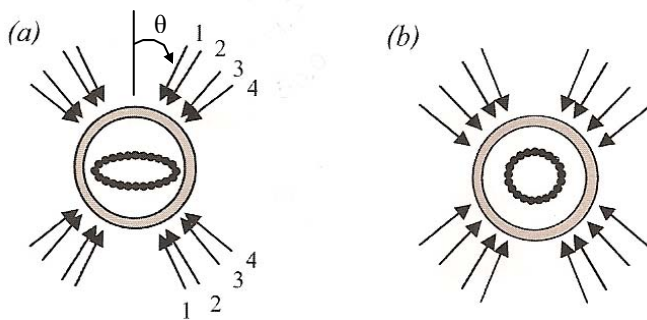


Figure 2. (a) If the NIF beams are pointed at the center of the capsule in direct drive there is a subsequent lack of drive at the equator due to the indirect drive beam configuration. (b) In direct drive the beams can be repointed away from the capsule's center, toward the equator, augmenting the implosion in this area.

The Laser MegaJoule (LMJ) is a 160-beam laser facility that is being constructed in Bordeaux, France and will have an indirect drive configuration, similar to the NIF. The LMJ will only have two rings of beams in each hemisphere, at angles of 33.2° and 49.0° from the axis. This makes the LMJ beam configuration less favorable than the NIF for direct drive and makes obtaining direct-drive uniformity a challenge. This work explored whether the beams of the LMJ

could be adjusted in order to obtain uniform direct-drive target implosions equivalent to the existing NIF designs.

Different parameters of the laser beams were adjusted including beam shape, defocus distance, and pointings. Designs were tested for experiments with two different types of targets: a spherical DT gas-filled glass (SiO_2) capsule with low energy (350 kJ) and a larger spherical cryogenic capsule with high energy (1.5 MJ). The glass capsule has a diameter of 0.15 cm. The gas density is $2.08 \times 10^{-3} \text{ g/cm}^3$ corresponding to 10 atm of DT. For the glass capsule the laser pulse used has a Gaussian profile as seen in Figure 3. The pulse reaches its peak at 2.5 ns and continues for 5.0 ns. Experiments using the glass target would test neutron diagnostics. The cryogenic capsule has a layer of frozen DT inside a thin plastic (CH) shell and is driven by the shaped laser pulse shown in Figure 3(b). The outer diameter of the cryogenic capsule is 0.338 cm and the inner diameter is 0.27 cm. The density of the frozen DT layer is 0.25 g/cm^3 and there is some DT gas inside the frozen layer with density $1.58 \times 10^{-5} \text{ g/cm}^3$. Experiments using the cryogenic target would obtain breakeven. It was found that the LMJ will be able to produce uniform target implosions equivalent to those of the NIF.

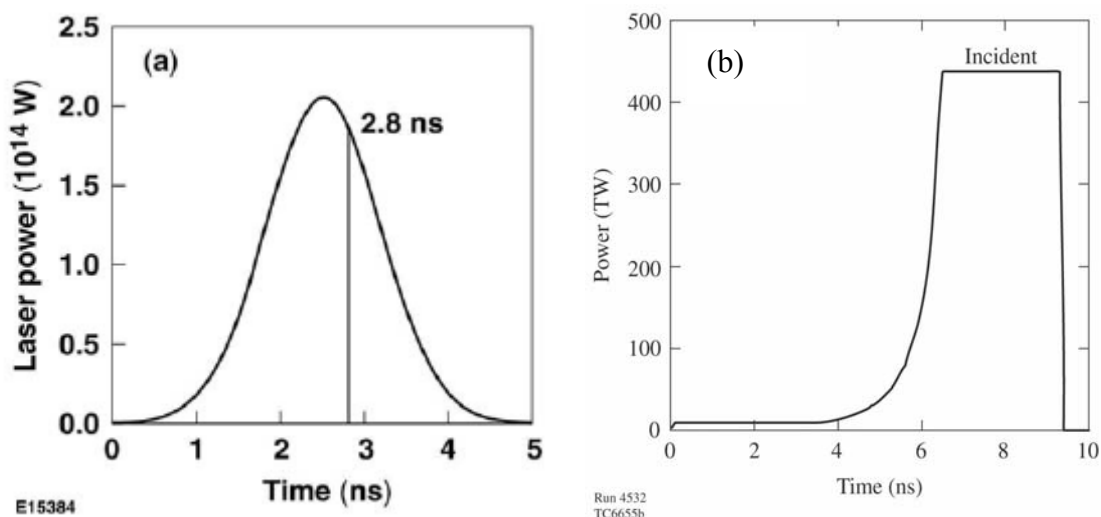


Figure 3. (a) Laser power as a function of time (ns) for the Gaussian laser pulse used on the glass target. At 2.8 ns, the glass shell has imploded to half its initial radius. [From Ref. 6] (b) Laser power as a function of time for the cryogenic target. [From Ref. 5]

2. Optimized Parameters

The first step to overcoming the unfavorable geometry of the LMJ and creating the optimum designs was to divide the first ring of beams at 33.2° into two separate rings.⁸ Each ring contains 10 quads, a quad being a group of four beams that enter the target chamber through a single port and are generally focused on the same area. Every other quad was shifted toward the upper pole for ring 1, while the other quads at 33.2° were shifted toward the equator, creating ring 2. Several parameters were adjusted or optimized in order to establish the optimum designs. The beam pointings were optimized for both target types. The beam pointings determine the location on the target where the beam will land. The beams are shifted through the tilting of an optics mirror (see Figure 4a). The pointings are measured by the distance shifted from the center of the target perpendicular to the original direction of the beam, as shown in Figure 4b. In addition, various parameters were optimized depending on the phase plate that will be available for each target. A phase plate is a piece of glass that is part of the optics each laser beam passes through (see Figure 4a). The phase plate can determine the size and shape of the beam spot as well as the intensity within the beam spot.

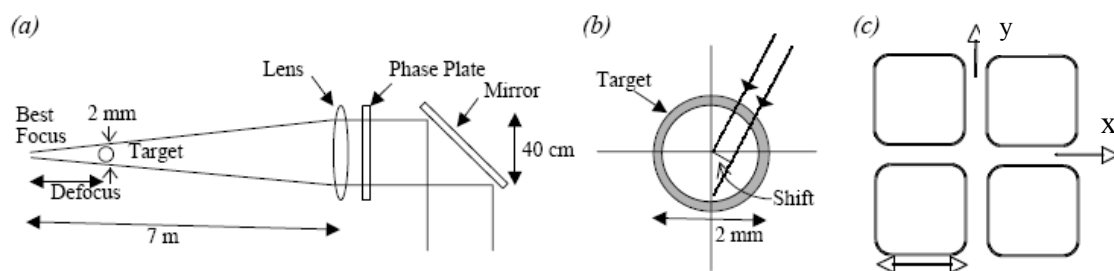


Figure 4. (a) The final optics that each beam will pass through. A beam can be repointed by tilting the mirror. A beam passes through the glass phase plate which determines the size, shape, and intensity of the beam spot. Also within the optics, changing the distance of the lens changes the focus of the beam spot. (b) When a beam is repointed, away from the center of the capsule, the distance of the beam shift is measured perpendicular to the original direction of the beam. (c) Four laser beams are grouped into a quad. To adjust the beam spot a quad can be split, by moving each beam in either the X or Y direction. [From Ref. 6]

2.1 Optimized Parameters for the Glass Target

For the glass target, it is assumed that the LMJ will have indirect drive phase plates similar to those on the NIF. These phase plates create small elliptical beam spots necessary for the beams to enter the hohlraum holes. However, for direct drive it is desirable to have larger beam spots that correspond to the size of the capsule. The grouping of the laser beams into quads on both the NIF and the LMJ is shown in Figure 4(c). Through the application of split quads each beam in a quad can be shifted in the X or Y direction to create a larger beam spot. The distance that each beam is shifted within the quad also affects the overall shape of the beam spot generated by the quad, as well as the intensity contours within the beam spot. In addition, the optics lens can be moved closer to the target along the line of the beam, as shown in Figure 4a. This results in the defocusing of the beam and creates a larger spot size of lower intensity. Through the use of split quads and defocusing, the beam spot size and intensity can be adjusted in order for the beams to blend together and provide uniform drive upon all areas of the target.

2.2 Optimized Parameters for the Cryogenic Target

For the cryogenic target it was assumed that custom phase plates would be available. Therefore, optimum phase plates were designed by optimizing the shape, size, and intensity of different beam rings. For each beam ring the intensity I is given as a function of radius r by the equation

$$I(r) = I_0 \exp [-(r/r_0)^n] \quad (1)$$

where n is the Gaussian order, which is responsible for the shape of the intensity profile within the beam, r_0 is the radius of the beam spot, and I_0 is the maximum intensity in the beam. Two additional parameters for each beam are the intensity cutoff and the elliptical θ_e . The intensity cutoff is a specific intensity value at which the beam spot ends, defined as a percentage of I_0 . The

elliptical θ_e is an angle which determines the ellipticity of the beam shape. This parameter can be understood as the beam spot being compressed in the vertical direction so that the intensity contours become ellipses. The ratio of the major (a) and minor (b) axes is given by $a : b = 1/\cos\theta_e : 1$.

However, an improved design was created using a new asymmetrical beam shape. The beam shape follows the Super Gaussian equation

$$I(r,\theta) = I_0 \exp [-(r/r_0(\theta))^{n(\theta)}] \quad (2)$$

which determines the intensity of the beam as a function of the angle θ . Here,

$$r_0(\theta) = r_{01} + r_{02} \cos \theta \quad (3)$$

$$n(\theta) = n_1 + n_2 \cos \theta \quad (4)$$

where $r_{01} = 1200 \mu\text{m}$, $r_{02} = 200 \mu\text{m}$, $n_1 = 2.5$ and $n_2 = 0.5$ in the design. For example, Figure 5 shows the beam spot used for ring 3 beams in (a) the symmetrical and (b) the asymmetrical cryogenic designs. In the symmetrical design $n = 2.5$ and $r_0 = 1200 \mu\text{m}$. In the asymmetrical design, $n = 2.0$ and $r_0 = 1400 \mu\text{m}$ at the top of the beam, and $n = 3.0$ and $r_0 = 1000 \mu\text{m}$ at the bottom. The intensity cutoff also had angle-dependent values. In addition the beam spot could be made elliptical similar to the symmetrical beam shape. The angle θ_e was 60° for the symmetrical beam spot and 55° for the asymmetrical beam spot.

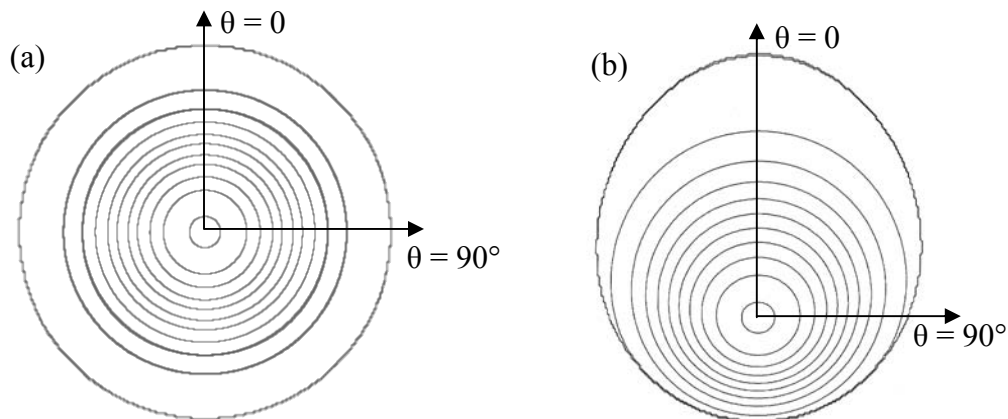


Figure 5. (a) Intensity contours (at 10% intervals) of a symmetrical beam shape with $n = 2.5$ and $r_0 = 1200 \mu\text{m}$. (b) Intensity contours of an asymmetrical beam shape that has parameter values that differ as a function of angle. The beam spot developed for ring 3 beams has a gradual decrease in intensity at the upper pole and a steeper decrease in intensity at the lower pole. This shape provides extra drive at the equator and allows for a greater absorption of laser energy.

Using the asymmetrical beam shape provides two distinct advantages. First, the asymmetrical beam shape has a more intense bottom half that provides extra drive needed at the equator, while the upper half has a gradual decrease in intensity which allows for the ring 3 beams to blend easily with the other rings. The second advantage of the asymmetrical beam shape is that the bottom half is more compact with a smaller radius so that less energy is lost due to laser rays passing by the imploding target.

3. Optimization Process and, Optimized Designs

The two-dimensional hydrodynamics simulation code *SAGE*⁹ was used to test a variety of designs for these targets.

3.1 Glass Target Optimum Design

Table 1. Parameter values for the glass target optimum design using indirect drive phase plates.

	Angle	Beam Pointings	Defocus Distance	Split Quad Y Shift (vertical)	Split Quad X Shift (horizontal)
Ring 1	33.2°	300 μm	2.625 cm	----	----
Ring 2	33.2°	-700 μm	2.625 cm	----	----
Ring 3	49.0°	-700 μm	2.625 cm	400 μm	200 μm

Table 1 gives the specific parameter values for the glass target optimum design. In Figure 6, ray trace plots show the rays of an incoming ring 3 beam and the density contours of imploding shells for both the NIF and LMJ glass target optimum designs. As the capsules implode they maintain their spherical shape through 2.8 ns. It is essential for uniformity to be consistent at 2.8 ns, at which time the majority of the laser energy has been deposited. Peak compression occurs slightly later, just after 3.0 ns. The small deviations from uniformity seen in

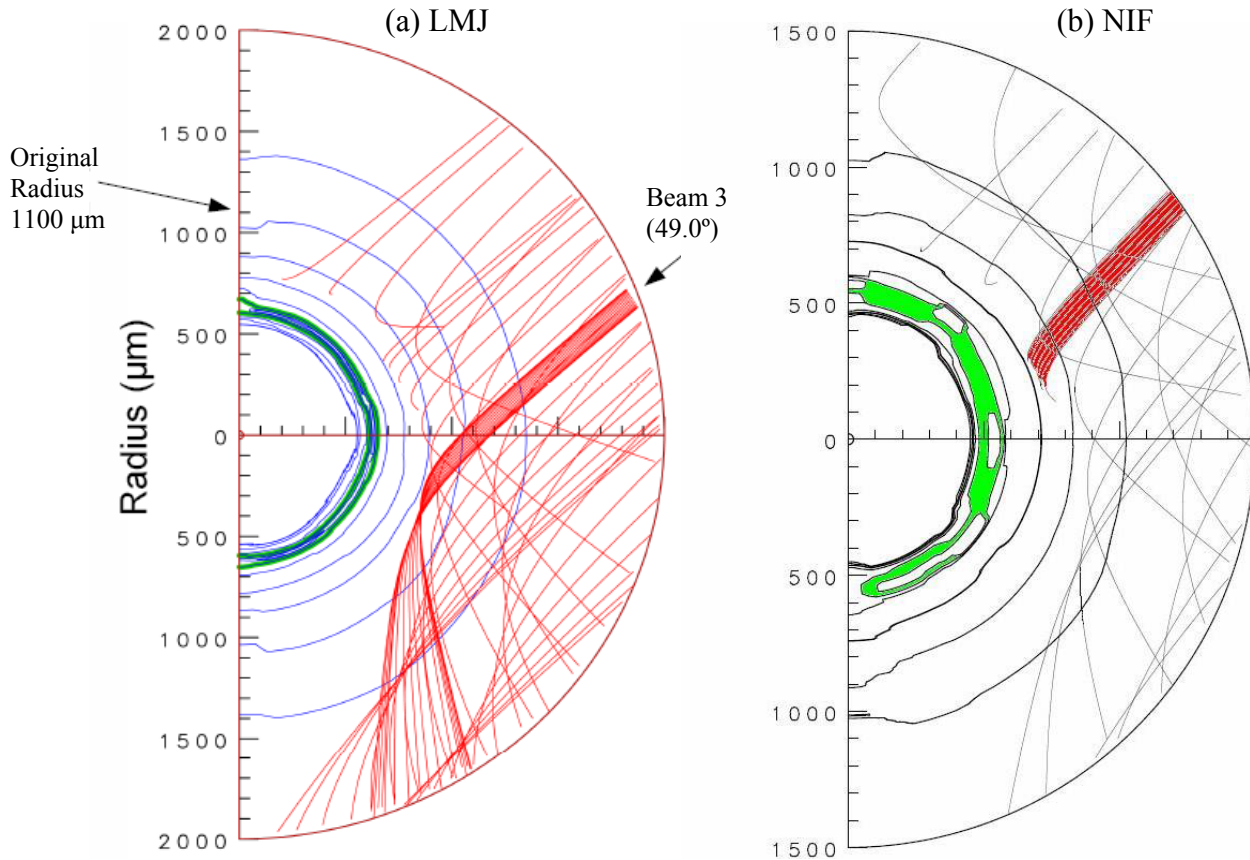


Figure 6. Ray trace plots generated by SAGE which display the rays (primarily red) and the density contours (blue and black) of the imploded glass capsules (green) at 2.8 ns. The green areas represent regions where the density is above four times the critical density. Laser beams can not penetrate beyond the critical density. (a) LMJ optimum design. (b) NIF design. Both (a) and (b) show that the capsules have maintained their spherical shape and imploded uniformly.

Figure 6 are shown more clearly in Figure 7, which gives the center-of-mass radius as a function of θ , the angle from the vertical axis, for the LMJ and NIF designs. Both graphs are relatively flat lines, indicating uniform drive at all angles. The LMJ design yielded an implosion with a low root mean square deviation of radius (ΔR_{rms}) of 5.2 μm , while the NIF design obtained a ΔR_{rms} of 6.5 μm at 2.8 ns. In addition, the velocity deviation was low; velocity uniformity was obtained within 2.5% for the LMJ design, which is comparable to the NIF design which obtained velocity uniformity within 1.7%.⁶

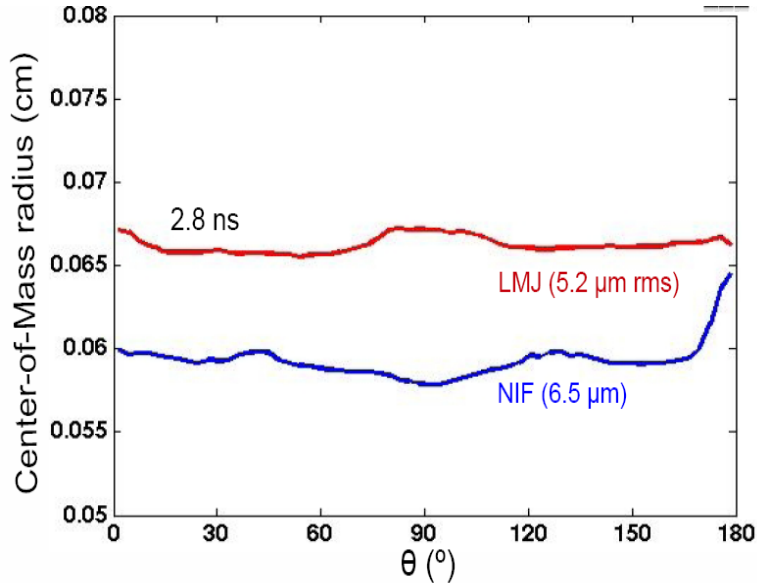


Figure 7. Center-of-mass radius of the imploding shell as a function of the angle θ from the vertical for both the LMJ and NIF glass target designs at 2.8 ns. The relatively flat lines represent the uniformity of the implosions at all angles.

The optimization process involved analyzing the simulations, primarily using ray trace plots such as Figure 6, and plots of the center-of-mass radius and velocity such as Figure 7. The results were evaluated at specific times, and promising runs had a low ΔR_{rms} and a low velocity deviation throughout the implosion. When a promising run was produced, specific parameter adjustments were more deeply explored in additional runs.

3.2 Optimum Cryogenic Design using Symmetrical Phase Plates

Table 2. Parameter values for the optimum cryogenic design using symmetric phase plates.

	Angle	Beam Pointings	Elliptical θ_e	Gaussian Order n	Radius R_0	Intensity Cutoff
Ring 1	33.2°	350 μm	----	2.5	1200 μm	1.0%
Ring 2	33.2°	-350 μm	50.0°	2.5	1200 μm	1.0%
Ring 3	49.0°	-800 μm	55.0°	2.5	1200 μm	1.0%

Table 2 gives the specific parameter values for the symmetrical cryogenic target optimum design. The ray trace plots in Figure 8 show a comparison between the shape of the LMJ and NIF capsules at 9.0 ns. In Figure 9 graphs of the center-of-mass radius as a function of θ

compare the implosion patterns of the LMJ and NIF designs at 9.0 ns. Both capsules preserved their spherical shape with the exception of slight protrusions at the equator, where there is a lack of drive. However, both capsules have imploded about $800\ \mu\text{m}$, half the original radius ($1600\ \mu\text{m}$). The LMJ design obtained a ΔR_{rms} of $12.4\ \mu\text{m}$, while the NIF design obtained a ΔR_{rms} of $11.4\ \mu\text{m}$. In addition, velocity uniformity for the LMJ design was obtained within 2.6%, which is comparable to the NIF design that obtained velocity uniformity within 2.7%.

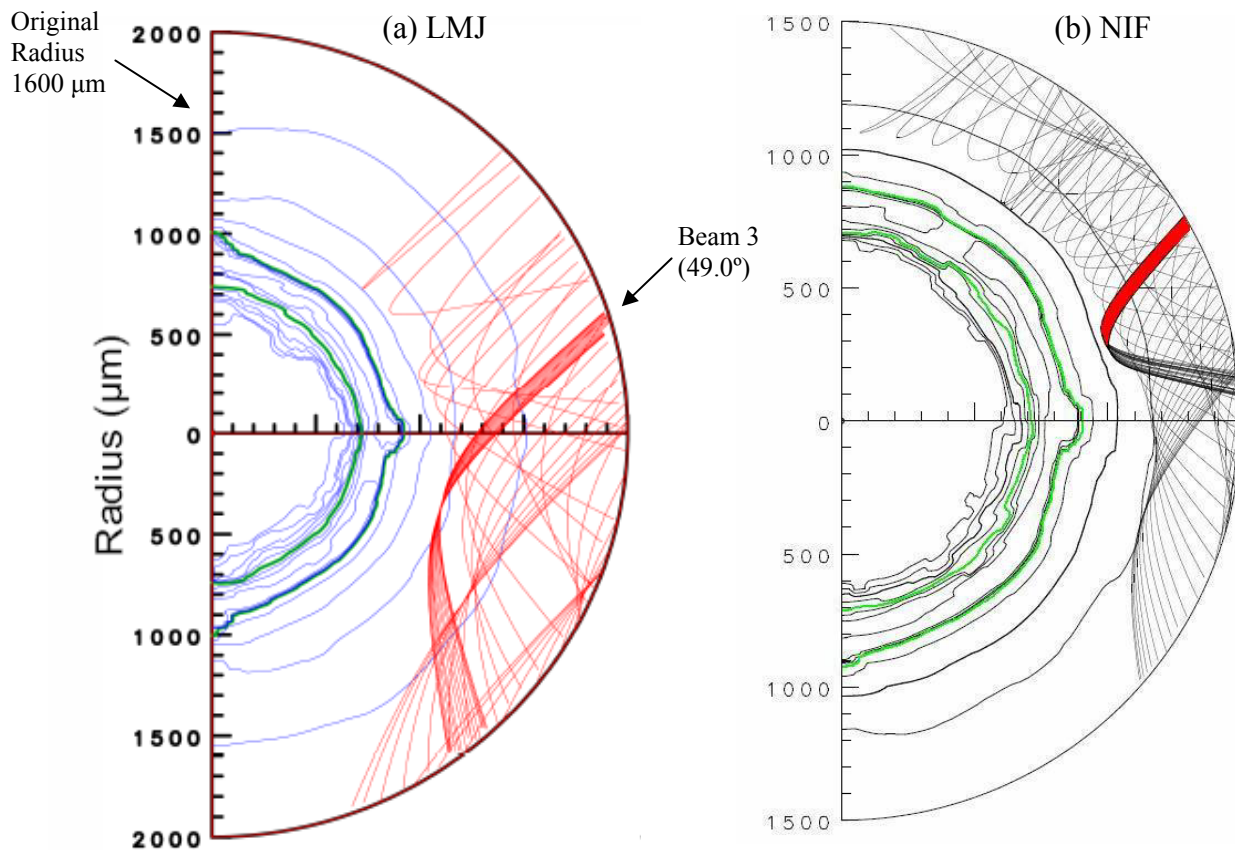


Figure 8. Ray trace plots generated by SAGE which display the rays (primarily red) and the density contours (blue and black) of the imploded cryogenic capsules (green) at 9.0 ns. (a) LMJ optimum design; (b) NIF design. Both (a) and (b) illustrate that the capsules have preserved their spherical shape until the end of the laser pulse.

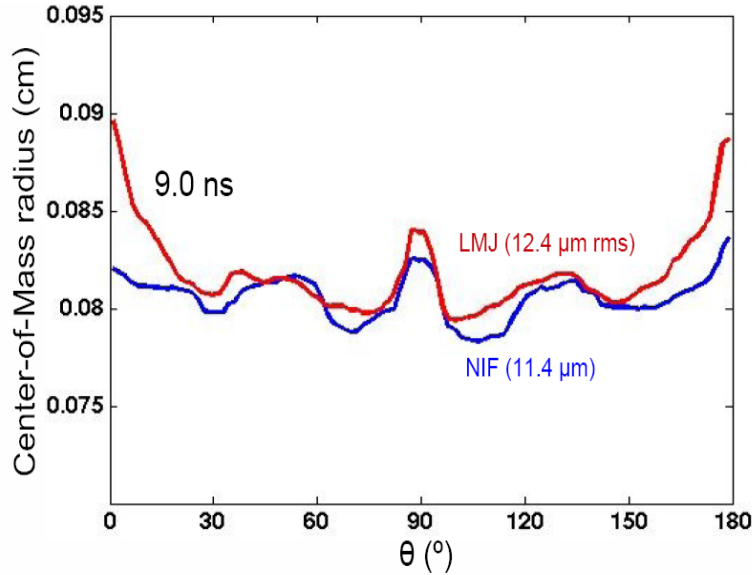


Figure 9. Center-of-mass radius of the imploding shell as a function of θ for both the LMJ and NIF cryogenic designs at 9.0 ns. Both implosion patterns show a lack of drive at the equator.

3.3 Cryogenic Design using Asymmetrical Phase Plates

Table 3. Parameter values for the optimum cryogenic design using asymmetrical phase plates.

	Angle	Beam Pointings	Elliptical θ_e	Gaussian Order n	Radius R_0	Intensity Cutoff	
Ring 1	33.2°	200 μm	30.0°	2.5	1200 μm	1.0%	
Ring 2	33.2°	-350 μm	40.0°	2.5	1200 μm	1.0%	
Ring 3	49.0°	-800 μm	60.0°	2.0	1400 μm	1.0%	Upper Pole $\theta=0.0^\circ$
				3.0	1000 μm	15.0%	Lower Pole $\theta=180.0^\circ$

Table 3 gives the specific parameter values for the second cryogenic design which employs the asymmetrical beam shape in Figure 5b for ring 3 (49.0°). This beam shape was developed in an attempt to reduce the protrusion at the equator of the symmetrical cryogenic design. The value of the asymmetrical beam shape can easily be seen in a comparison of the ray trace plots for the cryogenic design using asymmetrical phase plates (Figure 10) and the symmetrical optimum design (Figure 8a). The asymmetrical optimum design maintained its spherical shape through 9.0 ns, which is close to the end of the laser pulse. The ΔR_{rms} for the

asymmetrical design is $10.4\ \mu\text{m}$, which is more uniform than both the LMJ and NIF symmetrical designs.

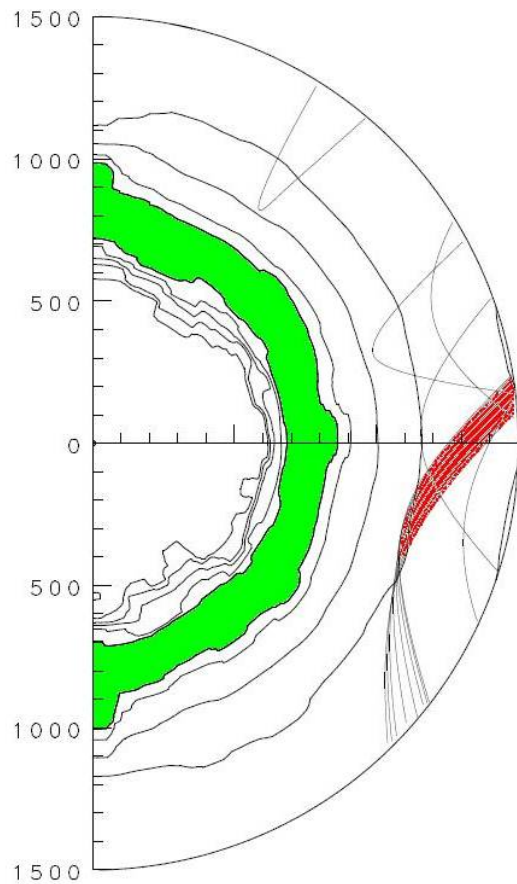


Figure 10. Ray trace plot generated by SAGE which displays the rays (red) and the density contours (black) of the imploding capsule (green) for the cryogenic design using asymmetrical phase plates. The ΔR_{rms} for the implosion is $10.4\ \mu\text{m}$ at $9.0\ \text{ns}$.

The advantage of the asymmetrical beam shape is clearly seen in Figure 11, which plots the center-of-mass radius as a function of θ for the symmetrical and asymmetrical phase plates. The protrusion at the equator with the asymmetrical phase plates is less than that of the symmetrical design. The asymmetrical beam shape has increased the impact of ring 3 beams at the equator and alleviated the problem posed by the unfavorable geometry of the LMJ. In addition, the LMJ asymmetrical design obtained velocity uniformity within 2.2%, which is comparable to the LMJ symmetrical design which obtained velocity uniformity within 2.6%.

In addition, the asymmetrical beam shape allowed for a greater absorption of laser energy. For the symmetrical design absorption was 62% while for the asymmetrical design

absorption increased to 64%. As a result of the higher absorption, the asymmetrical design has a smaller center-of-mass radius than the symmetrical design, as seen in Figure 11.

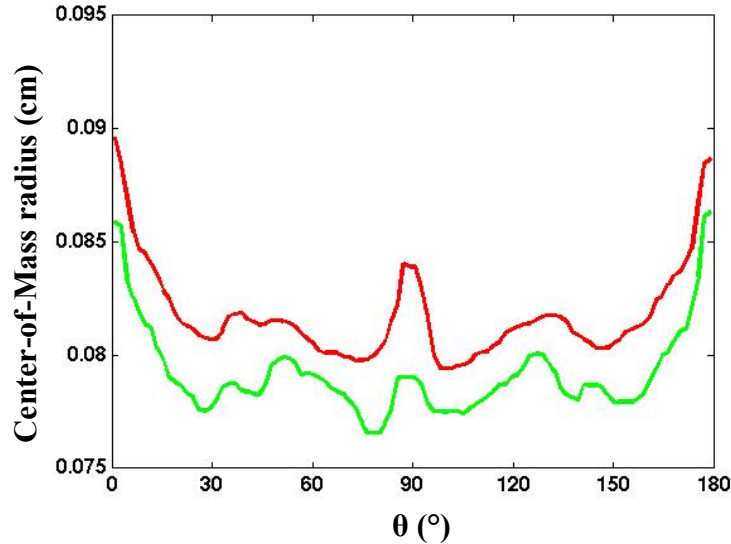


Figure 11. Center-of-mass radius of the imploded capsule as a function of θ for the LMJ design using symmetrical phase plates (red) and the LMJ design using asymmetrical phase plates (green).

Figures 8a, 10 and 11 show a weakness in drive at $\theta = 0$ and $\theta = 180^\circ$ for both the LMJ symmetrical and LMJ asymmetrical designs. These weak areas are most likely a result of the LMJ geometry, which has the first ring of beams at 33.2° in comparison to the NIF which has the first ring of beams at a lesser angle of 23.5° . This not a major problem because the solid angle affected is small. However, it is possible that the problem could be reduced through further optimization. One possible approach might be to point two beams out of each of the five quads of Ring 1 a little closer to the pole.

4. Conclusion

Three optimized polar drive designs have been developed for the LMJ laser facility. The designs are for two different types of targets: a spherical DT gas-filled glass capsule with low energy (350 kJ) and a larger spherical cryogenic DT capsule with high energy (1.5 MJ). The primary purpose of the gas-filled capsule is to produce high neutron yields necessary to test diagnostics. The second and third designs utilize the cryogenic capsule and allow for the

possibility of attaining ignition and breakeven. In particular, the third design uses an asymmetrical beam shape to enhance the uniformity of the implosion. The designs were optimized using hydrodynamic simulations to obtain levels of uniformity which are comparable to the uniformity of pre-existing NIF polar drive designs in spite of the unfavorable geometry of the LMJ. These designs show that the LMJ laser facility as well as the NIF will be compatible for both indirect drive and direct drive implosions.

5. Acknowledgments

I would like to thank my family for their encouragement throughout the program, and Jeremy P. Wyatt for his time and effort helping me prepare figures. Also, I would like to thank my advisor Dr. R. Stephen Craxton for his invaluable support and guidance. Finally, I am very grateful to Dr. Craxton and the Laboratory for Laser Energetics for giving me this extraordinary opportunity.

6. References

1. J. Nuckolls *et al.*, “Laser Compression of Matter to Super-High Densities: Thermonuclear (CTR) Applications,” *Nature* **239**, 139 (1972).
2. J. D. Lindl, “Development of the Indirect-Drive Approach to Inertial Confinement Fusion and the Target Basis for Ignition and Gain,” *Phys. Plasmas* **2**, 3933 (1995).
3. S. Skupsky *et al.*, “Polar Direct Drive on the National Ignition Facility.” *Phys. Plasmas* **11**, 2763 (2004).
4. Alexandra M. Cok, “Development of Polar Direct Drive Designs for Initial NIF Targets,” Laboratory for Laser Energetics High School Research Program (2006).
5. R. S. Craxton and D. W. Jacob-Perkins, “The Saturn Target for Polar Direct Drive on the National Ignition Facility,” *Phys. Rev. Lett.* **94**, 095002 (2005).
6. A. M. Cok *et al.*, “Polar-drive designs for optimizing neutron yields on the National Ignition Facility,” *Phys. Plasmas* **15**, 082705 (2008).
7. R. S. Craxton *et al.*, “Polar Direct Drive: Proof-of-Principle Experiments on OMEGA and Prospects for Ignition on the National Ignition Facility,” *Phys. Plasmas* **12**, 056304 (2005).
8. R. S. Craxton, “Hydrodynamic Simulations of Polar Direct Drive on the NIF and LMJ Based on Three-Dimensional Ray Tracing,” 45th Annual Meeting of the American Physical Society Division of Plasma Physics (2003).
9. R. S. Craxton and R. L. McCrory, “Hydrodynamics of Thermal Self-Focusing in Laser Plasmas,” *J. Appl. Physics.* **56**, 108 (1984).

Using Networked Data Services for System Analysis and Monitoring

Justin Owen

Using Networked Data Services for System Analysis and Monitoring

Justin Owen

Irondequoit High School

Advisors: Mr. Rick Kidder, Mr. Colin Kingsley, Mr. Michael Spilatro

Summer 2009

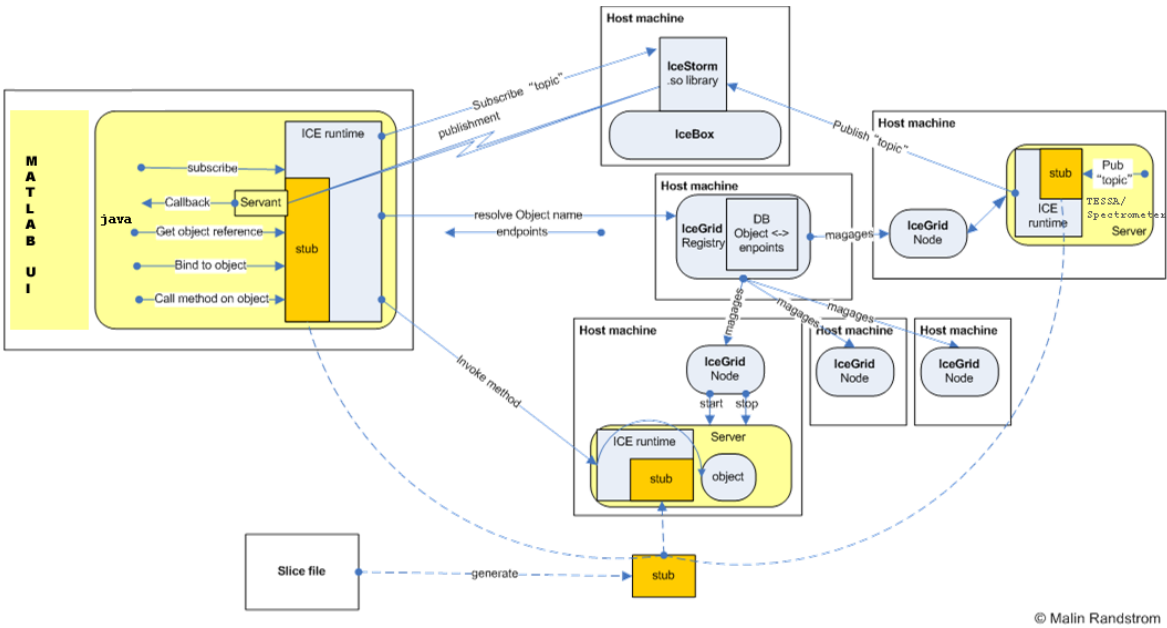
Abstract:

By developing and connecting instruments to a networked data service rather than monolithic applications, it is possible to make the instruments' data available to an entire network. This can enhance laser operation capabilities by allowing data from multiple instruments to be combined in real time in a computer program. This is referred to as orchestration. This project demonstrates orchestration by combining data from two operations diagnostic services into one client program. The service programs are the existing Time-Expanded Single Shot Autocorrelator (TESSA) and a spectrometer service that both produce data on the network. The focus program is a client application that is coded in Java and a middleware language called Internet Communication Engine (ICE) to receive data from the OMEGA EP front-end laser diagnostics.

Background:

The Laboratory for Laser Energetics (LLE) currently has numerous diagnostic and measurement systems on the OMEGA EP laser that collect data when it is preparing for and firing a shot. When the data is collected, it is normally stored in an archive of HDF4 data files with an .hdf file extension. This format is accepted by the scientific community and is extensible to easily provide for the many differing types of data found on the system. While it is very efficient to store archival data in this type of file, which can be referenced later, it is very inefficient for real time operations. The data would be significantly more useful if it could be monitored in real time (i.e., during shot preparation) without the overhead of storage to the file servers. For that purpose, these and some other of the OMEGA diagnostics have been associated with ICE, allowing for data from the diagnostics to be sent over the network in real time.

ICE is an object-oriented middleware platform designed to simplify networked programs, and is compatible with C++, Java, Python, and several other programming languages. ICE provides facilities for developing unified interfaces that any of the supported programming languages can interact with, as well as providing necessary network arbitration. ICE also provides the IceGrid (see Figure 1) locator service, which simplifies the task of finding the ICE objects that one wants to access on the network, and the IceStorm service, which handles multicasting data to other ICE enabled applications.



© Malin Randstrom

Figure 1. Depiction of ICE services in relationship to Java and the Matlab User Interface. Drawing is a revised IceGrid architecture drawing by Malin Randstrom, <http://upload.wikimedia.org/wikipedia/en/5/5a/ICEgrid.png>.

Among its diagnostic systems, the OMEGA EP laser currently has two spectrometers for measuring the laser spectrum on beamlines 1 and 2 (see Fig. 2),

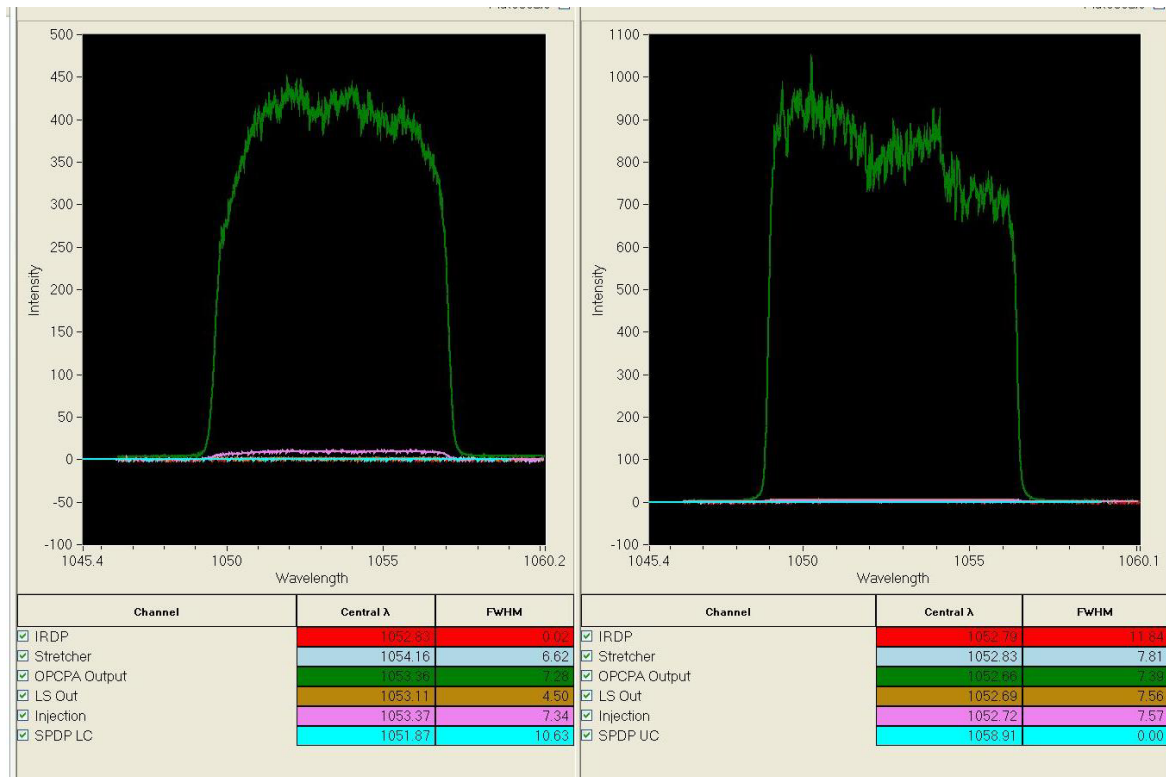


Figure 2 Spectrometer diagnostic display for the Omega EP laser system beamlines 1 and 2. Data recorded by the spectrometers on a typical shot, from beamline 1 (left) and beamline 2 (right). Spectra are superposed for various channels, corresponding to different positions along the laser beam paths.

and the Time-Expanded Single-Shot Autocorrelator (TESSA), which measures the short pulse (~1.0 ps) laser's pulse width (see Fig. 3).

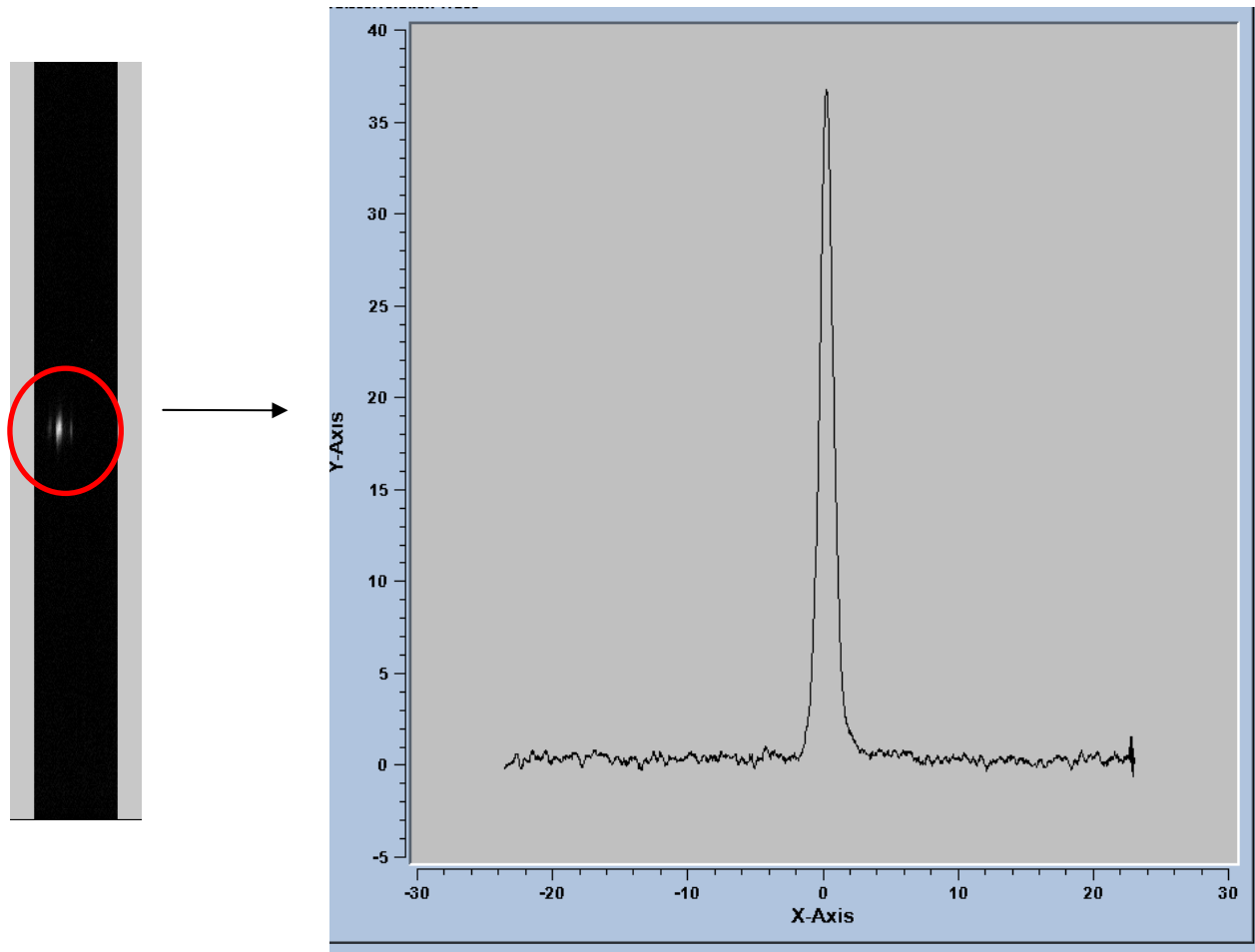


Figure 3 TESSA display of short pulse data captured from the upper compressor fed by Omega EP beamline 2. The image on the left is converted to the graph on the right, where the x axis corresponds to time. The full-width at half max is used to determine the temporal duration of the laser pulse.

Analysis of this data, combined with characterization details on system components, can provide predictive capabilities for the laser output. As such the spectrometers and TESSA have been configured to send the data they collect in real-time to a central IceStorm server, which can send the data to any programs on the network that "subscribe" to the instruments' "published" ICE events. IceStorm is a publish / subscription service provided as part of ICE.

Purpose:

The purpose of this project is to create an example program that can use IceStorm to combine the real-time data from multiple diagnostics to create useful information that can be viewed in real-time by those working with the OMEGA EP laser. The .hdf files in which the data is currently stored after collection cannot be used until the diagnostics have finished writing the files and so useful analysis on the data can only be performed after the collection is over. This leads to substantial overhead on the file systems by producing many pre-shot files that are not of archival quality. These files require significant resources to manage to ensure data integrity and cleanup after the files are no longer needed. This burdens developers and operation staff who are responsible for the diagnostic and laser systems. By providing the data service, file storage and overhead is eliminated and analysis can be performed in real-time during the set-up for a shot. The nature of IceStorm also means that multiple programs can use the real-time data feeds simultaneously. This provides flexibility where tasks can be broken between many client utilities.

In addition to orchestration, the project demonstrates the potential gains of developing a Service-Oriented Architecture on the LLE network. A Service-Oriented Architecture would consist of a set of “services” on the network with well-defined interfaces, so that any program that knows the interface for a service can use it; TESSA and the spectrometers sending data through IceStorm provide examples of services that produce data. A Service-Oriented Architecture for LLE would allow applications to interact with each other easily over the network, enabling programmers and use applications to create new, useful information.

Final Product:

The final product is a set of Java classes and ICE files for using the data services from the spectrometers and TESSA in a few configurations. The code is designed to be used by frontend programs such as Matlab to access the data being received from the services that run relevant analysis on the data.

The program was written to retrieve data from one spectrometer, both spectrometers, TESSA, or all three simultaneously; each program also has methods to provide just a subset of the available information it receives (e.g., just the frequency/intensity data from one spectrometer) depending on the service interface.

The spectrometer program has functionality to return a three-dimensional array of values, providing a graph of frequency and intensity for each channel on the spectrometers (see Fig. 2). The TESSA program returns an array of values representing the intensity at each point in time, a value representing the "timescale" (the difference in time between each point on the array), a value representing the "offset" of the pulse, or the width of the pulse at half its maximum intensity. It can also return a matrix with all ordered values.

Because the code was initially intended for use with Matlab, which is not multithreaded and does not support asynchronous event notification, a satisfactory interface that would allow Java to call Matlab functions could not be developed. The analysis function in Matlab must manually retrieve the data from the Java data handler program (see IceClient Java class below). Ideally, the program would be able to call an analysis function in Matlab as soon as it received data. The Java program, therefore,

“holds” the most recent set of data received from the spectrometer and TESSA services until Matlab calls the appropriate Java method to retrieve a copy of the data.

The code also includes an “IceClient” Java class that contains the code used to actually interface with Ice and IceStorm; the programs extend this class. This fortunately makes writing code for new services relatively simple, since any new code can also use the IceClient class instead of requiring unique server code to be written. A readme file is included with the code with recommendations on writing similar code for other IceStorm services; it also includes instructions on using the code.

Next Steps:

Future work on this project should first include modifying or creating an analysis program to take the spectrometer and TESSA outputs passed on by the program described here. Such an analysis program should be able to display the data and use it to provide predictions on laser pulse outputs of the OMEGA EP beam. Such a program could possibly be used to validate system configurations or automate part of the calibration process for the OMEGA EP laser. This could be combined with data taken on a previous shot to adjust the laser parameters to produce more optimal shots. This process saves time and labor in the OMEGA EP control room by automating sometimes tedious shot configurations.

More future work would involve connecting other instruments in the OMEGA EP laser and LLE to ICE services, so that more services can be integrated and used over LLE’s internal network.

Acknowledgments

I would like to thank Richard Kidder for giving me the opportunity to work on this project. I would like to thank Colin Kingsley and Mike Spilatro for advice regarding the scope and applications of this project. I thank Dan Gresh for doing some unpublished initial work on the project, and Ralph Russo for advice on programming in Ice. Finally, I would like to thank Stephen Craxton for coordinating the high school program.

Water Desorption from Metallic Surfaces at Room Temperature

Ben Petroski

Water Desorption from Metallic Surfaces at Room Temperature

Ben Petroski

Livonia High School

LLE Advisor: Dr. Walter Shmayda

March 2010

Abstract

Water adsorption and desorption is a major issue in industries that handle ultra-pure gases. For example, in the semiconductor industry, water desorption into pure gas streams can contaminate the entire stream and reduce the yield and lifetime of large-scale integrated devices. An experiment has been performed to understand the process by which water adsorbs and desorbs from metallic surfaces so as to help prevent moisture contamination. Tritium, which is a radioactive isotope of hydrogen, was used in this experiment as a tracer to label water molecules attached to metals and monitor the rate at which desorption occurs. Tritium is an ideal tracer because, as an isotope of hydrogen, it can replace hydrogen in water (H_2O) to form tritiated water (HTO). In this experiment, copper with HTO bound to its surface was exposed to a helium carrier with varying amounts of humidity and the rate of exchange between the carrier-borne H_2O and the surface-bound HTO was measured as a function of carrier humidity. Two processes control the rate of exchange: the arrival rate of water vapor to the surface when the metal is first exposed to the humidity and the rate of tritium diffusion from the metal when the upper oxide layers are tritium deficient in the later phase.

Introduction

Water molecules often attach to surfaces through a process named adsorption and similarly detach from a surface by desorption. As more water molecules attach, monolayers or multiple layers of water molecules are formed on the surface. The first

layer that adsorbs to the surface dissociates from H_2O into an H and an OH. The succeeding layers of H_2O bond to the hydrogen ends of the first layer (see Fig. 1).

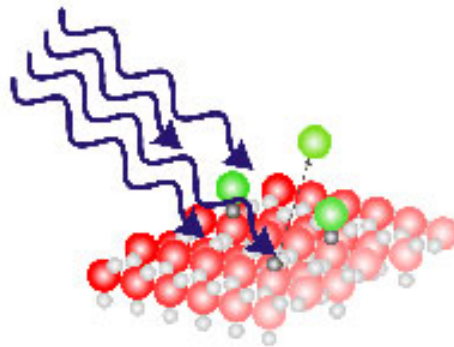


Fig. 1: A representation of the process of adsorption and desorption. The red and gray spheres are the adsorbed H_2O molecules while the green are H_2O molecules desorbing.

The water molecules that bond to the surface can be entrained into gases that are near the surface. In certain controlled settings, this is an issue because the water can contaminate pure gases. One of these settings is gas streams in industry.^{1,2,3} Due to the process of adsorption and desorption, pure gas streams are likely to become contaminated if water is present on the surface of pipes and equipment present in the gas stream. The process of water adsorption and desorption is a prominent concern in contamination control throughout industry settings.

The objective is to understand water adsorption and desorption so as to help prevent moisture contamination.^{4,5} In this process, tritium, an isotope of hydrogen that

contains one proton and two neutrons, is used as a diagnostic. There are two main reasons for the use of tritium in this experiment: (1) Because it is an isotope, it can interact with water and form tritiated water; and (2) Tritium is sensitive and can be identified if 1 in 10^{12} of particles in a system is a triton.

Experimental Setup

The purpose of the experiment being performed is to try and understand the process by which adsorption and desorption occur. To understand this, a basic replica was made of the process that industries use when transporting gases.

The experiment as shown in Figure 2 is started with a source of compressed helium from a tank that is sent through a helium purifier. The helium is then divided into two streams, both of which are controlled separately by mass flow meters. One of these streams remains dry, while the other is run through a water-filled humidifier (B0), thereby humidifying one stream. The combined flow rate of the two streams is limited to 100 ml/min by the operator; however, each stream has the potential to reach a flow rate of up to 200 ml/min. The streams then combine and pass through a dew point sensor used to measure the overall humidity of the stream. The sensor is connected to a small, digital readout that displays the dew point in degrees Celsius. Next, the helium passes through an exposure chamber containing a tritiated copper coupon. The water in the helium stream adsorbs onto the coupon's surface and a hydrogen exchanges with the tritium to form tritiated water, HTO or T_2O . These are two forms of water in which tritium has become part of the molecule. Then, the HTO or T_2O desorbs and the stream

continues into a bubbler containing 100 ml of liquid scintillation cocktail solution (LSC, B1). The helium stream deposits the majority of tritium that was “carried” into this bubbler.

Two small diameter hoses run between this bubbler and a Beta-RAM, a liquid scintillation counter that actively measures radioactivity in counts per minute/ml (CPM/ml). After this, the helium stream continues on to a bubbler (B2) filled with 100 ml of water where the remnants of the tritium are deposited. Dew point measurements were recorded manually throughout the runs through the use of the digital dew point sensor display.

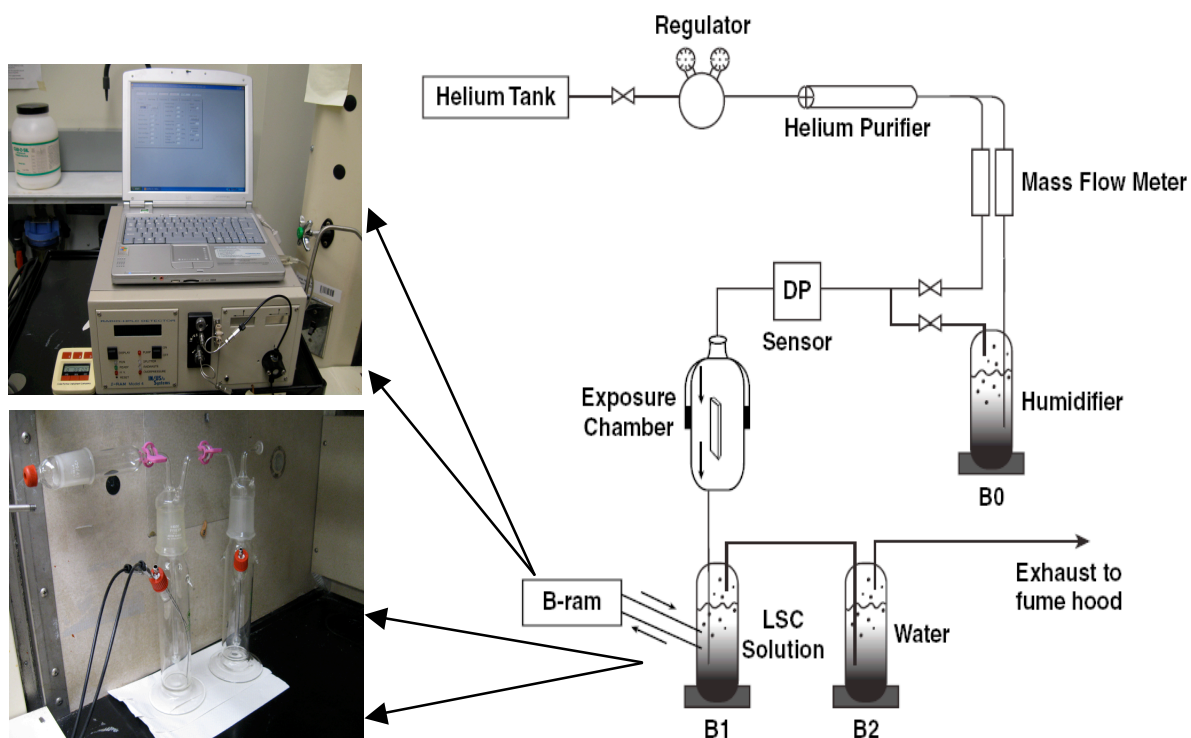


Fig. 2: Experimental system setup. Data was collected by way of the Beta-RAM software from the B1 bubbler

Data Processing

For the duration of the experiments, the system was constantly monitored by data acquisition software. The data acquisition software was a Beta-RAM system that was connected to a Beta-RAM program and a Microsoft Excel file. The Beta-RAM program recorded data in Excel after each minute of runtime. The data that was recorded automatically included the run number, the date, time, and the activity in CPM/ml. Data was taken from individual runs and compiled to reveal the entire data from an experiment. Concluding each run, a graph plotting the activity in the B1 bubbler against time was made in the Excel program. The system was also manually monitored before, during, and after the experiments. At the start and before concluding an experiment, the dew point was recorded, along with the time, date, and experimental information such as percent humidity or amount of HTO. In addition, when running pure water throughout the system, absent of tritium, the mass of the B0 humidifier was measured. This was done to understand the amount of water passing through the system and the loss in mass of water in the humidifier in relation to experiment duration and humidity of water within the carrier stream. This mass of water was then compared to the mass of water ($\dot{m} = \frac{dm}{dt}$) calculated to travel through the system during an experiment with the equation:

$$\dot{m} = \frac{P_V F_{carrier}}{R T_S} * \frac{M_W}{\rho} \quad (1)$$

where P_V is the water vapor pressure, $F_{carrier}$ is the flow rate of the purge stream

(liters/min), R is the universal gas constant, T_s is the temperature of the gas, M_w is the molecular mass of water, and ρ is the density of water (g/ml). In addition to monitoring the system, one-milliliter samples were collected after each run and measured in a liquid scintillation counter to calculate the final activity in each bubbler. The samples were counted for activity in counts per minute. This was done to calculate the amount of tritium removed from the coupon and therefore estimate the approximate amount of water adsorbing onto and desorbing from the coupon.

HTO Experiments

Various experiments were performed in order to achieve a greater understanding of how the system operates, more specifically system response times and Beta-RAM operation. Three experiments were run where the humidifier bubbler was deliberately contaminated with HTO. The first experimental run used 10 milliliters of HTO added to the humidifier, the next 20 ml, and the last 40 ml. The Beta-RAM system monitored the approximate activity of the LSC bubbler in counts per minute (CPM). The data was then graphed comparing the activity in CPM/ml and the time in minutes (see Fig. 3). The graph revealed three slopes, one for each amount of HTO added, that show the relationship between the concentration of HTO and activity against time. Figure 3 also shows a transition time between the slopes for each addition of HTO to the humidifier. Because the activity data for the graph was taken from the LSC bubbler, and activity started out in the humidifier, a certain amount of time was required for the activity to transfer through the system. As a result, there is a transition between slopes as the

activity is gradually increasing until it reaches a steady rate. This transition time is also the system response time, or the approximate amount of time it takes for the Beta-RAM system to respond to the change in activity. The results of these experiments showed that the approximate response time of the system was around 2 minutes. In addition, the normalization of these three slopes was found. The normalization N can be found with the equation

$$N = B / A \quad (2)$$

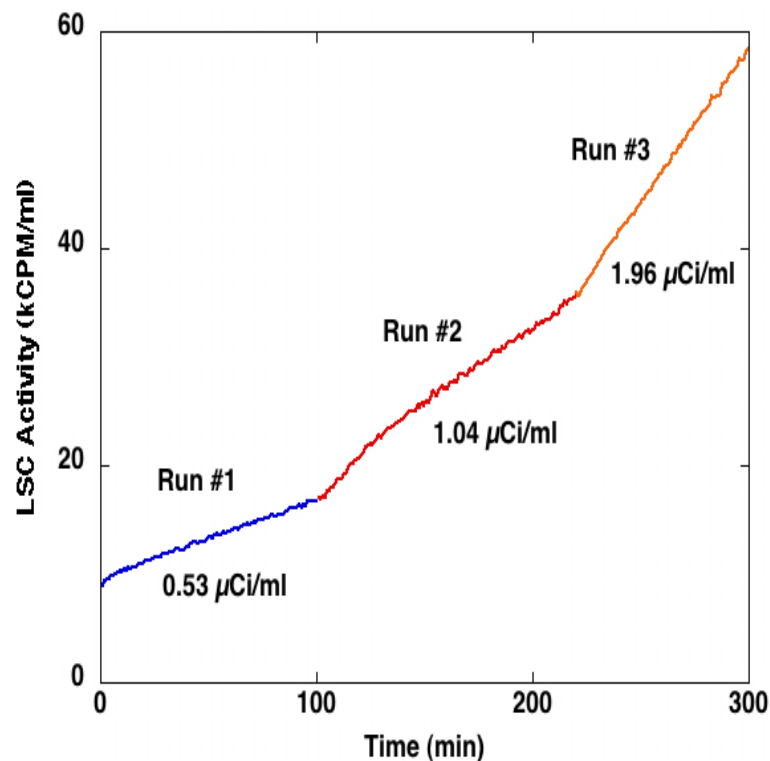


Fig. 3: Tritiated water runs prior to coupon experiments. The graph compares the activity (CPM/ml) versus time (minutes) of the 3 different tests: 10 ml of HTO, 20 ml, and 40 ml.

where B is the LSC solution's activity measured during a run and A is the concentration

of tritium ($\mu\text{Ci/ml}$) in the humidifier. After all the activities were normalized and then graphed as shown in Figure 4, the slopes were calculated and found to be the same for the 3 runs using 10 ml, 20 ml, and 40 ml of HTO in 100ml of water, respectively. The normalization is used to show that the flow rate of water through the system was constant as the activity within bubbler B0 was changed after each run. This slope represents the amount of water traveling through the system.

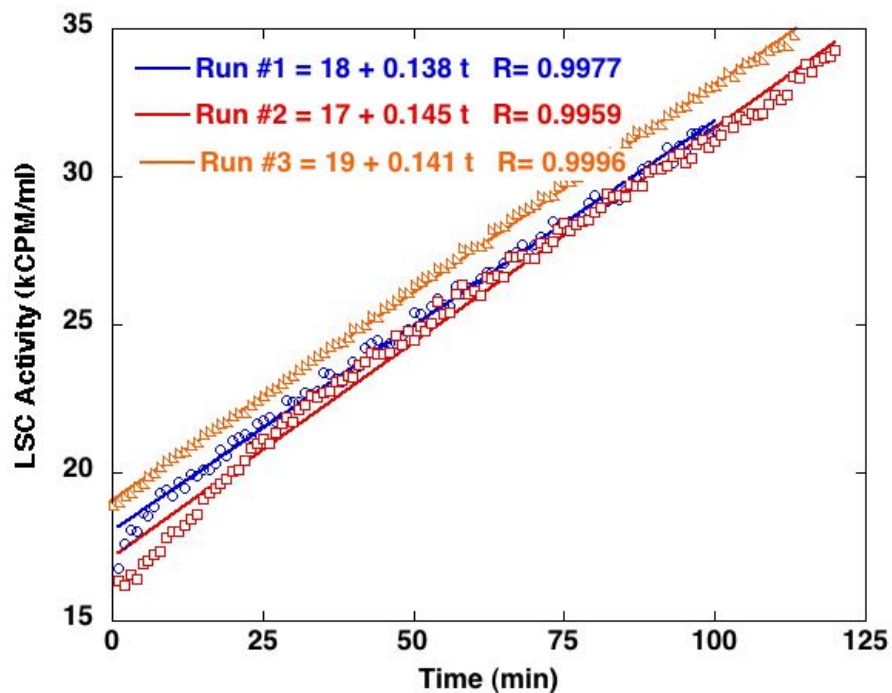


Fig. 4: Normalized data that reveals a constant flow of H_2O through the system during the tritiated water experiments.

Equation 3 can be used to calculate the activity increase in the LSC cocktail ($\dot{A} = \frac{dA}{dt}$)

$$\dot{A} = A * \dot{m} V \quad (3)$$

where A is the activity in the B0 bubbler, \dot{m} is given by equation (1), and V is the volume of liquid scintillator in the collector. By dividing \dot{A} by A for each experiment, the relation becomes independent of activity and reveals that the rate of water transfer in each run is identical.

$$\frac{\dot{A}}{A} = \dot{m} * V \quad (4)$$

The slopes of each curve in Figure 4 are identical as predicted by equation 4 and equal to approximately 0.17 ml/min when the flow rate is 100% wet.

The amount of water traveling through the system from the humidifier to the collector can also be calculated using the equations:

$$\dot{n} = \frac{P * \dot{V}}{R T} \quad (5)$$

and

$$ml\ of\ H_2O / \min = \dot{n} M_w \quad (6)$$

where \dot{n} is the number of moles of water per unit time, P is the water vapor pressure, \dot{V} is the volumetric flow rate of the carrier, t is time, R is the universal gas constant, T is the carrier temperature, and M_w is the molecular mass of water. This equation estimates that the amount of water traveling from the humidifier to the collector during

an experiment will be approximately 0.2 ml/min, a value close to that obtained in the experimental runs. This shows that the ideal gas law given by Eqn. 5 can be used to accurately predict water transport in the carrier.

Copper Coupon Experiments

Following the tritiated water experiments, experiments were performed with copper coupons that had been previously exposed to tritium. Several runs have been performed on two separate coupons. After compiling data collected from runs on the first coupon, several aspects of the system were understood. The first was the repeatability of the system. The system was first run dry at 100 ml/min of helium with a relative humidity of around 0.01%, yielding the blue curve in Fig 5, which graphs activity against time. After this run was concluded, another run was performed where one stream was humidified at a flow rate of 10 ml/min, while the other stream remained dry but moved at a flow rate of 90 ml/min. This run had an approximate relative humidity of 2%. Subsequently, another dry run was performed. By alternating from a dry run to a humidified run and then back to a dry run, the plots in Fig. 5 of the first and third runs, which were dry, reveal consistency after HTO had contaminated the system during the second run. The system was additionally run at a relative humidity of approximately 3%, revealing a similar data plot as the first humidified run. Before a third humidified run with a relative humidity of 11% was performed, the system was run dry for two runs to clear out any remaining HTO. The data that was graphed in Fig. 5 revealed that the dry run had a certain initial slope. When the humidity increased from a relative humidity of

0.013% to 2%, the initial slope of the curve increased, and when the humidity returned to 0.013%, the initial slope of the curve returned to its previous value for times below 100 min.

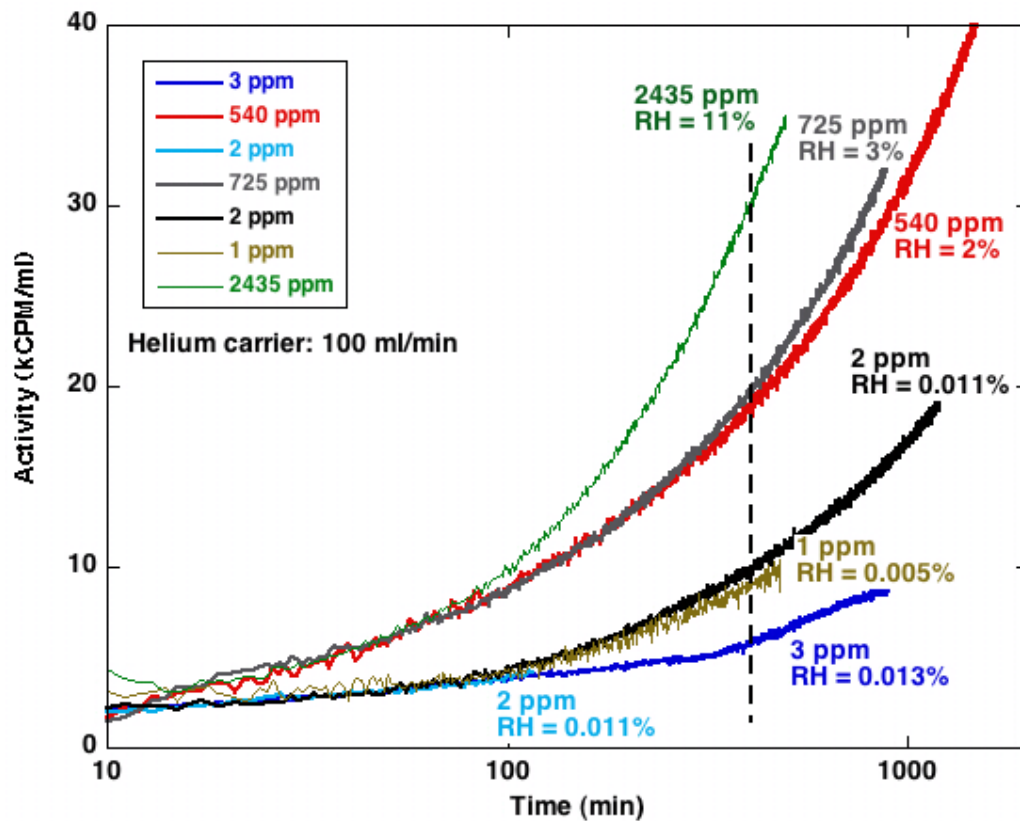


Fig. 5: Results from the first tritiated copper coupon experiments. The graphs compare the activity (CPM/ml) versus time (minutes) of 7 different tests with varying humidity in the helium stream.

A second observation was that as the relative humidity of the carrier increased, the amount of tritium desorption from the copper surface increased.

Another set of experiments was performed using a second coupon in which the

humidity of the runs was consistently increased from the first run to the last. In addition, the system was run dry at the beginning of each run for one hour to demonstrate that there is an immediate change in activity released from the coupon when the humidity is changed from dry to a specific humidity. The accumulation of activity in the collector is shown in Fig. 6 for each run. An expanded version of Fig. 6 is provided in Fig. 7 for times close to the point when humidity is introduced.

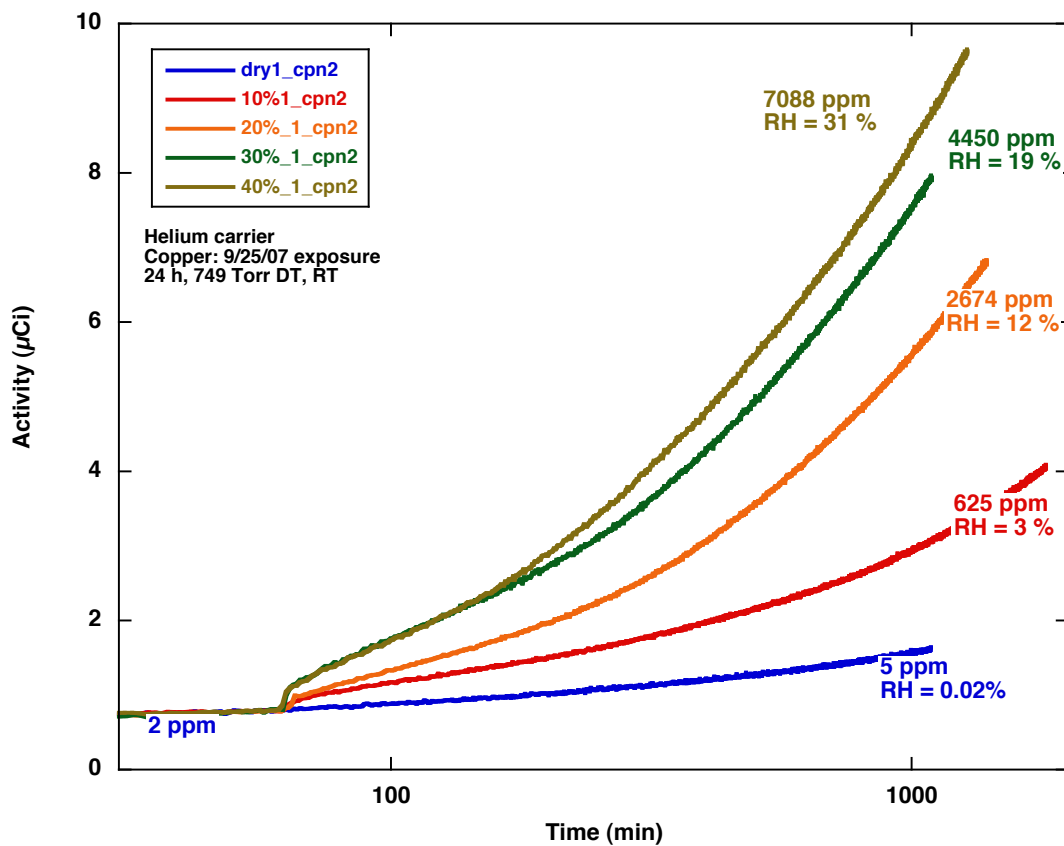


Fig. 6: Results from the second tritiated copper coupon experiments. The graphs compare the activity (CPM/ml) versus time (minutes) of 5 different tests with increasing amounts of humidity in the helium

Two more observations were made from these results. The first was that as the relative humidity increased, the initial rate of tritium desorption increased as shown in

Table 1.

Relative humidity in carrier (%)	Initial tritium desorption rate (nCi/min)
0.02	1.4
3	3.9
12	6.7
19	11.0
31	11.0

Table 1: Initial tritium desorption rates from a copper coupon as a function of the relative humidity of the carrier

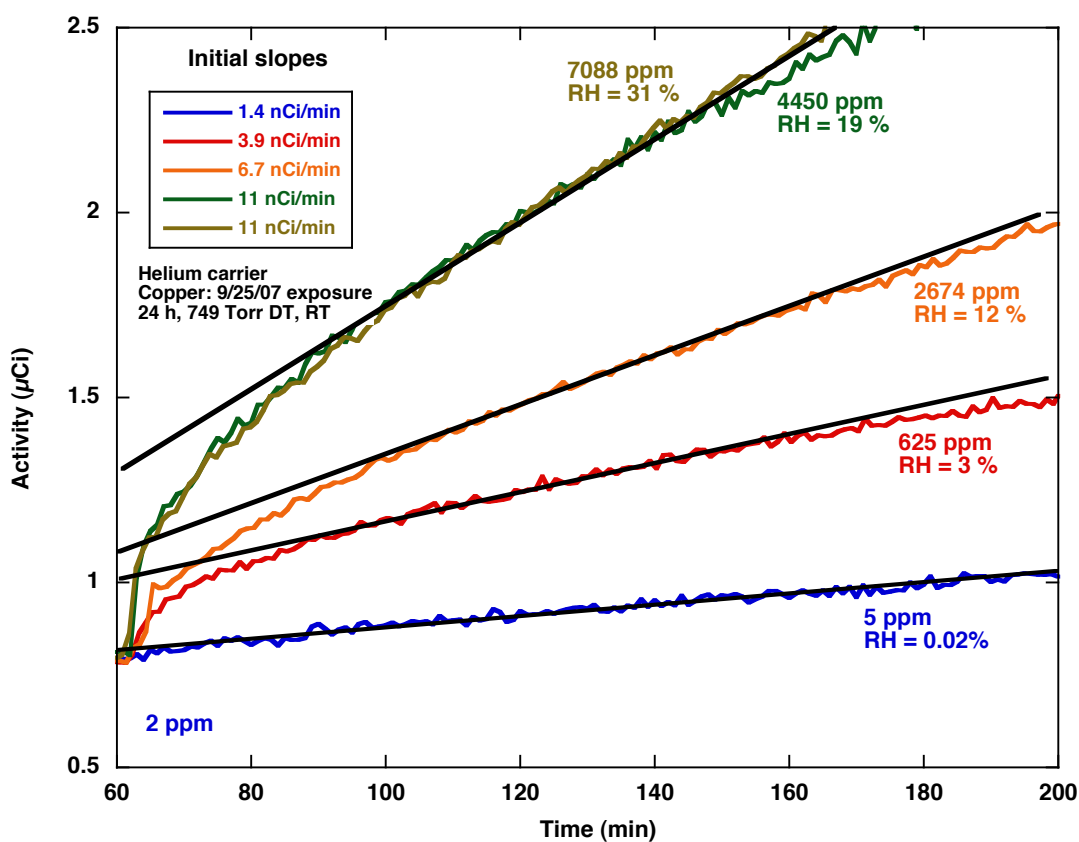


Fig. 7: Enlargement of Fig. 6 near the point in time when the carrier is humidified.

The second observation was that as the relative humidity increased, the initial desorption rate appears to reach a limit as seen in Table 1 and Figure 7. For each of the runs with a relative humidity between 19% and 31%, the slope of the curves remained around an average of 11.0 $\mu\text{Ci}/\text{min}$. Inspection of the data in Fig.7 shows that the curves begin to fall beneath the linear extrapolation with increasing time because the water layers on the surface of the metal are being depleted of tritium.

Tritium Removal Limits

There appear to be two different limits for tritium desorption. The first can be understood because, as the humidified helium stream passes over the copper coupon, there is a certain amount of tritium that can be removed from the top monolayers of water on the surface of the copper coupon (see Fig. 8). As this amount of tritium is depleted, the second limit of tritium desorption can be seen. This limit is the process by which tritium molecules that are in solution in the copper migrate through the water layers to the surface of the coupon as illustrated in Fig. 8. This was demonstrated from the result that, as the water vapor pressure in the experiment was increased, the slope of the activity in the first bubbler against time appeared to reach a limit.

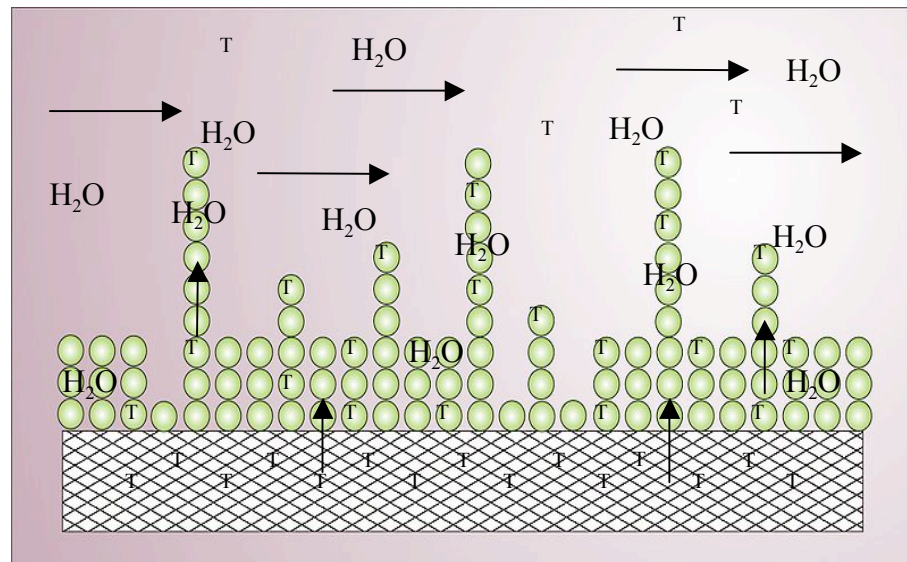


Fig. 8: Image depicting the process that occurs as a humidified helium stream passes over a tritiated copper coupon. It also shows the two limits to the process of adsorption and desorption.

Conclusion

Experiments have been performed to study and understand the processes by which water desorbs from copper. Tritium, which is a radioactive isotope of hydrogen, was used as a tracer to label water molecules attached to copper and monitor the rate at which desorption occurs. It was concluded that the rate of tritiated water (HTO) desorption from a copper surface increases with an increasing water vapor pressure. Therefore, the more humidified an environment is, the greater the desorption that will occur. Through these experiments, it was also found that the rate at which HTO desorbs approaches a limiting value. Additional experiments would provide more data to substantiate these conclusions.

Acknowledgements

I would like to thank my advisor, Dr. Walter Shmayda for his generous support and assistance throughout my research. I would also like to thank Dr. Stephen Craxton for the chance to take part in this internship and Collin Sowinski for assisting me throughout the project.

References

1. E. Shero *et al.*, Fundamentals of Moisture Interaction with EP Stainless Steel and Silicon Wafer Surfaces, Proceedings of the 41st Annual Technical Meeting of the Institute of Environmental Sciences, Mount Prospect, IL. **545**, 542 (1995).
2. T. Ohmi *et al.*, New Technique for the Measurement of Adsorbed Moisture Concentration on a Solid Surface, Rev. Sci. Instrum. 64 (9), **2683** (1993).
3. H. Izumi *et al.*, Behavior of Adsorbed Moisture on Solid Surfaces, Proceedings of the 41st Annual Technical Meeting of the Institute of Environmental Sciences, Mount Prospect, IL. **549-551** (1995).
4. W.T. Shmayda *et al.*, A Study of Desorption of HTO from Metal at Various Temperatures and Water Vapor Pressures, Fusion Sci & Tech. **54**, 519-522 (2008).
5. Collin Sowinski, Minimization of Tritium Contamination on Surfaces, 2008 Summer Research Program at the University of Rochester's Laboratory for Laser Energetics, LLE Report # 357

Parameter Optimization of 1-D Multi-FM SSD on the NIF

Aaron Van Dyne

Parameter Optimization of 1-D Multi-FM SSD on the NIF

Aaron M. Van Dyne

Laboratory for Laser Energetics, University of Rochester, 250 East River Road, Rochester, New York 14623

Abstract

This work investigates the parameters that affect 1-D Multiple Frequency Modulation (Multi-FM) Smoothing by Spectral Dispersion (SSD) on the National Ignition Facility and demonstrates that a high level of uniformity can be achieved using Multi-FM by employing an optimization procedure. The laser non-uniformity that directly drives an inertial confinement fusion target can imprint on the target's shell during the ablation process, leading to the exponential growth of non-uniformity leading to the shell's destruction. The SSD system mitigates imprint by causing the speckle pattern to evolve continuously, creating many statistically independent patterns that average over time. The 1-D Multi-FM SSD system uses multiple phase modulators with different frequencies in a single dimension. A MATLAB program was developed to optimize 1-D Multi-FM SSD by intelligently varying the parameters to minimize a metric based on time integrated laser non-uniformity and laser system constraints. The MATLAB program's algorithm is based on the Levenberg-Marquadt method to find optimal solutions based on local derivative values. The MATLAB program was able to produce realizations of 1-D Multi-FM SSD that have lower levels of non-uniformity compared to single modulator designs. The OMEGA-EP laser will be used as a test bed for the new designs.

1. Introduction

The laser systems known as OMEGA¹ and the National Ignition Facility (NIF)² require a high degree of laser-beam uniformity to perform direct-drive inertial confinement fusion (ICF)^{3,4} experiments. Laser non-uniformity seeds the Rayleigh-Taylor hydrodynamic instability, which consequently degrades performance.⁵⁻¹¹ OMEGA and the NIF employ various techniques to improve on-target irradiation uniformity and reduce the laser imprint on direct-drive target designs, such as smoothing by spectral dispersion (SSD)¹²⁻¹⁵ and continuous phase plates.^{16,17} The non-uniformity in the lower spatial frequencies is the most problematic because hydrodynamic instabilities can develop during their longer imprinting periods, and these frequencies are hardest to smooth with SSD.

Continuous phase plates offer control over the far-field intensity envelope even in the presence of typical laser system phase aberrations. High spatial frequency non-uniformity, known as speckle¹⁸, is a direct consequence of phase plates. To lessen the effect of this speckle,

SSD is employed, which smoothes the speckle on a time scale shorter than the target can respond hydrodynamically. SSD achieves this effect by continuously altering the speckle pattern over time. The time-integrated far-field spot ends up being sufficiently uniform for ICF experiments when the SSD system has sufficient bandwidth and divergence. The SSD system can be applied in orthogonal spatial dimensions: 1-D SSD alters the speckle in one spatial dimension, and 2-D SSD alters it in two spatial dimensions. Multiple frequency modulation (Multi-FM) SSD employs multiple phase modulators in the direction of modulation and provides increased flexibility in smoothing performance. Standard 1-D SSD, which refers to the traditional process with only a single modulator, is limited to one or two color cycles due to a coherent interference effect similar to that of a double slit.¹⁹ A color cycle is one cycle through all of the phases within the beam. For example, in a 1 color cycle system, each color would appear once in a color contour plot of near-field phase. Multi-FM employs many color cycles over many modulators which tends to mitigate this interference effect. Multi-FM 1-D SSD uses only 500 GHz of bandwidth as opposed to the 900 GHz of bandwidth for standard 1-D SSD, defined as one leg of the 2-D system originally proposed for the NIF, which used 17 GHz, 2 color cycles, and 100 μ rad of full-angle divergence. The reduced applied bandwidth implies that only a single frequency tripling crystal is necessary²⁰ as opposed to the two necessary for standard 1-D SSD. Multi-FM 1-D SSD, which offers numerous benefits over standard 1-D SSD, will be the focus of this work.

2. Optics and the Fourier transform

In optics there are two important regions: the near field and far field as seen in Figure 1. The near field is the region before the beam has passed through the lens, and the far field is the region near the focal plane of the lens. Based on Fourier optics, the far-field image is the Fourier

transform of the near-field image²¹. The Fourier transform is a mathematical operation that can be applied to any well-behaved function of any number of variables, eg. time and space. The Fourier transform of a continuous time-dependent function transforms it into a continuous spectrum of frequencies²². The equation representing a formal temporal transform is given by,

$$F(\omega) = \int_{-\infty}^{\infty} f(t) e^{i\omega t} dt \quad (1)$$

where $f(t)$ a function of time t , ω is an angular frequency, and $F(\omega)$ is the Fourier transform of $f(t)$. The equation for a 1-D spatial transform in the x -direction is given by,

$$F(k_x) = \int_{-\infty}^{\infty} f(x) e^{-ik_x x} dx \quad (2)$$

where $f(x)$ is a function of location in the x direction, k_x is a spatial frequency, and $F(k_x)$ is the Fourier transform of $f(x)$. The Fourier transform operators are used to examine the effect of smoothing in the far field.

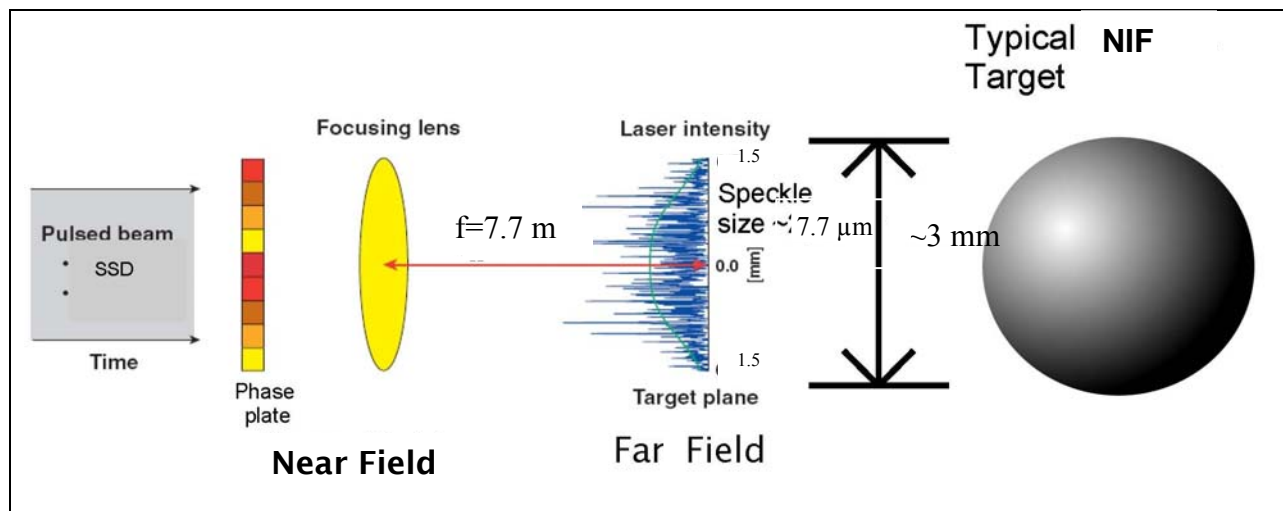


FIG. 1 A diagram showing the near field and far field for the NIF. The near field is the region before the lens, and the far field is the region near the focal plane of the lens. The phase plate shapes the beam to contain 95% of the enclosed energy in 3 mm, which slightly overfills the 3 mm target. The speckle size is on the order of $7.7\ \mu\text{m}$. This value comes from the equation $d=f\lambda/D$ where d is the speckle size, f is the focal length, D is the diameter of the beam, and λ is the wavelength of the light. For the NIF, $f=7.7\text{ m}$, $D=35.1\text{ cm}$, and λ is 351 nm .

3. Diffractive Optics

A diffractive optic known as a continuous phase plate is used to shape the far-field spot. This results in high spatial frequency artifacts, called speckle. This high spatial frequency speckle can be smoothed effectively by thermal conduction in the plasma around the NIF target unlike long-wavelength non-uniformity. The phase plate causes speckle because the beam is coherent. If a perfect beam passes through a lens, a diffraction limited spot is created in the far field. The width of this spot is defined as the distance from the center to the first zero and is determined by the equation $d=f\lambda/D$, where d is the spot size, f is the focal length of the lens, λ is the wavelength of the laser, and D is diameter of the beam or lens (whichever is smaller). For the NIF, the focal length is 7.7 m , the diameter is 35.1 cm , and the wavelength is 351 nm . This yields a spot size of $7.7\ \mu\text{m}$, but with the addition of phase aberration, this spot grows. When a strong phase aberration is added, such as that of the phase plate which makes the spot 400 times larger, the far field spot simply can be thought of as being many copies of the same $7.7\ \mu\text{m}$ spot distributed over the far-field plane.

4. The necessity of uniformity

In order to achieve ignition the target must be compressed by the laser such that the mixture of deuterium and tritium reaches a sufficiently high temperature and pressure. Uniform compression of the target is necessary to achieve this combination of temperature and pressure. This uniform compression requires a laser with a high level of uniformity. Hydrodynamic simulations show that ignition can be achieved using 1-D Multi-FM SSD, but further research could allow more flexibility in target and pulse shape choice. The 1-D Multi-FM smoothing system offers very promising options for achieving ignition. The system smoothes effectively and offers other benefits. These benefits include the feasibility of implementing the system in fiber optics as opposed to the bulk optics necessary for 2-D SSD. The Multi-FM system also requires only a single frequency tripling crystal.

5. SSD

The spot in the far field must be large enough to fill the 3 mm diameter target used on the NIF. There are two methods that can be employed: defocusing the far-field spot and employing a diffractive phase plate to shape the far-field spot. Each of these options has different consequences. The target can be placed outside of the focal plane creating a defocused spot as can be seen in figure 2a, but this creates a static long-wavelength non-uniformity that cannot be smoothed. The other option is to shape the spot using an engineered continuous phase element called a phase plate²³ that controls all the low spatial wavelengths that govern the overall spot shape. As previously mentioned, this results in high-frequency non-uniformity, known as speckle, figure 2b. Fortunately speckle can be smoothed. The method of smoothing used on OMEGA and the NIF is SSD, which involves continuously changing the speckle pattern to create many statistically independent random speckle patterns over time. The smoothing then occurs via

the temporal averaging of the independent patterns over time. This temporal averaging is possible because the speckle pattern changes faster than the target can respond hydrodynamically. The net laser non-uniformity imprinted on the target is reduced because the target reacts to a smoother spot. A version of SSD referred to as 1-D SSD involves the alteration of the speckle pattern in one spatial dimension, and as a result, there are striations in the far-field spot depicted in figure 2c. These striations are not seen in the far-field spot for 2-D SSD because this smoothing scheme alters the speckle pattern in two spatial dimensions. While 2-D SSD does yield a superior non-uniformity, 1-D SSD can be improved by using Multi-FM. It has been shown that employing the Multi-FM smoothing scheme is sufficient to achieve ignition²⁴. The 1-D SSD system also offers certain advantages because it can be done in a fiber and requires only a single frequency tripling crystal whereas 2-D SSD requires bulk optics and two frequency tripling crystals because for equivalent smoothing 2-D SSD requires more bandwidth.

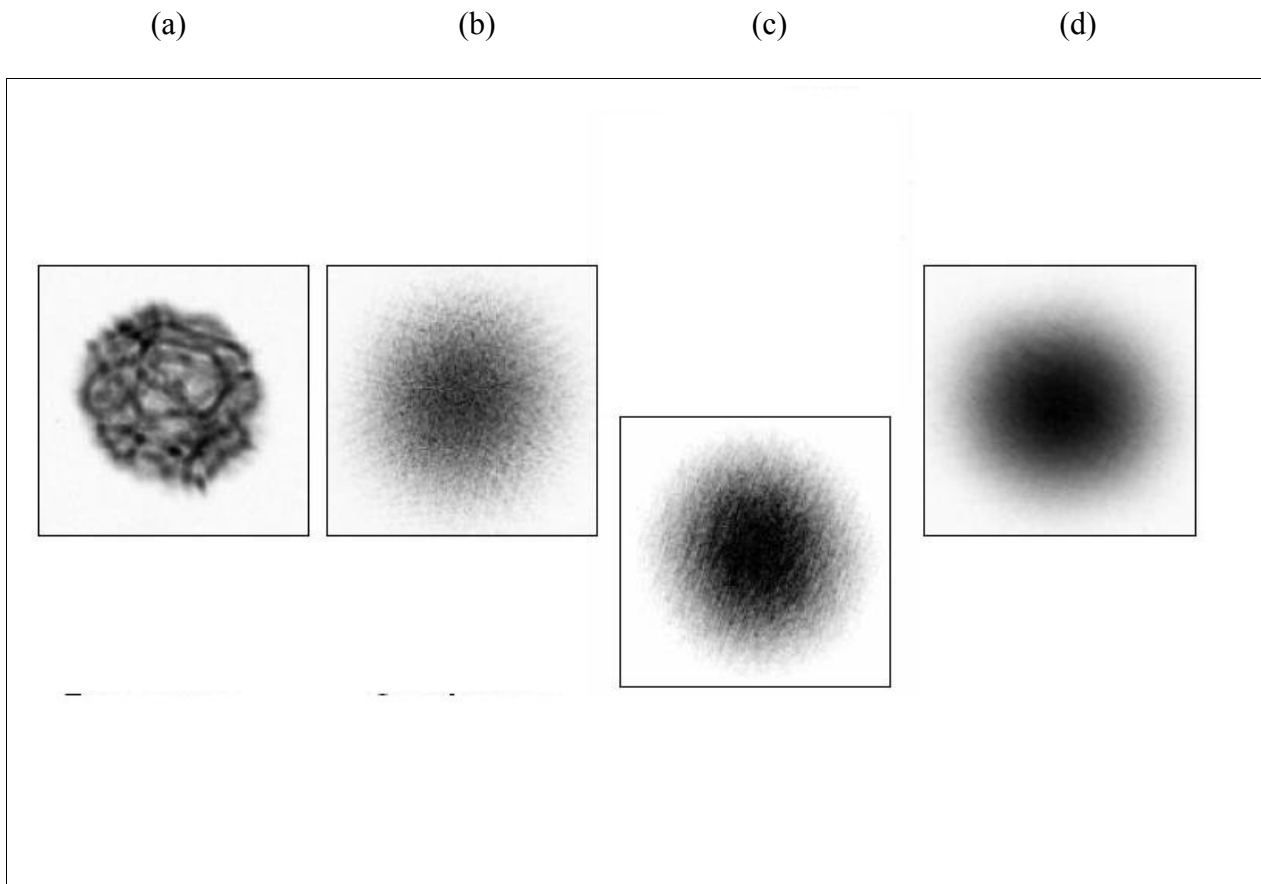
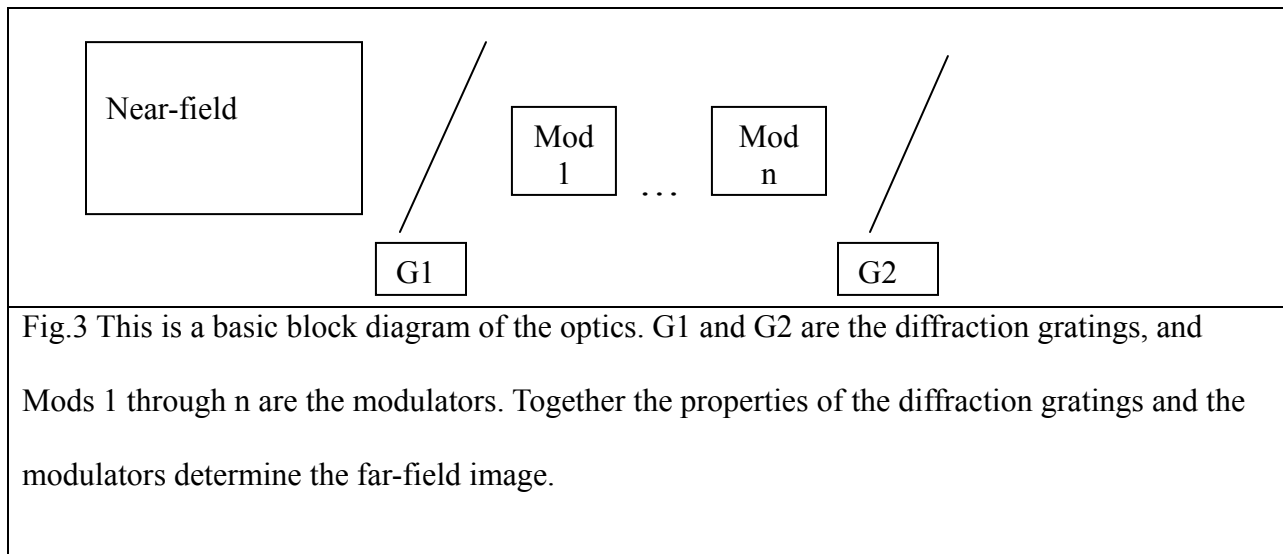


FIG.2 Far field spots for various techniques of illuminating the whole target and smoothing the beam. a) Defocused spot, target outside of focal plane with long-wavelength non-uniformity. b) Time-integrated far-field shaped by phase plate with high-frequency speckle. c) Time-integrated far-field spot with 1-D SSD applied. The striations are visible. d) Time-integrated far-field spot with 2-D SSD applied. There are no longer striations visible in the far-field spot.

6. Multi-FM

An alternative smoothing option denoted as 1-D Multi-FM SSD involves the use of multiple phase modulators in a single spatial dimension. There are two independent parameters involved in any form of FM for each modulator: modulation frequency and bandwidth. The grating dispersion is also an independent parameter of the system as a whole. The gratings and

modulators are shown in a block diagram of the optics, figure 3. Other important parameters can be derived from these parameters such as angular divergence, which is the spread in the far field. Certain constraints must be placed on any SSD system based on physical limitations of high-power laser systems: bandwidth and divergence. The bandwidth needs to be less than 500 GHz due to the pass band of a single frequency tripling crystal, and the angular divergence has to be less than 250 μrad due to the smallest pinhole in the NIF laser chain. It is also important that the modulation depth (a measure of how much each modulator's frequency varies) be greater than one in order to yield a side-peaked distribution,²⁵ which is better for uniformly irradiating the target. The proposed 1-D Multi-FM SSD system employs the benefit of multiple color cycles. Standard 1-D SSD is limited to one or two color cycles, figure 4a, due to a coherent interference effect similar to a double slit experiment. This interference effect results in a loss of smoothing at the resonances. The proposed 1-D Multi-FM SSD system takes advantage of multiple color cycles as can be seen in figure 4b. The colors are arranged in a quasi-random pattern of phase where the colors are out of synchronization with each other. It is this effect of having the separations of identical colors vary over time that mitigates the resonant effect.



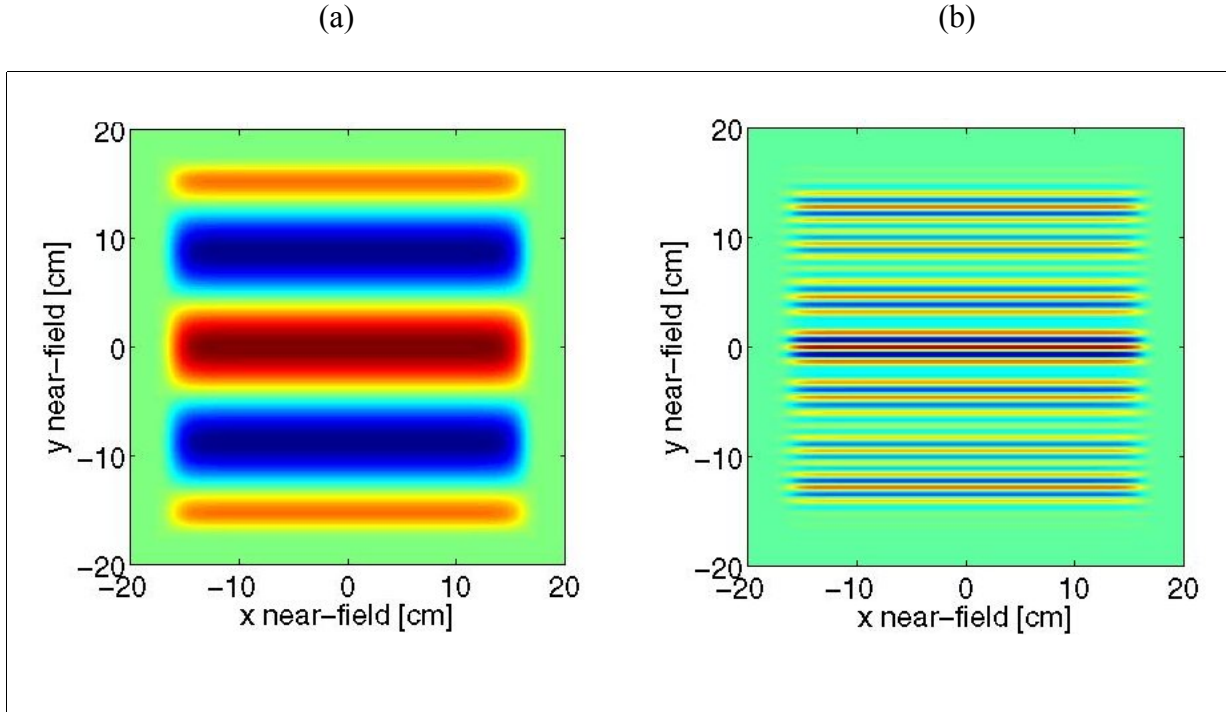


FIG. 4 Two similar color contour plots of phase in terms of x near-field and y near-field spatial coordinates. a) The plot illustrates Standard 1-D SSD with 2 color cycles. In this system the colors are in synchronization with each other creating an interference effect that causes a loss of smoothing at the resonances. b) The plot illustrates the fact that the Multi-FM system makes use of multiple color cycles and the colors are arranged in a quasi-random pattern. The colors in this system are not in synchronization, which mitigates the interference effect.

7. The code for optimizing the parameters

The optimization of a multi-variable function employs a metric that measures the overall effects of each parameter. The metric used in this work allows the effect of each parameter on the far-field non-uniformity to be evaluated. A code that optimizes the parameters was developed in MATLAB and is called, `Loop_analyzeMultiFM`. The code `Loop_analyzeMultiFM` controls another MATLAB code called `analyzeMultiFM`, which calculates certain values in the far field based on the SSD parameters. The code `Loop_analyzeMultiFM` alters various SSD parameters: the number of modulators, the frequency of each modulator, and the number of color cycles and modulation depths of each modulator. The code `analyze_MultiFM` then calculates certain values

such as the bandwidth, angular divergence, and asymptotic non-uniformity. After the parameters are optimized, the code also generates diagnostic plots of the far field in terms of divergence and bandwidth, a color contour plot of the phase in the near field, and the asymptotic non-uniformity in terms of the dimensionless spatial wave number l defined as $l \equiv kr$ where $k = 2\pi/\lambda$, λ = the spatial wavelength, and r = the target radius. The code `Loop_analyzeMultiFM` was written to vary the parameters that are fed to `analyzeMultiFM` in an intelligent manner. The parameters are the number of modulators and the frequencies, and the coefficients that help determine the number of color cycles and modulation depth of each modulator; eg. a total of 9 parameters when the number of modulators is 4. Based on these inputs, `analyzeMultiFM` determines bandwidth, modulation depth, the number of color cycles, temporal shear, as well as other values in the far field such as angular divergence and asymptotic non-uniformity. The temporal shear is how much the beam is offset in the temporal dimension by the optics.

The diagnostic outputs from `analyzeMultiFM` are combined to create a performance metric that attempts to limit far-field non-uniformity within realistic constraints. The performance metric is denoted as σ . These realistic constraints include: limiting the bandwidth, temporal shear, and angular divergence. The bandwidth has to be less than 500 GHz because of the frequency tripling crystals. The angular divergence has to be less than 250 μrad because of the smallest pinhole size in the NIF laser chain, and the temporal shear has to be less than 350 ps in order to not limit the pulse's rise time. It is preferable for the modulation depth to be greater than one because this prevents a highly center-peaked distribution. Three different ranges for the non-uniformity are used: the asymptotic non-uniformity over l -modes 60 to 80, l -modes 20 to 100, and l -modes 20 to 600. Each of the individual values that contribute to the metric has to be scaled, so that the resultant values are of a similar magnitude (referred to as

normalization). Each of these normalized terms is represented by β , which is used to develop sigma by the equation $\text{sigma}=\beta*\alpha$, where α determines the relative weight of each value. First the asymptotic non-uniformities are divided by the number of l-modes in their respective ranges. The asymptotic non-uniformities are then multiplied by a normalizing factor. The asymptotic non-uniformity over l-modes 60 to 80 is multiplied by 8,000. The asymptotic non-uniformity over l-modes 20 to 100 is multiplied by 20,000, and the asymptotic non-uniformity over l-modes 20-600 is multiplied by 36,680. The modulation depth, bandwidth, temporal shear, and angular divergence parts of the metric are normalized using the equation

$$\beta=e^{(\zeta-\gamma)/\chi} \quad (3)$$

where β is the normalized value, and χ , γ , ζ are values specific to the parameter. This method is used to keep the metric low as long as the parameter is within the physical limit but cause it to skyrocket if the parameter exceeds the physical limit. For the modulation depth ζ is 1.5, γ is the modulation depth, and χ is 1. These values were chosen in an effort to force the modulation depth to be greater than 1. For the bandwidth ζ is the bandwidth, γ is 500 GHz, and χ is 100GHz. For the divergence, ζ is the divergence, γ is 300 μrad , and χ is 100 μrad . These values were chosen in an effort to limit the divergence to being less than 250 μrad . For the temporal shear, ζ is the temporal shear, γ is 400 ps, and χ is 100 ps. This was chosen in an effort to force the temporal shear to be less than 350 ps. It was observed that the algorithm attempts to make some of the physical parameters much lower or higher than γ or ζ , the value modifying them, in order to achieve a very low sigma. Therefore, it may be noted that the γ or ζ used to modify the physical parameters are sometimes greater than the actual physical constraints. By making the modifying values larger than the actual constraint, the parameter gets much closer to the level that it is being constrained from crossing. This effect is important because in the case of the bandwidth, angular

divergence, and temporal shear, the best results are seen as the values grow larger, and the constraint exists because of a physical constraint of the laser system. The values ζ , γ , and χ can continue to be changed in the future to fine tune the algorithm.

In order to use β to develop sigma, the β values are weighted, to adjust the relative importance of each parameter. The weightings, α , chosen have a substantial impact on the optimal solutions that are found, so many combinations of weightings were tested to see which worked best. For example, if not enough weight is placed on the modulation depth, it begins to go substantially below 1. The majority of the weight has to be placed on the asymptotic level from l-modes 60 to 80 because these modes have been the most problematic in hydrodynamic simulations²³. The asymptotic non-uniformity over l-modes 60 to 80 has an α of 10, the asymptotic non-uniformity over l-modes 20 to 100 has an α of 5, the asymptotic non-uniformity over l-modes 20 to 600 has an α of 2, the modulation depth has an α of 6, the bandwidth has an α of 4, the angular divergence has an α of 3, and the temporal shear has an α of 3.

The actual algorithm used in the code Loop_analyzeMultiFM is based on the Levenberg-Marquardt method¹⁶, which uses local partial derivatives to determine how the free parameters should be varied. This algorithm varies one parameter at a time, and changes it by 5 percent until the derivative of sigma with respect to the parameter becomes positive, then goes back to the value that yielded the lowest sigma and changes it by 5 percent at a time in the other direction. The algorithm stops changing the parameters if sigma stops changing, the value of the parameter returns to the value that yielded the lowest sigma after the parameter has changed 5 times, or the value of the parameter exceeds limits placed on the parameter. The code then moves to the next free parameter and alters it. The code alters each of the free parameters in this cycle three times. The cycle is repeated because there is a non-linear relationship between the

parameters, so the parameters must be optimized based on the optimal values of the other parameters. It is also for this reason that the first parameter optimized is the coefficient for the number of color cycles, which was observed to be the most sensitive, and the last parameter to be optimized is the maximum modulation frequency, which was observed to be the least sensitive.

8. An Optimized Multi-FM System

An optimized 1-D Multi-FM SSD system with 500 GHz of bandwidth outperforms a standard 1-D SSD system with 900 GHz of bandwidth and is comparable to a full 2-D SSD system with 1 THz of bandwidth, and as a result, only a single frequency tripling crystal is necessary as opposed to the three necessary for standard 1-D SSD. An optimized system found by the code contains four modulators each defined by the previously discussed two independent parameters and the diffraction grating. Each modulator has a frequency between 25 and 50 GHz, a number of color cycles between 10 and 18, and all the indicators of bandwidth indicate a bandwidth just under 500 GHz. One measure of bandwidth is the correlation-width bandwidth, which is given by the following equation,

$$\text{Correlation-width bandwidth} = \frac{[\int F(\omega)d\omega]^2}{\int [F(\omega)]^2 d\omega} \quad (4)$$

where $F(\omega)$ is the function representing the pulse and ω is the frequency. The correlation-width bandwidth was by far the lowest of the measures of bandwidth because the wings of the function aren't equally weighted for center-peaked distributions. This fact caused an issue because the correlation-width divergence indicated a divergence well below 250 μrad full angle.

Unfortunately, the spread seen in figure 5, a plot of the far-field intensity in terms of divergence, appears to have too much intensity beyond the levels allowed by the pinhole. To rectify this, a different metric for divergence might be used in the future although this might be unnecessary if future optimal systems are more side-peaked. This center-peaked distribution is a result of low

modulation depths, which ranged from 0.6 to 1.1 for the modulators in this system. It was found that modulation depths over 1 smooth better and yield more side-peaked distributions. The other issue with this system is that its temporal shear is about 400 ps. This is an anomaly within the algorithm that must be worked out in the future because a temporal shear of greater than 350 ps limits the risetime of the pulse.

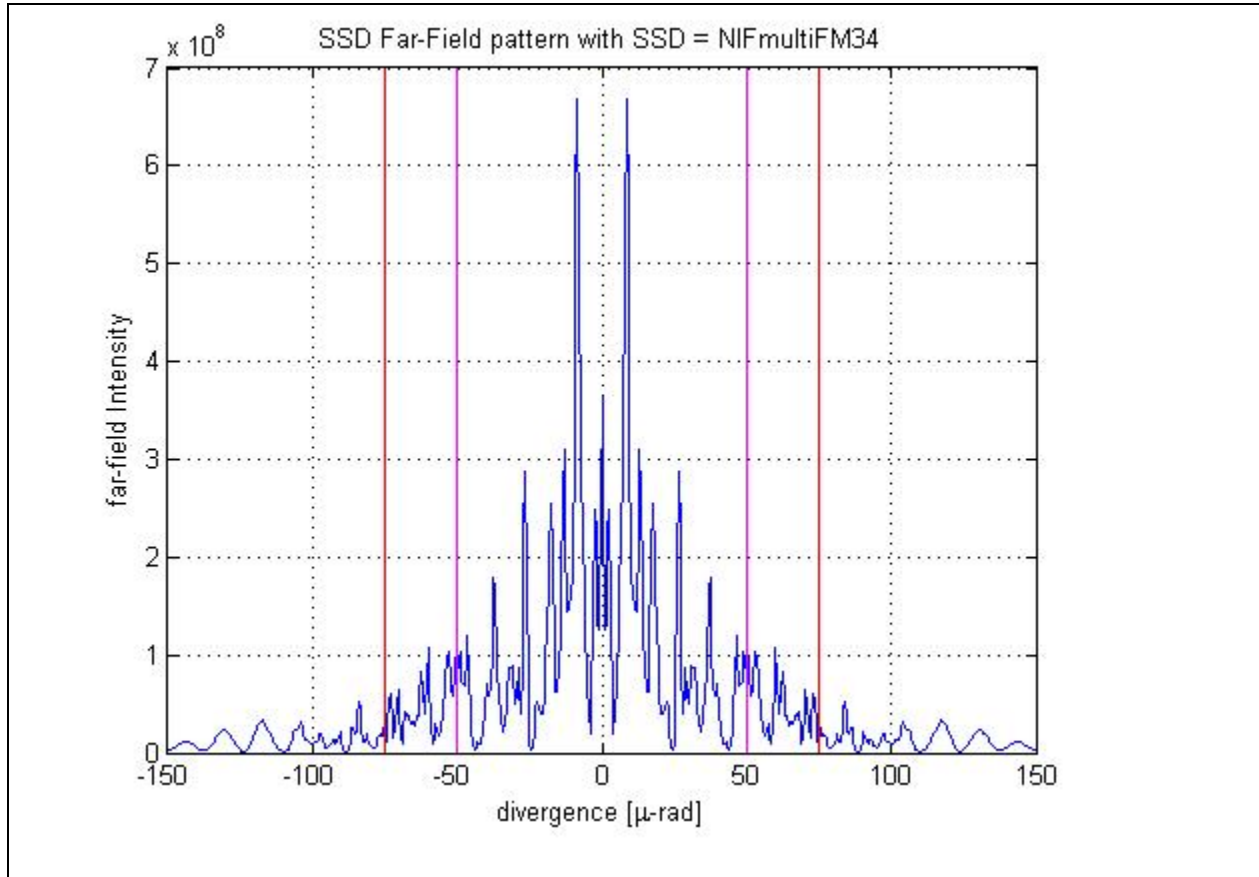
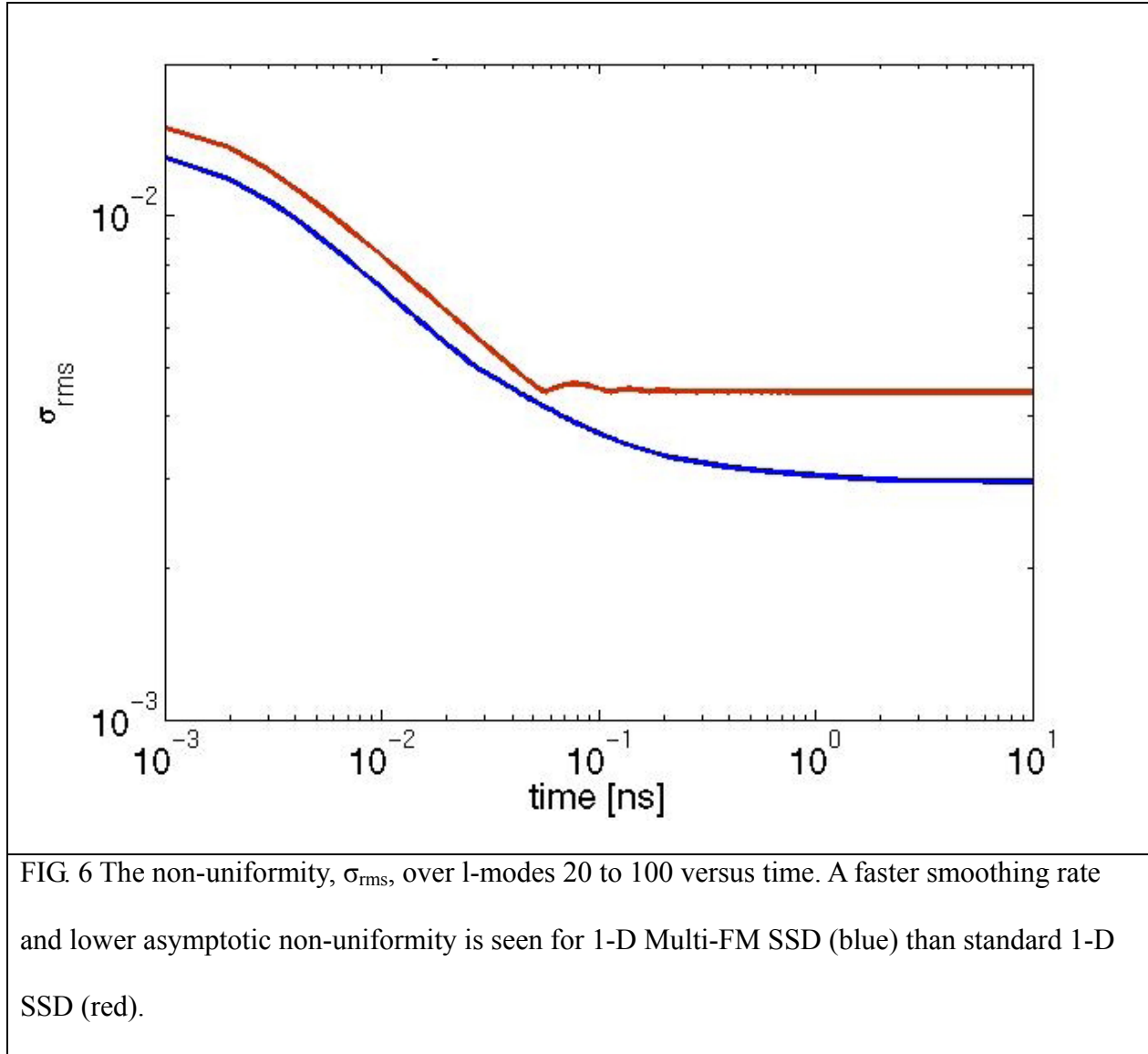


FIG. 5 Plot of far-field intensity vs. angular divergence. The far-field intensity does not flatten out sufficiently at the edges of the plot. At 125 μrad the far-field intensity must be almost zero in order to avoid encountering problems with the pinhole.

There are two ways of representing the far-field performance of an SSD system: the non-uniformity over time and the asymptotic non-uniformity versus l-mode. In both cases 1-D Multi-FM SSD outperforms standard 1-D SSD. A plot of the σ_{rms} non-uniformity over l-modes 20 to 100 versus time, figure 6, demonstrates a higher smoothing rate and lower asymptotic non-

uniformity for Multi-FM 1-D SSD than standard 1-D SSD.



Similarly, figure 7, a plot of asymptotic non-uniformity versus l-mode, demonstrates a lower asymptotic non-uniformity for all l-modes for Multi-FM 1-D SSD. It is important to note that the plot of asymptotic non-uniformity is over l-modes 2 to 600 whereas the plot of non-uniformity versus time is only over l-modes 20 through 100. This is because l-modes greater than 100 have low decoupling times, which means that the laser has hydrodynamically decoupled from the

target at that modal range, and that modal range is not affected as much by non-uniformity after this time, and l-modes less than 20 are not impacted as much by SSD, so the l-modes that were likely to be the most important are used in figure 7.

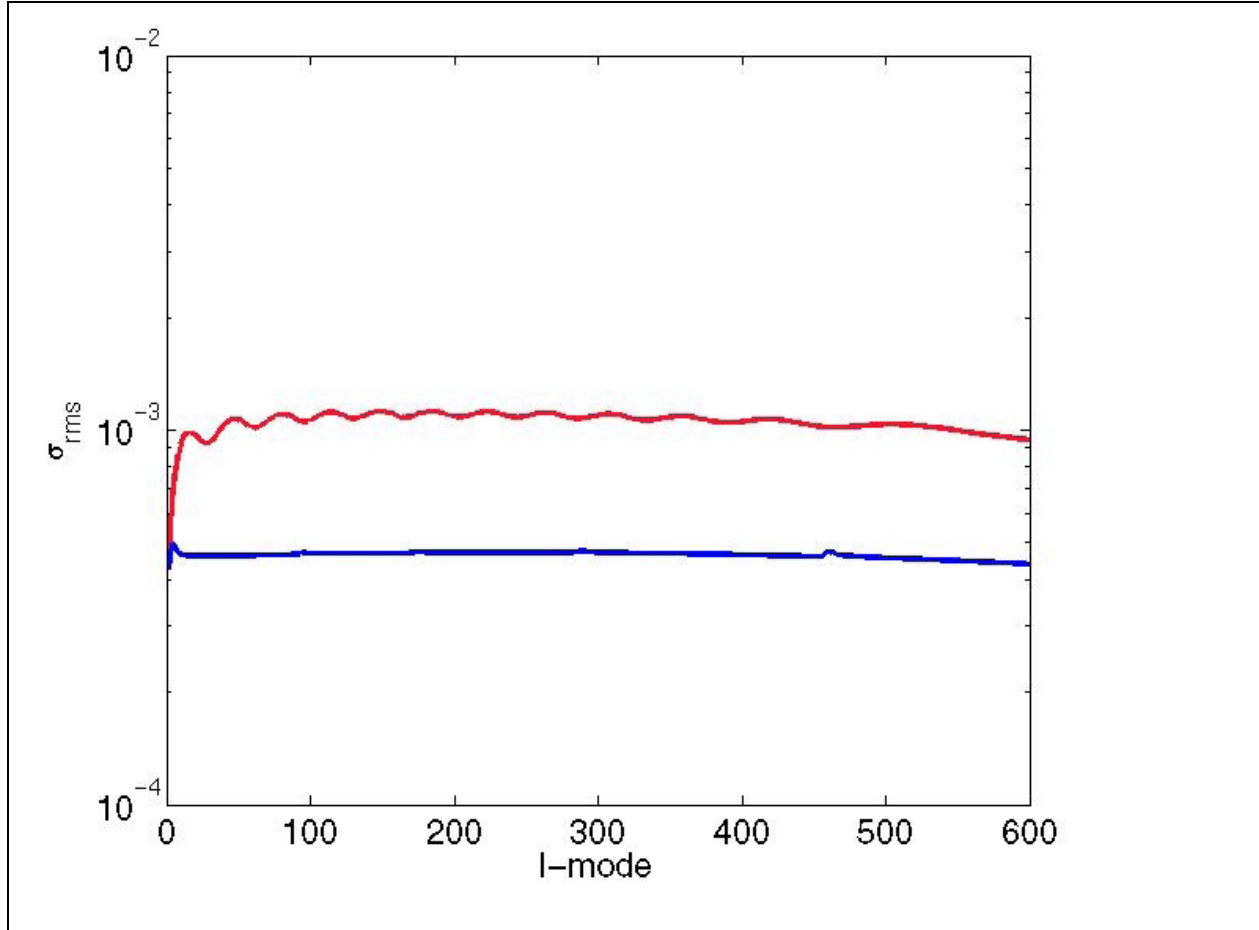


FIG.7 Plot of asymptotic non-uniformity versus l-mode. For all l-modes 1-D Multi-FM SSD (blue) has a lower asymptotic non-uniformity than standard 1-D SSD (red). More consistent smoothing over all the l-modes is also seen.

9. Conclusion

An optimized Multi-FM system with 500 GHz of bandwidth outperforms standard, single modulator, 1-D SSD with 900 GHz of bandwidth and is comparable to a 2-D SSD system with 1 THz of bandwidth.²⁴ This 1-D Multi FM system involves 4 modulators defined by several parameters. Each modulator has between 10 and 18 color cycles, a frequency between 25 and 50 GHz, and modulation depths between 0.6 and 1. In the future, it would be desirable to have

modulation depths greater than 1 because this will yield a more side-peaked distribution. The bandwidth was right around the maximum 500 GHz. The correlation-width measure of divergence indicates a value less than 250 μ rad, but inspection of a plot of far-field intensity versus deviation indicates otherwise. For this reason, a new measure of divergence is necessary, although the current measure may be satisfactory for more side-peaked distributions. The temporal shear was around 400 ps, which is greater than the desired limit of 350 ps, because the code consistently indicated that optimal solutions had a temporal shear of this magnitude in spite of attempts to limit it. When too much limitation was employed, the temporal shear dropped too low. This is an issue that must be worked out in the future. Multi-FM 1-D SSD is a promising concept, and Loop_analyzeMultiFM generated an optimal solution that demonstrates this in hydrodynamic simulations.²⁴

Acknowledgements

This project was completed during the Summer High School Internship program through the University of Rochester's Laboratory for Laser Energetics. This program was run by Dr. R.S. Craxton, and the project was completed with the supervision and aid of Dr. John Marozas. The Laboratory for Laser Energetics is supported by the United States Department of Energy Office of Confinement Fusion.

References

1. T. R. Boehly, D. L. Brown, R. S. Craxton, R. L. Keck, J. P. Knauer, J. H. Kelly, T. J. Kessler, S. A. Kumpman, S. J. Loucks, S. A. Letzring, F. J. Marshall, R. L. McCrory, S. F. B. Morse, W. Seka, J. M. Soures, and C. P. Verdon, "Initial performance results of the OMEGA laser system," *Opt. Commun.* **133**, 495-506 (1997).

2. J. Paisner, J. D. Boyes, S. A. Kumpman, W. H. Lowdermilk, and M. S. Sorem, “National Ignition Facility would boost US industrial competitiveness,” *Laser Focus World* **30**, 75-77 (1994).
3. C. P. Verdon, “High-performance direct-drive capsule designs for the National Ignition Facility,” *Bull. Am. Phys. Soc.* **38**, 2010 (1993).
4. S. E. Bodner, D. G. Colombant, J. H. Gardner, R. H. Lehmborg, S. P. Obenshain, L. Phillips, A. J. Schmitt, J. D. Sethian, R. L. McCrory, W. Seka, C. P. Verdon, J. P. Knauer, B. B. Afeyan, and H. T. Powell, “Direct-drive laser fusion: status and prospects,” *Phys. Plasmas* **5**, 1901–1918 (1998).
5. D. K. Bradley, J. A. Delettrez, and C. P. Verdon, “Measurements of the effect of laser beam smoothing on direct-drive inertial-confinement-fusion capsule implosions,” *Phys. Rev. Lett.* **68**, 2774–2777 (1992).
6. J. Delettrez, D. K. Bradley, and C. P. Verdon, “The role of the Rayleigh–Taylor instability in laser-driven burnthrough experiments,” *Phys. Plasmas* **1**, 2342–2349 (1994).
7. J. D. Kilkenny, S. G. Glendinning, S. W. Haan, B. A. Hammel, J. D. Lindl, D. Munro, B. A. Remington, S. V. Weber, J. P. Knauer, and C. P. Verdon, “A review of the ablative stabilization of the Rayleigh–Taylor instability in regimes relevant to inertial confinement fusion,” *Phys. Plasmas* **1**, 1379–1389 (1994).
8. R. Epstein, “Reduction of time-averaged irradiation speckle nonuniformity in laser-driven plasmas due to target ablation,” *J. Appl. Phys.* **82**, 2123–2139 (1997).
9. V. A. Smalyuk, T. R. Boehly, D. K. Bradley, V. N. Goncharov, J. A. Delettrez, J. P. Knauer, D. D. Meyerhofer, D. Oron, and D. Shvarts, “Saturation of the Rayleigh–Taylor growth of broad-bandwidth laser-imposed nonuniformities in planar targets,” *Phys. Rev. Lett.* **81**,

5342–5345 (1998).

10. F. J. Marshall and G. R. Bennett, “A high-energy x-ray microscope for inertial confinement fusion,” *Rev. Sci. Instrum.* **70**, 617–619 (1999).

11. F. J. Marshall, J. A. Delettrez, V. Yu. Glebov, R. P. J. Town, B. Yaakobi, R. L. Kremens, and M. Cable, “Direct-drive, hollow-shell implosion studies on the 60-beam, UV OMEGA laser system,” *Phys. Plasmas* **7**, 1006–1013 (2000).

12. S. Skupsky, R. W. Short, T. Kessler, R. S. Craxton, S. Letzring, and J. M. Soures, “Improved laser-beam uniformity using the angular dispersion of frequency modulated light,” *J. Appl. Phys.* **66**, 3456–3462 (1989).

13. S. Skupsky and R. S. Craxton, “Irradiation uniformity for high-compression laser-fusion experiments,” *Phys. Plasmas* **6**, 2157–2163 (1999).

14. J. E. Rothenberg, “Comparison of beam-smoothing methods for direct-drive inertial confinement fusion,” *J. Opt. Soc. Am. B* **14**, 1664–1671 (1997).

15. S. P. Regan, J. A. Marozas, J. H. Kelly, T. R. Boehly, W. R. Donaldson, P. A. Jaanimagi, R. L. Keck, T. J. Kessler, D. D. Meyerhofer, W. Seka, S. Skupsky, and V. A. Smalyuk, “Experimental investigation of smoothing by spectral dispersion,” *J. Opt. Soc. Am. B* **17**, 1483–1489 (2000).

16. T. J. Kessler, Y. Lin, J. J. Armstrong, and B. Velazquez, “Phase conversion of lasers with low-loss distributed phase plates,” in *Laser Coherence Control: Technology and Applications*, H. T. Powell and T. J. Kessler, eds., Proc. SPIE 1870, 95–104 (1993).

17. Y. Lin, T. J. Kessler, and G. N. Lawrence, “Design of continuous surface-relief phase plates by surface-based simulated annealing to achieve control of focal-plane irradiance,” *Opt. Lett.* **21**, 1703–1705 (1996).

18. J. W. Goodman, "Statistical properties of laser speckle patterns," in Laser Speckle and Related Phenomena, J. C. Dainty, ed., Vol. 9 of Topics in Applied Physics (Springer-Verlag, 1984), Chap. 2.
19. David Halliday, Robert Resnick and Jearl Walker, Fundamentals of Physics 540-542 (Wiley, 2004).
20. A. Babushkin, R.S. Craxton, S. Oskoui, M.J.Guardalmen, R.L. Kreck, and W. Seka, "Demonstration of the dual-tripler scheme for increased-bandwidth third-harmonic generation," Opt. Lett. **23**, 927-929 (1998)
21. J. W. Goodman, Introduction to Fourier Optics (McGraw-Hill, 1988).
22. R.N. Bracewell, "The Fourier Transform and Its Applications", 1986.
23. John A. Marozas, "Fourier transform-based continuous phase plate design technique: a high-pass phase-plate design as an application for OMEGA and the National Ignition Facility," J. Opt. Soc. Am. **A24**, 74-83 (2007).
24. Advisor, Dr. John Marozas, hydrodynamic simulations of a NIF scale ignition target generated based on 1-D Multi-FM SSD parameters described in this work.
25. A. B. Carlson, Communication Systems: An Introduction to Signals and Noise in Electrical Communication, McGraw- Hill Electrical and Electronic Engineering Series (McGraw-Hill, 1968) pp. 153–154.

Laser Beam Shaping with Optically Patterned Liquid Crystals

Marisa Vargas

Laser Beam Shaping with Optically Patterned Liquid Crystals

Marisa C. Vargas
Webster Thomas High School

Advisors: Christophe Dorrer, Kenneth L. Marshall

University of Rochester
Laboratory for Laser Energetics
Summer High School Research Program 2009

1. Abstract

Current laser beam shapers such as those used in the OMEGA EP laser system for spatial gain precompensation are made of small metal pixels arranged in a pattern to create a beam shaping device. Laser beam shapers can also be made from liquid crystals (LCs). Because of their unique properties, LCs can be oriented so that they transmit, block, or change the phase of incident light when viewed with the aid of polarizers. This orientation is controlled by a polymer alignment layer in close contact with the LC material. If this alignment layer is a linearly photopolymerizable polymer (LPP) and it is irradiated with polarized UV light, the LC molecules will align along the polymer chains. Irradiating the LPP through a mask, followed by rotating the substrate and irradiating again without the mask, allows the orientation of LCs in different regions of the substrate to be controlled. This process can be used to produce pixellated LC devices that function similarly to metal beam shapers, with both a greater variety of optical effects and a substantially higher laser damage threshold. Future applications of these devices could include erasable and rewriteable beam shapers and apodizers.

2. Introduction

In high-energy laser systems, optimal energy extraction below the damage threshold of the optical components is obtained using an incident beam with a uniform intensity distribution, e.g., a high-order super-Gaussian beam. However, the laser beam must pass through an amplifier with spatially varying gain before it becomes final output. When a uniform beam goes through this amplifier, the intensity in various parts of the beam is changed so that it is no longer uniform. A beam shaper is therefore used *before* the beam goes through the amplifier to precompensate for the effect that the amplifier has on the beam. The shaper transmission and the amplifier gain effectively “cancel out” and the final beam is uniform and high intensity, just as desired.

The OMEGA EP laser system currently uses metal laser shaping devices¹. These devices are made with a grid of microscopic pixels. Each pixel either has the metal removed to leave behind fused silica glass or the metal is still there. Even though each pixel is either full transmission or no transmission, these devices can be manipulated so that, on a macroscopic level, a grayscale between full transmission and no transmission may be achieved. For instance, a higher percentage of metal pixels will result in a shaper that locally lets a lower amount of light through, whereas a higher percentage of glass pixels will result in a higher local transmission.

These metal beam shapers have a damage threshold of around 0.2 J/cm^2 (at 1054 nm, 1 ns), which is very low. The photoalignment layer of liquid crystal (LC) devices has a damage threshold of $27\text{-}60 \text{ J/cm}^2$ (at 1054 nm, 1 ns),² which is much higher than that of the metal beam shaper. The only thing limiting the damage threshold of this device is the LC material itself which may range from $9\text{-}18 \text{ J/cm}^2$, depending on the type of LC. This has been proven in OMEGA, where LC waveplates and polarizers are currently used.²

Liquid crystals can be used in the same manner as the metal beam shapers. Liquid crystals can be combined with a polarizer and oriented in two ways so that one way blocks the passage of polarized light and the other way lets the same type of polarized light through (Figure 1). Ideally, they would be oriented in such a way that one of the two orientations would *completely* block that type of polarized light and the other would allow for *full* transmission.

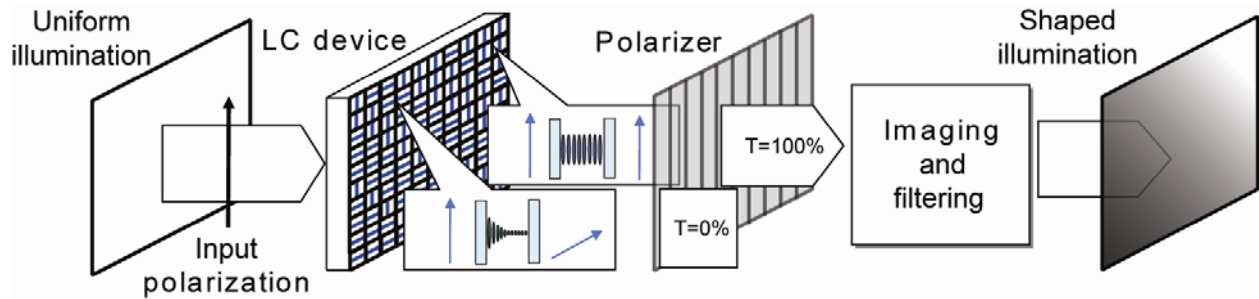


Figure 1: Principle of beam shaping by polarization engineering

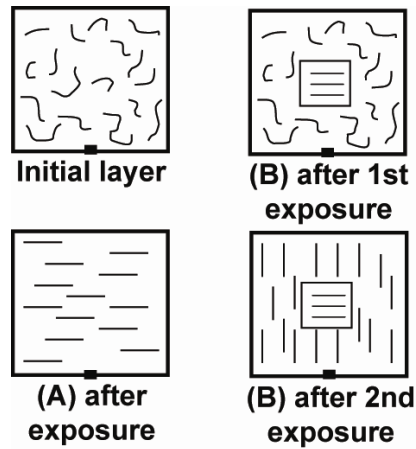


Figure 2: A substrate coated with an LPP before exposure (random orientation); substrate (A) after uniform exposure, substrate (B) after first exposure through a mask with a transparent central square, and substrate (B) after second exposure without mask. The lines on the substrate surfaces indicate orientation of LC molecules.

There are currently two methods used to align LCs on a surface. The first and standard method is mechanical buffing. In this process, LCs are aligned by rubbing the coated substrate with a velvet cloth. However, this is a very dirty process, so a new method for aligning LCs has emerged.³ This “photobuffing” process is a non-contact process, making it cleaner than mechanical buffing which involves a buffing mechanism actually making contact with the substrate, which in turn may impart foreign particles upon the surface.^{4,5} In the process of photobuffing a linearly photopolymerizable polymer (LPP) is deposited on a glass substrate. When the LPP is first laid down on the substrate,

the polymer molecules are in a random order (Figure 2). When exposed to polarized UV light, the long polymer chains line up perpendicular to the direction of the polarization. LCs will align themselves along these polymer chains. This process makes it possible to pattern LC cells. This can be done by irradiating the LPP with a mask and then rotating the substrate and irradiating a second time without a mask (Figure 2). With buffing, patterning is very difficult and rarely produces good results.^{6,7}

3. Experiment

Substrates were cut from glass microscope slides with a glasscutter. Pre-cut fused silica glass substrates were also used. These substrates were wetted with water and scrubbed with 0.05 μm deagglomerated alumina micropolish, rinsed with DI water, and then cleaned in an ultrasonic bath at 69°C for 60 minutes. The substrates were then dried with an air gun and put on a hotplate to dry at 110°C for 10 minutes.

The cleaned substrates were placed on a spin-coater and flooded with pure cyclohexanone. The spin-coater was covered with a glass dish for 2 minutes to prevent evaporation and allow cyclohexanone to equilibrate with the glass substrate and produce a saturated vapor atmosphere. Excess cyclohexanone was spun off at 3000 rpm for 30 seconds to remove it from the surface of the substrate so that the LPP could then be applied. Approximately 0.3 mL of 25% diluted ROLIC ROP-103/2CP (LPP) was then deposited on the substrate through a 0.2 μm PTFE 25 mm hydrophobic syringe filter. After waiting 30 seconds, the substrate was spun at 3000 rpm for 60 seconds. The coated substrates were allowed to air-dry for 10 minutes before being irradiated with UV light.

Photoalignment was accomplished by placing the substrates on a rotatable stage beneath a 500-watt UV lamp at 325 nm. They were placed beneath a “pile of plates” polarizer made of



Figure 3: apparatus used to hold Brewster's angle polarizer

fused silica microscope slides arranged at Brewster's angle of 56.1° (Figure 3). Photopatterning of the alignment layer was accomplished by irradiating one substrate at 0° rotation, with no mask. The second substrate was irradiated first with a patterned mask. Then, the mask was removed, the substrate was rotated 90° , and it was irradiated without any mask. Irradiation times between 1 and 5 minutes were used.

After being irradiated, substrates were baked on a hot plate at 130°C for 10 minutes. A “spacer epoxy” was created by dispersing glass microspheres into EPO-TEK[®] OG154 UV epoxy. To create a cell, a small amount of this “spacer epoxy” was placed on each of the four corners of the first substrate. The second substrate was placed on the first one in such a way that the initial direction of 0° of rotation in each substrate was 180° from that of the other (anti-parallel assembly). The epoxy was cured under a UV lamp for 3 minutes. The assembled cells were filled with nematic E7 on a hotplate at 82°C , sealed with epoxy around the edges, and allowed to cure for 15 to 20 minutes. The completed devices were then cleaned using acetone to remove any excess LC and epoxy from the optical surfaces.

4. Discussion

A contrast ratio (ratio of maximum transmission to minimum transmission) of up to 167:1 has been measured using an infrared laser. A contrast ratio of at least 1000:1 would be

necessary for use in a laser system. A higher contrast ratio could be achieved with improvements in the photolithography technique.

A correlation was found between exposure time and photoalignment resolution. Substrates that were irradiated with UV light for 5 minutes were found to be overexposed. Smaller features became blurred. Pixels that were supposed to be 10 μm

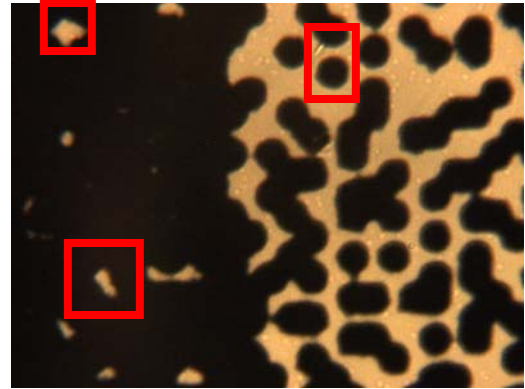
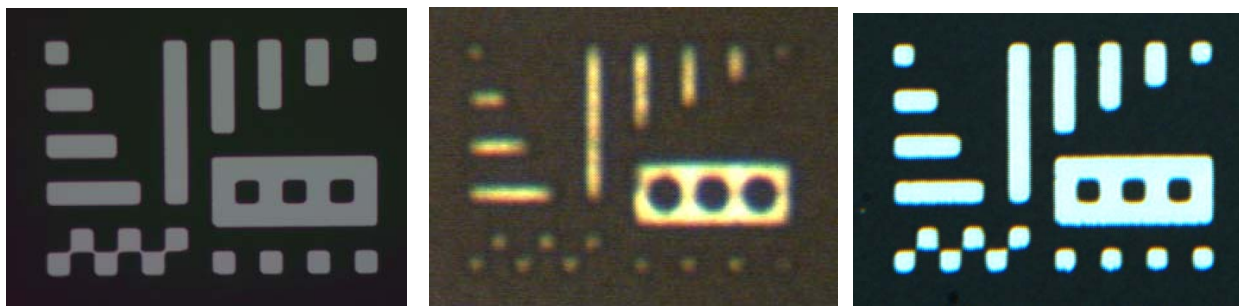


Figure 4: LC devices viewed through crossed polarizers created with a 10 μm pixel mask; all pixels should be the same size squares

became round blobs instead of squares (Figure 4). These pixels overtook regions of the other pixels, making them smaller than 10 μm . The overall transmission was changed. Less light was allowed through because the darker pixels had grown and overtaken the lighter ones. When compared side by side, the mask looked much more uniform and had square pixels. However, when a shorter exposure time of 1 minute was tried, photoalignment resolution greatly increased (Figure 5).



100 μm

Figure 5: metal mask (right), LC devices viewed through crossed polarizers: 5 min exposure time (middle), 1 min exposure time (left)

Regions of reverse twist were found in some cells. Reverse twist is a phenomenon that occurs in twisted nematic cells. If the LC molecules have no preferential twist direction, there is

a 50% chance as to which direction they will twist in. In these cells, domains are formed of the two different twist directions, and lines can be seen on the boundaries of these domains (Figure 6).



Figure 6: domains of reverse twist

This can be corrected by adding an anti-reverse twist agent (a small amount of a cholesteric LC) to the E7. This would give the LC molecules a preferred direction in which to rotate.

5. Conclusions

The purpose of this study was to determine whether photopatterning could be applied to pixels as small as 10 μm . It has been determined that this is indeed possible. With more careful and precise photolithography techniques, a sharper image with better contrast could be produced. This study was able to produce pixels much smaller than ever before using photoalignment.

There are many useful applications of the successful photoalignment of these small-sized pixels. These devices could be used in advanced laser systems such as OMEGA EP, eventually replacing the currently used metal beam shapers. Also, the photoalignment process has proven to be more reliable and hopefully will become more widely used in the near future.

Future experiments should be done to determine the optimal exposure time and exposure intensity. Photopatterning could be attempted on pixels smaller than 10 μm to see what sizes of features can be successfully photopatterned. Also, the possibility of making erasable and rewriteable devices with the use of glassy LCs and azobenzene “command layers” should be explored as a long term goal.

6. Acknowledgements

I thank Dr. R. Stephen Craxton for running the LLE high school program and giving high school students a research opportunity. I also thank my advisors, Christophe Dorrer and Kenneth L. Marshall for giving me instruction and supervision. Additionally, I thank all of the Materials Lab staff and students, especially Cathy Fromen and Zeyu Zhao and Mr. Allen Bolognesi from Precision Optical Imaging for his guidance and helpful comments on photolithography techniques.

References:

- [1] C. Dorrer (private communication)
- [2] K. L. Marshall, J. Gan, G. Mitchell, S. Papernov, A. L. Rigatti, A. W. Schmid, and S. D. Jacobs, "Laser-Damage-Resistant Photoalignment Layers for High-Peak-Power Liquid Crystal Device Applications," in *Liquid Crystals XII*, edited by I. C. Khoo (SPIE, Bellingham, WA, 2008), Vol. 7050, Paper 70500L.
- [3] M. Schadt, H. Seiberle, A. Schuster, and S. M. Kelly. *Jpn. J. Appl. Phys.*, **34**, 3240 (1995).
- [4] N. A. J. M. van Aerle, M. Barmantlo, and R. W. J. Hollering. *J. Appl. Phys.*, **74**, 3111 (1993).
- [5] J. M. Geary, J. W. Goodby, A. R. Kmetz, and J. S. Patel. *J. Appl. Phys.*, **62**, 4100 (1987).
- [6] M. Schadt, H. Seiberle, A. Schuster, and S. M. Kelly. *Jpn. J. Appl. Phys.*, **34**, L764 (1995).
- [7] J. Chen, D. L. Johnson, P. J. Bos, X. Wang, and J. L. West. *Phys. Rev. E.*, **54**, 1599 (1996).

**Bulk Etch Rate Properties of NaOH/Ethanol as a CR-39 Nuclear
Track Detector Etchant**

Kate Walden

**Bulk Etch Rate Properties of NaOH/Ethanol as a
CR-39 Nuclear Track Detector Etchant**

Katherine Walden

Wayne Central High School
Ontario Center, NY 14520

Advisors: Craig Sangster, Michelle Burke

Laboratory for Laser Energetics
University of Rochester
Rochester, NY

Summer 2009

Abstract

The bulk etch rate properties of NaOH/ethanol as a CR-39 nuclear track detector etchant were investigated. It was discovered that NaOH/ethanol is an aggressive bulk etchant that has a bulk etch rate greater than the standard NaOH solution etchant. The bulk etch rate properties of NaOH/ethanol were tested by etching CR-39 (polyallyl diglycol carbonate) in NaOH/ethanol of various temperatures and molarities. It was found that as temperature increased the bulk etch rate increased. However, the molarity of the NaOH/ethanol solution did not have a significant effect on the bulk etch rate. 1.5M NaOH/ethanol at 60°C yielded the fastest bulk etch rate of 27.3 $\mu\text{m/hr}$. The results obtained in this experiment will support a new CR-39 processing method that will include a background noise subtraction technique intended to enhance the accuracy of CR-39 diagnostics.

Introduction

CR-39 nuclear track detectors are used at the Laboratory for Laser Energetics (LLE) to record the products of inertial confinement fusion reactions conducted on the OMEGA laser system¹. As a part of the Magnetic Recoil Spectrometer,² CR-39 detectors are positioned around the OMEGA laser system fuel capsule. When the lasers are fired, intense heat and pressure implode the fuel capsule and charged particles are emitted. These charged particles, which include protons, alpha particles, and deuterium and tritium atoms, bombard and damage the CR-39 detectors. This results in latent tracks of damage typically ranging in diameter from 3 nm to 10 nm,¹ too small to be visible with an optical microscope.

The latent tracks are made visible by etching the CR-39 in a 6N NaOH at 80°C for 6 hours. During the etching, conical pits are created along the particle tracks because the damaged plastic along the track has a higher etch rate than the undamaged (bulk) plastic.¹ These pits range from 10 μm to 20 μm in diameter, large enough to be visible under an optical microscope. Etched CR-39 detectors are scanned under an optical microscope using the Charged Particle Spectroscopy (CPS) program developed by scientists at MIT. The CPS program uses the pit eccentricity, diameter and resulting contrast to calculate an energy spectrum of the particles ejected during the implosion. This information is then used to calculate the areal density³ of the target and to quantify the success of the reaction.

Unfortunately, data collected from CR-39 detectors can be compromised by defects (background noise) found in the bulk of the plastic created during the CR-39 manufacturing process. During the etching process, these defects are revealed as pits with

diameters comparable to those created along particle tracks (valid data pits) as shown in Figure 1. The CPS program cannot differentiate between defect pits and valid pits which can result in inaccurate data collection. A new etching process is being investigated at LLE and MIT that would enable scientists to identify background noise from data.

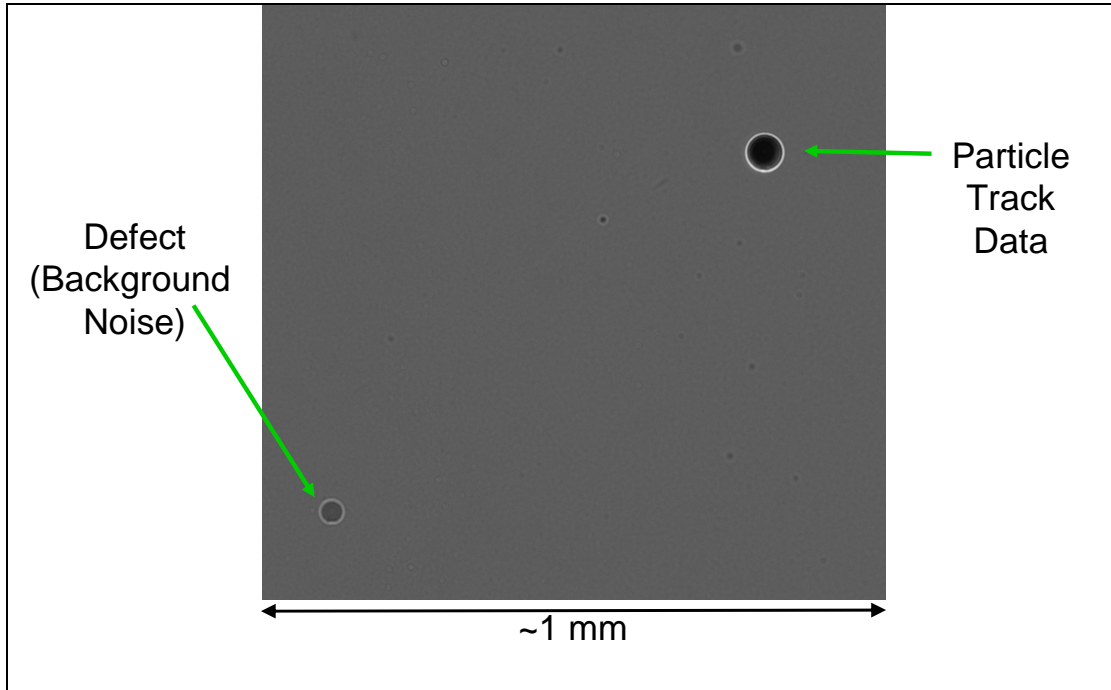


Figure 1: Image of CR-39 under an optical microscope after standard etching. The defect pit appears similar to the valid pit and would be identified as a valid pit by the CPS program.

Background Noise Reduction Technique

This process uses an accelerated, more aggressive etchant to remove some of the bulk material, and noise within it, while preserving the data tracks. This process begins with a standard etch of CR-39 in 6N NaOH at 80°C for 6 hours. The CR-39 detector is then scanned using the CPS program and an image of the CR-39 surface is recorded.

Next, the CR-39 is etched in NaOH/ethanol. NaOH/ethanol removes a large amount of bulk and a relatively small amount of particle track.⁴ Defects created during the manufacturing process are significantly shallower than particle tracks⁵ and are located intermittently throughout the CR-39 bulk. Therefore, the defect pits established after the initial standard etch are removed during the NaOH/ethanol etch, but the valid data track remains intact.

The CR-39 detector is etched again in 6N NaOH at 80°C for 6 hours to reestablish valid pit shape, and scanned by the CPS program. During this final NaOH etch, defect pits are also established, but can be differentiated from valid data because defect pits appear in different locations on the initial and final scan while valid pits appear in the same location.

For this new process to be viable, the bulk etch rate properties of NaOH/ethanol must be known. A substantial amount of bulk must be removed during the NaOH/ethanol etch to eliminate defects seen in the first scan. However, if too much CR-39 is removed, particle tracks are eliminated completely and the valid data are lost. In this experiment, the bulk etch rate of various NaOH/ethanol solutions were studied in an attempt to find a NaOH/ethanol solution with an efficient and reliable bulk etch rate.

Methods and Materials

In the present experiment, the bulk etch rate of CR-39 was tested in NaOH/ethanol solutions ranging from 1M to 4M at temperatures of 50°C, 55°C, and 60°C. 31 CR-39 detectors were tested, all of which had not been exposed to radioactive particles.

NaOH/ethanol solutions were prepared in a beaker using 10M NaOH and distilled water. Beakers were placed in a water bath to acquire and maintain the desired temperature, and covered to prevent evaporation.

Prior to etching, the thickness of each CR-39 detector was measured in five locations using a micrometer. CR-39 detectors were placed in NaOH/ethanol, and measured every 30 minutes for 3 hours. Prior to measurement, CR-39 detectors were rinsed with distilled water and dried. Before detectors were returned to the NaOH/ethanol, the solution was stirred.

The five measurements taken at each 30 minute interval were averaged to find the average thickness of the CR-39 detector at each interval. For each interval, the average thickness was subtracted from the initial average thickness to find the amount of CR-39 removed in millimeters. These values were plotted on a graph with x-values representing time in hours and y-values representing the amount of CR-39 removed in millimeters. A line of best fit was determined for the data (see Figure 2).

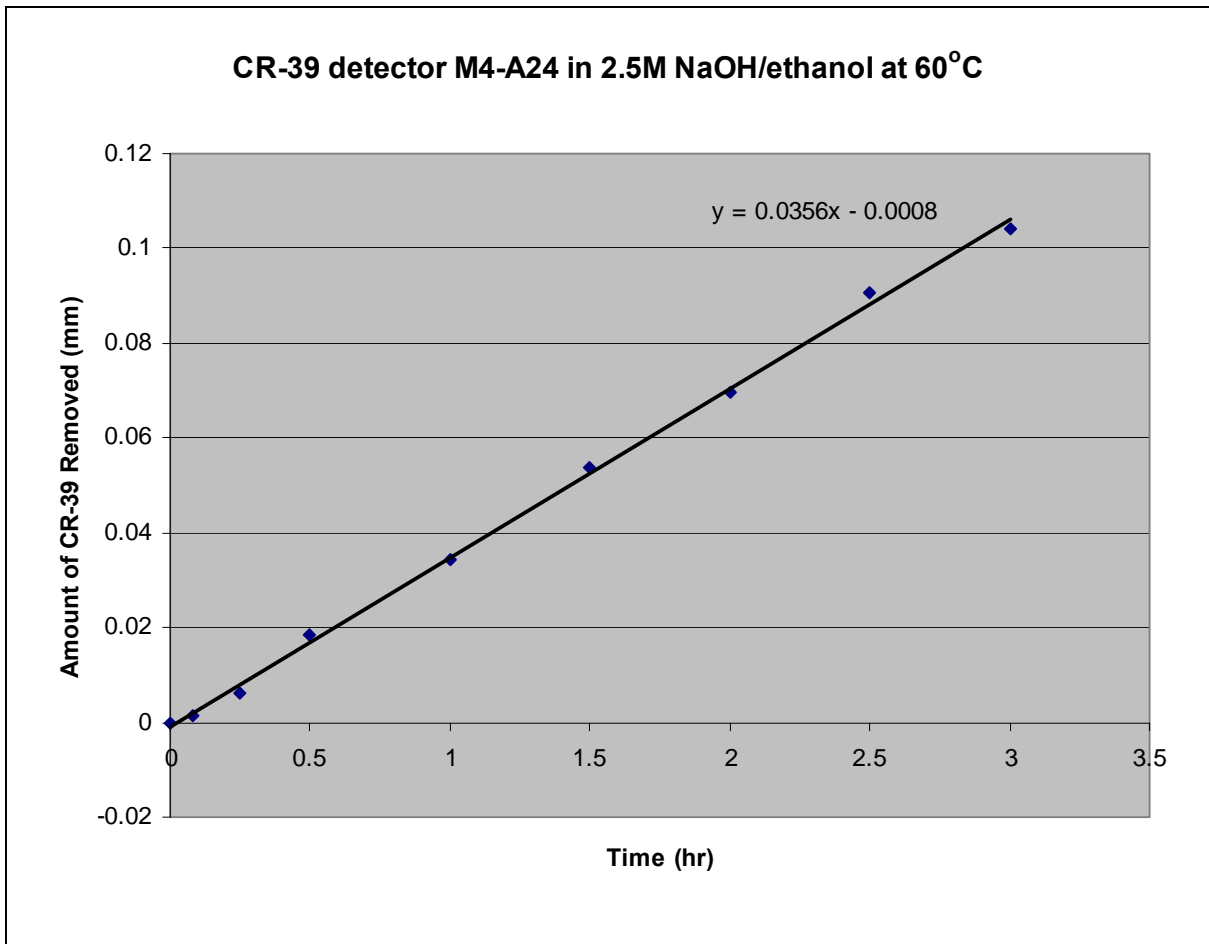


Figure 2: The amount of bulk removed from CR-39 detector M4-A24 in 2.5M NaOH/ethanol at 60°C over time. X-values represent time in hours. Y-values represent the amount of bulk removed in hours. A line of best fit was determined and its equation is shown.

The slope of the line of best fit was entered into the following equation

$$\frac{1000m}{2} = V_b$$

where m represents the slope of the line of best fit and V_b represents the bulk etch rate in $\mu\text{m/hr}$. The value m was multiplied by 1000 to convert from millimeters to μm and then divided by 2 to account for measuring both sides of the CR-39.

Results

1.5M NaOH/ethanol at 60°C yielded the fastest bulk etch rate of 27.3 $\mu\text{m/hr}$. As the temperature of NaOH/ethanol increased the bulk etch rate increased. Change in molarity had a greater effect on the bulk etch rate as temperature increased, but there is no apparent relationship between molarity and bulk etch rate for all temperatures. The bulk etch rate of NaOH/ethanol at 50°C was consistent despite changes in molarity. These results are summarized in Figure 3.

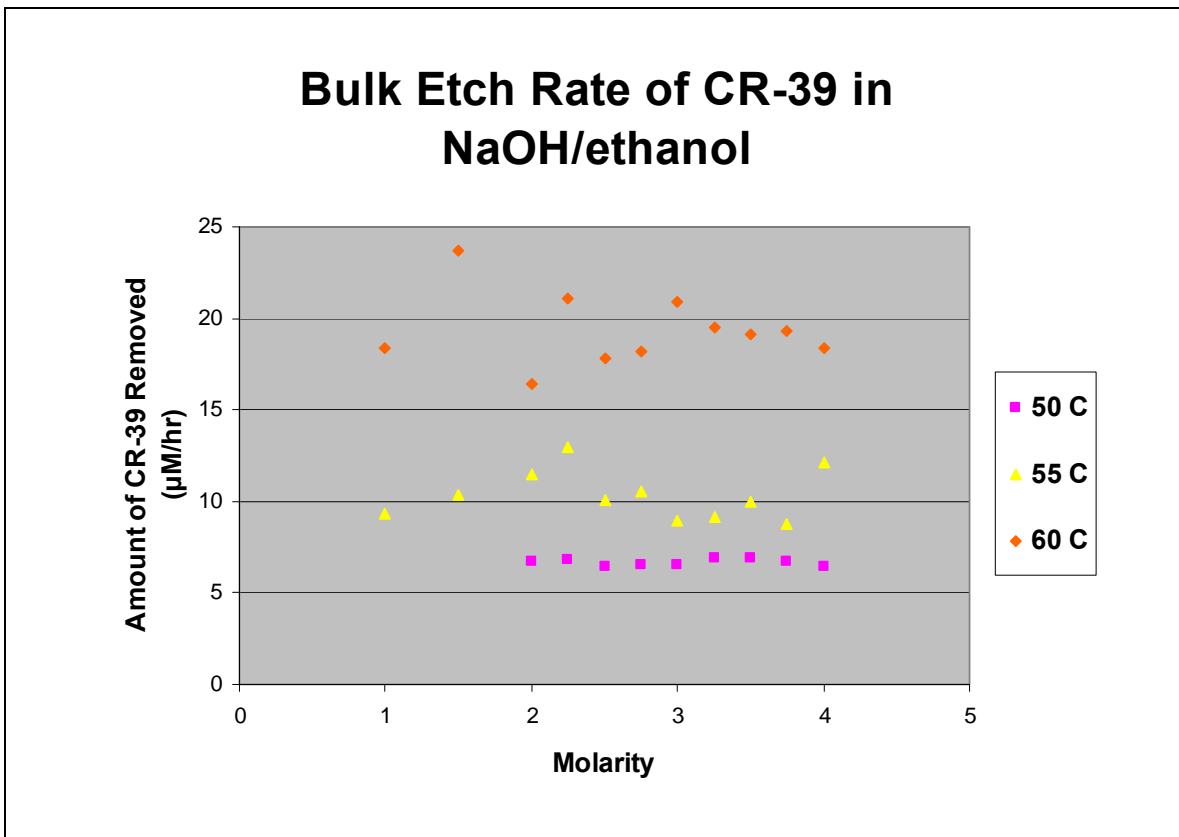


Figure 3: The bulk etch rate of CR-39 in NaOH/ethanol solutions. Values on the x-axis represent NaOH/ethanol solution molarity. Values on the y-axis represent the bulk etch rate in $\mu\text{m/hr}$. Each data point represents a CR-39 detector etched in NaOH/ethanol at the indicated temperature and molarity.

Discussion

The drastic variation in bulk etch rate at higher temperatures is suspected to be caused by sodium carbonate precipitate formed during etching.⁶ As temperature increased more precipitate formed, which may have insulated the CR-39 surface and hindered etching.⁴ At 55°C, the bulk etch rate increased with molarity from 1M to 2.25M then began to decrease. This finding correlates with data collected by K.F. Chan et al. who reported the bulk etch rate of CR-39 in 55°C NaOH/ethanol to increase with the molarity of NaOH/ethanol, reach a maximum at ~2.5N, and start to drop beyond 3N.⁴

The results obtained in this experiment demonstrate that the ideal NaOH/ethanol temperature for the proposed processing method is 50°C because it produced the most consistent bulk etch rates. This discovery of NaOH/ethanol at 50°C as a reliable and efficient bulk etchant supports the viability of the proposed background noise subtraction technique that will enhance the accuracy of CR-39 diagnostics on the OMEGA laser system.

Acknowledgements

I would like to thank my advisors Craig Sangster and Michelle Burke, and supervisors Robert Boni and Daniel Casey for their invaluable guidance, insight, and support. Also, I would like to thank Dr. Stephen Craxton, Program Director of the Laboratory for Laser Energetics' High School Summer Research Program, for providing this exceptional research opportunity.

References

- ¹ Hicks, Damien G. (1999) Charged Particle Spectroscopy: A New Window on Inertial Confinement Fusion. PhD thesis. Massachusetts Institute of Technology
- ² Frenje J.A., et al. “First measurements of the absolute neutron spectrum using the magnetic recoil spectrometer at OMEGA (invited).” *Rev. Sci. Instrum.* 79, 10E502 (2008).
- ³ Séguin, F.H., et al. “Spectrometry of Charged Particles from Inertial-Confinement-Fusion Plasmas.” *Rev. Sci. Instrum.* 74, 975 (2003).
- ⁴ K.F. Chan et al. “Bulk and track etch properties of CR-39 SSNTD etched in NaOH/ethanol.” *Nucl. Instr. and Meth. in Phys. Res. B* 263 (2007) 284–289
- ⁵ R. Mishra et al. “A better understanding of the background of CR-39 detectors.” *Radiation Measurements*, 40 (2-6), pp. 325-328. (2005)
- ⁶ K.C.C. Tse et al. “Comparative studies of etching mechanisms of CR-39 in NaOH/H₂O and NaOH/ethanol.” *Nucl. Instr. and Meth. in Phys. Res. B* 263 (2007) 300–305

Computational Modeling of Optically Switchable Azobenzenes

Victor Wang

Computational Modeling of Optically Switchable Azobenzenes

Victor Wang

Webster Thomas High School
Webster, NY

Advisor: Kenneth L. Marshall

Laboratory for Laser Energetics
University of Rochester
Rochester, NY

November 2009

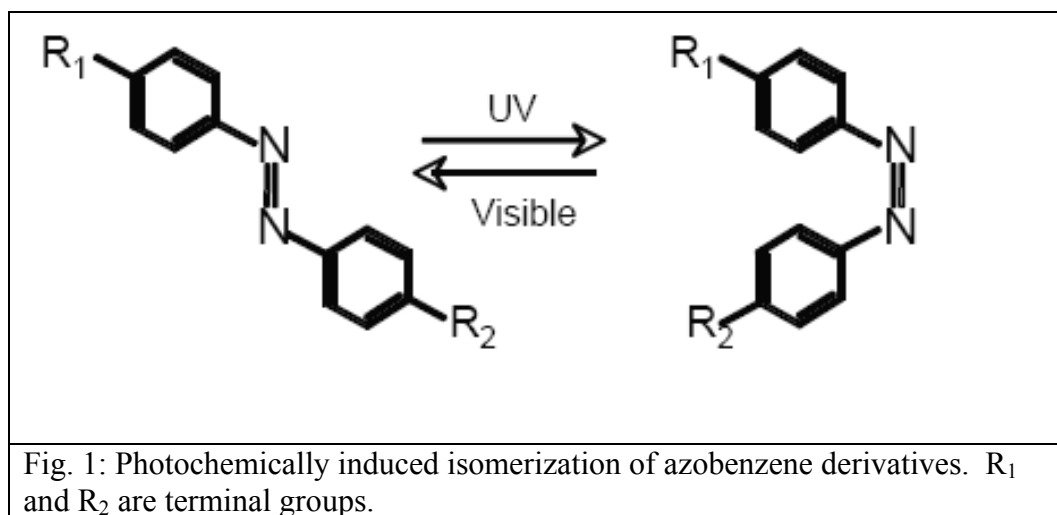
Abstract

Azobenzenes have a unique ability to undergo reversible isomerization between two geometrical isomer forms (the straight *trans* and the bent *cis*) when irradiated with the correct wavelength of UV or visible light. These systems are of interest because of their numerous potential applications as reversible photoswitchable absorbers. The azobenzenes can also be used as terminal groups in nickel dithiolene metal complexes, which have applications as photoswitchable absorbers in the near infrared region. To reduce the need to synthesize a large number of materials in order to establish structure-property relationships, computational chemistry was used to model the absorption spectra of these materials as a function of molecular structure. Time-dependent density functional theory (TDDFT) was used in this study to model the absorption spectra of azobenzene derivatives, and the process was refined to produce results closer to observed spectra than previous research. An alternative method, Zerner's intermediate neglect of differential overlap (ZINDO), was also investigated and the results were compared with those obtained with TDDFT. The TDDFT approach was found to give consistently better agreement with experimental data than the semiempirical ZINDO approach.

Introduction

Azobenzenes are noted for their ability to undergo photochemically induced isomerization. When irradiated with the correct wavelength of UV light, the rod-like *trans* isomer transforms into the bent *cis* isomer. Likewise, when irradiated with the correct wavelength of visible light, the bent *cis* isomer transforms into the rod-like *trans* isomer (Figure 1). Because of this rapid and reversible isomerization between *cis*-azobenzene and *trans*-azobenzene, azobenzene derivatives can change the optical

properties of liquid crystal “host” systems (e.g., birefringence and dichroism) when they are added to these materials as dye dopants, or “guests”.¹ Also, as the distance between the para carbon atoms in azobenzene is 9.0 Å in the trans isomer and only 5.5 Å in the cis isomer, physical properties can be changed.² Because of these chemical and physical changes, azobenzene derivatives have numerous applications in liquid crystal systems and digital data storage.^{2,3}



Nickel dithiolenes are noted for their intense absorption over a wide range of near-IR wavelengths between 600 nm and 1600 nm. The nickel dithiolenes dye consists of a zerovalent planar core with dithiolenes rings surrounding a nickel atom (Figure 2). Because of the zerovalent core, nickel dithiolenes dyes have high solubility in nonpolar solvents such as liquid crystal hosts. As some metal dithiolenes have inherent liquid crystal phases, they are easily dissolvable in liquid crystal hosts in relatively large quantities of up to 10 wt%.¹⁶

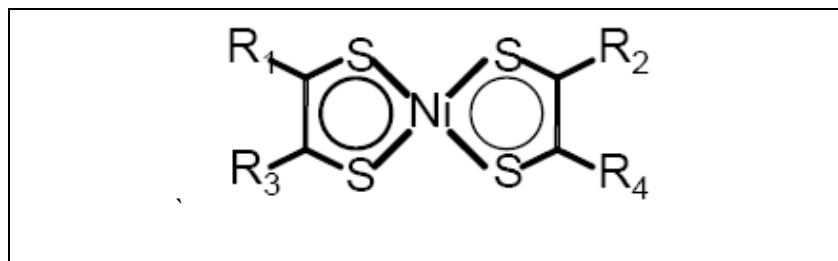


Fig. 2: Nickel dithiolene metal complex. R_1 - R_4 are terminal groups.

Due to these properties, nickel dithiolene metal complexes have numerous applications. For example, they are useful as photodetectors in fiber-optic systems at wavelengths of 1300 nm and 1550 nm, as Q-switching saturable absorbers in IR lasers at wavelengths between 950 nm and 1100 nm, and as IR sensor protection for the military. When the terminal groups are substituted with azobenzene derivatives, nickel dithiolenes are capable of producing large photochemically-induced changes in the optical properties of liquid crystal hosts when added as a dopant.⁴

However, nickel dithiolene metal complexes are expensive and time-intensive to produce, and as such, a trial-and-error procedure is extremely inefficient. Large numbers of these materials would need to be produced to establish structure-property relationships. Computational chemistry can predict these properties with minimal sacrifice in accuracy and immense savings in time and expense. Rather than synthesize large numbers of molecules to establish structure-property relationships, computational chemistry allows only the most promising molecules to be synthesized, thereby saving resources.

In this study, computational chemistry methods were refined to produce more accurate results than could be obtained previously. Two computational methods were used to predict the spectral properties of azobenzenes: time-dependent density functional theory (TDDFT) and Zerner's intermediate neglect of differential overlap (ZINDO), a

semi-empirical method. The TDDFT approach was found to give consistently more accurate results than ZINDO. The density functional theory (DFT) method B3LYP was likewise found to be consistently more accurate than the DFT method PME1PME when used with TDDFT. Several azobenzene derivatives were modeled more accurately than in previous research, but when TDDFT was applied to larger molecules, computational time increased. When TDDFT was applied to nickel dithiolene metal complexes substituted with azobenzene terminal groups, small basis sets sacrificed too much accuracy, while large basis sets caused free energy convergence errors, making it impossible to map the electron distribution.

2. Previous Research

Computational chemistry has previously been used to predict the properties of other molecules. The methods for excited state computation can be separated into three general categories: (1) ab initio methods such as Hartree-Fock and single configuration interaction (CIS); (2) semi-empirical methods such as ZINDO, and (3) DFT and TDDFT.

Ab initio methods do not use any empirical data and base calculations entirely on physical principles.⁵ As such, they are generally the most accurate methods, but have the highest computational cost, which grows exponentially with increasing complexity of molecular structure. The Hartree-Fock method is the most basic ab initio method. Electron orbitals are expressed as one-electron functions, and the multi-electron calculation is based on the sum of the single-electron functions. The Hartree-Fock method does not account for Coulombic electron repulsion but instead includes the mean field in the calculation. Because of this, the Hartree-Fock method can only give energy approximations greater than or equal to energy approximations made by the ground state

wave function.⁶ Post-Hartree-Fock ab initio methods start with the Hartree-Fock method and then proceed to correct for the Coulombic electron repulsion.

Semi-empirical methods use some empirical data to estimate unknown parameters, thereby decreasing computational cost and accuracy. Semi-empirical methods are based on Hartree-Fock methods, but some parameters are approximated or completely omitted. To correct for these approximations, semi-empirical methods fit results to best agree with empirical data or results obtained from ab initio calculations. Semi-empirical methods such as ZINDO are limited in accuracy by how similar the molecule at hand is to the molecule in the database used to parameterize the results. The ZINDO method is an extension of Intermediate Neglect of Differential Overlap (INDO) as it can cover a wider range on the periodic table.⁷

Density functional theory is a recent method that uses a 3-D electron density function rather than a many-electron wave function (Figure 3).⁸ The TDDFT modification maps the development of a perturbed system over time with density functions. The molecular system is perturbed with an impulse potential containing all frequencies, and the maximum absorption wavelengths can subsequently be computed.

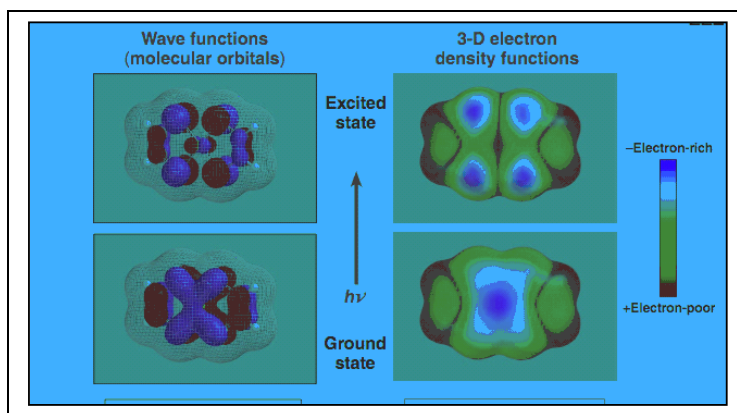


Fig. 3: Wave functions vs. density functions. Density functions require a significantly lower computational cost.

A previous study used TDDFT to predict the absorption spectra of azobenzenes, and the results were relatively accurate, with a mean absolute error of 47.1 nm.⁹ In this study we investigated alternative computational methods and refined the process used in earlier work to obtain more accurate results.

3. Methodology

All TDDFT and ground state energy calculations performed in this study used the Gaussian03 program¹⁰, but other programs were also used in the process. This process is detailed in Figure 4.

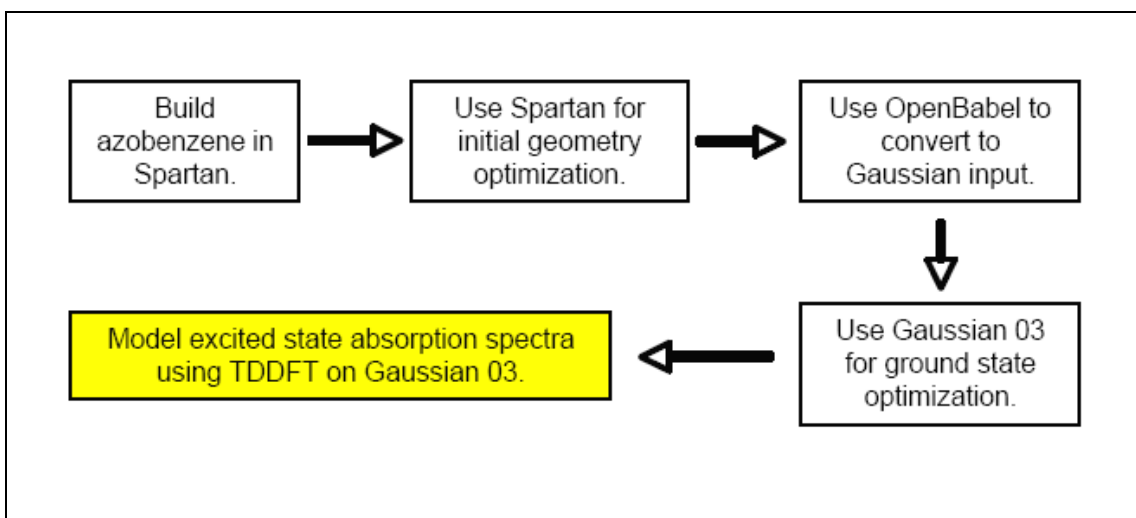


Fig. 4: Methodology used to predict excited state absorption spectra.

Spartan is a computational chemistry software package that allows for the visualization of molecules and initial geometry optimization. Spartan generates approximate Cartesian coordinates that can be converted to a Gaussian input file¹¹ using OpenBabel, a chemical language translator. The appropriate input is added to the newly converted input file, and the Gaussian03 program performs a more accurate geometry

optimization using DFT. Finally, these new coordinates are used as input for TDDFT in Gaussian03, which models the excited state absorption spectra.

In deciding which basis set should be used, previous studies were referenced.⁴ A previous study by Marshall *et al.* determined that the 6-311G(3d, 2p) basis set was the most appropriate for the ground state geometry optimization of nickel dithiolenes, and as such, this study used the same basis set for the ground state geometry optimization of azobenzenes. For modeling excited-state absorption spectra, the same basis set was used in this study as in a previous study⁹ for purposes of comparison. This is the 6-311+G(3d, 2p) basis set, in which the “+” notation indicates the addition of single diffuse functions to increase accuracy in modeling electrons farther from the nuclei of nonhydrogen atoms.

4. Selecting a DFT Method

There are three broad categories of standalone DFT methods, which make use of combinations of exchange and correlation functionals: (1) exchange-only; (2) pure; and (3) hybrid functionals. Exchange-only and pure functionals are based solely on Hartree-Fock exchange and DFT exchange-correlation, respectively. Hybrid functionals, however, are mixtures of Hartree-Fock exchange and DFT exchange-correlation. Two different hybrid DFT methods were considered for this study. PBE1PBE uses 25% electron-exchange and 75% electron-correlation weighting. PBE1PBE was used in a previous study to predict absorption maxima with a mean deviation of 47.1 nm from accepted values. An alternative DFT method, B3LYP, was considered. B3LYP uses the LYP expression for non-local correlation and the VWN functional III for local correlation.¹⁰ Five azobenzenes were selected based on a study conducted by Rau, Iacobescu and Meltzer, each of which produced three absorption maxima λ_{\max} ¹². The

calculated absorption maxima in this study, which used B3LYP, and in a previous study, which used PBE1PBE, are shown in Table 1 together with the experimental values and the molecular structures used.

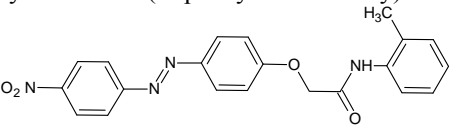
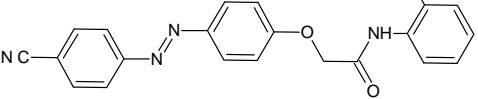
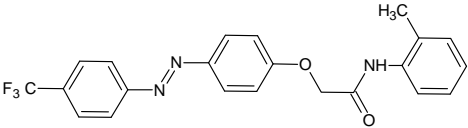
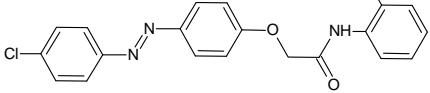
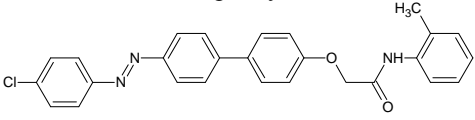
No.	Molecule	Experimental λ_{\max} (nm) ¹²	Calculated λ_{\max} (nm) (B3LYP)	Calculated λ_{\max} (nm) (PBE1PBE) ⁹
1	6''-methyl-4'-nitro-4-(N-phenylacetamidoxy)-azobenzene 	249	380	336
		369	427	383
		422	448	494
2	6''-methyl-4'-cyano-4-(N-phenylacetamidoxy)-azobenzene 	249	346	316
		353	362	368
		414	420	483
3	6''-methyl-4'-trifluoromethyl-4-(N-phenylacetamidoxy)-azobenzene 	286	341	303
		349	352	356
		406	417	475
4	6''-methyl-4'-chloro-4-(N-phenylacetamidoxy)-azobenzene 	247	333	294
		348	342	358
		402	414	465
5	4-(o-methyl-N-phenylacetamidoxy)-4'-[p-methyl-phenylazo] biphenyl 	262	313	312
		332	347	388
		412	415	476

Table 1: Wavelengths of three absorbance maxima for each of the five azobenzene derivatives modeled.

It is seen from Table 1 that the B3LYP DFT method is substantially more accurate than PBE1PBE for the longest wavelength and more accurate at the middle wavelength in four out of the five cases. At the shortest wavelength PBE1PBE comes close to the experimental value, but the errors are large in both models. Since the two longer-wavelength maxima are of greater practical interest, all further calculations in this study used B3LYP as the DFT method with TDDFT. Once sufficiently accurate results were obtained, other computational methods could be investigated, as could modeling nickel dithiolene dyes with azobenzenes substituted as terminal groups.

5. TDDFT and ZINDO

Two methods for determining the maximum absorption wavelengths were investigated in this study. As all experimental absorption maxima were for azobenzene derivatives in solution, the PCM model was used to account for solvent effects in TDDFT calculations. The PCM model separates the calculation into two parts: a solvent part and a solute part.¹³ Because this correction was incompatible with ZINDO as implemented in Gaussian 03, it was left out of ZINDO calculations. Table 2 shows the absorption maxima of ten azobenzenes predicted with both ZINDO and TDDFT. Overall, the TDDFT method was found to be consistently more accurate, being closer to experiment in seven out of the ten cases, while ZINDO gave better results for compounds 5, 9, and 10. For this comparison, only the absolute absorption maxima were considered, as experimental data for local maxima was not known for all molecules. However, experimental data of the absolute absorption maxima existed from a number of sources.^{12,14,15}

No	Structure	Accepted λ_{\max} (nm) ^{12,14,15}	Calculated λ_{\max} (nm) (TDDFT)	Calculated λ_{\max} (nm) (ZINDO)
1		369	427	446
2		353	362	338
3		349	352	341
4		348	342	333
5		332	347	336
6		415	467	311
7		468	484	359
8		486	464	450
9		342	416	341
10		420	448	445

Table 2: Absorbance maxima of ten azobenzene derivatives. Overall, TDDFT consistently predicts absorption maxima more accurately than ZINDO. (The first five structures are the same as in Table 1)

6. Free Energy Convergence Problems

While the main purpose of this study was to improve the accuracy to which azobenzenes could be modeled, nickel dithiolene metal complexes substituted with azobenzene terminal groups were nonetheless further investigated. However these complexes were never successfully modeled to any degree of accuracy. Calculations took several days to complete for each molecule, and the free energy looped infinitely and failed to converge. Because larger basis sets increase the computational cost and lead to convergence failures, smaller basis sets were used. Even with the smallest basis sets, calculations rarely converged, and results were never accurate.

7. Discussion/Conclusions

The TDDFT method can accurately, efficiently, and cost-effectively predict the spectral properties of azobenzene derivatives. TDDFT predictions with the B3LYP DFT method are more accurate than those with the PBE1PBE DFT method, and TDDFT can predict absorption maxima more accurately than ZINDO, with minimal computational cost. However, free energy convergence problems impeded the modeling of nickel dithiolene metal complexes substituted with azobenzene derivatives. Future research would include modeling these complexes using the Gaussian09 program. Also, Gaussian09 and other computational chemistry packages could be investigated for ZINDO's compatibility with the PCM correction for modeling molecules in solution. Thus, ZINDO could also be explored as a possible, more cost-efficient alternative to TDDFT in nickel dithiolene metal complexes.

\

8. Acknowledgements

This project was made possible by the support of several individuals. First, I would like to thank Mr. Kenneth L. Marshall for serving as my advisor and providing me with all the necessary resources. Next, I would like to thank the Laboratory for Laser Energetics for supporting the high school research program, as well as Dr. Stephen Craxton for selecting me for this opportunity. Tony Brancato and Eric Glowacki were especially helpful in the technical and conceptual aspects of this project, respectively. Lastly, I would like to thank all members of the materials lab at the Laboratory for Laser Energetics as well as my fellow interns for supporting me throughout the project.

References

1. Delaire, Jacques; Nakatani, Keitaro. *Chem. Rev.* 2000, 100, 1817-1845.
2. G.J. Ashwell, *Nature* 347 (1990) 617.
3. A. Kumano, O. Nimow, T. Kajiyama, M. Takayanagi, T. Kunitake, K. Kano, *Polym. J.* 16 (1984) 461.
4. Marshall, K. L. *et al*; "Using Time-Dependent Density Functional Theory (TDDFT) in the Design and Development of Near-IR Dopants for Liquid Crystal Device Applications"; *Proc. of SPIE* 2007 Vol. 6554, pp 65540F1-65540F13.
5. Levine, Ira N. (1991). *Quantum Chemistry*. Englewood Cliffs, New Jersey: Prentice Hall. pp. 455–544.
6. Cramer, Christopher J. (2002). *Essentials of Computational Chemistry*. Chichester: John Wiley & Sons, Ltd.. pp. 153–189.

7. M.C. Zerner; "ZINDO: A Semiempirical Quantum Chemistry Program", Quantum Theory Project; University of Florida, Gainesville, FL, 1996.
8. Hehre, W. J. *Ab Initio Molecular Orbital Theory* 1986 (Wiley, New York).
9. Wang, Ernest, "Computational Modeling of Spectral Properties of Azobenzene Derivatives"; LLE Summer High School Research Program, 2007.
10. Frisch, M.J. *et al.*, Gaussian 03, Gaussian, Inc., Pittsburgh, PA, 2004.
11. SPARTAN '04, Wavefunction, Inc., 18401 Von Karman Ave., #370, Irvine, CA 92715, 2003.
12. Rau, Gabriela; Iacobescu, Gabriela; Meltzer, Viorica. *Revue Roumaine de Chimie*. 2005, 50(2), 119-124.
13. Arnovilli, C.; Barone, V.; Carnmi, R.; Cancks, E.; Cossi, M.; Mennucci, B.; Pomelli, C. S.; Tomasi, J. *Adv. Quantum Chem.* 1998,32,227.
14. J Zhejiang Univ Sci B. 2005 June; 6(6): 584–589.
15. Eric Glowacki, private communication.
16. Marshall, K.L.; Painter, G.; Lotito, K; Noto, A.G.; Chang, P. *Molecular Crystals and Liquid Crystals*. 2006 Vol. 454, pp 47/449-79/481.

UV Probe Beam for Plasma Characterization and Channeling Experiments

Paul Watrobski

UV Probe Beam for Plasma Characterization and Channeling Experiments

Paul Watrobski

Penfield High School
Rochester, NY

Advisor: Dr. Wolfgang Theobald

Laboratory for Laser Energetics
University of Rochester
Rochester, NY
August 2009

Abstract

The OMEGA EP laser system will be used to study long-scale-length plasmas and the channeling of an ultra-intense infrared short-pulse beam through these plasmas. One of the primary plasma diagnostics will be grid image refractometry (GIR).¹ In GIR a collimated UV beam illuminates a grid that breaks the beam into a two-dimensional array of probe-beam ray bundles. These rays pass through a plasma, where they are affected by refraction. Analyzing the images of the grid then allows one to determine the plasma density. In the standard GIR approach the grid has a large stand-off distance from the plasma and the grid is imaged into the plasma. A new approach is studied here in which the grid is in close proximity to the plasma. The goal of this project was to study the basic optical properties of this GIR system, including the diffraction effects from the grid but ignoring the refraction due to the plasma. A PV-Wave program was written based on a simple ray-trace algorithm that included diffraction from the grid. The image quality was studied for various object planes and grid periods. An optimal position for the grid was found that resulted in crisp images, showing that this approach is viable.

I. Introduction

i. Laboratory for Laser Energetics (LLE)

The primary mission of the University of Rochester's Laboratory for Laser Energetics (LLE) is to study the physics of direct drive inertial confinement fusion (ICF). The controlled fusion of deuterium and tritium holds great promise for solving the world's energy problem. The National Ignition Facility (NIF) at Lawrence Livermore National Laboratory, which is largest and most powerful laser in the world, will make a credible ignition attempt by using the indirect drive concept. The OMEGA Laser Facility at LLE is a cornerstone in the US fusion program and plays a major role in the national effort for achieving ignition. With ignition at the NIF on the horizon, scientists work on advanced inertial fusion energy concepts that might be developed into future reactor designs. The laser requirements are relaxed and higher gains than in indirect drive might be possible.

One concept is the fast ignition (FI) concept² that uses a conventional high-energy laser facility

to compress the fuel capsule and then achieve ignition through a high energy particle beam generated by a separate, high intensity short-pulse laser. One of the primary research objectives of the recently built high intensity OMEGA EP laser facility is to investigate advanced ignition schemes such as fast ignition. The main issue in FI is to bring the particles as close as possible to the compressed core without losing too much of their energy. There are currently two viable FI concepts; one considers targets with a hollow re-entrant cone that keeps a clear path for a high intensity laser so that the particles are generated as close as possible to the dense core. The other is the channeling concept. Channeling employs two co-propagating short-pulse beams; the first pulse is used to push the plasma away and drill a channel close to the core so that the trailing second pulse is guided through the channel without significant energy loss. The second short pulse then produces the energetic particles that will ignite the target.

Channeling experiments are planned on the OMEGA EP laser by using long-pulse UV lasers to generate an extended plasma atmosphere and then send an ultra-intense infrared short-pulse beam through these plasmas. It is important to have optical diagnostics to characterize the pre-formed plasma and to measure the channel. The measurements will be compared to simulation predictions of the plasma density and the formation of the channel. One of the primary plasma diagnostics that will be used in these experiments is grid image refractometry (GIR)¹ with an ultraviolet probe laser with a wavelength of 263 nm.

ii. Grid image refractometry (GIR)

GIR is a technique for determining the two-dimensional density profiles of long scale-length laser-produced plasmas. Fusion plasmas are of the size of up to several millimeters with a density scale-length of several hundreds of micrometers. The density scale-length is defined as $n/(dn/dx)$ at a certain x -position in a density profile $n(x)$. The GIR concept employs a collimated UV beam that illuminates a grid so that the beam is split into a two-dimensional array of probe-beam ray bundles. These rays pass through the plasma, where they are refracted. The term “refractometry” is used to indicate that the refractive index of an optical medium is inferred from the refraction angles of this set of probe rays. In the previous method of GIR the grid had a large stand-off distance from the plasma

and was imaged into the plasma. A new approach is studied in this project in which the grid is placed in close proximity to the plasma. Figure 1 shows a schematic of the experimental setup.

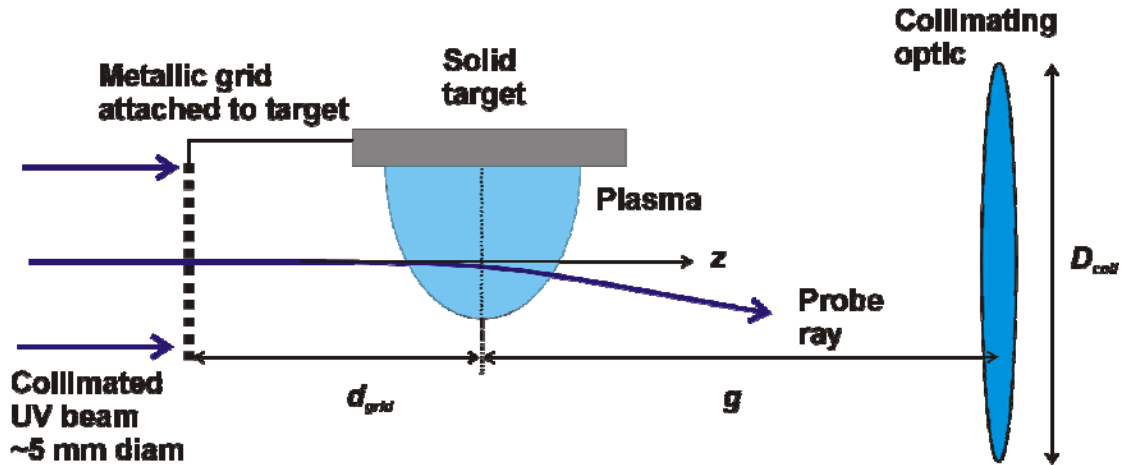


Figure 1: Schematic setup of a metallic grid placed in the collimated UV beam close to the target for GIR application. Typical parameters are: $d_{grid} \approx 1$ cm, $D_{coll} \approx 10$ cm, $g \approx 40$ cm, and a grid period of $P = 25$ μ m.

A collimated laser beam illuminates the grid which splits the beam into an array of pencil beams that pass through a plasma object. The refractive index, $\mu(x)$, inside the plasma varies according to the local electron density, and the amount of refraction that each bundle experiences depends on the gradient of the refractive index $d\mu/dx$. Different planes in the plasma must be imaged onto a detector. The apparent position of each probe ray must be measured for at least two object planes; in the current project three object planes separated by a distance of ~ 1 mm were chosen. The UV probe light is split up into three beams after transmission through the plasma. Each one images a different object plane onto a CCD camera. The deflection angles (in the x- and y-directions) are obtained by the difference of the associated grid elements in two object planes divided by the distance between those planes. In other words, the slope of each ray is measured by imaging various object planes that are slightly displaced along the beam axis. With this measurement the density contours of the plasma are retrieved using an inversion technique by assuming a cylindrical symmetry in the plasma (the axis of symmetry is along the normal of the solid target).

One issue of the new concept is that diffraction effects are significant. Coherent light passing through an array of slits will diffract. This leads to maxima and minima according to Huygens' Principle, see e.g. Ref. 3. Diffraction will affect the image quality of the grid. As a first step, the basic optical properties, including diffraction from the grid, were studied without taking the refraction in the plasma into account. The image quality will also depend on the distance of the grid from the object plane. In Figure 2 the zero diffraction order and a higher diffraction order are schematically drawn. The grid has a certain distance from the object plane, which is imaged by a lens. If the grid were located in the object plane, a perfect image of the grid would appear. A blurred grid image is expected in the case that the grid is shifted away from the object plane. The rays are no longer combined into a single point in the image plane. This is the result of diffraction. The blurring is minimized the closer the grid is located to the object plane. Image blurring is expected to be more significant for larger distances.

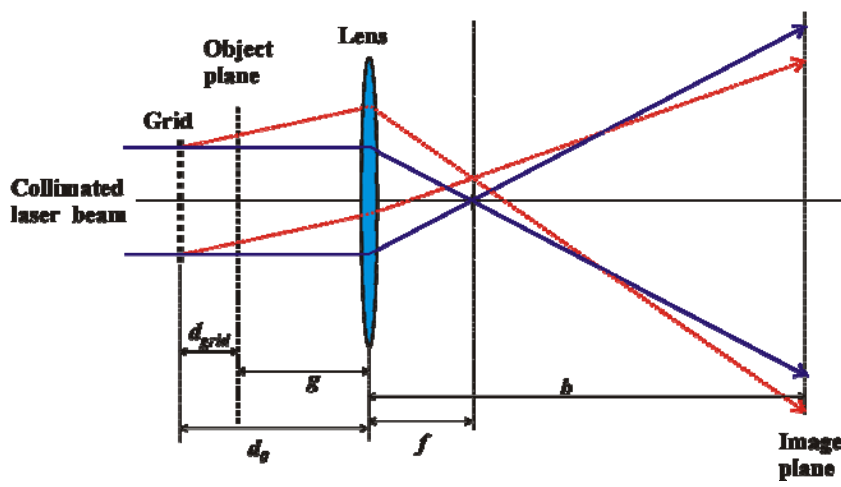


Figure 2: Different diffraction orders from a grid are imaged. The grid has a certain distance from the object plane that is imaged. As a result, the grid image is blurred due to the different diffraction orders.

Figure 3 shows a schematic for light diffraction through multiple slits. Diffraction is an effect where a wave, such as a beam of light, deviates from a rectilinear propagation path when passing through a small opening. According to Huygens's Principle, spherical waves emerge from each source point. Interference of those waves after the slit structure may be constructive or destructive depending on the angle θ with respect to the optical axis. One can consider the beam to be broken up into an array

of smaller bundles of light that have a certain angle, θ , with respect to the optical axis. The light bundles spread out and interfere with each other creating a pattern. The diffraction pattern is different for a single slit and for multiple slits. In multiple-slit diffraction, which is what occurs in GIR, the pattern produced has a uniform/periodic pattern of peaks and troughs. The intensity distribution in the far field from the diffraction of many slits can be written as a function of the diffraction angle⁴

$$I(\theta) = \frac{I(0)}{N_{slit}} \frac{\sin^2(\pi(w/\lambda)\sin\theta)}{[\pi(w/\lambda)\sin\theta]^2} \frac{\sin^2(N_{slit}\pi(p/\lambda)\sin\theta)}{\sin^2[\pi(p/\lambda)\sin\theta]}, \quad (1.1)$$

where N_{slit} is the number of slits, $I(0)$ is the intensity on the optical axis, p is the distance between two adjacent slits (this is also called the grid period), and w is the slit width. The light intensity is a function of the angle θ , which is the angle with respect to the optical axis. Figure 4 shows a calculation of the far field diffraction pattern from 6 slits using Eq. (1.1).

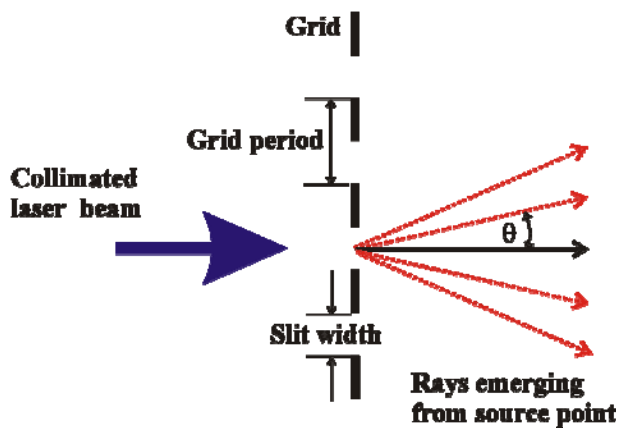


Figure 3: A collimated laser beam irradiates an array of multiple slits. According to Huygens' Principle, spherical waves emerge from each source point. Interference of those waves after the slit structure may be constructive or destructive depending on the angle θ with respect to the optical axis.

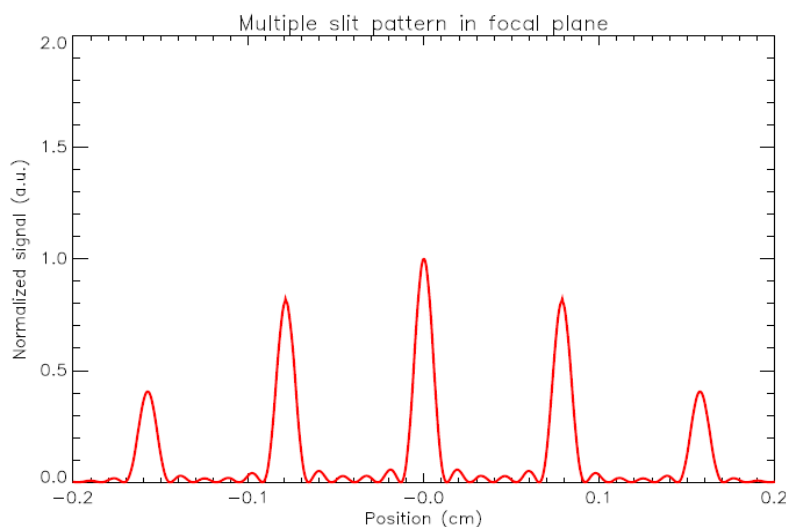


Figure 4: Interference pattern from a 6-slit grid in the focal plane of a lens.

II. PV-Wave Program

A PV-Wave program was written for imaging a grid structure including diffraction effects, see Figure 2. The program consists of three functions and a main program that calls upon them. The first of the functions creates an array of points for an object based on parameters given by the user. The main program calculates the final coordinates in the imaging plane, using a ray-trace formula of light through a thin lens, for the specified number of rays emitted from each point at specific angles at three different distances from the object plane. The second function calculates the intensity of each ray using the intensity formula given by Eq. (1.1). The third function creates the array for the image produced by rays. To make sure that the program was running properly, it was tested for the 1:1 imaging case (see Figure 5). In 1:1 imaging, the object is placed at $2f$, or two times the focal length of the lens, from the lens. From this distance, the image produced will be at $2f$ from the lens on the opposite side and will be an inversion of the object. The object and the image will be the same size making it easy to confirm the effectiveness of the program.

In the new GIR system a collimated UV laser beam illuminates a grid that is placed in close proximity to a plasma object (Figure 1). This creates a two-dimensional array of probe beam ray bundles that are passing through the plasma. The rays are refracted in the plasma much like in a lens, but the refraction varies locally. As a result the refraction angle varies over the ray array. The amount

of refraction depends on the refractive index in the plasma, which is a function of the free electron density. The refracted light is then collected by a lens, which images the grid onto a detector.²

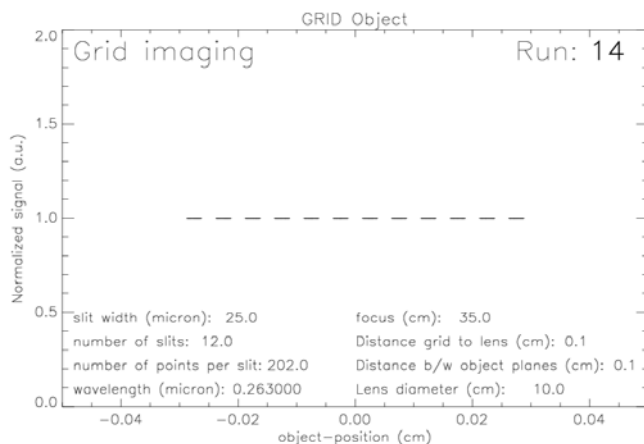


Figure 5: 12 slit grid placed at twice the focal length of a lens. The resulting image is identical to the object.

III. Results

i. 1D Line-outs

The grid image was calculated for various distances from the object plane without a plasma. Figure 6 shows intensity line outs of 1, 2, 3, 5, 6, and 9 mm distances of the grid from the object plane. The line-outs show that the pattern changes significantly when the grid is moved further away from the object plane. At a distance of 0.1 cm the grid pattern is clearly visible. At a distance of 0.2 cm, an additional modulation, which becomes stronger with greater distance, appears superimposed on the grid pattern. At a distance of 0.5 cm the contrast, which is the ratio of the intensity of the peaks and the troughs, is strongly reduced. Placing a grid at this distance would make it difficult to locate the center of each grid element, which is essential for the analysis in GIR. If the distance is further increased, the additional modulation eventually reduces and then at a distance of 0.9 cm a sharp image of the grid appears. It is observed that this cycle of image blurring and re-appearing of sharp grid images continues to occur if the distance is further increased. At multiples of the distance of ~ 0.9 mm, a sharp image of the grid is obtained. The distance when the first sharp image appears depends on the light wavelength and the grid period.

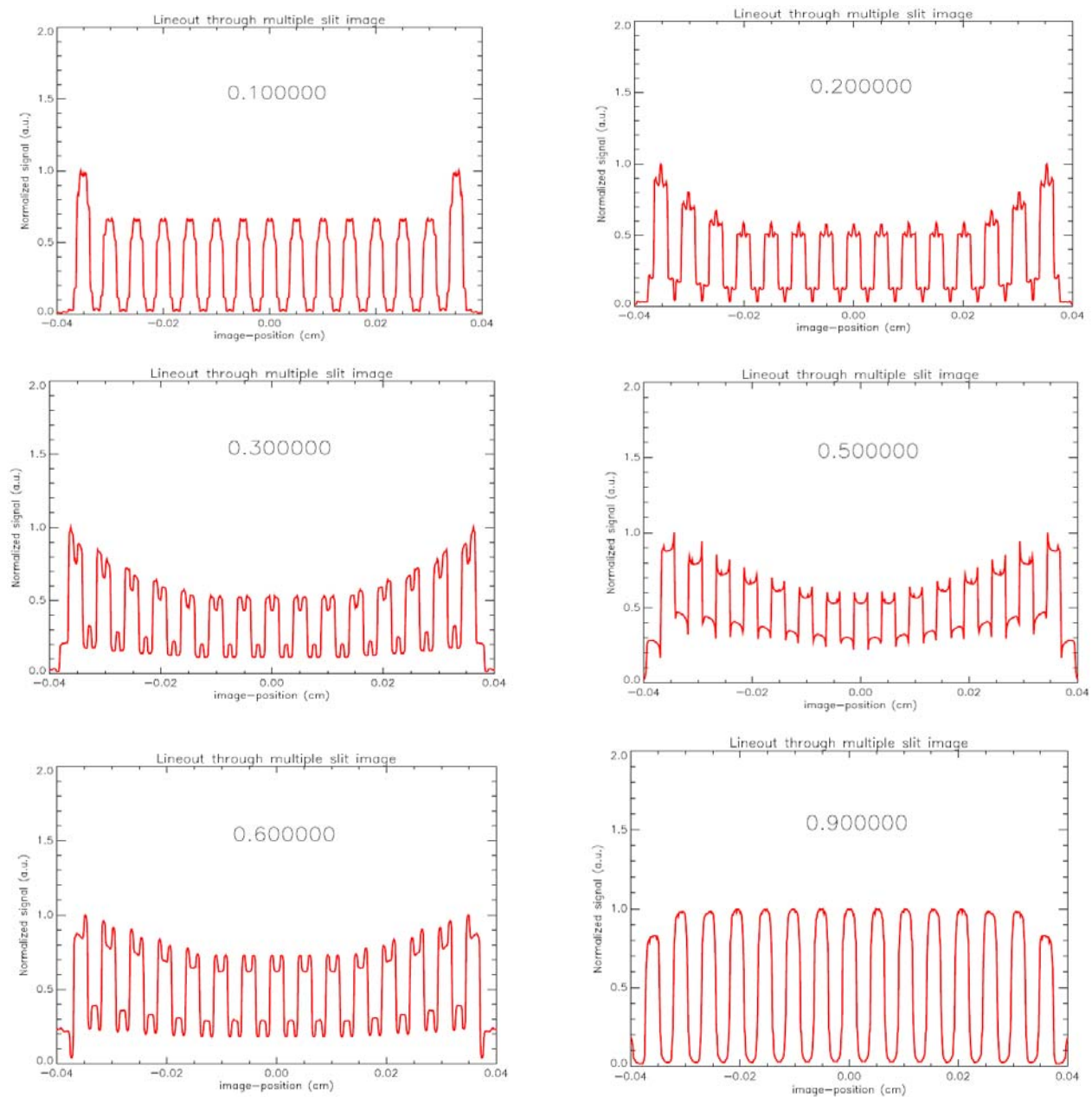


Figure 6: Multiple slit images were calculated for various object positions. The distances are given in centimeters. The light wavelength was 263 nm, the grid period was 50 μm , and the slit width was 25 μm .

ii. 2D Contour plots

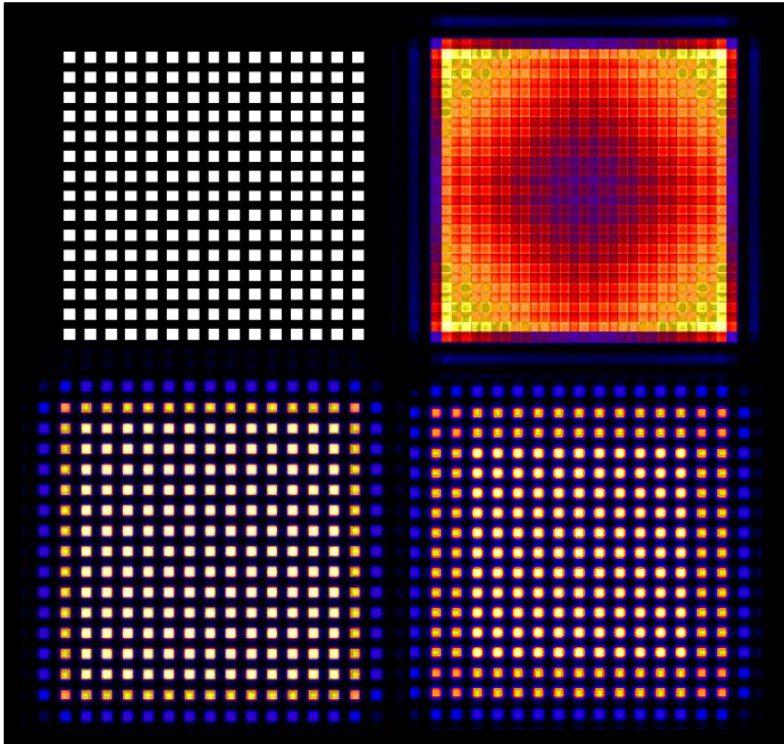


Figure 7: Calculated grid images for various distances (0, 0.5, 2, and 1 cm – beginning from top left, clockwise) behind the grid. No plasma was assumed. The light wavelength was 263 nm, the grid period 50 μm , and the slit width was 25 μm .

Similar calculations as shown in the previous section have been performed for a two dimensional grid (Figure 7). Again, the issue with placing a grid in close proximity to a plasma object is that with increasing distance from the grid, multiple beam interference rapidly leads to a blurring of the grid structure. Figure 7 shows calculated images of a grid at various distances (0, 0.5, 1, and 2 cm) behind the grid. At a distance of 0.5 cm the grid image is strongly distorted and would not be useful for GIR. At certain distances sharp grid self-images appear. This has to be taken into account when placing the grid from the plasma object. This effect is also known as the Talbot effect.

iii. Sharpening and blurring (Talbot effect)

The Talbot effect is a diffraction effect that was first observed in 1836 by Henry Fox Talbot.⁵ When a plane wave is transmitted through a grating, Talbot observed that sharp images of the grating appear at certain distances. Forty-five years later, Lord Rayleigh explained Talbot's observation as a result of Fresnel diffraction.⁶ He derived a formula for the distance, when the grating structure

replicates, which is now known as the Talbot length, $T_n = np^2 / \lambda$, where p is the grating period, λ is the light wavelength, and n is an integer number.

For example, in the case of the GIR application using a grid with 50 μm period, it needs to be placed 9.4 mm away from TCC to be at the exact first Talbot length. The 50 μm period gives sufficient spatial resolution for GIR. Within a distance of ± 1 mm from the Talbot length a reasonable image quality is maintained.

Adding plasma in the path of the interfering beam arrays might complicate the data analysis. The problem is that waves from different slits interfere and the unique optical path of each individual beamlet is lost, which is essential for GIR. It is not yet known how plasma refraction and diffraction will affect the grid imaging. A simple estimate is performed to assess this effect (see Figure 8): Considering an interference maximum in the Talbot plane, beams from many slits interfere constructively. Outer slits with a large lateral distance from S1 can contribute to the interference maxima S1 in higher diffraction order, but energy decreases strongly with higher order. Within a distance $x_m = p^2 / m\lambda$, all the interfering beams up to order m stay in a lateral region of less than the grid period, p , which is about the spatial resolution of the technique. Taking an order of $m = 5$, the corresponding distance is $x_5 \approx 2$ mm ($p = 50 \mu\text{m}$, $\lambda = 0.25 \mu\text{m}$), which is comparable to the plasma size. This estimate shows that the diffraction effects are probably tolerable and GIR might be a viable technique when using a grid in proximity to the target. However, this has to be first proven experimentally.

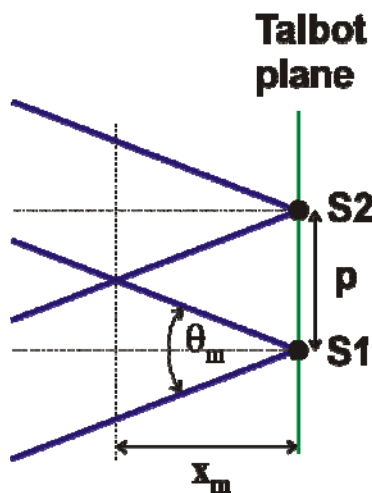


Figure 8: Schematic showing the cone of beams from multiple slits interfering in the Talbot plane producing a self image of a grid. The angle θ_m corresponds to a certain diffraction order m .

IV. Conclusion

A new approach in grid image refractometry (GIR) has been studied theoretically in which the grid is in close proximity to the plasma object. The project studied the basic optical properties of this GIR system, including the diffraction effects from the grid but ignoring the refraction due to the plasma. A PV-Wave program has been written based on a simple ray-trace algorithm that includes diffraction from the grid. The image quality was studied for various object planes and grid periods. An optimal position for the grid was found that resulted in crisp images, showing that this approach is a promising approach to plasma analysis. It has been shown that the diffraction effects from the grid are due to the Talbot effect, which explains why sharp images of the grid were observed at certain multiple distances of the first Talbot length. The results that were obtained are encouraging and show that the new GIR method might be sufficient in analyzing the refraction effects of the irradiated plasma. It is now important to test the method experimentally and to show that it is a viable method even when refraction in the plasma is taken into account.

V. Acknowledgements

I must offer a great thanks to my advisor Dr. Wolfgang Theobald for his immense help and guidance. I would also like to thank Dr. Craxton for this incredible opportunity at the Laboratory for Laser Energetics. The scientific experience and knowledge I have gained is invaluable. I also would like to give thanks to my parents and teachers for initiating and encouraging my hunger for knowledge.

VI. References

-
- ¹ R. S. Craxton et al., Phys. Fluids B 5, 4419 (1993).
 - ² Tabak M et al, Phys. Plasmas 1 1626 (1994).
 - ³ E. Hecht, Optics, (Addison Wesley, San Francisco, 2002), p. 443 ff.
 - ⁴ Ibid., p.462.
 - ⁵ F. Talbot, "Facts relating to optical science N. iV," Philos. Mag. 9, 4041-407 (1836).
 - ⁶ Lord Rayleigh, "On copying diffraction-gratings, and on some phenomenon connected therewith," Philos. Mag. 11, 196-205 (1881).

Including Emissivity in the Analysis of Implosion Radiographs

Mia Young

Including Emissivity in the
Analysis of Implosion Radiographs

Mia Young

Penfield High School

Penfield, New York

LLE Advisor: Reuben Epstein

Laboratory for Laser Energetics

University of Rochester

Rochester, New York

August 2009

Abstract

In order to achieve ignition conditions in inertial confinement fusion (ICF) experiments, it is necessary for the imploding target to reach very high densities. To measure the properties of the target while it implodes, X-ray radiography is employed. The target is backlit, and the resulting radiograph is recorded using a pinhole camera. The optical thickness profile of the target is then inferred from the intensity profile recorded in the radiograph. In the simple analysis for obtaining the radial opacity profile of the target from the optical thickness profile in the radiograph, the target is treated as an absorbing spherical shell, with no emissivity. However, it may be necessary in some cases to be able to account for a significant amount of self-emission from the target. By including both an emitting center and an emitting outer shell in a simple model of an imploded target, we show that visible self-emission at the outer edge of a radiograph indicates a corresponding emission contribution to the apparent absorption seen in the inner part of the radiograph and that the apparent and actual absorption contribution can differ significantly. The relationship between this difference and the visible self-emission may provide the means for correcting for self-emission in obtaining radial density distributions from radiograph analyses.

Introduction

The Laboratory for Laser Energetics at the University of Rochester is pioneering nuclear fusion by conducting laser driven, direct-drive inertial confinement fusion experiments. In order to achieve ignition, or a state in which fusion reactions are self-sustaining, it is necessary for the plastic coated deuterium-tritium (DT) targets to reach densities of several hundred grams per cubic centimeter and temperatures of approximately 100 million degrees Celsius¹. Given that high temperatures and densities must be reached to achieve fusion conditions, it is desirable to know the density of the DT target during the implosion.

Using Radiography to Determine Density

In free-free absorption of x-rays, the opacity, κ_{ff} of an object is directly related to its density ρ by the equation

$$\kappa_{ff} = \frac{k\rho^2}{(k_B T)^{1/2} (h\nu)^3}, \quad (1)$$

where k is a constant, T is the temperature, k_B is Boltzmann's constant and $h\nu$ is the photon energy. The temperature may be modeled with a simulator, and the photon energy is a known property of the backlighter, but the value of opacity must be measured to be able to solve for the density.

If the opacity is constant, it is related to the optical thickness, τ , of the object along a backlighter ray path by the equation

$$\tau = \kappa L \quad (2)$$

where L is the length of propagation of the backlighter ray. By employing radiography and observing the attenuation of the backlighter intensity, the optical thickness is calculated using

$$\tau = \ln\left(\frac{I}{I_0}\right), \quad (3)$$

where I is the final intensity observed in the radiograph and I_0 is the initial backlighter intensity, in arbitrary units.

Because of self-emission from the high temperature target, the final intensity may include not only the backlighter radiation, but a contribution from the target as well. Thus, the apparent optical thickness, τ_{app} , and the actual optical thickness, τ_{act} , are unequal and must be related to each other so that τ_{act} can be inferred from measurements of τ_{app} .

Radiative Transfer and Optical Thickness

The solution to the equation of radiative transfer for constant emissivity and opacity, given by

$$I = \frac{\varepsilon}{4\pi\kappa} + \left(I_0 - \frac{\varepsilon}{4\pi\kappa} \right) e^{-\tau}, \quad (4)$$

is used to model the change in intensity as a beam travels through an absorbing and emitting object, where I_0 is initial intensity, I is final intensity, ε is the emissivity, κ is the opacity, and τ is the optical thickness.² When an object either emits or absorbs, simplified forms may be used. For an object of thickness L with emissivity only,

$$I = I_0 + \frac{\varepsilon L}{4\pi}, \quad (5)$$

and, with opacity only,

$$I = I_0 e^{-\kappa L} \quad (6)$$

The target we modeled consisted of three distinct shells, which either emitted or absorbed exclusively, as shown in Fig. 1. We calculated the corrections for obtaining the actual optical thickness profile due to the opacity alone from the apparent optical thickness one would infer from the radiograph by assuming that the net effect of opacity and emissivity was entirely due to opacity. To accomplish this, four distinct possibilities

for the path of the backlighter emissions must be studied, as is shown in Fig. 2.

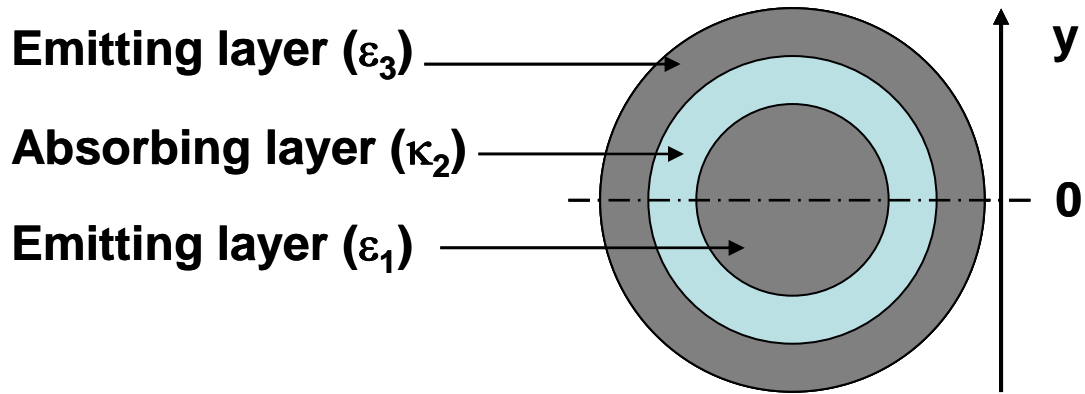


Fig. 1 The target is modeled with an emitting layer surrounding an absorbing layer, all surrounding an emitting core.

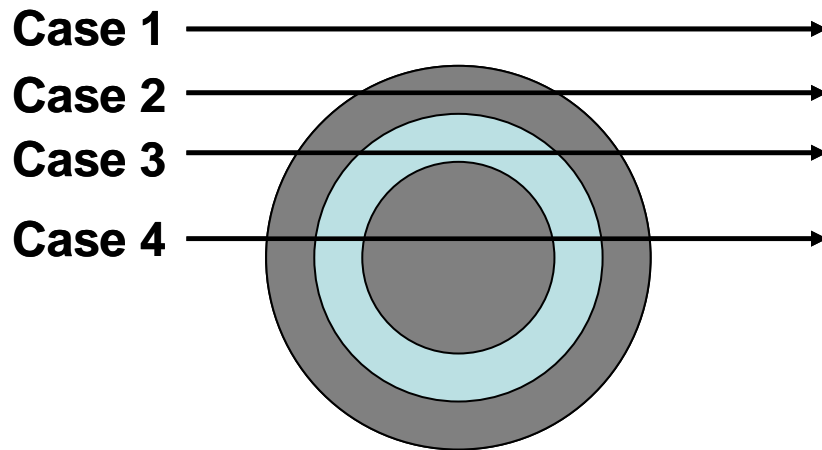


Fig. 2 Four possibilities for the path of backlighter emissions

In each case, the final intensity is modeled based on the emissivity and opacity of each layer of the target, the succession of path segments along the propagation path as it passes through each layer of the target, and the initial intensity of the backlighter. The four distinct cases are Case 1,

$$I = I_0, \quad (7)$$

Case2,

$$I = I_0 + \frac{\varepsilon_3 L_3(y)}{4\pi}, \quad (8)$$

Case 3,

$$I = \left(I_0 + \frac{\varepsilon_3 L_3(y)}{4\pi} \right) e^{-\kappa_2 L_2(y)} + \frac{\varepsilon_3 L_3(y)}{4\pi}, \quad (9)$$

and Case 4,

$$I = \left[\left(I_0 + \frac{\varepsilon_3 L_3(y)}{4\pi} \right) e^{-\kappa_2 L_2(y)} + \frac{\varepsilon_1 L_1(y)}{4\pi} \right] e^{-\kappa_2 L_2(y)} + \frac{\varepsilon_3 L_3(y)}{4\pi}. \quad (10)$$

By dividing both sides of the equations by the initial intensity, the equations become expressions for $e^{-\tau_{app}}$. For Case 1, we have

$$e^{-\tau_{app}} = 1, \quad (11)$$

for Case2,

$$e^{-\tau_{app}} = 1 + \frac{\varepsilon_3 L_3(y)}{4\pi I_0}, \quad (12)$$

and for Case 3,

$$e^{-\tau_{app}} = \left(1 + \frac{\varepsilon_3 L_3(y)}{4\pi I_0} \right) e^{-\tau_{act}} + \frac{\varepsilon_3 L_3(y)}{4\pi I_0}, \quad (13)$$

where

$$\tau_{act} = \kappa_2 L_2(y). \quad (14)$$

For Case 4, the ray propagates through the absorbing layer twice, so, for this case alone,

$$\tau_{act} = 2\kappa_2 L_2(y), \quad (15)$$

and

$$e^{-\tau_{app}} = \left[\left(1 + \frac{\varepsilon_3 L_3(y)}{4\pi I_0} \right) e^{-\tau_{act}/2} + \frac{\varepsilon_1 L_1(y)}{4\pi I_0} \right] e^{-\tau_{act}/2} + \frac{\varepsilon_3 L_3(y)}{4\pi I_0}. \quad (16)$$

The actual optical thickness is then solved for algebraically in Cases 3 and 4, as those are the only cases impacted by absorption. For Case 3, we have

$$e^{-\tau_{act}} = \frac{e^{-\tau_{app}} - \frac{\varepsilon_3 L_3(y)}{4\pi I_0}}{1 + \frac{\varepsilon_3 L_3(y)}{4\pi I_0}}, \quad (17)$$

and for Case 4,

$$e^{-\tau_{act}/2} = \frac{-\frac{\varepsilon_1 L_1(y)}{8\pi I_0} + \sqrt{\left(e^{-\tau_{app}} - \frac{\varepsilon_3 L_3(y)}{4\pi I_0} \right) \left(1 + \frac{\varepsilon_3 L_3(y)}{4\pi I_0} \right) + \left(\frac{\varepsilon_1 L_1(y)}{4\pi I_0} \right)^2} / 4}{1 + \frac{\varepsilon_3 L_3(y)}{4\pi I_0}}. \quad (18)$$

Equation (18) gives the correct result in the limit of zero emissivity,

$$\lim_{\varepsilon_1, \varepsilon_3 \rightarrow 0} e^{-\tau_{act}} = e^{-\tau_{app}}. \quad (19)$$

The chosen problem was to consider the effect of emissivity ε_3 on the Case 3 result. We assume that we are given a radiograph and that we wish to infer the opacity κ_2 from the Case 3 portion of the radiograph. If an emissivity ε_3 is present, then it will be visible in the Case 2 portion of the radiograph, according to Eq. (12). If ε_3 can be inferred using Eq. (12), then ε_3 can be used in Eq. (17) for Case 3 to obtain τ_{act} from τ_{app} . The opacity κ_2 is then obtained from τ_{act} using Eq. (14). Although it is clear in principle that a procedure such as this will succeed, we have not yet worked out the details of how this would work in practice. However, we have modeled the effect of ε_3 on τ_{act} using Eqs. (11) through (18). To demonstrate by example the effects of emissivity on a radiograph, pairs of simulations were run, one in which there was no self emission

and one in which there was significant self emission along the backlighter path in Layer 3. One such result is shown in (Fig. 3).

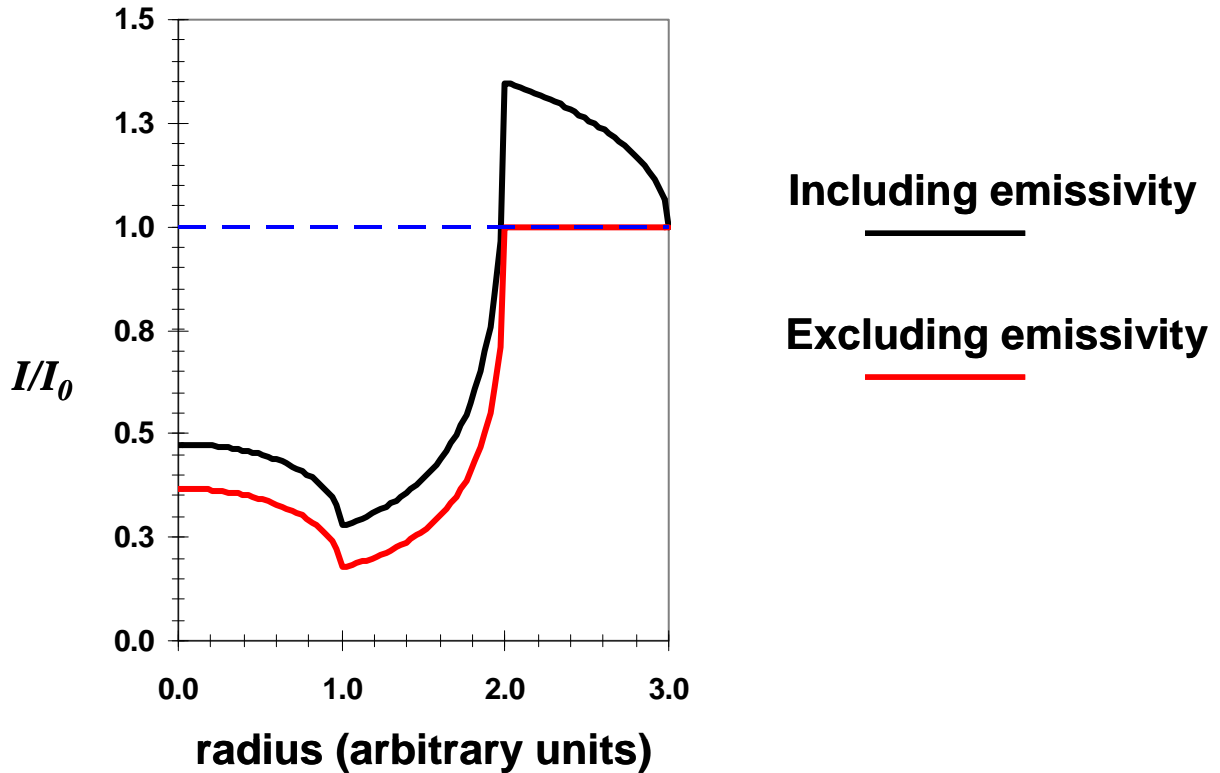


Fig. 3 Radial optical thickness profiles with and without including a strong, thick emitting outer layer.

Figure 3 shows the radial transmission profile of a radiograph of an absorbing shell with an inner radius of 1 and a thickness of 1, in arbitrary units. The red curve shows the radiograph that would be obtained with a shell with a central optical thickness of 1. The black curve is the radiograph of the same absorbing shell with a very thick outer emitting layer with the same thickness as the absorbing layer. The emissivity is an arbitrary value chosen so that its maximum intensity on the radiograph, at a radius in the image plane corresponding to the inner radius of the emitting layer, is nearly equal in

magnitude to the intensity lost at the center of the radiograph due to absorption. The choice of a central optical thickness of 1 is a good intermediate value for radiography, since it is a robust signal representing a loss of most of the backlighter intensity, and, at the same time, the minimum intensity recorded in the radiograph is far enough above zero transmission so that the emission signal will not easily overwhelm the absorption signal. For the radiograph to be interpreted as an absorption shadow, the intensity should, as much as possible, be the result of the absorption of the backlighter intensity, without a large modification due to self-emission. If the transmission of the absorbing layer is very small, then small contributions due to self emission can make a relatively large contribution to the intensity. In this example, the apparent increase in the transmission due to the emitting layer is about 23%, which is quite modest, considering the strength and size of the emitting layer. Examples such as this can serve as benchmarks for accepting or rejecting radiographs to be analyzed in terms of absorption alone. Figure 4 shows two examples where the reduced size and strength of the emitting layer results in smaller corrections.

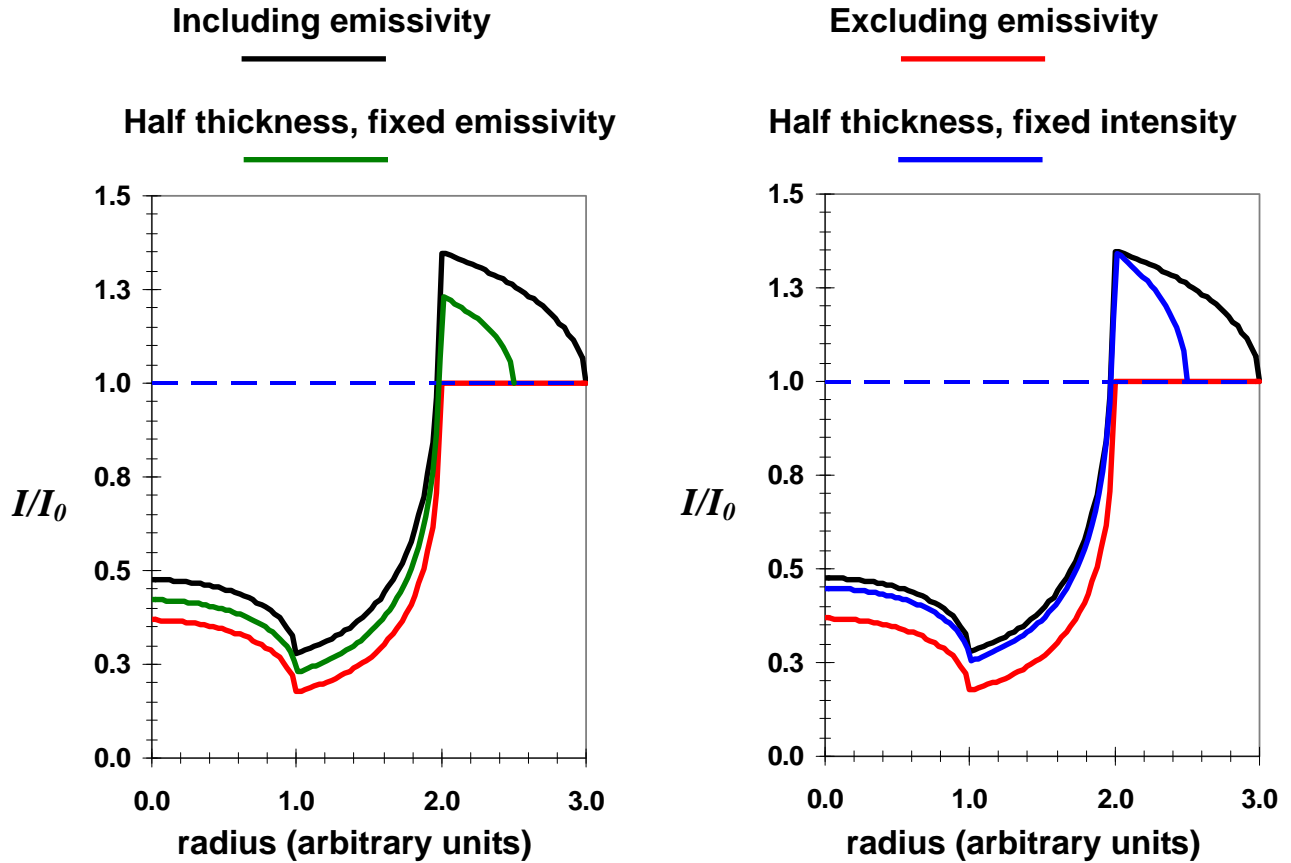


Fig. 4 Radial optical thickness profiles showing the change in the apparent optical thickness due to the effects of an emitting layer. The green curve, when compared with the black curve, show a reduced effect when the emitting layer is reduced to half the thickness of the emitting layer producing the black curve. The red and black curves are identical to those in Fig. 3. The blue curve shows that reducing the thickness of the emitting layer reduces the effect on the apparent transmission, even if the apparent intensity of the emission is kept constant.

A thinner emitting layer can result in a radiograph with a smaller self-emission modification, one that may be ignored, possibly, depending on the desired degree of precision. In Fig. 4, the green curve shows that the emission effect in the radiograph is reduced nearly in proportion to the reduction in the thickness of the emitting layer, keeping the emissivity at the same value as used for the result shown in Fig. 3,

represented here again by the black curve. In this case, the volume of the emitting layer has been reduced to only slightly larger than the volume of the absorbing layer, which is still larger than what would seem reasonable in a well-designed radiography experiment. Nevertheless, the resulting 10% emissivity effect in the radiograph can be considered modest, perhaps even negligible by some standards of precision. The blue curve is a similar example of a reduced self-emission effect with a thinner emitting layer, but the emissivity in this example has been increased to keep the intensity of the emission ring in the radiograph constant. These results illustrate how the apparent thickness and intensity of the Case 2 portion of the radiograph together indicate the effect of self-emission on the apparent Case 3 transmission.

Conclusions and Future Work

Based on the examples shown above, it is clear that a correction may be needed to infer the opacity profile of an object from its radiograph when self-emission is seen in the radiograph, although there may be cases where the correction can be neglected, to an acceptable degree of approximation. Experiments involving radiography should be designed to minimize the effects of self-emission, and examples such as those shown here can be a useful guide.

If this work were to be continued, one could consider the application of the Abel transformation to infer opacity profiles from radiographs.³ Considering the equation of radiative transfer as a means to move from the opacity distribution of the target itself to the shadow pattern it creates, the Abel transform can be thought of as a means to infer the opacity profile of a target based on the shadow created by it. Just as a term is included in the solution to the equation of transfer, Eq. (4), to account for self-emission, it would be useful if a simple correction to the Abel transform could be found to account for self-emissions from the target.

References

- 1 L. H. Gresh, R. L. McCrory, and J. M. Soures, *Introduction to Inertial Confinement Fusion*, Laboratory for Laser Energetics, Rochester, 2009, <http://www.lle.rochester.edu/pub/documents/ext/ICF.pdf>.
- 2 Chandrasekhar, S., *Radiative Transfer*, Dover Publication, New York, 1960. Originally, Oxford University Press, 1950; Epstein, R. *Equation of Transfer*, private communication, Laboratory for Laser Energetics, Rochester, 2009.
3. Wikipedia, *Abel Transform*, http://en.wikipedia.org/wiki/Abel_transform; Bracewell, R., *The Fourier Transform and its Applications*, 3rd Ed.. New York: McGraw-Hill., 2000, pp. 351-356.

Resonance and Damping Characteristics of Cryogenic Fusion Targets

Harvest Zhang

Resonance and damping characteristics of cryogenic fusion targets

Harvest Zhang

Brighton High School
Rochester, NY

Advisor: Mr. L. D. Lund

Laboratory for Laser Energetics
University of Rochester
Rochester, NY
November 2009

Abstract

Targets for direct drive inertial confinement fusion experiments on the OMEGA Laser at the University of Rochester were tested on a shaker apparatus to determine target motion behavior under vibrational excitation. Frequency response functions were used to determine that each target has two distinct dominant resonance frequencies, one for each principal axis, both around the 130-150 Hz range. Damping was estimated by the half-power bandwidth and exponential decay methods to be around 1% of critical damping. Both methods gave almost identical values for the damping within the experimental uncertainties. Target displacement given an applied acceleration was measured to be within the 300-400 $\mu\text{m/gn}$ range. A program was written to visualize three-dimensional target motion at high frame rates to investigate cross-coupling, the excitation of vibrations in the target along an axis transverse to the direction of applied acceleration. The visualization confirms the existence of distinct target resonance axes. The data obtained and methods developed to analyze target behavior will eventually help to design improved target support structures, which will reduce target vibration induced by equipment in the target chamber during a laser shot, resulting in better alignment, higher radiation uniformity and thus higher fusion reaction efficiency.

1 Introduction

Nuclear fusion promises to provide a sustainable and environmentally safe form of energy for the future. Several large facilities, including the National Ignition Facility in Livermore, CA and the Laser Megajoule in France, are experimenting with inertial confinement fusion, where a spherical capsule containing hydrogen fuel is heated and compressed by a large number of laser beams to yield alpha particles, neutrons, and a large amount of energy [1]. At the

Laboratory for Laser Energetics at the University of Rochester, fusion experiments are carried out on the 60-beam OMEGA laser [2].

The laser radiation must be distributed as uniformly as possible over the surface of the capsule to ablate the surface evenly and create a uniform implosion. This requires a smooth capsule surface and proper alignment of the capsule in the center of the target chamber [3]. It is therefore crucial for the capsule to be stationary in order to achieve uniform irradiation.

There are various sources of excitation of target motion in the target chamber. The cryogenic pumps create a steady state vibration, and the thermal shroud that covers the target transiently excites the target when it is pulled upwards to clear the target for the shot [4], [5]. Therefore, it is important to know how a target behaves over a large range of frequencies and how well the target damps out after the excitation.

A typical target used in OMEGA laser fusion experiments is shown in Fig. 1. The capsule, with a diameter of just under 1 mm, is glued on top of an approximately 2 mm long SiC fiber with a diameter of 17 μm . This stalk is then glued to the outside of a polyimide tube a little over a centimeter long, and the polyimide tube is then fixed inside a stainless steel tube which is attached to the base of the target assembly (not shown in Fig. 1). The entire target, including the base, stalk, and capsule, has a mass of just under 0.2 g, with an overall length of just under 34 mm.

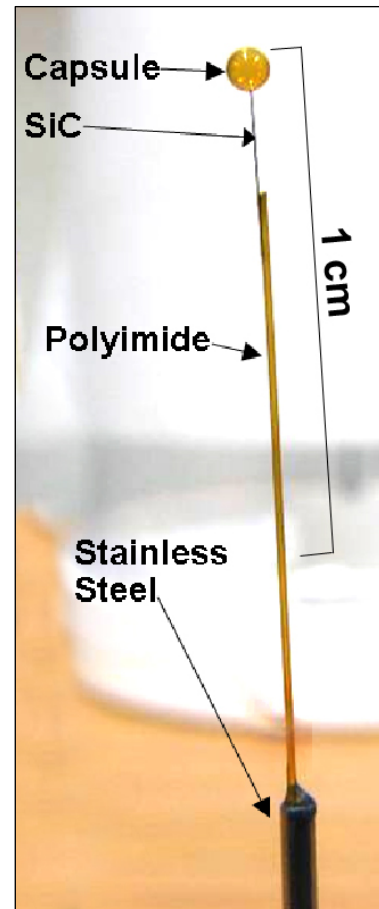


Fig. 1 Photo of a mass equivalent fusion target

The capsule is mounted on a very long stalk that is subject to vibration. Note the asymmetry at the joints between materials, which results in two dominant resonance frequencies in two principal axes at right angles to each other.

The capsules needed for fusion are thin plastic shells only 5 μm thick, on the inside of which there is a 100 μm layer of cryogenic deuterium and tritium ice at 20 K. As the mass of the capsule affects target behavior under vibration, the capsules tested at room temperature have thicker plastic walls but no deuterium-tritium, so that the mass of a test capsule is equivalent to the mass of a deuterium-tritium filled capsule.

In these experiments, targets were tested in a shaker apparatus, which applied vibrational excitations to the target at various frequencies. The dominant resonance frequencies, transmissibility (capsule displacement divided by applied acceleration), and amount of damping were measured by two different methods. A program was also written to aid visualization of the path of target motion under excitation. The data suggests that these targets resonate at two distinct frequencies in the 130 Hz to 150 Hz range in the directions of the principal axes. Additionally, increased target stiffness was found to correlate with increased resonance frequencies, decreased transmissibility, and decreased damping. These findings are helpful to the search for better materials and designs for target support structures, which will eventually be optimized to minimize target vibration.

2 Experimental

2.1 The shaker apparatus

A shaker apparatus is used to excite the target. The base of the target's stalk magnetically mounts into a collet on the shaker stage, which is connected to a shaker driver that provides acceleration in the X direction. Two quadrant-cell photoreceivers [6] detect the position of the capsule, one in each of the shaker's X and Y directions, and an accelerometer attached to the

stage measures input acceleration in the X direction. The position data collected is then transferred by means of an analog-to-digital converter [7] to a computer program.

Targets were tested in two orientations to account for their design asymmetry. As shown in Fig.

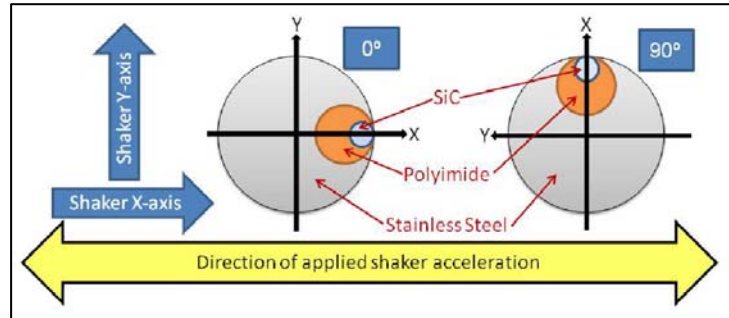


Fig. 2 Overhead diagram of shaker and target axes

The target's X and Y axes rotate with the target, while the shaker's axes remain constant. The shaker always applies acceleration in its X-axis direction.

2, the target's X-axis is defined as a line drawn in the X-Y plane which intersects both the center of the stainless steel tube and the two points of tangency where the different materials join together. In the 0° position, the target's X and Y axes line up with the shaker's X and Y axes, and the target's X-axis is longitudinally excited. In the 90° orientation the target is rotated about the Z-axis, and the target Y-axis is longitudinally excited.

Using this setup, target behavior and damping are measured by two different methods as described in the next two sections.

2.2 Frequency response functions and half-power bandwidth damping

The target's motion at the capsule can be approximated by treating it as a driven, damped single degree of freedom oscillator [8]. The capsule is thus treated as a particle subject to an oscillatory force at frequency ω provided by the shaker, a restoring force proportional to its displacement, and a damping force proportional to velocity. The particle's position is given by the real part of the complex position $x(t)$, which obeys the equation of motion

$$\frac{d^2x}{dt^2} + \gamma \frac{dx}{dt} + \omega_0^2 x = a_0 e^{i\omega t} \quad (1)$$

where γ is the damping constant, ω_0 is the resonance frequency, and a_0 is the amplitude of the applied force divided by the particle's mass. Setting $x=x_0e^{i\omega t}$ where x_0 is the amplitude of oscillation, we can derive the complex transmissibility T , which is defined as x_0/a_0 :

$$T = \frac{x_0}{a_0} = \frac{1}{\omega_0^2 + i\omega\gamma - \omega^2}. \quad (2)$$

The modulus of T , when plotted against frequency as in Fig. 3(a), is known as the frequency response function (FRF). Its units are distance divided by acceleration in units of gravity. In order to obtain an FRF, the shaker is used to output sine waves in chirps, each chirp

sweeping through a range of frequencies, and the displacements of the capsule in the X and Y directions and the acceleration applied to the shaker stage during the chirp are measured. A fast Fourier transform is used to convert this time-domain data into the frequency-domain FRF [6]. The domain was set at 0 Hz to 500 Hz, giving a frequency resolution of 0.3125 Hz, as the analog-to-digital converter is only capable of 1600 lines

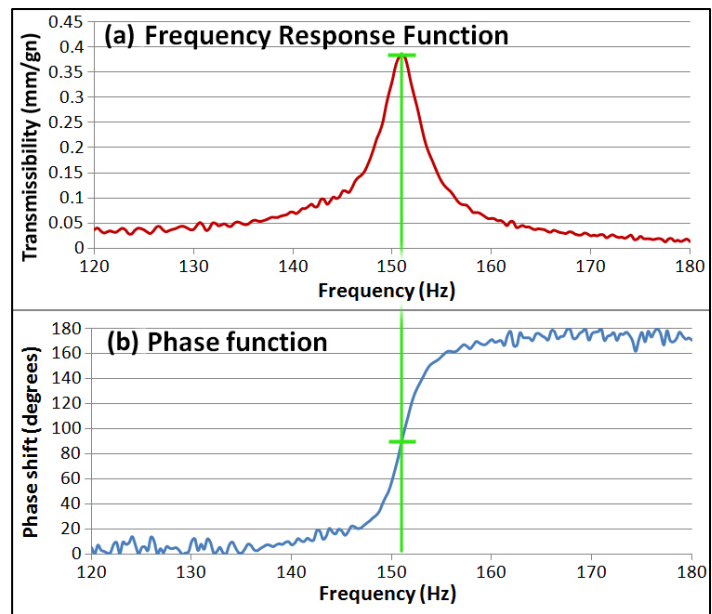


Fig. 3 A typical target frequency response function (a) and phase function (b).

The green cursor shows the resonance frequency at which the transmissibility has its peak, the same frequency at which the phase function, the phase of the complex transmissibility without the negative sign, crosses 90°.

of resolution. Thirty chirps are performed, and the resulting FRFs are averaged. The phase of T was plotted in Fig. 3(b) as the phase function.

Equation (2) indicates that away from resonance, the $i\omega\gamma$ term is negligible due to the γ term being very small. Thus, x_0/a_0 will be positive for applied frequencies lower than ω_0 ,

meaning that the displacement is in phase with the acceleration, resulting in a phase shift of 0° left of resonance. Similarly, x_0/a_0 will be negative for applied frequencies higher than ω_0 , meaning that the displacement is out of phase with the acceleration, resulting in the 180° phase shift right of resonance in Fig. 3. At resonance ($\omega=\omega_0$), the displacement and acceleration are 90° out of phase. Resonance frequencies from FRFs were confirmed to line up with the frequencies at which the phase function is at 90° .

Coherence data, which measures the degree to which the input acceleration oscillation and the target displacement oscillation have a constant relative phase, was also collected. High coherence at a certain frequency ensures that the transmissibility measured is truly the result of excitation at that frequency [7]. The coherence function was used only as a visual check to make sure that the coherence near the dominant resonance frequency was close to 100%.

Defining the half-power points as the frequencies in the FRF at which the square of the transmissibility is half the square of the resonance transmissibility, $|T|^2=(1/2)|T_0|^2$, it can be shown from Eq. (2) that the damping coefficient $\gamma = \Delta\omega$, the difference in frequency between the two half-power points. However, it is more useful to express the damping as the ratio γ/γ_c where γ_c is the critical damping (defined below), since this allows for comparisons between different targets. The general solution of the damping is found by removing the driving term from Eq. (1) and setting the complex displacement $x = x_0 e^{i\omega t}$ (with complex ω), from which a quadratic equation can be solved for ω leading to two roots, giving

$$\mathbf{x} = \mathbf{x}_0 \left(e^{-\frac{\gamma t}{2}} \right) \left(e^{\pm \frac{it}{2} \sqrt{-\gamma^2 + 4\omega_0^2}} \right) \quad (3)$$

where the $e^{-\gamma t/2}$ term gives an exponential decay envelope and the other term gives an oscillation as long as $\gamma < 2\omega_0$. Since critical damping is defined as the lowest possible value for damping that

will preclude all oscillation, the argument of the square root can be set equal to zero, leaving $\gamma_c = 2\omega_0$. Therefore, the damping ratio λ is given by

$$\lambda = \frac{\gamma}{\gamma_c} = \frac{\Delta\omega}{2\omega_0}. \quad (4)$$

The *Damping Estimator* component of the graphical user interface (GUI) program *Target Motion Characterization* was written in Matlab to perform half-power bandwidth damping calculations. As seen on the right panel of Fig. 4, it identifies the resonance peak (large red circle), uses linear interpolation to approximate the half-power bandwidth points (smaller red circles), and then uses Eq. (4) to estimate the damping ratio as a percent of critical damping.

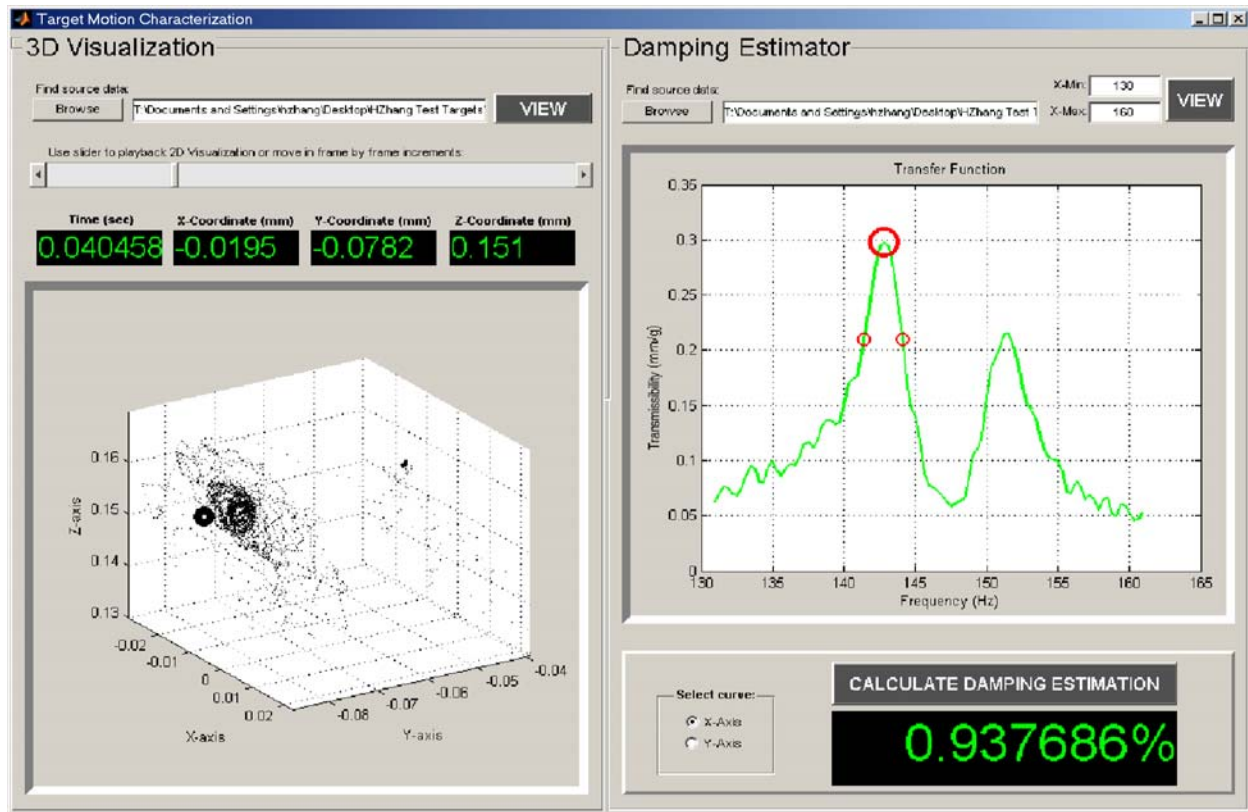


Fig. 4 The two components of the *Target Motion Characterization* GUI program

On the right is the *Damping Estimator* GUI. The large red circle indicates the resonance peak, and the smaller red circles indicate the half-power points. The damping ratio, shown at the bottom in green, has been calculated for this particular peak. On the left is the *3D Visualization* GUI, which displays a rotatable parametric plot of all the points in space the capsule occupies during an excitation. The thick black circle indicates the current position of the center of the capsule. The coordinates of the capsule and the time are displayed on the green readouts. The slider is used to play back the visualization, which is currently hardware limited to just under 100,000 frames per second.

2.3 Time-domain transient excitation and exponential decay damping

The exponential decay method of estimating damping uses transient excitations measured in the time domain. A sine wave excitation at the target's dominant resonance frequency (as found from the FRF) is applied, the goal being to excite only the dominant resonance mode. The duration of the excitation is set long enough so that the target reaches a maximum amplitude of vibration, at which point the excitation is turned off and the target undergoes a symmetrical, exponentially decaying series of oscillations at one frequency, as seen in Fig. 5.

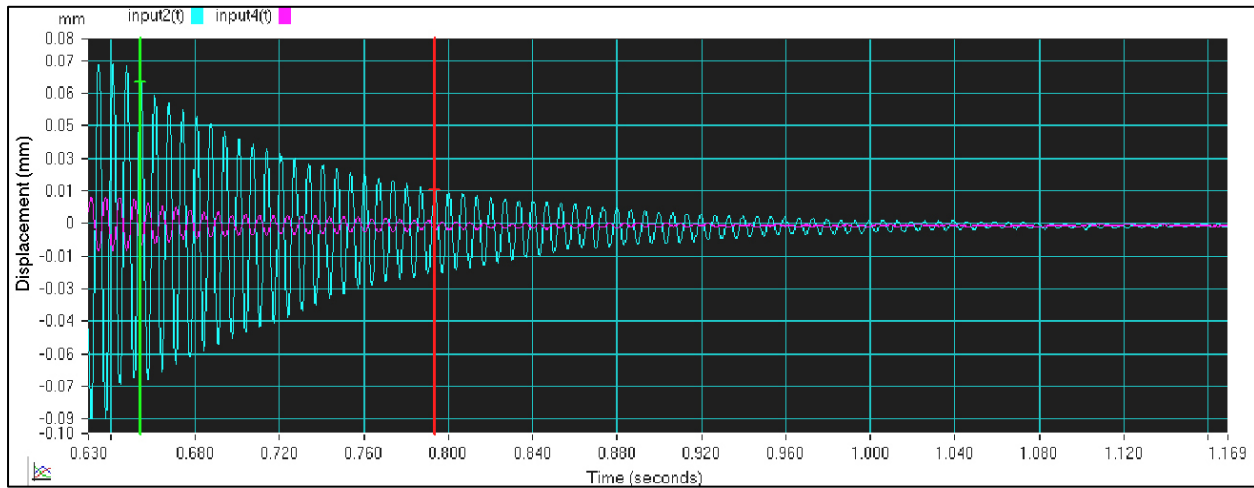


Fig. 5 A time-domain graph of target motion following a transient excitation at the resonance frequency. The X-axis displacement is shown in cyan and the Y-axis displacement (due to cross-coupling) in magenta. The green and red cursors indicate two peaks that are used to calculate the damping.

The damping coefficient γ can be measured directly from the exponential decay envelope term of Eq. (3), $A = A_0 e^{-\gamma t/2}$, where A is the amplitude of the oscillation. Equivalently, γ can be measured from any two peaks during the decay t_0 and t_n , with respective amplitudes A_0 and A_n , where the length of one period is given by $2\pi/\omega_0$. Recalling that $\gamma_c = 2\omega_0$, it is easy to show that the damping ratio λ is given by

$$\lambda = \frac{\gamma}{\gamma_c} = \frac{1}{2\pi n} \ln \frac{A_0}{A_n}. \quad (5)$$

A few issues remain; the shaker stage itself has a small but significant shift in the X-axis that is slow returning to 0 when the excitation is turned off, and slight errors in target alignment

set the stationary point a few microns above or below 0. Note that the peak displacement must be small (80 μm in Fig. 5) in order to prevent the capsule from falling off the stalk. To reduce the errors due to these effects, two positive peaks and the two following negative peaks are run through the calculations separately, and the values calculated are averaged so that the positive error in one measurement balances out the negative error in the other. Future calculations will implement an additional GUI in *Target Motion Characterization* which will minimize shaker-shift and positioning errors by averaging the positive and negative amplitudes of oscillation and then directly fitting an exponential decay curve to the resultant amplitudes.

2.4 *Variability testing*

Variability tests were carried out to determine the repeatability of the resonance frequency, transmissibility, and damping values calculated by both methods. Most of the variability involves the precision to which the target can be placed in the collet at exactly the same angle trial after trial; if the angle is even slightly off, the axes of the target and the shaker will not be directly aligned and thus the resonance frequency, transmissibility and damping ratio may change.

For the half-power bandwidth variability test, the target was first aligned in the 0° direction, tested once, removed from the collet, and then replaced in the collet as close to the same angle as could be visually determined. The measurements were taken again and this process was repeated seven times. The target was then rotated to the 90° orientation and the shaker was realigned so that the initial X and Y positions of the target were both at the origin. Seven more trials were taken in this orientation. The standard deviations were then calculated for the resonance frequency, the resonance transmissibility, and the damping ratio.

The exponential decay test was done in a similar way, except that due to the small amplitude of the target excitation, realignment was necessary for every trial in order to get the decay as centered about 0 mm as possible (see Fig. 5). Here, the goal was not just to determine precision across trials, but also to determine an optimum way of selecting peaks to use in the exponential decay calculation so as not to include the aforementioned errors regarding target alignment and shaker stage movement. Thus, seven trials were done in the 0° orientation and then repeated in the 90° orientation. The frequency of excitation was determined by the corresponding resonance frequency of each target axis, as found in the half-power variability test. For each single trial, transmissibility was calculated by dividing the peak steady state amplitude of the target at resonance by the peak acceleration delivered by the shaker driver. Six exponential decay damping values were taken per trial. The standard deviation was calculated for the transmissibility and the damping ratio.

2.5 *3-dimensional high frame rate target visualization*

As the second part of the program *Target Motion Characterization, 3D Visualization* was written to better understand exactly where the target is during an excitation. It takes displacement data in all three axes over a period of time and then graphs the data parametrically, allowing a 3-dimensional playback of the target position frame by frame as well as an overall view of all the points where the target has been, as shown in the left side of Fig. 4. In this way, it is easy to gain a general idea of the target's range of motion, as darker areas represent areas where the target is found most frequently. The analog-to-digital converter currently limits the program to a maximum of 4096 frames at 96154 frames per second. The GUI allows for rotation of the graph and playback of the target at whichever viewing angle is of interest.

3 Results and Analysis

3.1 Frequency response functions and half-power bandwidth damping

Fig. 6 shows frequency response functions for target 2 in the tables below, oriented at 0° in Fig. 6(a) and 90° in Fig. 6(b). The red curves are FRFs of the target axis under longitudinal excitation. The blue curves are FRFs of the target axis under transverse excitation. The highest peaks in Fig. 6(a) and Fig. 6(b) are at different frequencies, confirming that the asymmetry of the targets results in different resonance behavior in different orientations.

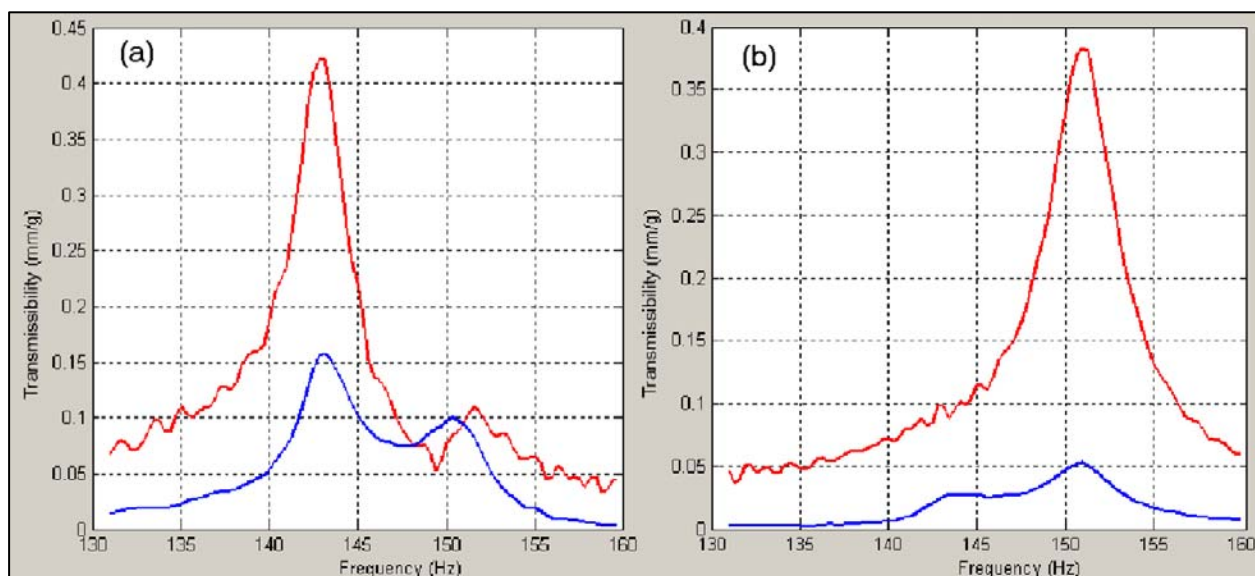


Fig. 6 Frequency response functions for (a) 0° and (b) 90°

The red curves show the target's motion under longitudinal excitation for the target's X-axis in (a) and the Y-axis in (b). The blue curves show the cross-coupled motion of the non-driven, transversely excited target axes.

A second peak is seen in the blue curve of Fig. 6(a), corresponding to the Y-axis resonance frequency. This occurs because the target was not placed in the collet at precisely 0° , causing a small amount of excitation at the Y-axis resonance frequency due to cross-coupling. Dual peak cases like this one are present in other targets for the same reason.

Usually, these peaks are less than 10 Hz apart, as is seen in Table 1, which gives the resonance frequencies for the three targets tested. Axes in all tables refer to the target's axes. An error of one standard deviation as determined by variability testing is reported for target 2 in this

and similar tables. The standard deviation is low due to the resolution being 0.3125 Hz; measurements either always return the same resonance frequency value, thus causing the 0.0 Hz standard deviation in the Y-axis of target 2, or alternate between two frequencies 0.3125 Hz apart, resulting in low standard deviations like the 0.15 Hz in the X-axis of target 2. Thus, the precision to which resonance frequency measurements can be made is limited by the resolution to about 0.3 Hz.

Table 1. X and Y resonance frequencies obtained from the frequency response function

FRF Method	X-axis	Y-axis
Target 1	148.8 Hz	145.6 Hz
Target 2	142.9 Hz \pm 0.15 Hz	150.9 Hz \pm 0.0 Hz
Target 3	134.1 Hz	135.9 Hz

Average resonance transmissibility values are given in Table 2. The precision of these measurements is questionable because the standard deviation is high, at 54 $\mu\text{m/gn}$ for a 423 $\mu\text{m/gn}$ measurement. These measurements seem to reflect a general trend of transmissibility close to 400 $\mu\text{m/gn}$, with no further precision determinable due to the high variability.

Table 2. X and Y resonance transmissibility obtained from the frequency response function

FRF method	X-axis	Y-axis
Target 1	410 $\mu\text{m/gn}$	389 $\mu\text{m/gn}$
Target 2	423 $\mu\text{m/gn}$ \pm 54 $\mu\text{m/gn}$	378 $\mu\text{m/gn}$ \pm 34 $\mu\text{m/gn}$
Target 3	449 $\mu\text{m/gn}$	454 $\mu\text{m/gn}$

Damping calculations from the half-power bandwidth method, however, showed greater precision. Table 3 shows the damping ratio present in these targets in the X and Y axes under longitudinal excitation. Considering that the standard deviation in the X axis is almost a tenth of a percent, this method estimates the damping ratio at 1% for all three targets.

Table 3. X and Y damping ratio obtained from the frequency response function

FRF method	X-axis	Y-axis
Target 1	1.1%	1.1%
Target 2	1.0% \pm 0.07%	1.1% \pm 0.01%
Target 3	1.2%	1.1%

3.2 Time-domain transient excitation and exponential decay damping

Table 4 shows resonance transmissibility data for targets 1 and 2. The input frequencies for each test are as measured for each target in Table 1.

Table 4. X and Y resonance transmissibility obtained from time-domain transient excitation

Time Domain	X-axis	Y-axis
Target 1	No data	404 $\mu\text{m/gn}$
Target 2	268 $\mu\text{m/gn} \pm 12 \mu\text{m/gn}$	249 $\mu\text{m/gn} \pm 10 \mu\text{m/gn}$

The transmissibility data from Table 4 is somewhat puzzling when compared with the corresponding data from the FRFs shown in Table 2. The Y-axis data for target 1 compares favorably, as the 404 $\mu\text{m/gn}$ calculated from the transient excitation at resonance is within one standard deviation (34 $\mu\text{m/gn}$) of the 389 $\mu\text{m/gn}$ obtained from the FRF. Target 2, however, shows a large discrepancy: 268 $\mu\text{m/gn}$ and 249 $\mu\text{m/gn}$ for transient excitation versus 423 $\mu\text{m/gn}$ and 378 $\mu\text{m/gn}$ from the FRF. A probable cause for this discrepancy is that the single applied excitation frequency could have been at a slightly different frequency from the target's actual resonance frequency. Future work would involve performing the same test with a series of different excitation frequencies near the resonance frequency. It is still worth noting that the standard deviations are much lower for transmissibility measured by this method, at a repeatability of about 10 $\mu\text{m/gn}$ for a measurement around 250 $\mu\text{m/gn}$.

Damping ratios calculated by the exponential decay method are shown in Table 5. They generally agree with the values obtained from the half-power bandwidth method. The standard deviations are lower (0.01% and 0.02% in Table 5 for the X and Y axes, respectively, compared with 0.07% and 0.01% for the half-power bandwidth method from Table 3). Although the damping

Table 5. X and Y damping ratio obtained from the exponential decay method

Time Domain	X-axis	Y-axis
Target 1	No data	1.06%
Target 2	0.89% $\pm 0.01\%$	0.96% $\pm 0.02\%$

ratios at 0.89% and 0.96% are only 0.07% apart, it is a significant enough shift given the low standard deviation to show that the two axes of the target have different amounts of damping.

3.3 Target motion visualization

The *3D Visualization* component of the *Target Motion Characterization* GUI was used to interpret the target's motion path. One of the first applications of this GUI was to better understand cross-coupling. The time-domain transient excitation data, the same data used to calculate exponential decay damping, was run through the visualization GUI to see what the path of the target was and in particular to observe the target's motion along the unexcited axis. Three transient excitations were performed on the target with the same frequency and applied acceleration, with the only variable being the angle of the target about the Z-axis. Two-dimensional scatterplots of points the target occupied in the X-Y plane during the steady-state and damping periods were obtained, as shown in Fig. 7.

In Fig. 7(a), the target's X-axis is aligned with the shaker's X-axis, and so there is minimal cross-coupling along the shaker's Y-axis. In Fig. 7(b), however, the target has been rotated counterclockwise, evidently about 20° , as visible by the dense streak that indicates the target's X-axis, along which the target oscillates as it damps out. Under excitation,

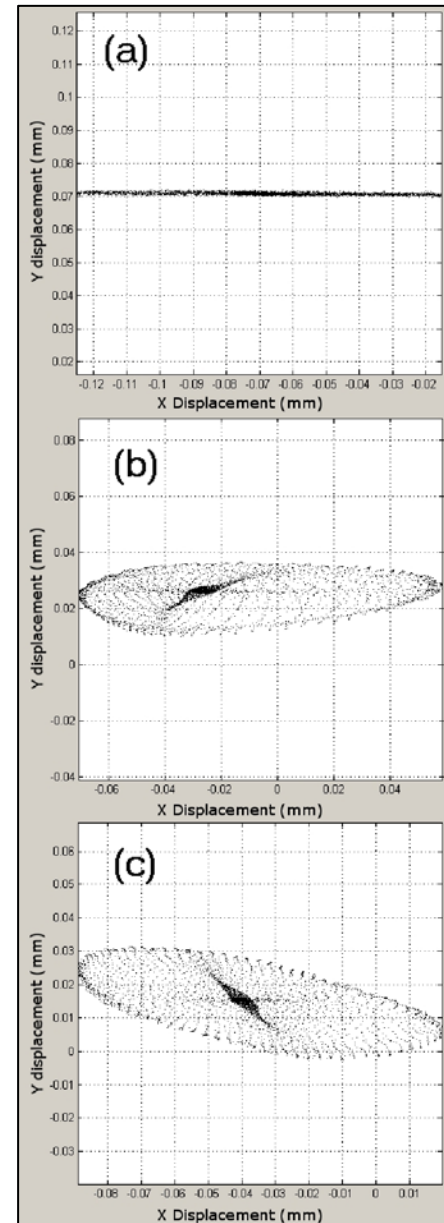


Fig. 7 X and Y target displacement with the target rotated at (a) 0° , (b) 20° , and (c) -45°

The target undergoes a complex motion path and displays cross-coupling when its principal axis is not aligned with the shaker's X-axis (b, c).

the target oscillates clockwise along the roughly elliptical perimeter, and when the excitation is turned off, the motion path gradually changes to follow the straight, dense streak in the direction of the target's orientation. After a while, the target transitions to oscillating counter-clockwise along the small, dense elliptical shape near its stationary point. Further research is needed to fully understand the complex path of the target, which incorporates factors such as precession and different damping ratios and resonance frequencies for both target axes. These results show that the target acts most like a single degree of freedom system when its principal axes are aligned with the shaker's direction of acceleration, which is why tests were done in the 0° and 90° orientations only. Figure 7(c) reinforces the correlation. Here the target is rotated clockwise from the original position to approximately 45° , and the target's motion as it damps out is very similar to that of Fig. 7(b).

3.4 Target construction and motion behavior

Type 1 polyimide targets of the kind shown in Fig. 1 were compared with an experimental SiC target to establish general trends. Also, polyimide targets have several variables where they differ in construction, mainly because they are still manually and individually fabricated. The effect of these variables on target motion was also explored.

The experimental SiC target closely resembles the standard Type 1 targets in construction, except that the polyimide stalk section is replaced by a SiC stalk of similar diameter. Therefore, this stalk is much stiffer and less compliant than the polyimide stalks. As the SiC target construction is similar to that of the polyimide target, it is still asymmetrical, and so there are two primary resonance frequencies, as shown in Table 6. Note that the SiC target resonance frequencies are more than double the resonance frequencies obtained for the Type 1 polyimide targets, at around 364 Hz and 373 Hz for the X and Y axes, respectively.

Table 6. Properties of an experimental SiC target

SiC target	X-axis	Y-axis
Resonance frequency	364.1 Hz	372.8 Hz
Resonance transmissibility	183 $\mu\text{m/gn}$	216 $\mu\text{m/gn}$
Damping ratio	0.38%	0.35%

Transmissibility and damping values for the SiC target are averaged values from both the half-power bandwidth and exponential decay methods.

Table 6 also shows that the resonance transmissibility in the SiC target is virtually cut in half, from around 400 $\mu\text{m/gn}$ to only around 200 $\mu\text{m/gn}$. This seems to support the trend that resonance modes at higher frequencies have lower transmissibility values. Furthermore, although the damping ratio is only around 0.4%, far lower than the 1% measured for Type 1 targets, this should not mean that the SiC target takes longer to reach a negligible amplitude than Type 1 targets. Preliminary tests indicate that due to the lower transmissibility causing a lower amplitude of oscillation, the total decay time to a negligible value for a SiC target is shorter than that of a Type 1 target, if both are given the same acceleration at resonance. Further testing of the total time needed for a target to reach negligible motion and the correlation with resonance frequency, transmissibility, and damping ratio is needed in order to confirm this hypothesis.

The three Type 1 targets tested showed variations in the diameter of the SiC stalk and the length of the polyimide stalk (see Table 7). These play a role in determining the overall stiffness of the target, which relates predictably to the target's resonance frequency, transmissibility, and damping ratio. In comparing the stiffer SiC target to the more compliant polyimide Type 1 target, it is seen that stiffer targets have a higher resonance frequency, lower transmissibility, and lower damping, given the same general target design but different materials. In Table 7, similar trends can be seen by comparing the properties of the type 1 targets.

Table 7 clearly shows a correlation between stiffness and resonance properties: Target 3, which has a thin SiC stalk and a long polyimide stalk, both making it more compliant, has the lowest resonance frequency of all three targets as well as the highest approximate

transmissibility. It is also the best damped, potentially due to the long polyimide stalk. Comparing targets 1 and 2 gives inconclusive results, because target 2 has a thicker SiC stalk than target 1, making it less compliant, but a longer polyimide stalk, making it more compliant.

Table 7. Target fabrication variables and resonance properties for Type 1 polyimide targets

	Target 1	Target 2	Target 3
SiC stalk diameter	17 μm	18 μm	16 μm
Polyimide stalk length	11.3 mm	11.7 mm	11.8 mm
Resonance frequency (X, Y)	148.8 Hz, 145.6 Hz	142.9 Hz, 150.9 Hz	134.1 Hz, 135.9 Hz
Resonance transmissibility	$\sim 400 \mu\text{m/gn}$	$\sim 400 \mu\text{m/gn}$	$\sim 450 \mu\text{m/gn}$
Damping ratio (X, Y)	1.1%, 1.1%	0.9%, 1.0%	1.2%, 1.1%

Based on these results, further research will focus on creating target structures that maintain small transmissibility and high resonance frequency but are better damped. One experimental target structure that could have these properties has a polar mount configuration, where two strands of a ductile heavy metal fluoride glass called ZBLAN [9] connect to the capsule at its two poles, held together with a C-frame.

4 Conclusions

Measurements were made to characterize the damping behavior at resonance of cryogenic fusion targets used in the OMEGA laser. Frequency, transmissibility, and damping ratio data at resonance were collected and analyzed. It has been shown that Type 1 polyimide targets have relatively high damping at around 1% of critical as measured by two independent methods, and that a high damping value comes at the cost of relatively high transmissibility, which makes for larger amplitude oscillations. Comparisons between Type 1 targets and with experimental SiC targets suggest that the stiffness of the target influences the target's resonance and damping characteristics in predictable ways, at least for single-stalk target designs such as

these. Future research will test these findings on a larger number of Type 1 targets and also focus on developing new types of target mounts in order to increase the resonance frequency, decrease the transmissibility, and increase the damping.

A GUI program, *Target Motion Characterization*, has been written that analyzes experimental data and displays high frame rate visualizations of the target's path of motion under complex excitations in three dimensions. The visualization indicates that these targets have two principal axes at right angles to each other and that the shaker needs to excite the target along one of these axes in order to minimize the amount of cross-coupling present in the target's motion.

Ultimately, the goal is to be able to measure the frequencies and amplitudes of excitations from the target chamber, replicate them using the shaker setup, and then optimize the target design to produce the least transmissibility and thus the least motion. This will eventually lead to reduced target motion at the time of the laser shot, leading to more accurate positioning of the target in the OMEGA chamber center and thus increasing the uniformity of the implosion.

Acknowledgements

I would like to thank Mr. L. D. Lund for being my research advisor and helping me with the project; Dr. R. S. Craxton for reviewing my findings and suggesting improvements for this report; Mr. M. Bonino for providing guidance and test targets; and Dr. D. R. Harding for his advice and suggestions for experiments to perform.

References

- [1] J. Nuckolls, L. Wood, A. Thiessen, and G. Zimmerman, "Laser compression of matter to super-high densities: thermonuclear (CTR) applications," *Nature*, vol. 239, pp. 139-142, Sept. 1972.
- [2] T. R. Boehly et al., "Initial performance results of the OMEGA laser system," *Optics Communications*, vol. 133, pp. 495-506, January 1997.
- [3] R. Orsagh et al., "Structural dynamics of cryogenic target assemblies," *LLE Review*, vol. 108, pp. 179-188, July-Sept. 2006.
- [4] D. R. Harding et al., "Producing cryogenic deuterium targets for experiments on OMEGA," *Fusion Science and Technology*, vol. 48, pp. 1299-1306, Nov. 2005.
- [5] T. C. Sangster et al., "Cryogenic DT and D₂ targets for inertial confinement fusion," *Physics of Plasmas*, vol. 14, pp. 1-10, April 2007.
- [6] H. S. Cho, *Optomechatronics: fusion of optical and mechatronic engineering*. Boca Raton, Florida: CRC Press, Taylor & Francis Group, LLC., 2006, pp. 189-192.
- [7] J. S. Bendat and A. G. Piersol, *Random Data: Analysis and Measurement Procedures, Third Edition*. New York: John Wiley & Sons, Inc., 2000, pp. 394-447.
- [8] A. D. Nashif, D. I. G. Jones, and J. P. Henderson, *Vibration Damping*. New York: John Wiley & Sons, Inc., 1985, pp. 117-154.
- [9] C. C. Chen, Y. J. Wu, and L. G. Hwa, "Temperature dependence of elastic properties of ZBLAN glasses," *Modern Chemistry and Physics*, vol. 65, pp. 306-309, Aug. 2000.